universität wien

DISSERTATION

Titel der Dissertation

„New approaches in the virtual reconstruction of fragmented specimens: applications in surgery, forensics, and anthropology“

Verfasser

Sascha Senck

angestrebter akademischer Grad

Doctor of Philosophy (PhD)

Wien, 2012

Studienkennzahl lt. Studienblatt:	A794685437
Dissertationsgebiet lt. Studienblatt:	Biologie
Betreuer:	Ao. Univ.-Prof. Dr. Gerhard W. Weber

To my father

Contents

List of Figures

List of Tables

ABSTRACT

The main theme of this thesis is how different scenarios of missing data estimation influence the uncertainty of virtual reconstructions. Using a combination of tools from Virtual Anthropology and Geometrics Morphometrics, a variety of problems is approached comprising major problems that arise during the anatomical reassembly of fragmented fossil crania and the geometrical reconstruction of missing data. The focus is on the quantitavive description of accuracies and uncertainties in fossil reconstructions using landmarks and semilandmarks from different reference samples. Furthermore, new approaches for the anatomical reconstruction of severly damaged crania are introduced.

When dealing with the reassembly of fragments in a virtual environment, every single step can be saved in a detailed protocol and used as a basis for subsequent modifications. This creates a large number of different reconstructions, considering the uncertainty of the reconstruction itself. Reconstructions of incomplete fossil specimens are needed in varying contexts from studies of ontogeny, phylogeny or biomechanics.

I exemplify these approaches by reconstructing several virtually fragmented specimens from extant and extinct species, and applying part of this information to the *Australopithecus afarensis* specimens A.L. 444-2. Furthermore I investigate morphological integration in the hominoid craniofacial complex, showing patterns of covariation that could be of potential help estimating the uncertainty in the anatomical reconstruction of fragmented specimens.

Das Hauptaugenmerk dieser Arbeit liegt auf der virtuellen Rekonstruktion von Schädeln, die sich durch das Fehlen eines großen Teils der Schädelknochen auszeichnen. Mithilfe von Methoden der virtuellen Anthropologie und Geometrischen Morphometrie kann dabei eine Vielzahl von Problemen konfrontiert werden, die während der Rekonstruktion von fragmentierten fossilen Schädeln entstehen können. Denn jede Schädelrekonstruktion weisst generell eine gewisse Ungenauigkeit auf. Diese wird von verschiedenen Faktoren beeinflusst, z.B. Größe der fehlenden Schädelteile oder der Rekonstruktionsmethode. Ein Schwerpunkt dieser Arbeit liegt deshalb in der Untersuchung der Auswirkungen verschiedener Faktoren auf die Ungenauigkeit fossiler Rekonstruktionen mithilfe von *landmarks* und *semilandmarks*. Darüber hinaus werden neue Ansätze für die anatomische Rekonstruktion von stark beschädigten Schädeln eingeführt.

Bei der Rekonstruktion von fossilen Schädelfragmenten in einer virtuellen Umgebung wird jeder einzelne Schritt in einem ausführlichen Protokoll gespeichert. Dies ermöglicht die Erstellung einer großen Anzahl von verschiedenen Rekonstruktionen. Da eine Rekonstruktion niemals perfekt sein wird, berücksichtigt dieser Ansatz das mangelnde Wissen darüber, wie das Original-Indiviuum wirklich aussah. Mit anderen Worten zeichnet sich jede Rekonstruktion durch einen gewissen Grad an Ungenauigkeit aus. Die Ermittlung dieser Ungenauigkeit ist umso wichtiger, da heute hohe Maßstäbe an die Qualität von virtuellen Modellen gestellt werden, die in unterschiedlichen Studien der Ontogenie, Phylogenie und Biomechanik eingesetzt werden.

Ich veranschauliche diese Ansätze durch die Rekonstruktion mehrerer virtuell fragmentierter Individuen und wende die gewonnenen Informationen unter anderem in der Rekonstruktion des *Australopithecus afarensis* Individuums A.L. 444-2 an. Desweiteren untersuche ich die morphologische Integration im kraniofazialen Komplex von Individuen der Überfamilie *Hominoidea*, um Kovariationsmuster aufzuzeigen, die während der Schätzung der Ungenauigkeit von anatomischen Rekonstruktionen von potenzieller Hilfe sein konnten.

CHAPTER 1: FOREWORD

1. FOREWORD

Most hominin cranial fossils are incomplete, whereas many conventional analyses of gross morphology require that specimens be complete. Different approaches for the imputation of missing data emerged in the last decade that found application in various fields such as craniomaxillofacial surgery (Benazzi et al., 2011b; Benazzi and Senck, 2011), bioarchaeology (Benazzi et al., 2009b), and anthropology (Ponce De León and Zollikofer, 1999; Neubauer et al., 2004; Grine et al., 2010; Watson et al., 2011). Reconstructions of incomplete fossil specimens were incorporated in varying contexts from studies of ontogeny (Gunz et al., 2010) and phylogeny (Gunz et al., 2009a) to biomechanics (Strait et al., 2010). Especially recent biomechanical analyses on primate skulls using finite element analysis (FEA) require a complete geometry of the input models (Strait et al., 2009; O'Higgins et al., 2011). Regardless of assumptions about functional constraints, integration, symmetry, species affinity, and taphonomy on which any reconstruction is based (Gunz et al., 2009b; Weber and Bookstein, 2011), the completeness of the skull is a fundamental pre-requisite. In virtual reconstructions that will be used as models for FEA, the geometry of the reconstructed missing area will substantially influence the transmission of forces and consequently the outcome of the analysis. In other words, the uncertainty of the shape of a reconstructed bone is influencing the uncertainty of the biomechanics because geometry is one of the central factors for these computations. Therefore, information about the uncertainty is needed to evaluate biomechanical analysis, i.e. one needs data on the shape variation of the resulting reconstructions prior to further analyses.

In my thesis I will address several issues that arise during the reconstruction of fragmented specimens:

(1) Anatomical reconstruction of fragmented specimens: a new approach:
During the anatomical reconstruction of fossils, isolated fragments have to be placed and oriented relative to each other. If there are no anatomical clues or constraints that guide the reconstruction, e.g. broken edges that clearly connect two parts, the result will show a degree of matching uncertainty. A way to estimate the positional interdependencies in the craniofacial complex is to apply morphological information of reference samples and use this information during the reconstruction process.

(2) Consequences of reference sample choice during geometric reconstruction:
Most hominin cranial fossils are incomplete, requiring reconstruction prior to deployment in subsequent analyses. However, complete reference crania from the same taxon are often absent for fossils. One part of my thesis will deal with the investigation of the consequences of intraspecies and interspecies reconstructions by estimating missing data in several virtually fragmented models of hominoid crania (extant and fossil). Using a sample of *Homo*, *Pan*, *Pongo* and several fossils I will investigate the posterior distribution and uncertainty of the generated multiple intraspecies and interspecies reconstructions.

(3) Morphological integration and facial orientation:
During the anatomical reconstruction of fossils, isolated fragments have to be placed and oriented relative to each other. If there are no anatomical clues or constraints that guide the reconstruction, the result will show a degree of matching uncertainty. A way to estimate the positional uncertainty of a structure in the craniofacial complex, for example of the face relative to the basicranium, is to investigate the integrational pattern of rigid relationships between these cranial modules in extant species. This information will yield estimations of the uncertainty of the modules´ position and can be of potential help during the reassembly of cranial (fossil) fragments.

The outcome of any analysis strongly depends on the level of preservation of skeletal remains. Fragments recovered from a fossil site, archaeological field, or crime scene are often incomplete, for example due to taphonomic processes that occur over time or because of damage during recovery. Consequently, an estimation of missing (craniofacial) bone is required to obtain a basis for subsequent analyses. Virtual reconstructions of fossil or historic specimens are used in a wide range of applications, ranging from biting simulations of *Australopithecines* (Strait et al., 2009; Strait et al., 2010) and soft tissue reconstruction in forensic cases (Claes et al., 2010). Regardless of assumptions about functional constraints, integration, symmetry, species affinity, and taphonomy on which any reconstruction is based (Gunz et al., 2009b; Weber and Bookstein, 2011), the completeness of the skull is a fundamental basic requirement.

Two basic methods for skull reconstruction can be recognized. 1) A traditional approach, that is time-consuming and prone to subjectivity where missing parts are manually moulded via modelling clay or plaster (Tattersall and Sawyer, 1996; Wilkinson and Neave, 2001; Kimbel et al., 2004a). 2) A computer-assisted approach which uses tools of Virtual

Anthropology in order to increase the reproducibility of the results using reference samples and quantitative methods (Weber et al. 2003; Gunz, 2005; Zollikofer and Ponce de Leon, 2005; Gunz et al., 2009b; Weber and Bookstein, 2011). The combination of virtual reconstruction and GMM offers a number of advantages compared to traditional reconstruction, amongst others expenditure of time and reproducibility. The first part of my thesis will deal with the anatomical reconstruction in different scenarios of missing data by employing standard procedures and introducing a new combination of methods of VA and GMM.

Particularly for fragmented fossils where no reference sample is available from the same species due to the scarcity of specimens, a careful assessment of the posterior distribution of the reconstructions (based on different references) is required. Zollikofer and Ponce de Leon (2005) have suggested that fossil reconstructions should use reference samples drawn from the same species as the specimen being reconstructed. Furthermore, the reference sample should represent the shared ancestral pattern of variation rather than patterns of variation characteristic of the derived taxa. The reason is to avoid biasing the reconstructions towards "preconceived morphologies". But this approach is problematic in view of the extremely small samples of fossil material available for many of the most interesting hominid species. In most cases it is impossible to collect a reference sample from the population to which the damaged fossil individual belonged. Guidelines are particularly needed for fragmented fossils for which no reference sample is available from the same species, or for which allocation to a species is disputed.

Gunz et al. (2009b) demonstrated reference sample dependency on reconstructed shape features of the supraorbital region in the *Homo erectus s.l.* specimen KNM-WT 15000. Nevertheless, the consequences of the choice of the reference on the outcome of the TPS reconstruction have not yet been studied for a larger sample consisting of several species. In this thesis I will investigate this aspect of virtual reconstruction. I will estimate missing data for hominoid crania using a geometric reconstruction using thin plate splines (TPS) in order to examine the resulting error, i.e. the posterior variance and posterior distribution of the reconstructions with regard to the choice of the reference sample. Not only the specific characteristics of the fossil, the reference sample, and the reconstruction method, but also the regions that are missing have an influence on the results. Since the combination of these factors lead to different estimations, there exists no ‘‘all-purpose’’ reconstruction. Different assumptions and reference samples will potentially lead to equally plausible reconstructions

that differ in shape, but these different estimates might still support a single conclusion (Gunz et al., 2009b). The knock-out analysis simulated in this part of the thesis is specifically tailored for the *Australopithecus afarensis* specimen A.L. 444-2 (Kimbel et al., 2004a), characterized by two separate and large missing areas in the face and the neurocranium. To explore the consequences of reference choice in a hominoid wide sample, I will extend the approach by estimating missing data for some other important fossils, i.e., Mladec 1, Petralona, and Sts 5 that were virtually fragmented by way of experiment. Thereby, I will gain data about the difference in accuracy and uncertainty for fossil reconstructions in comparison to the intraspecies and interspecies reconstructions of extant hominoids.

The orientation of the face relative to the basicranium (facial orientation or facial kyphosis) is highly variable in hominoids. This imposes a high degree of uncertainty when trying to reconstruct the maxillary position in fragmented specimens. One part of my thesis will therefore deal with the investigation of the covariation pattern of the rigid relationships among the maxillary bone and the cranial base in selected hominoid species (*Pongo pygmaeus*, *Pan troglodytes*). This will provide estimations of uncertainty for fossil reconstructions and information about associations of facial orientation with distinct features of the hominoid craniofacial complex.

During the anatomical reconstruction of fossils, isolated fragments have to be placed and oriented relative to each other, either applying a traditional approach in which fragments are manually placed and connected (Tobias, 1967; Kimbel et al., 1984; Kimbel and White, 1988; Kimbel et al., 2004; Caspari and Radovcic, 2006; Curnoe and Tobias, 2006) or a computer-assisted approach which uses tools of virtual anthropology (Zollikofer et al., 1998a; Ponce de Leon, 2002; Gunz, 2005; Zollikofer and Ponce de Leon, 2005; Gunz et al., 2009b; Benazzi et al. 2011). In three dimensions, any positioning of two objects introduces six degrees of freedom, three translational and three rotational, all of which are independent. As the number of fragments in a reconstruction increases, so does the uncertainty of matching, for example when fossil fragments are joined along eroded fracture lines. The principal source of uncertainty arises from the uncertain position of these fragments relative to each other. If there are no anatomical clues or constraints that guide the reconstruction, e.g. broken edges that clearly connect two parts, matching uncertainty may lead to error propagation over the reconstructed morphology as a whole (Zollikofer and Ponce de Leon, 2005).

A way to estimate the positional uncertainty of a structure in the craniofacial complex is to investigate the integrational pattern of rigid relationships between cranial modules in

extant species and apply this information during the reassembly of cranial fossil fragments. The idea is that the pattern of morphological covariation observed in the comparative sample helps to estimate the morphological covariation in the fossil specimen. To investigate changes in midfacial orientation and the shape of the cranial base that occur together, I analyze the patterns of their covariation using partial least squares (Rohlf and Corti, 2000). The partial least squares (PLS) method explores the interrelations between two or more blocks of observations. This provides estimations of uncertainty of the palate orientation, i.e. the degree of freedom of its rigid motion that may, among other things, help reconstructing hominid cranial fossils or forensic cases.

1. Zusammenfassung

Die meisten fossilen Schädel von Vor- und Frühmenschen sind unvollständig, zerbrochen oder deformiert. In vielen Fällen sind Schädelreste auch von einer Kombination dieser Faktoren betroffen. Viele gängige (statistische) Analysen der Morphologie und Anatomie setzen allerdings voraus, dass Individuen vollständig sind. Um dieser Tatsache gerecht zu werden, wurden unterschiedliche Ansätze für die Imputation der fehlenden Daten, d.h. die Vervollständigung der Datenmatrix, in den letzten Jahren entwickelt. Diese finden Anwendung in verschiedenen Bereichen wie Mund-, Kiefer- und Gesichtschirurgie (MKG, auch Kranio-Maxillo-Faziale Chirurgie; Benazzi et al., 2011a; Benazzi und Senck, 2011), Bioarchäologie (Benazzi et al., 2009b) und Anthropologie (Ponce de León und Zollikofer, 1999; Neubauer et al., 2004; Grine et al., 2010; Watson et al., 2011). Der Großteil dieser Ansätze verwendet einen computergestützen Ansatz, der Werkzeuge der virtuellen Anthropologie und Geometrischen Morphometrie (Geometrics Morphometrics) nutzt. Dadurch werden die Reproduzierbarkeit, der Zeitaufwand und der Schutz der Originalfragmente erhöht (Gunz, 2005; Zollikofer und Ponce de Leon, 2005; Gunz et al, 2009b; Weber und Bookstein, 2011). Im klinischen Bereich können operative Eingriffe simuliert werden und eine optimale Behandlung, zum Beispiel durch am Computer geplante und entworfene Prothesen, sichergestellt werden (Kokemueller et al., 2008).

Fossilien können nach ihrer Rekonstruktion in unterschiedlichen Bereichen wie Studien der Ontogenie (Gunz et al., 2010) und Phylogenie (Gunz et al., 2009a) oder der Biomechanik (Strait et al., 2010) verwendet werden. Speziell biomechanische Analysen von Primatenschädeln mithilfe der Finite-Elemente-Methode (FEM) stellen heute hohe Anforderungen an die Qualität von virtuellen Schädelmodellen (Strait et al, 2009; O'Higgins et al, 2011). Somit kann eine Rekonstruktion des fossilen Schädels zu einer obligatorischen Bedingung werden (Benazzi et al., 2011a). Unabhängig von Annahmen über funktionale Einschränkungen, Integration, Symmetrie, Artzugehörigkeit und Taphonomie, auf denen eine Rekonstruktion basiert (Gunz et al., 2009b; Weber und Bookstein, 2011), ist die Vollständigkeit des Schädels eine grundlegende Voraussetzung. In virtuellen Rekonstruktionen, die als Modelle in der FEM eingesetzt werden, hat die Geometrie der rekonstruierten Teile wesentlichen Einfluss auf die Übertragung von Kräften und beeinflusst damit das Ergebnis der Analyse. Mit anderen Worten, die Unsicherheit der Form eines rekonstruierten Knochens beeinflusst die Genauigkeit biomechanischer Untersuchungen, weil die Geometrie ein zentraler Faktor für die Berechnungen ist. Deshalb sind Informationen über

diese Unsicherheit, die während der Rekonstruktion auftreten, erforderlich. Zum einen, um die Verwendbarkeit solcher Rekonstruktionen für biomechanische Analysen zu bewerten - zum anderen um generelle Aussagen über den Informationsgehalt und den Informationsgewinn in morphologischen Studien durch die Verwendung von Rekonstruktionen zu untersuchen.

In meiner Dissertation werde ich auf einige Problemstellungen eingehen, die sich bei der Rekonstruktion von fragmentierten Schädeln ergeben:

(1) Anatomische Rekonstruktion von unvollständigen Individuen - ein neuer Ansatz:
Während der anatomischen Rekonstruktion von Fossilien müssen isolierte Fragmente platziert und zueinander ausgerichtet werden. Gibt es keine anatomischen Hinweise oder Einschränkungen, die ein zweifelsfreies Zusammenfügen ermöglichen, z. B. durch Bruchkanten, die eindeutig eine Verbindung aus zwei Teilen darstellen, wird das Ergebnis einen gewissen Grad von Unsicherheit bzw. Ungenauigkeit aufweisen. Eine Möglichkeit, um die Rekonstruktion in solchen Fällen zu erleichtern, ist die Einbindung der Informationen von Lagebeziehungen einzelner Module des kraniofazialen Komplexes (zum Beispiel der Schädelkalotte relativ zum Gesichtsschädel) und der Verwendung von grundlegenden Merkmalen des Säugerschädels (wie zum Beispiel der bilateralen Körpersymmetrie) anhand von Referenz-Stichproben (*reference samples*).

(2) Konsequenzen der Wahl des *reference samples* in der geometrischen Rekonstruktion:
Der Großteil der homininen fossilen Schädel ist unvollständig, was deren Rekonstruktion erfordert, bevor sie in nachfolgenden Analysen verwendet werden. Allerdings sind komplette Referenz-Schädel der gleichen Art in der Regel sehr selten für fossile Hominini. Ein Teil dieser Arbeit wird sich deswegen mit der Untersuchung der Folgen von Rekonstruktionen widmen, die fehlende Daten in künstlich fragmentierten Schädel-Modellen (rezent und fossil) schätzen. Besonderes Augenmerk wird dabei auf die Konsequenz der Wahl des *reference samples* gelegt, das heißt, es werden für die verschiedenen Rekonstruktion Individuen der gleichen und anderer Arten verwendet.

(3) Morphologische Integration und Orientierung des Oberkiefers:
Während der anatomischen Rekonstruktion von Fossilien müssen isolierte Fragmente platziert und relativ zueinander ausgerichtet werden. Wenn es keine anatomischen Hinweise oder

Einschränkungen gibt, die beim Zusammenfügen der Einzelteile hilfreich sein könnten, wird das Ergebnis einen Grad an Ungenauigkeit zeigen. Eine Möglichkeit, diese Unsicherheit der relativen Lage einer Struktur zu einer anderen im kraniofazialen Komplexes zu schätzen (zum Beispiel Gesicht relativ zur Schädelbasis), besteht in der Analyse der integrativen Muster der Lagebeziehungen zwischen diesen Schädel-Modulen in rezenten Arten. Diese Informationen können möglicherweise während der Rekonstruktion von (fossilen) Schädelfragmenten verwendet werden, liefern aber in jedem Fall Angaben über die Variation der Deklination beziehungsweise Elevation des harten Gaumens gegenüber der Schädelbasis.

Das Ergebnis einer Analyse der Schädelsmorphologie hängt stark vom Erhaltungsgrad der Knochenreste ab. Fragmente aus einer fossilen Fundstätte, einem archäologischen Feld oder einem Tatort sind oft unvollständig, zum Beispiel weil sie durch taphonomische Prozesse oder aufgrund von Schäden während der Bergung beschädigt wurden. Folglich kann eine Rekonstruktion der fehlenden (kraniofazialen) Knochenteile erforderlich werden, um die Grundlage für spätere Analysen zu schaffen. In der heutigen Zeit werden virtuelle Rekonstruktionen fossiler oder historische Fundstücke und Individuen in einer breiten Palette von Anwendungen eingesetzt, die von Kausimulationen in Australopithecinen (Strait et al., 2009; Strait et al., 2010) bis zur Weichteilrekonstruktion in forensischen Fällen (Claes et al., 2010) reichen.

Generell existieren zwei grundlegende Methoden zur Rekonstruktion von beschädigten und bruchstückhaft erhaltenen Knochen oder Schädeln: 1) Ein traditioneller Ansatz, der zeitaufwändig und anfällig für subjektive Einflüsse ist, und bei dem fehlende Teile manuell mithilfe von Modelliermasse oder Gips geformt werden (Tattersall und Sawyer, 1996; Wilkinson und Neave, 2001; Kimbel et al., 2004); 2) einen computergestützen Ansatz, der Werkzeuge der virtuellen Anthropologie nutzt, um die Genauigkeit und Reproduzierbarkeit der Ergebnisse mithilfe von *reference samples* und quantitativer Methoden, zu erhöhen (Gunz, 2005; Zollikofer und Ponce de Leon, 2005; Gunz et al., 2009b;. Weber und Bookstein, 2011). Die Kombination von virtuellen Rekonstruktionen und Geometrics Morphometrics bietet dabei eine Reihe von Vorteilen im Vergleich zu herkömmlichen Rekonstruktionen, unter anderem die Verringerung des Zeitaufwands und eine verbesserte Reproduzierbarkeit. Der erste Teil meiner Dissertation wird sich mit der anatomischen Rekonstruktion in verschiedenen Szenarien fehlender Schädelteile beschäftigen. Durch den Einsatz von mittlerweile standardisierten Rekonstruktionsmethoden und der Einführung einer neuen Kombination von Methoden der Virtuellen Anthopologie und

Geometrics Morphometrics werden verschiedene Fragestellungen angegangen. Das Ziel ist die Rekonstruktion von Schädeln, die einen großen Teil an fehlender Knochensubstanz aufweisen oder deren einzelne Schädelteile ohne Bruchkanten voneinander getrennt sind.

Besonders für fragmentierte Fossilien, bei denen kein *reference sample* der gleichen Spezies verfügbar ist, vor allem aufgrund der generellen Knappheit der kompletten fossilen Schädel, ist eine sorgfältige Bewertung der Variation verschiedener Rekonstruktionen (basierend auf den verschiedenen *reference samples*) erforderlich. Zollikofer und Ponce de Leon (2005) haben vorgeschlagen, dass fossile Rekonstruktionen ein *reference sample* der gleichen Spezies verwenden sollten. Darüber hinaus sollte das *reference sample* eher den letzten gemeinsamen Vorfahren repräsentieren, statt Individuen, die charakteristisch für die Art sind. Dadurch soll vermieden werden, dass die Rekonstruktion in eine bereits „vorgefasste„ Richtung verzerrt wird. Jedoch ist dieser Ansatz in Anbetracht der knappen Verfügbarkeit von komplettem fossilem Material für viele der interessantesten Hominiden problematisch. In den meisten Fällen ist es unmöglich, ein *reference sample* der gleichen Spezies, aus der das zu rekonstruierende Fossil stammt, zu finden. Daher sind Leitlinien für fragmentierte Fossilien, für die kein *reference sample* der gleichen Spezies zur Verfügung steht oder bei denen die Zuordnung zu einer Spezies umstritten ist, dringend notwendig.

Gunz et al. (2009b) zeigten eine Abhängigkeit der rekonstruierten Merkmale in der Supraorbitalgegend beim *Homo erectus s.l.* Individuum KNM-WT 15000 vom gewählten *reference sample*. Dennoch sind die Auswirkungen der Wahl des *reference samples* auf das Ergebnis von Rekonstruktionen, die auf *thin-plate splines* (TPS) basieren, noch nicht für eine größere Stichprobe (bestehend aus mehreren Arten) untersucht worden. In dem zweiten Teil der Doktorarbeit werde ich daher diesen Aspekt der virtuellen Rekonstruktion untersuchen. Ich werde fehlende Daten in hominiden Schädeln mithilfe der geometrischen Rekonstruktion (mithilfe von TPS) schätzen, um die daraus resultierenden Fehler zu untersuchen, d.h. die Verteilung der Rekonstruktionen im Hinblick auf die Wahl der Referenz. Nicht nur die spezifischen Eigenschaften des Individuums, sondern auch das *reference sample*, die Rekonstruktionsmethode und die Form der fehlenden Regionen haben einen Einfluss auf die Ergebnisse. Da die Kombination dieser Faktoren zu unterschiedlichen Einschätzungen führt, gibt es keine "Allzweck" - Rekonstruktion. Vielmehr können unterschiedliche Annahmen und *reference samples* potenziell zu gleichermaßen plausiblen Rekonstruktionen führen, die sich in ihrer Form unterscheiden. Dennoch können diese unterschiedlichen Rekonstruktionen die gleiche Schlussfolgerung unterstützen (Gunz et al., 2009b).

Die Knock-out-Analyse, die in diesem Teil der Arbeit simuliert wird, ist speziell auf das *Australopithecus afarensis* Individuum A.L. 444-2 (Kimbel et al., 2004) zugeschnitten, welches durch zwei große Lücken im Gesicht und Schädel charakterisiert wird. Diese Untersuchung wird Daten über die (Un-)Genauigkeit fossiler Rekonstruktionen in Bezug auf die Wahl des *reference samples* liefern, und somit wertvolle Information für die Rekonstruktion von Hominiden darstellen.

Ein weiterer Umstand, der die Rekonstruktion von fossilen Schädeln erschwert, ist die morphologische Variation in der Ausprägung von Merkmalen im kraniofazialen Komplex von Primaten. Ein Bespiel für diese variable Ausprägung ist die Orientierung des Gesichtsschädel relativ zur Schädelbasis (Deklination oder Elevation des Kieferschädels) in Hominiden. Dies resultiert in einem hohen Maß an Unsicherheit bei dem Versuch, die Position des Oberkiefers in fragmentierten Individuen zu rekonstruieren. Ein Teil meiner Arbeit wird sich daher mit der Untersuchung der Kovariation der Lagebeziehungen zwischen den Kieferknochen und der Schädelbasis in ausgewählten Arten (*Hylobates muelleri*, *Pongo pygmaeus*, *Pan troglodytes*) befassen. Dies ermöglicht Schätzungen über die Ungenauigkeit von fossilen Rekonstruktionen und liefert Informationen über die Kovariation der Oberkiefer – und Unterkieferorientierung mit unterschiedlichen Merkmalen des kraniofazialen Komplexes in Gibbons, Orangutans und Schimpasen.

Während der anatomischen Rekonstruktion von Fossilien müssen isolierte Fragmente platziert und ausgerichtet, entweder durch die Anwendung eines traditionellen Ansatz, bei dem Fragmente manuell platziert werden (Tobias, 1967; Kimbel et al., 1984; Kimbel and White, 1988; Kimbel et al., 2004; Caspari und Radovcic, 2006; Curnoe und Tobias, 2006) oder mithilfe eines computer-gestützten Ansatzes, der Werkzeuge der virtuellen Anthropologie verwendet (Zollikofer et al., 1998; Ponce de Leon, 2002; Gunz, 2005; Zollikofer und Ponce de Leon, 2005; Gunz et al., 2009b). In drei Dimensionen hat jede Positionierung zweier Objekte sechs Freiheitsgrade, drei translatorische und drei rotatorische, die alle unabhängig voneinander sind. Steigt die Anzahl der Fragmente in einer Rekonstruktion, steigt auch die Unsicherheit, mit die Fragmente relativ zueinander platziert werden, zum Beispiel wenn Bruchkanten von fossilen Fragmenten erodiert sind. Die Hauptquelle der Unsicherheit ergibt sich dabei aus der unsicheren Lage dieser Fragmente zueinander. Gibt es keine anatomischen Hinweise oder Einschränkungen, die bei der Rekonstruktion helfen könnten, z. B. durch klar definierte Bruchkanten, führt dies zu einer ansteigenden Unsicherheit, die sich auf die komplette Rekonstruktion auswirken kann (Zollikofer und Ponce de Leon, 2005).

Eine Möglichkeit die variablen Lagebeziehungen von Strukturen im kraniofazialen Komplex zu schätzen, ist die Untersuchung integrativer Muster, zum Beispiel zwischen Schädelbasis und Oberkiefer. Die Untersuchung der morphologischen Kovariation in einer rezenten Spezies kann potentiell helfen, Anhaltspunkte für die morphologische Kovariation in fossilen Spezies zu finden. Um den gegenseitigen Einfluss der Orientierung des Oberkiefers und der Form der Schädelbasis zu untersuchen, analysiere ich die Muster ihrer Kovariation mithilfe von *Partial Least Squares* (PLS; Rohlf und Corti, 2000). Dies ermöglicht Schätzungen der Variation der Oberkiefer-Orientierung, d.h. der Freiheitsgrade seiner „starren“ Bewegung. Dies kann zum einen bei der Rekonstruktion von Fossilien oder forensischen Fällen hilfreiche Informationen liefern, darüber hinaus aber auch neue Einsichten über die Kovariation in der Orientierung des Gesichtsschädels relativ zur Schädelbasis gewähren.

CHAPTER 2: INTRODUCTION

2. INTRODUCTION

2.1. Anatomical reconstructions of incomplete specimens

A crucial task for anthropologists and paleoanthropologists is the reconstruction of the appearance, posture, and dietary behaviour of extinct hominoids. In this context reconstruction means the attempt to assemble fossil remains in an anatomically "correct" manner, whereas restaurations are artistic interpretations how one individual of a species might have appeared. Reconstructions are not restricted to the reassembly of the physical appearance but also concern various aspects of the geological history, such as paleoclimate or bioarcheology. But all of these efforts have one goal in common: reconstructing human evolution by studying fossil remains, including all the accessible information available from its geological past.

If we seek a principled way to do such reconstructions some preconditions have to be satisfied. First a profound and comprehensive examination of the disturbances than can occur to biological forms has to be performed. Weber and Bookstein (2011) introduced four mjor types of disturbances that can be found when dealing with the reconstruction of forms:

Type 1: The original form is no longer available but all the parts of the original are present. The main task in this scenario is the reassembly of the single fragments, representing a kind of 3d jigsaw puzzle.

Type 2: Parts of the form are missing and have to be estimated. This will introduce a certain degree of uncertainty in the resulting reconstruction, depending on the amount of morphology missing.

Type 3: The original form is deformed. To correct the deformation one needs to have some knowledge of their quality. Since fossils often show a combination of the first three types, deformation in complex structures like crania are very difficult to correct.

Type 4: Foreign material like deposits and accumulation of sediments covered and/or penetrated the form, making parts of it inaccessible.

Since many fossil specimens that are discovered show a combination of these disturbances, there is no exact reconstruction because every step of restoring its original state introduces some uncertainty. Hence, a reconstruction can never duplicate the original but only represents an approximation (Weber and Bookstein, 2011). Nevertheless, we can make use of several basic principles of the skulls bauplan when reconstructing fossil crania, substantiating a principled way of carrying out reconstructions. By using information about bilateral

symmetry and the smoothness of structures, e.g. of the neurocranium, we can exploit general knowledge about factors constraining form. Furthermore, knowledge about group specific form factors can be used if the classification to a species is accurate. Then intraspecific information of autapomorphies and patterns of variation and covariation that characterize the concerned species can be exploited during the reconstruction process. Finally, individual form factors can serve to identify and correct deformations, e.g. if one side of the structure is complete and unaffected by deformation, additionally minimizing the uncertainties of a reconstruction (Gunz et al., 2005b; Gunz et al., 2009b; Weber and Bookstein, 2011). The following section will give a more comprehensive overview of the possibilities and pitfalls during the reconstruction process, and section 3.2.2.3 will give a more theoretical summary of methods of missing data estimation.

2.1.1. Traditional vs. virtual approaches

In this section I generally introduce reconstruction methods and compare traditional to virtual approaches, discussing the advantages and handicaps. Depending on the field of application, traditional approaches use gypsum, modelling clay, or dental wax. In paleoanthropology, a traditional way of reconstructing fossil specimens is to assemble the fossil remains around a solid core of plaster. The missing portions are afterwards filled with modelling gypsum (**Figure 1**). There are several main disadvantages that can be observed when employing this approach:

a) The resulting model is subject to gravity during drying, i.e. the position of the placed fragments can change during the reconstruction process. This introduces an error that is very difficult to correct after the model is completely hardened.
b) The process is very time consuming. Since there is no prefect solution for a reconstruction, it is desirable to have many alternative reconstructions to investigate the uncertainty of the results. The expenditure of time for the production of multiple reconstructions is therefore tremendous using traditional methods.
c) Missing parts are manually moulded (via gypsum) and therefore prone to subjectivity, because the reconstructor incorporates his own preconceptions into the final model.

Despite these disadvantages, traditional reconstructions persist until today (Tattersall and Sawyer, 1996; Wilkinson and Neave, 2001; Kimbel et al., 2004). An alternative approach, circumventing most of these disadvantages is presented by virtual anthropology and discussed

below. Dealing with fossil fragments in a computer environment protects the original fossil material and compensates for the influence of gravity that is imposed on every reconstruction in real life. Throughout the thesis the *Australopithecus afarensis* specimens A.L. 444-2 will be employed as an example for the use of reconstruction methods. Because it summarizes a set of difficulties that arise during reconstruction, no matter manually or in a virtual environment, it illustrates the limitations and preconceptions that are involved in every reconstruction process. Details about Australopithecines and A.L. 444-2 are presented in section 2.2.1.4 and 3.1.1.1.

Probably the most obvious disadvantage during traditional reconstructions is imposed by gravity. If a bony structure, e.g. a skull or a pelvis, is in a fragmentary state, the first step is the establishment of the physical stability of the whole structure. When assembling the single fragments (either the originals or casts of the originals), each fragment has to be precisely placed in order to glue the parts together, representing a major source of "gravitational" influence. Since the used glue or plaster has to dry, single parts can move during the time of drying, possibly introducing shifts and leading to an overall offset in the desired positions of the singles pieces. To prevent these movements, one can apply devices to stabilize single parts, e.g. wooden or plastic sticks. **Figure 1a** represents a traditional reconstruction of A.L. 444-2 showing wooden sticks that are stabilizing the neurocranium at the height of the porus acusticus externus. It is obvious that the resulting reconstruction looks rather fragile, making further investigations difficult. **Figure 1b** represents a different reconstruction of A.L. 444-2 in which the single fragments were assembled around a core of plaster. This reduces the risk that the fragments move and shift during drying, on the other hand requiring many steps of manually adjusting the inner core to accommodate the single fragments.

In contrast, working in a virtual environment, gravity does not influence the reconstruction process. In addition, each fragment can be moved in three dimensions without the risk of damage. Another advantage is that visualization parameters can be changed to improve the look of the scene and fragments can be colored for the ease of identification. Furthermore, helpful virtual tools like surface deformation maps can be applied to assist during the identification of cracks, sutures, and topography (**Figure 2**). A disadvantage that is shared with traditional methods that use casts is the loss of color information, i.e. texture. This information could potentially help to check if breaking edges were a consequence of taphonomic processes or originated from post mortem damage during the recovery. Also surface patches, characterized by colored sedimentary deposits can be of potential use during the reassembly of fossil fragments.

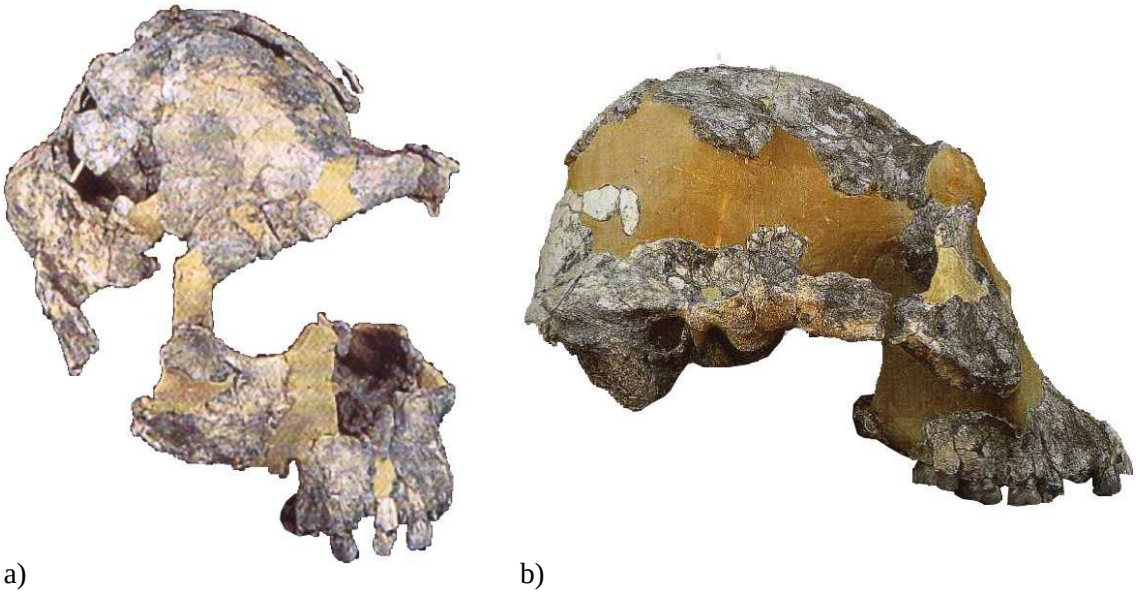

a) b)

Figure 1 A.L. 444-2. Reconstructions using traditional methods. a) assembly of single fragments using wooden sticks (connecting the posterior calvaria and the right parietal fragment) as supporting structures (source: http://www.modernhumanorigins.net/al444-2.html; photograph by Donald Johanson). b) reconstruction around a inner core consisting of plaster (source: Johansson and Edgar, From Lucy To Language, 2006; photograph by William H. Kimbel)

The second major advantage of virtual approaches is minimizing the expenditure of time. During traditional reconstructions, for every single model that is created one needs to produce the casts of all the fragments that are used. Then, every reconstruction has to begin from the scratch, discarding the potential clues that were made during the former reconstruction, for example from the continuity of muscle attachments. Since there is no perfect precision when working manually, it is impossible to produce the same configuration twice, e.g. when one intends to leave one part of the reconstruction unchanged. This is of interest when investigating the posterior distribution of multiple reconstructions (Gunz et al., 2009b; Benazzi et al., 2011a). Most of the traditional approaches did not explicitly assume any uncertainty in the produced reconstruction, mainly because the expenditure of time to produce several alternative models is tremendous.

When dealing with the reassembly of fragments in a virtual environment, every single step can be saved and used as a basis for subsequent modifications. This creates a large number of different reconstructions, considering the uncertainty of the reconstruction itself. Since no reconstruction will ever be perfect, this approach takes our lack of knowledge into account how exactly the individual to be reconstructed really looked like. Yet, even though the computer environment yields transformation matrices of arbitrary precision, these interactions are not objective (Gunz, 2005). One has to be aware that any estimation of missing parts, whether manually or in a computer environment is based on assumptions. Even

though this affects both approaches, virtual reconstructions allow the production of multiple models in a shorter time compared to traditional methods. The different models that were produced using specific protocols can then be treated as separate individuals in a principal component analysis (Zollikofer et al., 2005; Gunz et al., 2009b; Benazzi et al., 2011a). The variation between the reconstructions that are due to different assumptions can thus be evaluated in the light of the scientifc question (Gunz, 2005).

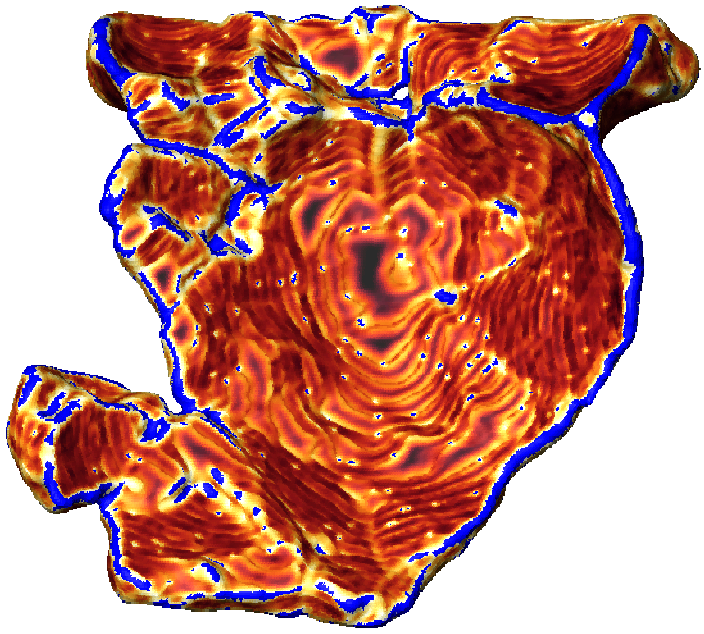

Figure 2 A.L. 444-2 frontal bone. The color gradient codes the mean of the two principal curvatures computed for each triangle. Areas with dark grey areas show the least curvature, bright yellow indicate pornounced curvature, blue represents curvature that are out of the color gradient and represent (breaking) edges.

A good example for the preconceptions that are incorporated in each reconstruction, and that can be overwhelming depending on the degree of missing data, is the composite reconstruction of Kimbel et al. (1984; 1988). This composite skull consists of 12 specimens and was created to overcome the lack of complete *Australopithecus afarensis* specimens until the recovery of A.L. 444-2 and A.L. 822-1. Because the sample consists of various specimens, the authors not only had to deal with missing data but also with the variability within this sample. Since neither sex nor age of the fragments could be determined without doubt, the composite reconstruction was highly assumptious. Furthermore, there is an ongoing discussion about the level of sexual dimorphism and about patterns of allometry that complicates the interpretation of the results (Leutenegger and Shell, 1987; Henry M, 1991; Richmond and Jungers, 1995; Lockwood et al., 1996; Plavcan et al., 2005; Reno et al., 2005;

S.-H, 2005; Seth D, 2005; Scott and Stroik, 2006). Evaluating their composite reconstruction in the light of the A.L. 444-2 skull, Kimbel et al. (2004a) find several differences between the two specimens that may be due to a priori preconceptions that were incorporated. They state that the "very flat slope and low elevation of the frontal in the composite reconstruction have been recognized as partly artificial […], which is now confirmed by the new Hadar skull" (p. 112). Another source of uncertainty in the composite reconstruction was the placing of the facial skeleton. By rotating the viscerocranium ventrally, they produced a "more klinorynch hafting of the face on the brain case, as suggested by A.L. 444-2, and, at the same time, necessitate the steeper frontal squama" (p. 112). The variation in facial orientation leads to a less apelike forward projection of the palate (relative to sellion) in A.L. 444-2 than does the composite reconstruction. Finally, Kimbel et al. (2004a) acknowledge the pitfalls during the reconstruction process, especially in a composite reconstruction:
"As a further illustration of the hazards involved with joining skull components of different individuals, we note that the maxillary dental arcade of A.L. 417-1d occludes nearly perfectly with Lucy's mandible, A.L. 288-1i; yet substantially shallower total facial height is achieved with this artificial combination than when A.L. 417-1d is occluded with its own, much deeper, mandible (417a)! (p. 113)".

Another field of research that is representing a good example for the transition from traditional, manual methods to modern, virtual tools is forensics, espeacially in the context of soft tissue reconstruction. When human skeletal remains are recovered in a forensic context, physical anthropological procedures are used for bone reconstruction and individual identification (Krogman and İşcan, 1986). Based on the analysis of bones, the biological profile of the individual which consists in determining sex, age, ethnic group, pathologies, or traumata is assessed (Krogman and İşcan, 1986; Cattaneo, 2007). Mainly in forensic anthropology but also in bioarchaology, if a general description of the individual does not elicit a possible match from the missing persons list or the historic figure under study, the next step is an attempt to reconstruct the face from the skull (Gerasimov, 1971). In such cases, the craniofacial skeleton is used for facial approximation based on soft tissue thickness data taken on specific facial areas (Gerasimov, 1971; Krogman and İşcan, 1986; Iscan and Helmer, 1993). The outcome of the analysis strongly depends on the level of preservation of skeletal remains. Skeletons recovered from a crime scene or archaeological field are often incomplete because of animal scavenging, perimortem injuries, damage due to explosion or conflagration, damage during recovery, or due to taphonomic processes over time (Krogman and İşcan,

1986). Consequently, an estimation of missing craniofacial bone is required to have the basis for soft tissue reconstruction. The recovery of the craniofacial skeleton in a fragmentary state significantly impedes any attempted facial reconstruction (both by manual techniques - regularly described as “forensic art” (Prag and Neave, 1997; Taylor, 2001; Wilkinson, 2004) - and by computer-aided methods for facial reconstruction (Clement and Marks, 2005; Claes et al., 2006; Vandermeulen et al., 2006; Claes et al., 2010)) and skull-photo/painting (usually portraits for historical figures) superimposition (Glaister and Brash, 1937; Koelmeyer, 1982; Brown, 1982 ; Ubelaker et al., 1992; Bajnóczky and Királyfalvi, 1995; Yoshino et al., 1997; Solla and Iscan, 2001; Iscan et al., 2005; Benazzi et al., 2009b; Benazzi et al., 2010)). Regardless of the accuracy, limits, and merits of facial reconstruction and skull-photo/painting superimposition techniques, the completeness of the skull is a fundamental pre-requisite. Two basic methods for skull reconstruction can be recognized. 1) A traditional approach, that is time-consuming and prone to subjectivity where missing parts are manually moulded via dental wax or hot paste employing organic and inorganic component (Wilkinson and Neave, 2001; Wilkinson, 2006). 2) A computer-assisted approach which uses tools of Virtual Anthropology in order to increase the reproducibility of the results using metric techniques (Zollikofer et al., 1995; Zollikofer et al., 1998b; Neubauer et al., 2004; Gunz, 2005; Zollikofer and Ponce de Leon, 2005; Zollikofer et al., 2005).

2.1.1.1. Virtual reconstructions of fossils: introducing the standard approaches

Using the standard toolkit of VA and GMM including mirror imaging, reflected relabeling, and thin-plate splines I reconstructed several aspects of the *Australopithecus afarensis* specimens A.L. 444-2 (**Figure 3**). The detailed reconstruction protocols are given in the results chapters.

a) Frontal bone: the left side of the frontoparietal fragment (**Figure 3a**) is mostly intact and minimally deformed. Plastic deformation has affected the right side of the specimen through moderate superomedial rotation of the supraorbital region and adjacent temporal surface. The ends of both zygomatic processes, the glabellar mass and adjacent medial orbital walls, the inferior part of the right temporal surface and almost all of the floor of the anterior cranial fossa are missing. This fragment is retro-deformed by restoring bilateral symmetry using a best-fit midplane.
b) The posterior calvarium originally consists of three major pieces: the occipital squama with an attached fragment of the posterior right parietal bone and parts of the two temporal bones, including the petrous portions (**Figure 3b**). The two halves of the

occipital were originally compressed toward the midline, thus the parts were overlapping in the nuchal plane along a sagittally oriented break that approximates the midline. Kimbel et al. (2004a) separated the two halves and reattached them along the break in their "proper" position (p.16), but still the left and right halves of the nuchal plane are offset vertically "by 2 to 3 mm". To correct this offset and restoring bilateral symmetry I used reflection relabelling, a method described in section 3.2.3.2.2.

c) Mandible: The right side and anterior corpus of the mandible were recovered in three pieces, not including teeth (**Figure 3c**). Since the corpus is broken along a line running from the left I2/C interdental septum diagonally to the base below the right canine, several steps of manual alignment were carried out.

d) The maxilla was recovered in three primary pieces: the entire right half, the left half anterior to the M2 position, and the alveolar bone and parts of the maxillary sinus walls (**Figure 3d**). It is both plastically deformed and broken along a major crack that runs anterior-posteriorly, thus several steps including mirror-imaging and TPS had to be applied.

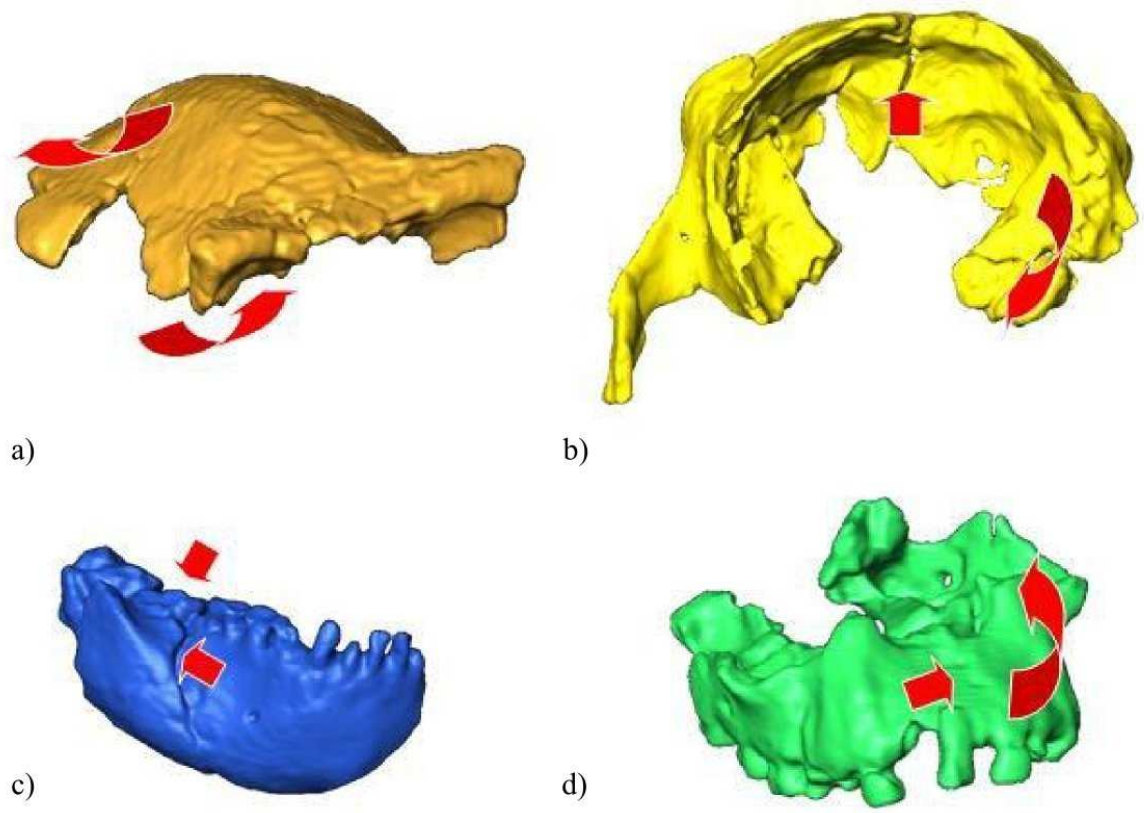

Figure 3 Major parts of the A.L. 444-2 cranium. a) frontal bone, b) posterior calvaria, c) mandible, and d) maxilla. Straight red arrows inidicate major cracks, rolling arrows indicate areas of morphological deformation due to taphonomic processes

Furthermore, I reconstructed the endocast of the Cioclovina Upper Paleolithic calvarium, one of the earliest reliably dated European modern human fossils (Figure 4). Endocasts both natural and virtual can provide evidence on size and shape characteristics, blood supply trajectories and neurological features of the brain. This information could not be assessed otherwise for fossil individuals, allowing comparative analyses crucial to our understanding of human brain evolution. For example, Prossinger et al. (2003) applied filter algorithms and image editing techniques to volume data of the Homo heidelbergensis cranium from Steinheim to electronically remove encrustations. In doing so, they were able to reveal the directions of its deformations and showed the similarities and differences between the frontal and sphenoidal sinuses of the Steinheim, Petralona, and Broken Hill (Kabwe) crania.
Cioclovina is one of the earliest reliably dated modern human fossils found in Europe. This example is illustrates one of the major advantages of VA: being able to visualize internal structures of the cranium is in a non-invasive manner.[1]

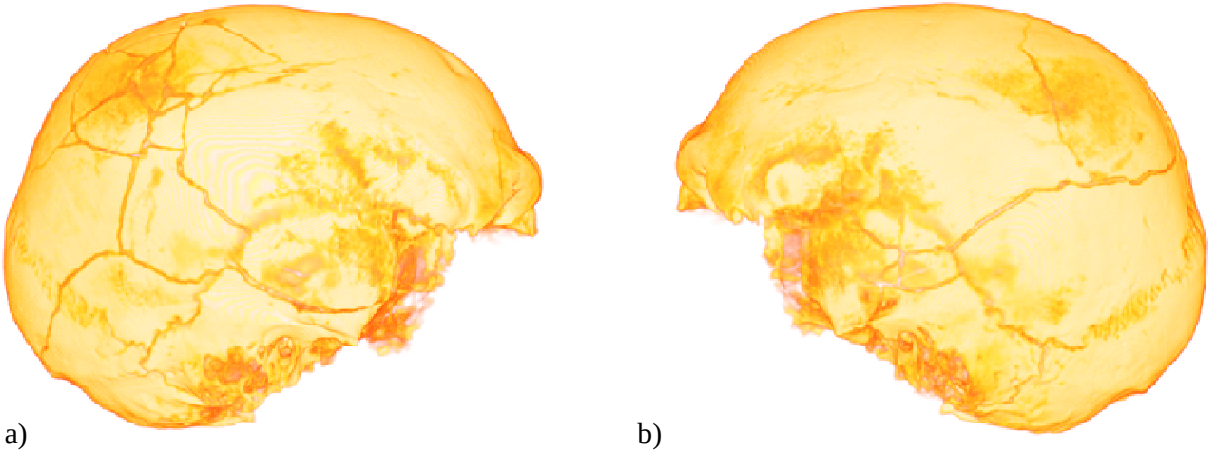

a) b)

Figure 4 Cioclovina cranium from the a) right and b) left side. Using the volume texture display mode it is possible to visualize differences in density distribution, showing major cracks characterizing the specimens

2.1.2. Beyond mirror imaging: New approaches during anatomical reconstructions

Here, I provide a pilot study for the virtual reconstruction of specimens that are missing a large portion of the cranium, including the midsagittal plane. Thus the use of mirror imaging, a standard procedure in the reconstruction process, is impossible. In contrast to traditional

[1] This reconstruction has been published in: Kranioti et al. (2011). "Virtual Assessment of the Endocranial Morphology of the Early Modern European Fossil Calvaria From Cioclovina, Romania." The Anatomical Record: Advances in Integrative Anatomy and Evolutionary Biology 294(7): 1083-1092.

methods this virtual approach is not as time consuming and exploits biological information based on a reference sample and quantitative methods.

The outcome of any analysis strongly depends on the level of preservation of skeletal remains. Fragments recovered from a fossil site, archaeological field, or crime scene are often incomplete, for example due to taphonomic processes that occur over time or because of damage during recovery. Consequently, an estimation of missing (craniofacial) bone is required to have the basis for subsequent analyses. Virtual reconstructions of fossil or historic specimens are used in a wide range of applications, ranging from biting simulations of *Australopithecines* (Strait and Ross, 1999) and soft tissue reconstruction in forensic cases (Claes et al., 2010). Regardless of assumptions about functional constraints, integration, symmetry, species affinity, and taphonomy on which any reconstruction is based (Gunz et al., 2009b; Weber and Bookstein, 2011), the completeness of the skull is a fundamental pre-requisite.

Two basic methods for skull reconstruction can be recognized: 1) a traditional approach, and 2) a computer-assisted approach which uses tools of Virtual Anthropology and Geometric Morphometrics (GMM). The combination of virtual reconstruction and GMM offers a number of advantages compared to traditional reconstruction, amongst others expenditure of time and reproducibility. The present study reviews two difficult cases that often appear in the various fields mentioned above, but that exceed the limits of traditional approaches:

a) A large part of the cranium is missing but a smaller fraction of the mid-sagittal plane is still preserved, and
b) A large part of the cranium is missing but there is no clue to the actual midsagittal plane.

While in the first case mirror imaging can be used to restore the bilateral symmetry of the specimen, the second case imposes a number of difficulties when applying a traditional approach. Since one cannot establish a midsagittal plane that could be used to mirror the existing part, restoring bilateral symmetry by simple mirror imaging is impossible.

To introduce the new approach, I virtually produce two damaged cases for a) and b) and reconstruct the missing parts using tools from the Virtual Anthropology and geometric morphometric methods (GMM) (Bookstein, 1991b; Gunz et al., 2009b; Neeser et al., 2009). In the first case, mirroring can be used along with GMM because the midsagittal plane is partially preserved. In the second case, the position of the midsagittal plane is estimated based on a sample of reference specimens before subsequent reconstruction steps. Both procedures involve bilateral symmetry as the main assumption for reconstruction, thus the resulting forms

are symmetrized whereas the original crania would have shown directional or fluctuating asymmetry to various extents (Mardia et al., 2000). However, the advantage of this method is that it can be applied in cases where traditional approaches would fail due to the large amount of missing data. Due to the time and effort needed to build this pilot study, the amount of virtually damaged cases is limited, including instead a very extreme case of bone loss in order to demonstrate the applicability of the approach. To estimate the accuracy of the two knockout simulations, the residuals between (semi)landmarks of the original individual and each reconstruction are computed. Furthermore, the effects of the choice of the reference form - dolichocephaly versus brachycephaly, sexual dimorphism and asymmetry - on the accuracy of the reconstructions are evaluated.

2.1.2.1. Applying the new approach on fossil data: maxilla and A.L. 444-2

Since half of the maxilla is severely deformed (**see Figure 3**), missing portions have to be estimated. But there is a major difficulty: in such cases simple mirror imaging or reflected relabelling cannot be applied - there is just too much morphological information missing. The approach introduced above could provide a tool to deal with these difficult scenarios. Using the information of a more or less complete *Australopithecus afarensis* maxilla (A.L. 200-1), I am trying to reconstruct these fragments. By using the best-fit midsagittal plane of the reference specimen I examplify the procedures described above for fossil cases. The results are then compared to the original reconstruction by Kimbel at al. (2004a).

2.1.3. Comparing 3-dimensional virtual methods for reconstruction in craniomaxillofacial surgery[2]

Another field where tools of virtual anthropology and geometric morphometrics are applied is surgery. The introduction of computer-assisted preoperative planning (CAPP) and computer-assisted surgery (CAS) has improved the outcome of cranio-maxillofacial surgical intervention in the last decade (Kokemueller et al., 2008). Advances in imaging techniques and with the help of CAD/CAM software provide the surgeon an opportunity to preoperatively perform virtual manipulations of the patients´ CT data (Pham et al., 2007). Doing so, the entire surgical procedure is simulated in the computer, and a physical model of

[2] This analysis is published in: Benazzi and Senck (2011) Comparing 3-Dimensional Virtual Methods for Reconstruction in Craniomaxillofacial Surgery. Journal of Oral and Maxillofacial Surgery 69(4): 1184-1194. Both authors participated equally in the composition of the publication.

the planned outcome can be produced (Wong et al., 2005; Gateno et al., 2007; Xia et al., 2007).

Preoperative planning is therefore crucial in two ways: a) to investigate the problem that has to be solved, and b) to find the best solution using less invasive procedures (Hassfeld and Mühling, 2001). In the last years several preoperative planning procedures were introduced and several applications were developed for their simplification. Several software packages provide facilities to perform translations of 3D objects in a virtual space (see section 3.2.1.3), which is useful in the repositioning of displaced craniofacial elements. Pham et al. (2007) developed a technique for back conversion of the MIMICS software to DICOM format. Surgeons were able to perform complex virtual reconstructions with MIMICS software and then converted the data to DICOM for use in any surgical navigation device. Mischkowski et al. (2006) developed software for the visual tracking of real anatomical structures in superimposition with 3D rendered CT or MRI scans for navigated translocation of bony segments. Furthermore, some surgeons prefer to simulate surgery on physical models produced by rapid prototyping techniques (RPT), usually stereolithography, onto which it is possible to customize implants or to precontour fixation plates. Starting from a three-dimensional mesh a model is built slice by slice from bottom to top, in a basin of liquid polymer that hardens when struck by a laser beam (Weber and Bookstein, 2011).

This information can be directly transferred to the patient by point-to-point computer assisted navigation, e.g. using the position of screws defined a priori (Klug et al., 2006). Nevertheless, other researchers emphasized some limitations of this approach, e.g. a bias of model reshaping due to the artistic aptitude of the technician and its reductive utility in certain complex situations (Wong et al., 2005).

Independent of the approach, the aim of operation planning in oral and maxillofacial surgery is optimising the surgical outcome, thus restoring function, form and aesthetic appearance (Hassfeld and Mühling, 2001; Schmelzeisen et al., 2004; Kokemueller et al., 2008; Voss et al., 2009). Aesthetic appearance is moreover connected with the correction of facial asymmetry to a certain degree. In order to restore facial symmetry, a standard procedure for preoperative planning is performed using mirroring imaging if the defect is unilateral, reconstructing the asymmetric portion with its normal counterpart working as a reference (Schmelzeisen et al., 2004; Hohlweg-Majert et al., 2005; Wong et al., 2005; Gateno et al., 2007; Kokemueller et al., 2008). Nevertheless, Metzger et al. (2007), after comparing the preoperative planning by mirroring of the unaffected side to the affected side with the surgical outcome, verified that the accuracy of this approach could be influenced by the natural

asymmetry of the skulls. They demonstrated that the reposition of the zygomatic bone remains a challenge despite CAS procedures. Even if some inaccuracy in surgical reconstruction could be masked by natural asymmetry of faces, the authors suggested that for large defects other planning tools, e.g. dynamic 3D deformation, should be used.

It is well recognized that asymmetry characterizes human paired and unpaired skeletal segments (Auerbach and Ruff, 2006; Gawlikowska et al., 2007; Auerbach and Raxter, 2008). In regard to the skull, particularly for facial bones, the more asymmetric the shape, the less reliable is the establishment of the midsagittal plane that is essential for mirroring procedures. Accordingly, mirroring the unaffected side in more or less symmetric skulls/faces could be a proper solution for bone reconstruction, while for more asymmetric skulls/faces other solutions are required.

Techniques for bone reconstruction based on geometric morphometric methods (GMM) that were developed in anthropology and paleoanthropology provide valuable ressources for the restoration of form and function in the surgical field. By means of virtual reconstructions, the problems related to asymmetry, deformation (Ogihara et al., 2006) and missing data can be approached (Gunz et al., 2004; Gunz et al., 2005b; Benazzi et al., 2009a; Benazzi et al., 2009b), while at the same time minimizing subjective choices of the operator and raise the reliability and reproducibility of the outcome (Benazzi, 2009a; Weber and Bookstein, 2011).

To show that virtual reconstructions are a valuable tool in preoperative planning, a virtual osteotomy of the left zygomatic bone of fifteen CT data-based human skulls was performed. The outcomes of three virtual reconstruction techniques were compared to the original removed bone: 1) the mirroring of the unaffected hemiface; 2) mirroring and subsequent registration of the unaffected hemiface onto the affected side; 3) thin plate spline (TPS) warping of the mirroring unaffected hemiface onto the affected side.

2.2. Virtual reconstruction of modern and fossil hominoid crania: consequences of reference sample choice[3]

Most hominin cranial fossils are incomplete, whereas many conventional analyses of gross morphology require that specimens be complete. Different approaches for the imputation of

[3] This topic has been presented at the AAPA 2011: Senck et al. (2011) Cross-species virtual reconstruction of fossil and extant hominoid crania. AMERICAN JOURNAL OF PHYSICAL ANTHROPOLOGY Volume: 144, Supplement: 52, Pages: 269-270

missing data emerged in the last decade that found application in various fields such as craniomaxillofacial surgery (Benazzi et al., 2011b; Benazzi and Senck, 2011), bioarchaeology (Benazzi et al., 2009b), and anthropology (Ponce De León and Zollikofer, 1999; Neubauer et al., 2004; Grine et al., 2010; Watson et al., 2011). Reconstructions of incomplete fossil specimens were incorporated in varying contexts from studies of ontogeny (Gunz et al., 2010) and phylogeny (Gunz et al., 2009a) to biomechanics (Strait et al., 2009; Strait et al., 2010). Especially recent biomechanical analyses on primate skulls using finite element analysis (FEA) set high standards on the quality of virtual models (Strait et al., 2009; O'Higgins et al., 2011; Weber et al. 2011). Thus a reconstruction of various aspects of the fossil skull can be mandatory (Benazzi et al., 2011a). Regardless of assumptions about functional constraints, integration, symmetry, species affinity, and taphonomy on which any reconstruction is based (Gunz et al., 2009b; Weber and Bookstein, 2011), the completeness of the skull is a fundamental pre-requisite. In virtual reconstructions that will be used as models for FEA, the geometry of the reconstructed missing area will substantially influence the transmission of forces and consequently the outcome of the analysis. In other words, the uncertainty of the shape of a reconstructed bone is influencing the uncertainty of the biomechanics because geometry is one of the central factors for these computations. Therefore, information about the uncertainty is needed to evaluate biomechanical analysis, i.e. one needs data on the shape variation of the resulting reconstructions prior to further biomechanic simulations. Particularly for fragmented fossils where no reference sample is available from the same species due to the scarcity of specimens, a careful assessment of the posterior distribution of the reconstructions (based on different references) is required.

Zollikofer and Ponce de Leon (2005) have suggested that fossil reconstructions should use reference samples drawn from the same species as the specimen being reconstructed. Furthermore, the reference sample should represent the shared ancestral pattern of variation rather than patterns of variation characteristic of the derived taxa. The reason is to avoid biasing the reconstructions towards "preconceived morphologies". But this approach is problematic in view of the extremely small samples of fossil material available for many of the most interesting hominid species. In most cases it is impossible to collect a reference sample from the population to which the damaged fossil individual belonged. Beyond that, the allocation to a particular taxon is often disputed among experts. Guidelines are particularly needed for fragmented fossils for which no reference sample is available from the same species, or for which allocation to a species is disputed.

One way to deal with the choice of reference is to employ a statistical reconstruction, utilizing group form constraints (Weber and Bookstein, 2011), e.g. by applying a multiple multivariate regression. This approach exploits the morphological information present in a reference group or population (Gunz, 2005). Regression-based methods assume that there is a strong statistical pattern describing the "integration" - the covariance - of the features that make up the morphological pattern. The available morphological information from the damaged specimen combined with pattern information from undamaged specimens to estimate morphology in the missing regions.

Concerning the choice of the reference, Neeser et al. (Neeser et al., 2009) claimed that "morphological similarity appears to be of less importance than large reference samples" [p.16] which "is likely due to the shared, and presumably evolutionarily conserved, pattern of covariation seen across the primate order" [p.16]. It is their view that exploiting information from integration patterns for the estimation of missing data can overcome the deficiency of a small or missing reference sample. Neeser and colleagues simulated random knockout of points using a dataset of 29 anatomical landmarks and concluded that regression-based methods outperform TPS-based estimation when using such a sparse anatomical representation. But as Gunz et al. (2009b) pointed out, the 29 landmarks used in Neeser et al. (2009) do not capture the morphology of the reference and target specimen in sufficient detail to make any reliable prediction of missing coordinates. The data configuration they used did not incorporate semilandmarks in large unattended regions. I will show in this part of the thesis that including semilandmarks in the process of missing data estimation improves the results considerably compared to Neeser et al. (2009).

Another disadvantage using multiple linear regression is that the linear relationship is "overfitted" in the case when the completed forms are used in the statistical analyses. For this reason Gunz et al. (Gunz et al., 2009b) recommended geometric reconstruction rather than regression-based methods. Geometric reconstruction is based on the smoothness properties of the thin-plate spline and requires only a single reference form (template), which might be the Procrustes mean shape of a species. But the consequences of the choice of the reference on the outcome of the TPS reconstruction have not yet been studied for a larger sample consisting of several species. For example, Gunz et al. (2009b) demonstrated reference sample dependency on reconstructed shape features of the supraorbital region in the *Homo erectus* s.l. specimen KNM-WT 15000. The authors showed that the reconstructed outlines of the orbits and the glabellar region are slightly but consistently different depending on the group of the reference specimen. They showed that the posterior distribution of the

reconstructions reflects the shape differences among the reference crania that served as references (the prior distribution) used to estimate the missing data. Consequently, using a modern human sample as reference, the reconstructed area looks like a modern human while a chimpanzee reference sample produces reconstructions that look like apes. By investigating the consequences in an extended interspecies sample including many species and therefore a wide range of hominoid craniofacial morphology, one can investigate the uncertainty produced during the reconstruction process.

In this study I aim to investigate this aspect of virtual reconstruction. I estimate missing data for hominoid crania using TPS in order to examine the resulting error, i.e. the posterior variance and posterior distribution (expressed as the distance between the original and the reconstruction) of the reconstructions with regard to the choice of the reference sample. Not only the specific characteristics of the fossil, the reference sample, and the reconstruction method, but also the regions that are missing have an influence on the results. The task of reconstructing an incomplete specimen of an unknown taxon is therefore a combination of three different sources of uncertainty: 1) selection of a reference taxon, 2) sampling variation of specimens within that taxon, and 3) taphonomic variation of the fossil, both the parts that are missing and the parts that are present but potentially deformed. The set-up of this approach ignores the uncertainties of taphonomy, and reconstruction bias and reconstruction variance is combined in a single mean-square at each missing semilandmark.

Since the combination of these factors lead to different estimations, there exists no "all-purpose" reconstruction. Different assumptions and reference samples will potentially lead to equally plausible reconstructions that differ in shape, but these different estimates might still support a single conclusion (Gunz et al., 2009b). It is not feasible to simulate all the possible sizes, shapes, and locations of all potential cranial defects. I therefore take a particular scenario as an example, that represents a realistic and at the same time very difficult case. The knock-out analysis is specifically tailored for the *Australopithecus afarensis* specimen A.L. 444-2 (Kimbel et al., 2004a), characterized by two separate and large missing areas in the face and the neurocranium (**Figure 1**). I declare the areas that correspond to the absent ones in A.L. 444-2 (~ 50% of the face and 30% of the neurocranium) to be missing in every individual of the hominoid sample, and estimate the coordinates of the missing area via TPS. On the one hand, this allows drawing conclusions about the choice of the reference during geometric reconstruction in estimating large defects. On the other hand, I can investigate the uncertainties that will arise in a geometrical reconstruction of A.L. 444-2. I expect that the closer the reference shape is to the target shape, the more accurate the

reconstruction will be. To explore how this works with significantly different shapes from other species than A.L. 444-2, I extend the approach by estimating missing data for some other important fossils, i.e., Mladec 1, Petralona, and Sts 5 that were virtually fragmented by way of experiment. Thereby, we gain data about the difference in accuracy and uncertainty for fossil reconstructions in comparison to the intraspecies and interspecies reconstructions of extant hominoids. Finally, a quantitative guide on how to choose the reference in interspecies reconstructions for those species that were employed in the sample is introduced. This guideline uses associations of the bending energy between the template and target that we obtained during TPS-based reconstructions.

2.2.1. Cranial diversity in hominoids: the reference sample

Here I describe the characteristics of cranial anatomy in hominoids (**see Figure 5**). Since the outcome of intra- and interspecies reconstruction highly depends on the shape of the reference, a detailed knowledge about cranial morphology of every species involved is mandatory for a thorough discussion of the results.

2.2.1.1. Anatomically modern *Homo sapiens*

Modern humans have an average brain size of about 1350 ccm (**Figure 5a**). The forehead rises sharply, eyebrow ridges are very small or more usually absent. Schwartz and Tattersall (2002b) and Lieberman et al. (2002; 2004) have pointed to several features of the human skull that do appear among hominoids to be autapomorphic for *Homo sapiens*: longer and more flexed anterior cranial base; an overall diminution of facial size, and an increased globularity of the neurocranium; extreme lateral placement of the styloid process, the stylomastoid foramen lying posteromedially at its base; the narrow, high occipital plane of the occipital bone; the retention into the adult of a discernible arcuate eminence; fully segmented cranial sutures, with some segments deeply interdigitated; the bipartite brow; symphyseal region of the mandible as seen from below thicker than the corpora on either side; and the unique inverted-T-shaped chin (Schwartz and Tattersall, 2010).

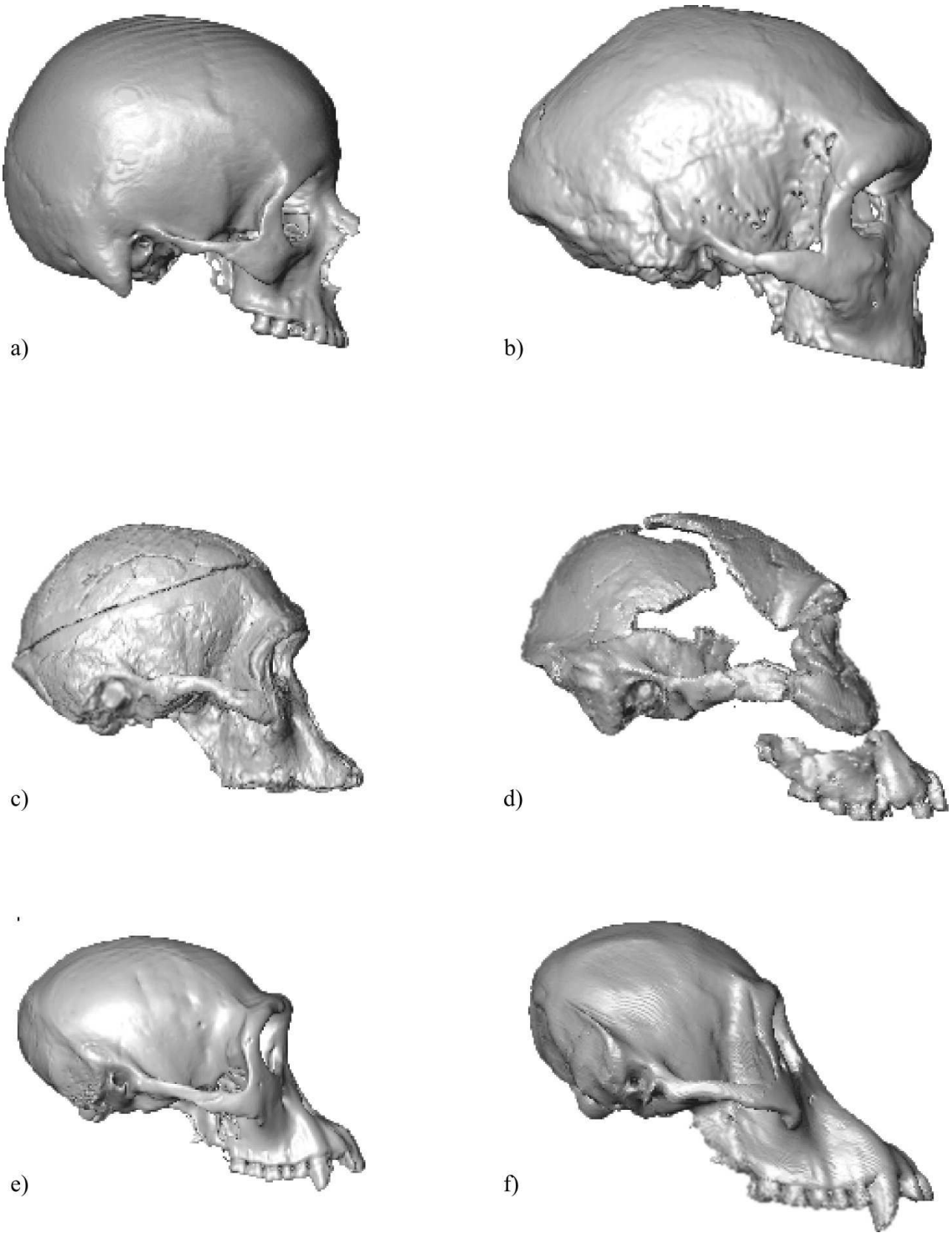

Figure 5 Hominoid craniofacial variability. Overview of the species included in the analysis. a) *Homo sapiens*, b) *Homo heidelbergensis*, c) *Australopithecus africanus*, d) *Australopithecus afarensis*, e) *Pan troglodytes*, f) *Pongo pygmaeus*

2.2.1.2. *Homo heidelbergensis*

Specimens included in this species (e.g. Bodo, Arago, Kabwe, Steinheim) share general features like a superior margin of the orbit that is marked by a blunt edge, but also show a considerable morphological variety (e.g. concerning the endcranial volume: 1100–1400 ccm). The sample includes one specimen of *Homo heidelbergensis* from Petralona (Kokkoros and Kanellis, 1960). It possess a quite massive and broad lower face lying below hugely developed and very tall supraorbital margins that reach their maximum thickness at about mid-orbit. The superior margin of the orbit is marked by a blunt edge above that demarcates the twisting front surface of the torus from a posttoral sulcus behind which is nonetheless quite shallow. In comparison to Bodo, Petralona has higher-placed nasal apertures with shorter, significantly less protruding nasal bones (lower parts of the nasal bones are missing in Petralona). At the same time, Petralona and Bodo share relatively large nasal aperture. Petralona shows a remarkable degree of sinusial inflation, for the frontal (sinuses penetrate posteriorly far into the frontal) but also for the huge maxillary sinuses. In Petralona the "occipital torus" runs transversely straight across the occipital for almost the full width of the braincase (**Figure 5b**). However, the superior nuchal line lies very low, yielding an almost horizontal nuchal plane (Schwartz and Tattersall, 2002b).

2.2.1.3. *Australopithcus africanus*

Australopithcus africanus specimens have rather globular cranium and barely any ectocranial superstructures like sagittal or nuchal crests (**Figure 5c**). The endocranial capacity is between 400 - 550 ccm, somewhat larger than those of *A. afarensis*. Concerning the neurocranium, there is only a moderate separation of lambda and inion.

The glabella is rather prominent and situated at the level of the supraorbital margin. The forehead rises slightly from the glabella to bregma. Most specimens show a moderate pneumatization of the mastoid region. They are characterized by a moderate to marked maxillary alveolar prognathism with a nasoalveolar clivus delineated from the floor of the nasal cavity by a distinct ridge. The lateral margins of the pyriform aperture are variably rounded by the presence of anterior pillars that are set anterior to the level of the anterior surfaces of the zygomatics. The incisive canals open into the inclined surface of the nasal floor as a capacious incisive fossa. The alveolar margins of the maxillary canine and incisor sockets are arranged in an anteriorly convex line (Rak, 1983).

2.2.1.4. *Australopithcus afarensis*

Australopithecus afarensis is a “fossil hominin species known from at least four East African Rift Valley sites ranging from northern Ethiopia in the north to northern Tanzania in the south” (Kimbel et a., 2004, p. 3) with an geological age between approximately 3.6 and 3.0 million years ago. The endocranial capacity is between 400-500 ccm (**Figure 5d**). The craniofacial complex is characterized by a strong alveolar prognathism with convex a clivus. The palate is shallow, especially anteriorly and the dental arcade is long, narrow, and straight sided. The facial skeleton exhibits large, pillar-like canine juga separated from the zygomatic processes by deep hollows. The zygomatic processes are large, located above P4/M1, and oriented at right angles to the tooth rows with inferior margins that are flared anteriorly and laterally. The occipital region is characterized by compound temporal and nuchal crests in larger specimens, with a concave nuchal plane that is shortening anteroposteriorly- The distance between lambda and inion is short. The large masteoid processes are pneumatized and flattened. The mandibular fossae are shallow with weak articular eminences placed only partly under the braincase. The occipital condyles show a strong ventral angulation (Kimbel and Delezene, 2009).

2.2.1.5. *Pan troglodytes*

Chimpanzees have a cranial capacity less than 500 cc. The frontal contour is low and retreating, the occipital more curved in comparison to orangutans. *P. troglodytes* has a prominent supraorbital torus which is usually continuous across the glabellar region as well as above each orbit, although in some individuals it can be divided by a shallow depression (**Figure 5e**). A supratoral sulcus delimits the torus from the frontal squama (Shea, 1988). The parietal region is flat. The orbits are more or less rectangular and normally broader than high. The interorbital breadth is greater than in the orangutan, connected to a broader ethmoid complex of African apes (Aiello and Dean, 2002). Chimpanzees show in contrast to *Pongo* an extensive frontoethmoid sinus that originates from ethmoidal air-cells. Frontotemporal contact predominates on the lateral cranial wall of the chimpanzee and gorilla. Compared with the orangutan, chimpanzees exhibit longer and narrower neurocrania set at a lower level relative to the facial skeleton (klinorhynchy) (Bilsborough and Rae, 2007).

2.2.1.6. *Pongo pygmaeus*

Generally, orangutans have a cranial capacity less than 500 cc (**Figure 5f**). The most marked contrast between the skulls of *Pan* and *Pongo* involve an upward rotation of the palate, a concavity of the midfacial region, and the relative lack of a supraorbital torus in the orang-utan (Shea, 1985). The zygomatics are flared, the nasal cavity is taller than broad, and the maxillary sinuses invade the interorbital pillar (Bilsborough and Rae, 2007). The orbits are ellipsoid, showing "separate semicircular supraorbital costae rather than a continuous torus" (p. 1040, Bilsborough and Rae, 2007). The interorbital distance is small compared to *Pan* and *Gorilla*, therefore the ethmoid is set at a lower level than in the African apes and medio-laterally narrow (Montagu, 1943). The nasal bones are narrow in the lateral dimension, and can continue beyond the frontomaxillary suture, and show an extreme variablity in terms of shape (Selenka, 1898). Finally, in comparison to the Great Apes and, *Pongo* lacks a frontoethmoid sinus (Winkler, 1991).

2.3. Facial orientation and integration in the hominoid cranium

The cranium consists of two main parts: the facial skeleton and the neurocranium. Cranial shape can be determined by the proportions of the both skeletal parts. The great ape profile is distinct from that of hominids. This is primarily due to the combined effects of an absolutely smaller brain and neurocranium and an absolutely larger facial skeleton and masticatory system in great apes. The facial skeleton is comprised of the supraorbital region, the orbital cavities, the nose and nasal cavity and the jaws. Broadly speaking, this can be designated as the upper, mid-facial and lower-facial regions. While each region has an independent function, they all influence the morphology of the facial skeleton and each region also has some effect upon the way in which the facial skeleton is joined to the neurocranium. Perhaps the most powerful influence on facial morphology is the masticatory system. This system in particular dominates the morphology of the upper, middle and lower face of hominoids.

2.3.1. Facial orientation

The orientation of the face relative to the basicranium is an important aspect of interspecific variation and in models of hominoid evolution and systematics (Hofer, 1952b; Biegert, 1957; Hofer, 1960; Shea, 1985; Ross and Ravosa, 1993; Bastir et al., 2007; Begun, 2007). Orangutans are characterized by a structural condition known as airorhynchy, an upwardly deflected face relative to the basicranium. In contrast, African apes exhibit an increased ventral flexion of the face relative to the cranial base (klinorhynchy; Hofer, 1952). However, there is considerable overlap in facial orientation, both within and between species (Angst, 1967; Shea, 1988; Leslie, 2010).

2.3.2. Facial prognathism in hominoids

The facial skeleton is separated from the neurocranium by the bones of the cranial base so that the ethmoid, sphenoid and temporal bones form a boundary between the face and the brain. The degree to which the face projects beyond the neurocranium has been the subject of many studies and usually it is the bones of the cranial base that are used as reference points from which to measure the degree of facial prognathism (Moore and Lavelle, 1974). Huxley (1863) defined the craniofacial angle as the angle between the most anterior point on the maxilla, the most anterior point on the sphenoid bone and the most anterior point of the foramen magnum. Using this angle, Huxley (1863) was able to identify major differences in the degree of prognathism within and among groups of animals including modern humans.

Comparative studies of facial angles in primates clearly demonstrate that infant great apes have flat or orthognathic faces like modern humans. However, the small facial angles of juvenile apes become progressively large with age as the degree of prognathism increases until skeletal maturity (Krogman, 1931; Ashton, 1957). Some primates, *Papio*, for example, are extremely prognathic and a possible cause may relate to the need for a large nose. Other primates (e. g. *Theropithecus*) are still prognathic but have much taller faces (nasion to mid-palatal line) that probably relate to an increasingly hard graminivorous diet. Clearly, complex interactions in facial morphology are unlikely to be measured using a single facial angle.

Early fossil hominids are an extremely variable group and few generalizations can be made about the cranial form in any one taxon. A great deal has been said about the general proportions of the face in early hominids and, in general, it is true that the hominid facial skeleton is reduced in size and less prognathic than it is in great apes. Within each early

hominid taxon, however, there is great variation. Specimens of *Australopithecus* exist which are very prognathic (Sts5) but others have much more retruded facial skeletons (Sts 71, Sts 19). Primates not only show different degrees of prognathism, but also varying degrees of facial rotation.

2.3.3. Klinorhynchy vs. airorhynchy

To characterize the positional relations between the jaw skeleton and the cranial base, Hofer (1952) introduced the terms klinorhynchy and airorhynchy. The term klinorhynchy refers to a bending of the jaw skeleton in relation to the cranial base towards the ventral side; airorhynchy is a bending towards the dorsal side in relation to the cranial base (**Figure 6**).

The upper jaw of humans and of most other primates, including the African apes, is bent in the sense of a klinorhynchy (Biegert, 1957; Hofer and Spatz, 1963; Starck, 1979). Conversely, the position of the upper jaw to the cranial base in the orangutan has been described as showing airorhynchy by several authors (Biegert, 1957; Angst, 1967; Shea, 1985). Many potential consequences of this configuration have been hypothesized, for example Biegert (Biegert, 1957) assumed a relation between the size of the angle and the reduction of the sphenoidal sinus in orangutans.

In 1952, Hofer proposed a classification of cranial types based on the angular relationship between the splanchnocranium and neurocranial portions of the skull. Within the primates, he established four categories:

1. klinorhynchy: facial skeleton directed ventrally with respect to the cranial base (**Figure 6a**)
2. orthocrany: the long axes of the facial and basicranial skeletons in longitudinal alignment
3. airorhynchy: facial skeleton directed dorsally with respect to the cranial base (**Figure 6b**)
4. klinocrany: cranial base and facial skeleton both flexed ventrally around their junction.

Hominoids in general exhibit a more dorsal flexing of the face relative to the cranial base (airorhynchy) than non‐hominoids, showing orbital axes and palates that are shifted dorsally relative to the cranial base (Ross and Ravosa, 1993; Ross and Henneberg, 1995). The functional basis for this is disputed and may well have multiple causes (Ross and Ravosa,

1993). For *Pongo*, several authors hypothesized that many of the orangutans´ cranial traits could be related to its airorhynchy (Delattre and Fenart, 1956; Biegert, 1957; Shea, 1985; Brown and Ward, 1988; Shea, 1988a). Biegert (1963) argued that the laryngeal sac in *Pongo* is is determining its skull form. Shea (1988) suggests that laryngeal morphology is merely one potential influence for the airorhynchous condition, being influnced by other factors such as the lack of the frontal sinus and interorbital breadth.

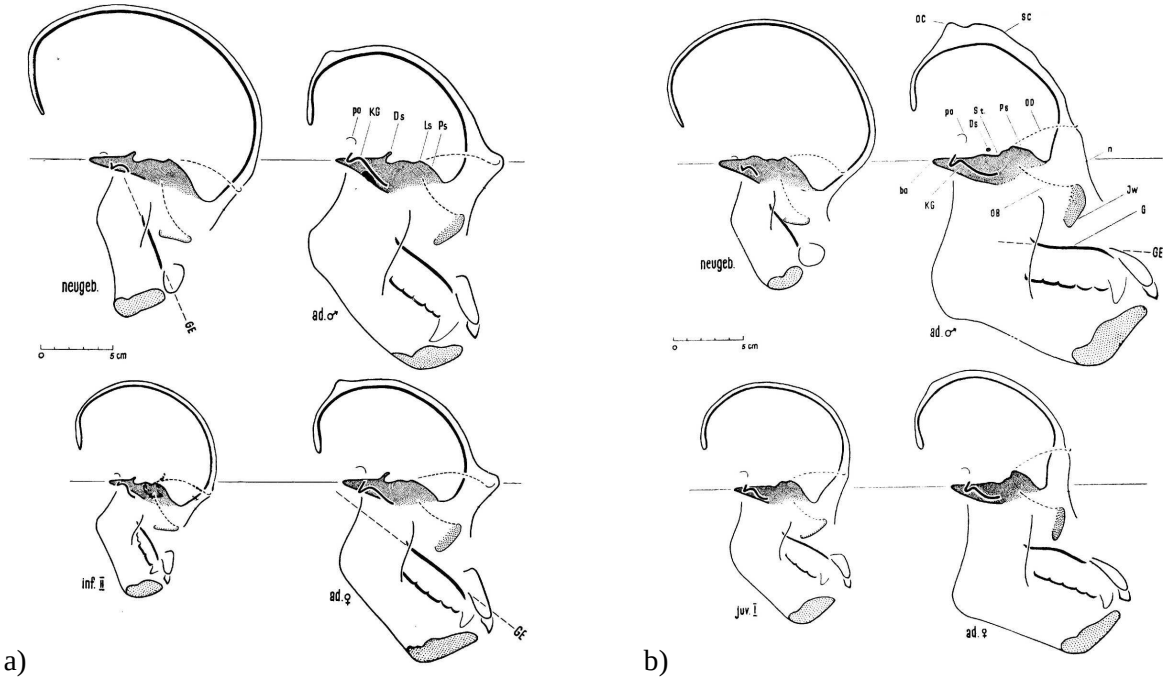

Figure 6 Sagittal profiles from a) *Pan* and b) *Pongo*. Skulls are aligned according to the occipital clivus plane. The left row represents infantile (top) and juvenile (bottom) specimens, the right row adults. The upper row represents male skulls, the lower females (According to Biegert, 1957).

In constrast to *Pongo*, African apes exhibit longer, lower, narrower neurocrania connected at a lower level relative to the face (klinorhynchy; Shea, 1988). Much more of the modern human face is rotated backwards and downwards underneath the brain case and more of the modern human brain has overgrown the top of the facial skeleton. One result is that the bones of the modern human cranial base, those which lie between the face and the brain, show a higher flexion compared to great apes (Lieberman et al., 2000a). Traditional measures quantified the degree of flexure using reference points such as F. caecum, basion, and the pituitary point (problematic point because it coincides with the site of the bend in the cranial base): the angle between these three points is the cranial base angle. This angle serves to emphasize how flat the great ape basioccipital is with respect to the anterior cranial fossa and how flexed the human basioccipital is.

2.3.4. Morphological integration in the hominid skull

At least three main units can be identified in the craniofacial complex: the basicranium (cranial base), the neurocranium (cranial vault), and the splanchnocranium (face). These modules derive from embryologically distinct regions and serve different functional purposes. Modules exist at many different levels of the biological hierarchy (from cells to organ systems) and must therefore be defined with respect to a specified level (from nucleotide sequences to behavior), and to the processes that occur at that level (Moss and Young, 1960; Cheverud, 1982; Enlow and Hans, 1990; Bolker, 2000; Hallgrímsson et al., 2007). The coordinated variation among different parts of an organism is referred to as morphological integration (Olson and Miller, 1958). Olson & Miller (1958) proposed that functionally and developmentally associated characters will be highly correlated and as a result have a higher potential to co - evolve. In their model, morphological traits were treated as inter‐related "numerical sets" and integration was defined and quantified as covariation between traits.

The cranium is a complexly integrated structure, comprising several different semi‐independent units characterized by differential skeletal growth patterns, muscle activity and bony spaces in which brain and pharynx grow (Moss and Young, 1960). The degree of relatedness between and within phenotypic elements varies with varying levels of developmental and functional interactions, subsequently giving rise to semi‐distinct components or modules. In the literature concerning morphological integration, modules are frequently defined as units that are tightly integrated internally but relatively independent from other such modules. Anatomical modules are considered integrated when there are mechanisms (embryological, developmental, functional or genetic) that connect them morphologically or evolutionarily respects (Cheverud, 1996; Rolian and Willmore, 2009).

There is some debate as to whether primates follow a common pattern of integration in the cranium. Some researchers have suggested that homologous cranial regions, in particular those outlined in the functional matrix hypothesis (Moss and Young, 1960; Moss, 1997b, 1997d, 1997a, 1997c) covary across the primate clade, indicating a shared pattern of integration among all hominoids (Cheverud, 1982, 1988, 1995; Ackermann and Cheverud, 2004) but not all studies support this assumption (Ackermann and Cheverud, 2000; Polanski and Franciscus, 2006; Mitteroecker et al., 2008).

Bastir and Rosas (2005) and Bastir et al. (2008) inspired by Enlow's counter-part model (Enlow and Hans, 1996), examined the hierarchical nature of integration between the human face and basicranium. Their results implied that the basicranium does not represent an

integrated overall entity but stated that the lateral elements covary to a higher degree with the mandible than with the midline of the cranial base. The key concept in the functional matrix hypothesis by Moss (1997a, 1997b, 1997c, 1997d) stating that soft tissues such as the brain, muscles, and sinuses are suggested to be morphologically integrated with adjoining bony elements. Developmental variation in the ontogeny and phylogeny of these soft tissues is hypothesized to influnce the morphogenesis of skeletal anatomy (Moss, 1997b, 1997c). According to Moss (1997b) the integration of different functional cranial components can be interpreted within the concept of Enlow's counterpart analysis (Enlow et al., 1969; Bhat and Enlow, 1985). Enlow et al. (1969) hypothesize that growth counterparts of the craniofacial system are dividing the facial skeleton into an arrangement of morphogenetically interacting modules. These components are categorized in two distinct regions: the anterior and posterior face, which are separated by the posterior maxillary plane (Enlow and Hans, 1996; McCarthy and Lieberman, 2001; Bastir and Rosas, 2005). McCarthy and Lieberman (2001) suggested that the anterior face (nasomaxillary complex; Enlow and Hans, 1996) including the orbits, constitutes a morphologically integrated facial block (Lieberman et al., 2000a). Furthermore, different studies propose a relative independence in the positioning of the facial skeleton in relation to the neurocranium possibly reflecting different modules in humans (Lieberman et al., 2000b; Zollikofer and Ponce de León, 2002; Bastir et al., 2004), australopithecines (McCollum, 1999), and chimpanzees (Bastir and Rosas, 2004). Also Lieberman (2000a; 2000b) highlighted the role of the basicranium in generating overall integration in the primate cranium, and suggested that the base and face were semi‐independent from each other.

2.3.4.1. Facial orientation and morphological integration with the cranial base[4]

Facial variation may be a component of a suite of other morphological traits of the cranial base, the braincase and the mandible that are likely morphologically integrated (Enlow and Hans, 1996; Lieberman et al., 2000a). Shea (1986) hypothesized that variation in facial orientation is linked to modifications of the ethmoid and the cribriform plate, resulting in the displacement of the ethmoid complex accompanied by adjustments of the middle face. Some authors suggest that the orientation of the anterior cranial base affects the orientation of the upper face directly and palate orientation indirectly through the integration of palate and orbits (Ross and Ravosa, 1993).

[4] This topic has been presented at the ESHE 2011: Senck et al. (2011) Morphological integration between palatal orientation, cranial base and orbits in *Pan* and *Pongo*.

All of these hypotheses assume a certain level of integration between the cranial base and the face, but there is no unambiguous evidence regarding how the shape of the cranial base covaries with facial orientation. For example, although results of Ross & Ravosa (1993) do not support a structural link between midfacial orientation and the angulation of the cranial base in strepsirhine primates, nevertheless in haplorhines the cranial base angle is positively correlated with angles of facial kyphosis and orbital axis orientation. Ross & Henneberg (1995) found a strong correlation between anterior facial kyphosis and anterior cranial base angulation, though the high degree of basicranial flexion of the humans in their sample might have been the reason for the larger correlations observed. On the other hand it has been proposed that the size and shape of the face reciprocally influence basicranial morphology and orientation as well (bidirectional hypothesis; Biegert, 1957, Bastir, 2004, Bastir and Rosas 2010).

Several concepts and hypotheses have been formulated trying to interpret associations between shape changes of the basicranium and changes in midfacial orientation but are not confirmed (Enlow et al., 1969; Shea, 1986; Ravosa, 1991; Ravosa and Shea, 1994; Enlow and Hans, 1996; McCarthy and Lieberman, 2001). On the one hand, this might be due to the fact that using qualitative descriptions or only simple morphometric approaches, it is generally impossible to make causal statements. Only in the last decade has the cooperation of developmental genetics on experimental animals and morphometrics yielded deeper insights into the mechanisms of structural interactions in the craniofacial complex (López et al., 2008; Martínez-Abadías et al., 2011). On the other hand, the previous available morphometric methods lacked any (statistical) approach to facial orientation vis a vis basicranial and upper facial shape, whether casual or not. The drawbacks of earlier studies can be summarized as three major issues: 1) the deployment of traditional morphometric approaches that apply different sets of reference planes for registration to extract angles, e.g., of the facial kyphosis (Ross and Ravosa, 1993). Such quantification tend to be heterologous across species (see Strait and Ross 1999 for discussion of the use of the Frankfurt horizontal plane; see Leslie, 2010: posterior maxillary plane) and generally seem to be too simplistic for studying the complicated interactions within the craniofacial complex. 2) The employment of dissected specimens which reduces the number of individuals under study to a minimum (Hofer, 1954; Biegert, 1957; Shea, 1986; Winkler, 1988). 3) deployment of radiographs (Ross and Ravosa, 1993; Ross and Henneberg, 1995; Lieberman and McCarthy, 1999; Bastir and Rosas, 2004, 2006; Bastir et al., 2010; Leslie, 2010) which only allow to capture morphological information in the midline of the cranial base. Even analyses on the integration of the lateral

basicranium and the face were based on such radiographs (Bastir and Rosas, 2004, 2006), but it seems obvious that discussions of covariation patterns between the three dimensional basicranial and facial complex and facial position and orientation are best done in three dimensions.

Traditional studies of facial orientation utilized different representations of the midface (nasal cavity and roof of the oral cavity) to analyze topographic and structural relationships between the neurocranium and splanchnocranium [a) the nasal floor (Kummer, 1952 ; Starck, 1953; Ross and Ravosa, 1993); b) the hard palate excluding the nasoalveolar clivus/premaxilla (Hofer, 1952; Biegert, 1957; Angst, 1967; Thenius, 1970); c) the alveolar plane (Delattre and Fenart, 1956; Vogel, 1966; Shea, 1985); d) the molar occlusal plane (Delattre and Fenart, 1956; Vogel, 1966; Ravosa and Shea, 1994)]. In this 3D analysis I pursue another approach by investigating covariation patterns of the craniofacial complex in relation to rigid relationships between the middle face represented by the hard palate (excluding the nasoalveolar clivus) and the cranial base.

To investigate changes in midfacial orientation and the shape of the cranial base that occur together, I analyze the patterns of their covariation using partial least squares (Bookstein, 1996b; Rohlf and Corti, 2000). The PLS method explores the interrelations between two or more blocks of observations. One advantage of this approach is that it will be possible to estimate the orientation of the upper jaw in relation to the shape of the sphenoid bone. This provides estimations of uncertainty of the palate orientation, i.e. the degree of freedom of its rigid motion that may, among other things, help reconstructing hominid cranial fossils or forensic cases.

Both genera, *Pan* and *Pongo*, are characterized by a huge variation in midfacial orientation. Studying patterns of covariation between and within the species can allow conclusions about similarities and differences in the covariation of the basicranium and the orientation of the middle face among the two species. I extract the rigid motions of the palate using a Procrustes based approach, and then study covariation patterns using PLS. This overcomes most of the disadvantages of traditional approaches such as the employment of reference planes for registration (e.g. Frankfurt horizontal plane or the posterior maxillary plane) that are known to be unstable within and across species (Leslie, 2010), and also allows us to visualize patterns of covariation in relation to facial orientation in three dimensions using a reasonable sample size. I will investigate how the shape of the middle and anterior cranial fossa covaries with the orientation of the palate in 3D. This will address a long

discussed issue about association between the basicranium and the face in chimpanzees and orangutans.

According to Enlow and Hans (1996), the cranial base is the bridge between the neuro- and facial cranium upon which the face is constructed, and they suggested that variations in the cranial base are associated with corresponding variations in the form and orientation of the face, including the mandible.

2.3.4.2. Facial orientation and morphological integration with the mandible[5]

The orientation of the face relative to the basicranium (facial kyphosis) is an important factor in interspecific variation and models of hominoid evolution and systematics (Hofer, 1960; Angst, 1967; Ross and Ravosa, 1993). Orangutans and gibbons are characterized by a structural condition known as airorhynchy, an upwardly deflected face relative to the basicranium (**Figure 7**). In contrast, African apes exhibit an increased ventral flexion of the face relative to the cranial base (klinorhynchy; Shea, 1985). However, a considerable overlap in facial orientation, both within and between species, is known (, 1957b; Angst, 1967; Shea, 1988). This kind of facial variation has been proposed to participate in a suite of other morphological traits of the mandible, the cranial base, and the braincase that are likely morphologically integrated (Enlow, 1990; Lieberman et al., 2000a; Lieberman, 2011). For example, a change in the orientation of the maxilla would impact on the mandibular shape to maintain functions such as mastication and mechanical protection of hyo-laryngeal structures. The aim of this pilot-study is to investigate patterns of covariation in the middle and lower face that may represent spatial and structural relationships in relation to variation in facial orientation.

The following section is an overview of the (mandibular) morphology in *Hylobates* and *Pongo*.

[5] This topic has been presented at the AAPA 2010: Senck et al. (2010) Covariation between facial and mandibular shape in *Hylobates* and *Pongo* with respect to facial orientation. AMERICAN JOURNAL OF PHYSICAL ANTHROPOLOGY, Supplement: 50, Pages: 212-213

2.3.4.2.1. *Hylobates*

Overall, the gibbon neurocranium is thin walled, the vault low and ovoid in profile with a capacity of about 80–125 ccm (**Figure 7a**). The orbits are rectangular and relatively large, with strongly developed lateral margins. The torus, though not continous, develops laterally above the orbits. The interorbital breadth is large, showing short and broad nasals that are usually fused. Overall the face is short, broad, and fairly projecting (from Bilsborough and Rae, 2007).

The palate and mandible are long and both the corpus and symphysis are comparatively lightly built. The hylobatid ramus is generally short, wide, and upright, showing slight expansion of the gonial region (from Bilsborough and Rae, 2007).

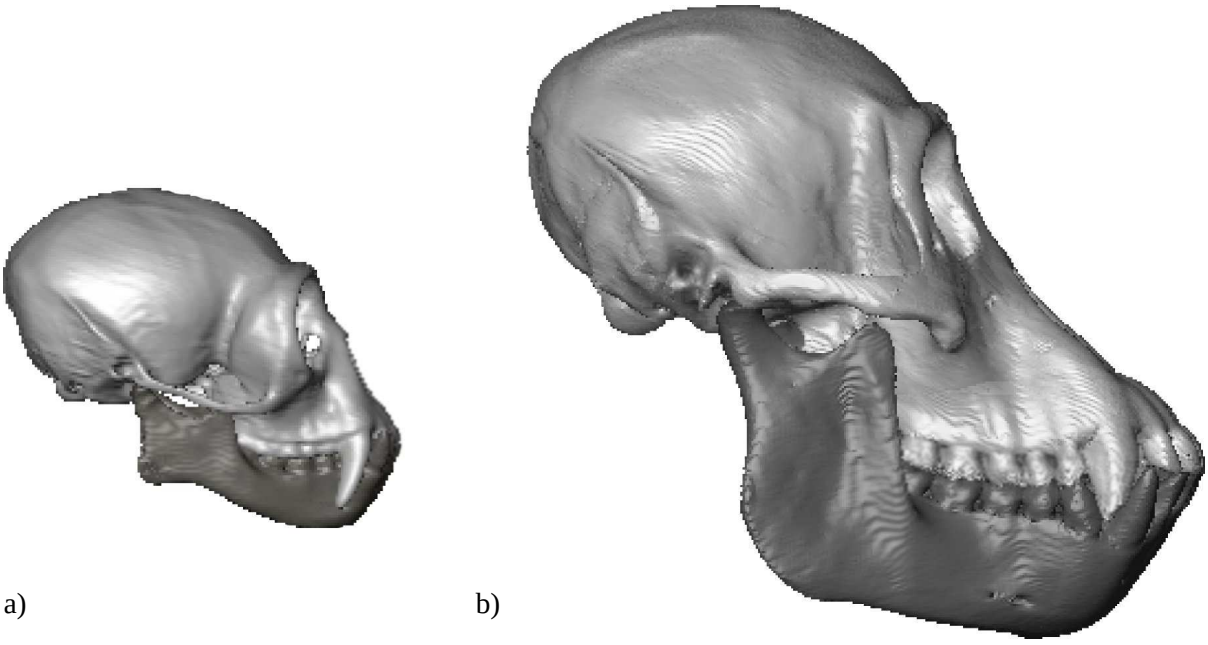

a) b)

Figure 7 a) *Hylobates muelleri* and b) *Pongo pygmaeus*. Cranium (light grey) and mandible (dark grey).

2.3.4.2.2. *Pongo*

Charateristics of the orangutans´ craniofacial morphology is given in section 2.2.1.6. The orangutan mandible is massive, the symphysis characterized by a robust superior transverse torus and a pronounced inferior transverse torus protrude back as far as P4 or M1 (Brown, 1997; **Figure 7b**). The corpus is deep and comparatively short in relation to the corpus. The platysma muscle is strongly developed and extends laterally over much of the facial

musculature (Bilsborough and Rae, 2007). According to Brown and Ward (1988) the huge platysma is associated with the extensive laryngeal air sac system in *Pongo*. The authors hypothesize that it regulates the air pressure and volume within the sac during vocalization (see Bilsborough and Rae, 2007).

Morphological variation in the masticatory apparatus is influenced by varying functional demands during development. This variation is represented by changes in morphology and biomechanical efficiency which have been correlated with dentitional, dietary, and age-related allometric growth changes (Winkler, 1991). Hence the mandible is tightly integrated with the face, variation in craniofacial morphology include mandibular characteristics such as symphyseal height, mandibular angulation, corpus morphology, ramus breadth (Björk, 1969; Enlow and McNamara, 1973; Bhat and Enlow, 1985b; Enlow and Hans, 1996). In humans, dolicocephalic faces co-occur with an elongated and narrow braincase, less flexed basicrania, an open-angled mandible, a rounded inferior basal border of the mandibular corpus than brachyfacial morphologies. This is assumed to be functionally correlated with developmental adjustments to structural and functional requirements (Enlow and Hans, 1996; Bastir et al., 2004). Furthermore, studies of covariation between mandibular and facial traits in adult humans (Zollikofer and Ponce de León, 2002; Rosas and Bastir, 2004; Bastir and Rosas, 2005) seem to reveal quantitatively significant patterns of morphological integration of the face.

I conduct a partial least squares (PLS) analysis within each species to find correlated pairs of linear combinations (singular vectors) between the mandible and face (Rohlf and Corti, 2000). Singular vectors are represented by latent variables (one per block; Bookstein et al., 2003) that explain the largest amount of covariation between the two original sets of variables (Bookstein, 1991b; Rohlf and Corti, 2000; Bookstein et al., 2003a). This is the first analysis in three dimensions that tries to quantify patterns of covariation between the face and mandible in gibbons and orangutans.

2.3.4.3. Morphological integration and virtual reconstructions

As I hypothesized in section 2.3.4.1, it is possible to estimate the orientation of the upper jaw in relation to the shape of the sphenoid bone and orbits with the introduced approach of rigid motions. This provides estimations of uncertainty of the palate orientation, i.e. the degree of freedom of its rigid motion that may theoretically help reconstructing hominid cranial fossils or forensic cases. But can this really be of help in the reconstruction of hominoid fossils?

When extant species are used as analogues for fossil ones, an assumption is commonly made that the fossil species and the living species vary in the same way (Ackermann, 2003). There is some debate as to whether primates follow a common pattern of integration in the cranium. While some of these studies do not support this assumption (Ackermann and Cheverud, 2000; Marroig and Cheverud, 2001; Polanski and Franciscus, 2006), other studies are indicating a shared pattern of integration among all hominoids (Cheverud, 1982, 1988, 1995; Ackermann and Cheverud, 2004). While such assumptions are the basis for many analyses (Richmond and Jungers, 1995), there is a growing disbelief in their accuracy. Several studies investigated whether and how variation and covariation patterns differ among populations in two living to evaluate the utility of using surrogate models of variation and covariation for evaluating fossil relationships (Ackermann and Cheverud, 2000; Ackermann, 2002; Ackermann and Cheverud, 2002; Ackermann, 2003). Ackermann (2003) states that patterns of variation and covariation are not equal, even among closely related, morphologically homogeneous primate species which also counts for the comparison between African apes and humans. But the author also states that while patterns of variation are not equal among African apes and humans, they consistently share patterns of morphological correlation and integration.

Therefore, even if we cannot directly apply the observed patterns of covariation from extant species, a firm understanding of how living morphologies vary is mandatory in order to better comprehend the complex interactions of different components of the craniofacial complex.

CHAPTER 3: MATERIAL AND METHODS

3. MATERIALS AND METHODS

Since each analysis comprises a different set of specimens, I present the tables with the included specimens in the Methods sections that deal with the separate studies. The following section is an overview of the specimens included.

3.1. MATERIALS

The following section is an overview of the specimens and samples included in the various analyses that were carried out.

3.1.1. Fossil material

Several fossil specimens were included in the in several aspects of my thesis. The following section introduces the specimens that were included.

3.1.1.1. A.L. 444-2

Throughout the dissertation A.L. 444-2 will be used to exemplify the methods that were used and developed. The A.L. 444-2 skull was found in February 1992 in sediments of the Kada Hadar Member and consists of fragments representing about 75%–80% of a single hominin skull, with a geological age of 3.0 +/- 0.02 Myr (Kimbel et al., 2004). This specimen was recovered in approximately 50 fragments, not including isolated teeth, tooth crown and root fragments, and indeterminate bone scraps. Kimbel at al. (2004) joined these fragments to form eight major parts:

(1) Frontal bone with attached anterosuperior fragment of right parietal
(2) Left parietal with adhering superior fragment of squamous temporal
(3) Small posterior fragment of right parietal, located approximately midway along bregma–lambda arc and in contact with the left parietal along the sagittal suture
(4) Posterior calvaria, composed of the occipital squama and both tempora bones
(5) Right zygomatic bone

(6) Maxilla, with RI1, RC, RP4–M3, LI1, LC, and LP3–M3
(7) Partial nasal bones
(8) Right mandible corpus and symphyseal region, with left and right incisors, partial RC, damaged RP4–M1.

Of those fragments, four were considered for an anatomical reconstruction: the frontal bone, the posterior calvaria, the maxillary bone, and the mandible. A detailed reconstruction protocol for each fragment is presented in the results chapter. Except for the nasal bones, those parts were CT-scanned with a resolution of 0.41mm and a slice thickness of 1mm in Vienna, Austria.

3.1.1.2. Cioclovina

The specimens was discovered in 1941, during phosphate mining of the Peştera Cioclovina cave, South Transylvania (Harvati et al., 2007) and constitutes a well preserved calvarium (Figure 4). The specimen is dated by recent direct AMS ^{14}C to an age of 29,000+-700 ka (Olariu et al., 2005) and 28,510±170 (ultrafiltration pretreatment; Soficaru et al., 2007) and assigned to the Aurignacian. It preserves the cranial vault and much of its cranial base, while the face is almost entirely absent: only the frontal aspect of the orbits and the upper part of the nasal bones are preserved. The cranium is in good condition and appears to have suffered minimal postmortem distortion.

This study was conducted on a computed tomography (CT) scan of the original Cioclovina calvaria. Scanning was performed using a Siemens sensation 64 medical CT scanner in the facilities of the Centrul De Sanatate Pro-Life SRL, Bucharest. The scanning direction was coronal (transverse). Slice thickness of 0.625 mm, X-ray tube voltage 120 kV and tube current 304 mA were used. All slices were formatted in the same size of 512×512 pixels. The reconstruction diameter and pixel resolution were 223 mm and 0.44 mm.

3.1.1.3. Sts 5

The *Australopithecus africanus* specimen Sts 5 represents a well-preserved partial cranium missing the complete dentition with a geological age of about 2.5 million years (Broom, 1947). Recent palaeomagnetic analyses of the Sterkfontein palaeocave deposits including the

deposition in which Sts5 was recovered, re-estimate the geological age of Sts 5 at 2.16 – 2.05 Ma (Herries and Shaw, 2011).

It was recovered in two pieces because the explosion that was intended to loosen the rock of the Sterkfontein cave (near Johannesburg) separated a part of the cranial vault from the rest of the skull. It preserves most of the neurocranium, showing a break that approximately separates the cranial vault from the rest of the skull. While the braincase is almost entirely present, the face is lacking teeth with the exception of some preserved root sockets.

Sts 5 was scanned in 1997 in Johannesburg, South Africa, with a medical CT (Siemens Somatom Plus 4, sequential, matrix x/y/z 512/512/130, voxelsize 0.39063/ 0.39063/1.0 mm, 140kV, 129mA).

3.1.1.4. Petralona

This adult specimen represents an externally almost complete cranium, only lacking the right zygomatic arch, the lower part of the nasal bones, and some details of the mastoid region. The Petralona 1 skull was discovered in 1960 in a cave near Thessaloníki, northeastern Greece (Kokkoros and Kanellis, 1960). A discussion concerning the age of this skull is persistent since its discovery. In the beginning it was believed to be contemporary with Neanderthals, perhaps no older than 80,000 years. Later analyses, however, yielded strongly diverging estimations between an age of 200,000 and 700,000 years (Hennig et al., 1981). More recent analyses point to a geological age within the range of 150,000 and 250,000 years (Grün, 1996).

The affinities of this specimen have almost been as controversial as its dating. Early studies described the Petralona cranium as a Neanderthal (Kanellis and Savva, 1964) while more recent interpretations place it among the Arago/Kabwe group (Hublin, 1984; Stringer, 1985), recognized as the species *Homo heidelbergensis*.

Petralona 1 is housed at the Department of Geology, Aristotle University of Thessaloniki in Greece. A CT-scan of the Petralona skull was performed with the use of a commercial medical scanner (Siemens ART, Siemens, Erlangen, Germany), at Thessaloniki, Greece. Serial images were obtained from the entire fossil using clinical scan protocols: conventional 2 mm slices, 1 mm tablefeed, 130 kV, 100 mA with the following reconstruction parameters: 512x512 matrix with a 12 bit grey scale and 1 mm slice reconstruction (Le Floch-

Prigent N. and Moschidou-Polizois A., 1991). Since the window during scanning was improperly adjusted, the anterior aspect of the maxilla is omitted.

3.1.1.5. Mladec 1

This adult specimen was found in the Bocek´s Cave in the vicinity of the village Mladec in Czech Republic by J. Szombathy in 1881 (Szombathy, 1900, 1925). During several excavations more than 100 specimens from the large Main Cave (e.g. Mladec 1 and 2) and from the Quarry Cave (e.g. Mladec 5 and 6) were recovered. Among these, Mladec 1, 2, and 8 are consistently dated to around 31,000 years (Wild et al., 2005). Mladec 1 is a largely intact cranium of an almost adult individual, characterized as female (Wolpoff et al., 2006). It is missing parts of the right frontal, parietal and squamosal and teeth except left and right M1-2. The cranium is long and narrow, the orbits are low and rectangular, and the supraorbital region is bipartite with supraorbital swellings that fuse across glabella (Schwartz and Tattersall, 2002b). Weber et al. (2006) morphometrically compared cranial shape between the Mladec 1, 5, and 6 specimens, "anatomically modern humans" and Neanderthals, and conclude that the Mladec fossil firmly groups with the modern sample. Mladec 1 was scanned in Vienna, Austria, with a medical CT with a voxelsize of 0.466798/ 0.466798/0.75 mm.

3.1.2. Modern sample

The sample consisted of computed tomography (CT) scans of modern humans, chimpanzees, orangutans and gibbons (the depository for each specimen is listed in the corresponding tables that list the sample for each analysis). Since the amount and composition of the sample is differing in the different analyses, I introduce the exact number of specimens used within the respective section.

3.2. METHODS

This section introduces methods of data acquisition as well as data manipulation.

3.2.1. Reconstruction of CT-data

The half-maximum height protocol was used to reconstruct each cranial surface from the CT scans via the software package Amira 5.2 (Mercury Computer Systems, Chelmsford, MA). The procedure uses the histogram of the CT grey values to determine the appropriate border between materials (here bone and air) based on the Half Maximum Height Value (Spoor et al., 1993). This value is then used as threshold for the generation of surfaces from CT data. After segmentation, the extraction of 3-D surfaces from volume data, surface models are created in Amira using the *SurfGen* function, creating stl-files. **Figure 8** shows an example of the reconstruction of an orangutan cranium and endocast.

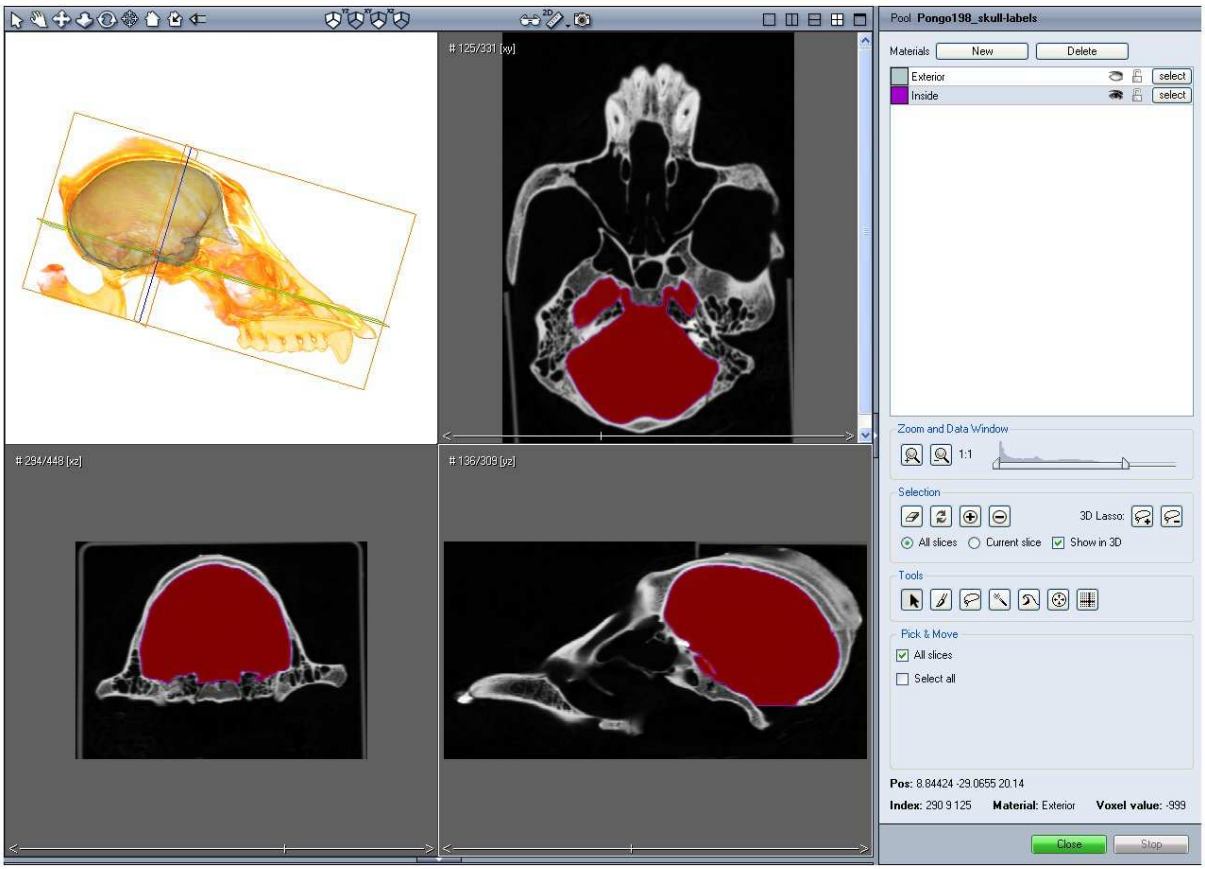

Figure 8 Reconstruction of a orang-utan skull and its endocast.

3.2.2. Geomtric Morphometrics

The comparison of anatomical features of organisms is a central element of biology. The taxonomic-morphological classification of organisms and the understanding of the diversity of biological life are historically based on the description of biological forms (Adams et al., 2004). In this context, morphometrics represent the study of shape variation and its covariation with other variables (Bookstein, 1991; Dryden and Mardi, 1998). In the middle of the 20th century there was already a quantitative description of morphological shape using statistical analysis for the description of patterns of shape within and between groups. In the 1980s finally, the focus was on coordinates of landmarks and the preservation of geometric information about their relative positions. An advantage of this appraoch is that the results of multivariate analyses can be projected back into “physical space” instead of being restricted to the mere visualization using scatter plots. For the comprehension of the analytical methods of this approach represented by Geometrics Morphometrics, definitions of form, shape, and size are needed (**Figure 9**).

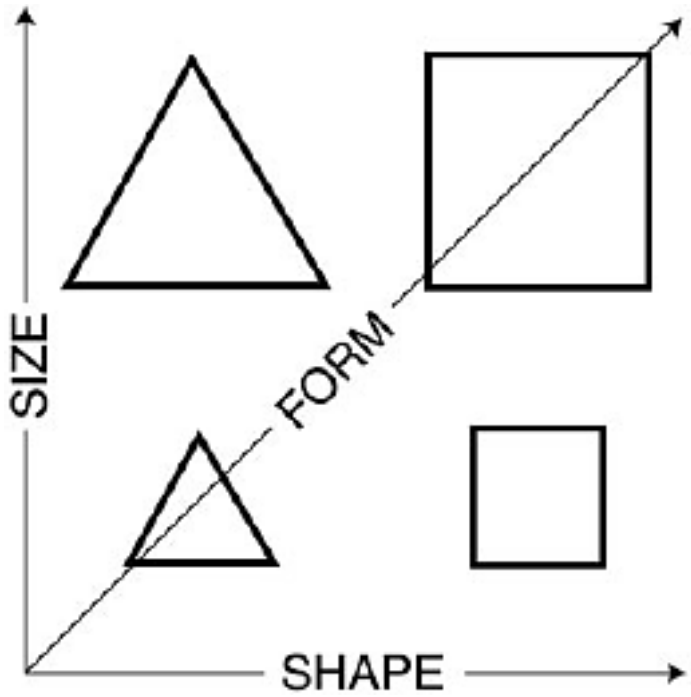

Figure 9 Relationship of form, shape and size (after Richtsmeier et al., 2002)

Form is described as the combination of size and shape. In this context the size measure is any positive, real-valued measure of an object (Slice, 2005). The size has long been considered an important component in the comparison of biological structures. It tends to dominate the variability between the sexes, populations, species and even individuals (e.g.

by allometric effects). If the main interest is focused on shape differences between groups, i.e. size is regarded as a nuisance parameter, size can be disconnected from other factors (see below).

Shape is defined as the geometric properties of an object that are invariant with respect to location, scale and orientation. This definition illustrates the focus on geometric properties, which do not change if the position or orientation of the sample varies. In addition, shape is not influenced by an enlargement or reduction of the object. A shape variable is any geometric measure of an object, which is invariant in terms of location, scale and orientation of an object. Coordinates of points and precisely defined groups of distances between these points are correct shape variables, as far as they preserve the geometric information of the structures they describe (Dryden & Mardia, 1998).

The toolkit of Geometric Morphometrics (GM) comprises all methods of data recording, processing and visualization for the study of form, which are characteristic for modern morphometric methods (Rohlf and Marcus, 1993). This expression represents especially those methods which are related to the accurate collection and analysis of shape information as defined above. This distinguishes GM from morphometric methods described as "traditional". Those methods do not necessarily maintain sufficient information to reconstruct the spatial relationships among structures that are defined by the measured values. Since the entire geometric information is saved using GM, the results of multidimensional multivariate analyses can be projected back into physical space. This allows the visualization of the results which would often be impossible using alternative methods (Slice and Ross, 2009).

Because of the limitations which are inherent in the traditional methods, both for outline - (see below) as well as landmark data, alternative methods for the quantification and analysis of morphological shape were needed. D. Kendall (1984) developed a strict statistical theory of shape analysis, which offered the possibility to combine multivariate statistical methods with methods for the direct visualization of biological form. This was referred to as a "morphometric synthesis" or even "revolution" (Rohlf and Marcus, 1993; Bookstein, 1996a). Morphometric methods which are based on landmarks began with the collection of two-or three-dimensional coordinates of biologically defined landmarks. But the direct analysis of these coordinates as (shape) variables is not possible because the position, orientation, and scaling varies between the objects. Therefore, the variation that is not based on shape is mathematically removed before such variables can be analyzed. This is achieved using a

Procrustes Superimpostion. Once the variation is eliminated, the variables become shape variables and can be used to statistically analyse the sample (Zelditch et al., 2004).

3.2.2.1. Procrustes superimposition

Over the past 20 years, a standard set of procedures for the shape analysis of landmark data has been established that is today applied in almost all morphometric investigations (Adams et al., 2004). First, the centroid for each configuration is determined (see **Figure 10**). Then every landmark configuration (representing single objects) is centered on their origin by subtracting the coordinates of the centroids of the corresponding coordinates from each landmark configuration. Afterwards the centered landmarks are scaled so that they all have the same Centroid Size (CS: the square root of the summed squared deviations of the coordinates from their centroid; Dryden and Mardia, 1998). In the absence of allometry, CS does not correlate with shape and is therefore the preferred size measure in GM. As a convention, CS is set to 1 for all landmark configurations. In the last step, by choosing a reference or consensus configuration (mean shape of all landmark configurations), the rotation, i.e. the sum of squared distances between the homologous landmarks is minimized.

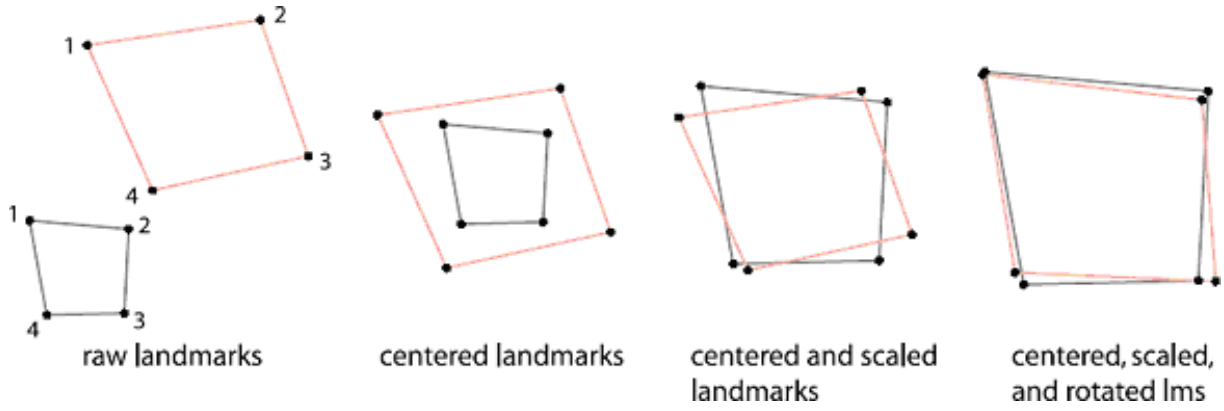

Figure 10 Procrustes superimposition: translation to the same centroid, scaling to the same Centroid Size, and rotation to minimize the summed squared distances between the corresponding landmarks. From Mitteroecker and Gunz (2009).

For more than two objects this process is called Generalized Procrustes superimposition (**Figure 10**). The space (shape space), in which the Procrustes distances are used, is due to David Kendall (see above) and is the fundamental structure, on which GM is based (**Figure 11**).

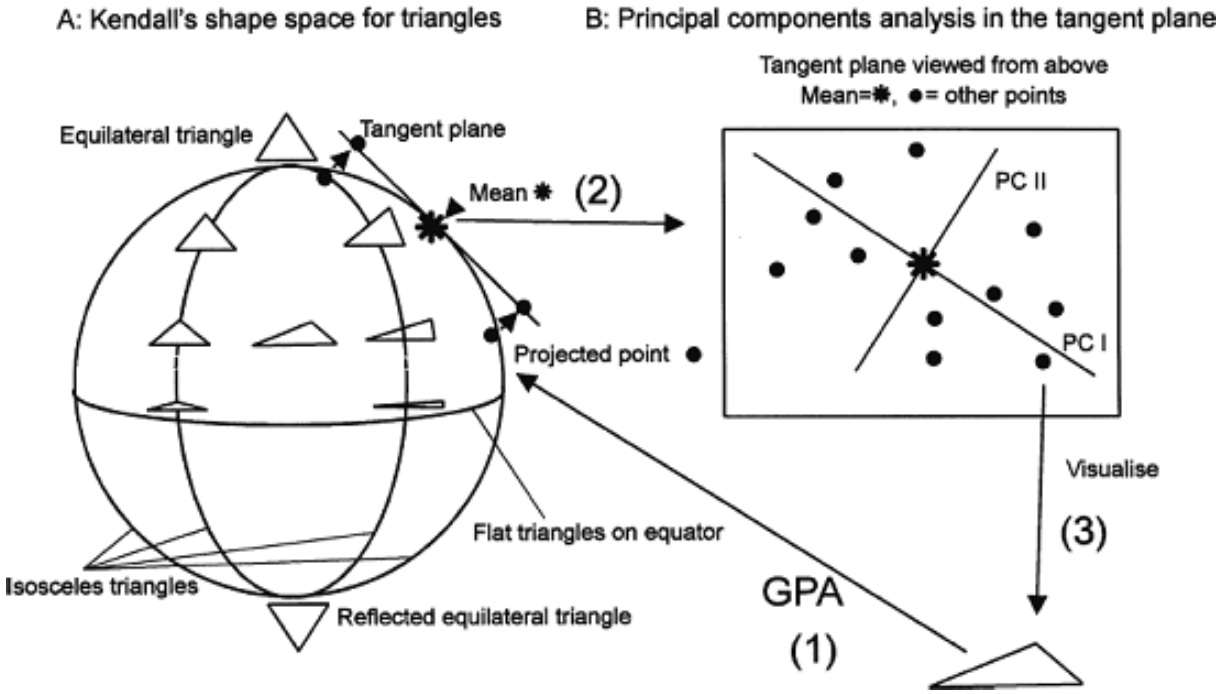

Figure 11 A) Representation of Kendall's shape space for triangles. (B) A schematic indicating the projection of points representing triangles in Kendall's shape space into a space tangent to the mean triangle (arrows) and the principal components of shape variability (PC I, PC II) in this tangent space.

Since Kendall's Shape Space is a non-Euclidean space, the use of common multivariate methods are not permitted. To make this possible, the points are projected on an Euclidean "Tangent Space". This resulting space is roughly the same as the original positions of the non-Euclidean space. Since this space is multidimensional for complex shapes, it is only displayed for triangles (**Figure 11**). Each point in this shape space represents the shape of a configuration of points in Euclidean space, regardless of size, location and orientation (Dryden and Mardi, 1998). In shape space scatter points correspond to variations of complete landmark configurations (and thus to individuals) and not just variations of each landmark (Slice, 2001).

Figure 11 shows a schematic representation of this mathematical procedure. The Generalized Procrustes Analysis (GPA) is used for the registration of objects, which are then represented by points in the shape space (1). This is followed by the projection of points that are represented by complete landmark configurations in the Tangent Space and the extraction of the main components of shape variation in this space (2). Finally, the graphical representation of shape variability, which is represented by the principal components (PCA; see below) (3). The R code for the GPA that is used in this thesis is listed in **Appendix 1**.

3.2.2.2. Landmarks

Landmarks are often the same points that are used traditionally to define distances or angles. In contrast to traditional methods however a coordinate system has to be set up in which the positions of the landmarks can be included before gathering landmark data (Richtsmeier et al., 2002). A number of selection criteria were introduced by Zelditch et al. (2004) that should always be valid for landmarks:

(1) Landmarks are homologous anatomical loci.
(2) Landmarks remain relatively constant in their position to other landmarks.
(3) Landmarks adequately capture the morphology of the object.
(4) Landmarks must ensure intersubjective repeatability and reliability.

Landmark coordinates are differing in the quality of information they encode. This has to some extent defined by the classification of Bookstein (1991) as landmarks of Type I, II, III.

1. Type I - landmarks are characterized with respect to discrete anatomical juxtapositions of tissues, e.g. by sutures.
2. Type II - landmarks are arc or curvature maxima, that are connected with local structures.
3. Type III - landmarks are mathematically projective extreme points, such as the endpoints of the greatest length, width, etc., and with respect to a distant defined structure.

Of these, the two- or three-dimensional positions of types I and II are most completely defined in relation to local morphology and all dimensions are more or less biologically informative. Type III - landmarks, however, are "unsatisfactory" because their meaningful information is only in the context of remote defining structure. Variation perpendicular to this direction has a substantial arbitrary component (Bookstein, 1991). A detailed description of the definition of the anatomical landmarks used in this thesis is given in **Appendix 2**.

An issue that is accessible through an object of landmark coordinates is the dimensionality of shape variation, i.e. the number of dimensions (degrees of freedom) which are necessary to represent shape (Dryden and Mardi, 1998). The simple construction of triangles is used as a common example (**Figure 11**; O'Higgins, 2000). Each triangle in a plane requires only six numbers (the coordinates) for its complete geometric description. One degree of freedom is assigned to translation along each axis, one for scaling and another one for orientation. This results in 6 - 2 - 1 - 1 = 2 degrees of freedom for the variation of shape

(Slice, 2005). It should be noted that because only two remaining dimensions remain to encode shape, the possibility to investigate the structure of this space graphically is offered. This is one of the reasons why triangles have an important role in the research of shape theory (Zelditch et al., 2004; Slice, 2005). As the number of nuisance parameters for plane configurations is defined, the main formula for the dimensionality of shape of p points in two dimensions is: 2p - 2 - 1 - 1 = 2p – 4. For three-dimensional data, the formula is: 3p - 3 - 3 - 1 = 3p – 7. In three dimensions are three dimensions that need to be translated, three angles of rotation and an additional scaling parameter that needs to be calculated. The general dimensionality of the shape variation for an arbitrary number of points p in any number of dimensions k is: pk - k - k (k - 1) / 2 - 1 (Slice, 2005).

3.2.2.3. Semi-landmarks

As traditional anatomical landmarks only capture the cranial geometry quite incompletely, I included curve and surface semilandmarks to the set of anatomical landmarks in order to add morphological information. An example for a bony structure that is underrepresented by anatomical landmarks is the cranial vault. Much morphological information is omitted when only using the few neurocranial landmarks, e.g. bregma and lambda. If one includes semilandmarks or not is depending on the question and the scope of the analysis. The analyses in this thesis that are dealing with the virtual reconstruction in various aspects (the first two sections of this thesis) include semilandmarks on curves and surfaces. Especially surface semilandmarks add valuable information to these analyses, since we have to deal with large missing portions of the neurocranium. The third chapter concerning facial orientation and morphological integration does not include surface semilandmarks, because on the cranial base and the face I could digitize fairly enough anatomical landmarks and curves.

The method of sliding semilandmarks was initially introduced in Bookstein (Bookstein, 1991) and explicitly discussed and used in Bookstein (1997; 1999). Gunz et al. (2005b) extended this approach to three dimensions and delivered guidelines for the practical application of these methods. As part of the digitization process, semilandmarks were allowed to slide along curves and surfaces to minimize the bending energy (see 3.2.2.4.1) of the thin-plate spline (Bookstein, 1991; see 3.2.2.4.2) computed between each reference and target specimen. This iterative procedure approximates curves by sets of chords calculated as vectors of two neighboring (semi)landmarks, and surfaces by their triangulations. That means that semilandmarks do not slide on the actual curves and surfaces themselves but rather along

tangent vectors to the curve or the tangent planes to the surface. The sliding of semilandmarks is an iterative process involving the following sequential steps (Gunz et al., 2005a; Mitteroecker and Gunz, 2009):

1. Computation of the Procrustes mean shape of the sample and tangent vectors for each semilandmark for each specimen of the sample.
2. Sliding the semilandmarks along the tangents to minimize the bending energy relative to the Procrustes mean shape.
3. Projecting each slid semilandmark to the nearest point on the curve or the surface, because the position may not be on the actual curve or surface any more.

Relaxed semilandmarks can be considered as geometrically homologous points. A detailed description of the algebra for sliding semilandmarks by minimizing the bending energy is given in the **Appendix 3**.

3.2.2.4. Bending energy

“Bending energy is a metaphor borrowed for use in morphometrics from the mechanics of thin metal plates” (Slice et al., 2009b). Any thin-plate spline has a bending energy, the (idealized) physical energy required to bend an infinite, infinitely thin metal plate into the specified form from an initially flat configuration. By extension, any deformation of a landmark configuration modeled in this way has a bending energy, the sum of the energies of its three “plates” (Bookstein and Green, 1993). While in physics bending energy is a real measurement that is quantified in corresponding units, there is an alternative formula that is still meaningful in morphometrics: bending energy is proportional to the integral of the summed squared second derivatives of the "vertical" displacement - the extent to which it varies from a uniform tilt (Slice et al., 2009b).

3.2.2.5. Thin-plate splines

Bookstein (1989; 1991) developed the method of thin-plate splines (TPS) to compute deformation grids, statistical analogues to the ones that were drawn by Thompson (1917). The algorithm computes a mapping function between two point configurations that maps

anatomical landmarks while the space between these landmarks is smoothly interpolated. The grid is interpolated by minimizing the bending energy of the deformation.

In two dimensions, the TPS interpolation function from a reference to a target configuration can be applied to vertices of a regular grid in order to visualize shape differences between two geometric objects, for example two mean shapes (**Figure 12**). In three dimensions deformation grids can be confusing when visualizing shape differences in more than one plane. For the visualization in three dimensions the algorithm can be employed to deform a surface model (**Figure 12**). Using the TPS interpolation function, shape changes are visualized by means of surface warps. These are produced by taking the landmark coordinates of the mean shape and adding the a combination of eigenvectors or singular vectors of the shape coordinates that are obtained during principal component analysis (PCA; see 3.4.2.3.3) or partial least squares analysis (PLS; see 3.4.2.3.3).

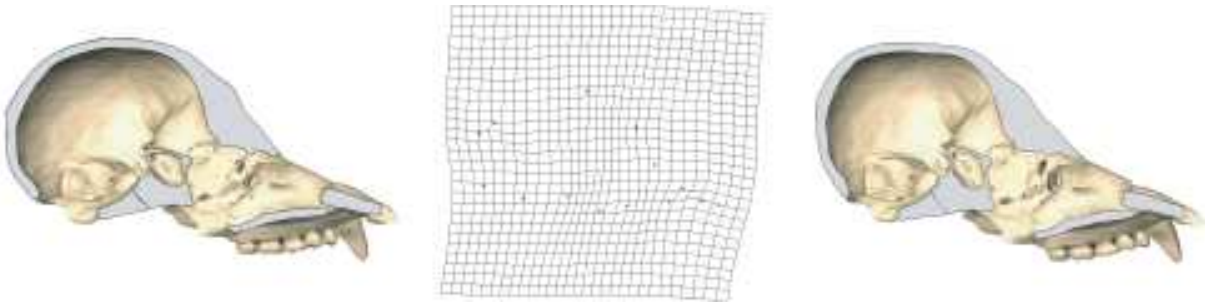

Figure 12 Surface morphs and TPS deformation grid for two mean shapes.

When visualizing form changes, the exponential function of the corresponding loadings for lnCS has to be added. Eigenvectors are linear combinations of the original shape variables and can be visualized as scores (i.e., projections of the original variables onto the axes) or as deformations (Gunz and Harvati, 2007). To these ends, the triangulated surface of a single specimen is deformed using TPS. Using the software Amira 5.2, the landmarks and semilandmarks of this specimen are used to warp the surface points from the original configuration in Procrustes space into the mean shape configuration with different multiples of the eigenvectors added. Note that the surface areas where there is no (semi)landmark information are interpolated by the TPS (Gunz and Harvati, 2007). The standard TPS formulas according to Bookstein (1997) are given in **Appendix 3**.

3.2.2.6. Landmark and semilandmark data

Landmarks and semilandmarks were digitized using the open-source software Edgewarp3D (Bookstein and Green, 2002) and AMIRA 5.3 (Mercury Computer Systems, Chelmsford, MA). For the reconstruction sections in this thesis, several 3D-templates of anatomical landmarks and semilandmarks were created to capture the geometry of the cranial surface. Each template is presented in the section that deals with the actual analysis, since number and spatial distribution of the landmarks and semilandmarks are varying from study to study. For example, since the analysis of facial orientation (see section 1.3) included morphological information of the cranial base, endocranial landmarks were added to the template. Anatomical landmarks that were not required were omitted. A detailed description of the definition of each landmark is given in the Appendix (**Appendix 1**).

As substantial surface information is omitted using only traditional anatomical landmarks, I included curve and surface semilandmarks. As part of the digitization process, semilandmarks are allowed to slide along curves and surfaces to minimize the bending energy of the TPS computed between each specimen and the sample Procrustes average. Once relaxed, semilandmarks can be considered as homologous points (see 3.2.2.4). For each analysis, the template was warped onto each complete specimen cranium by iterative thin-plate spline (TPS; Bookstein, 1991). This procedure aligns the template and target according to homologous landmarks present in both models.

3.2.3. Methods of virtual reconstruction

Most hominin cranial fossils are incomplete, requiring reconstruction prior to the analysis of gross morphology. Missing data can be estimated by geometric morphometrics using mirror imaging and reflected relabelling or by using information from complete specimens, e.g. by using TPS or multivariate multiple regression. The following paragraphs describe the methods used in the reconstruction chapters.

3.2.3.1. Manipulation of objects in a virtual environment

During the anatomical reconstruction of fossils, isolated fragments have to be placed and oriented relative to each other, either applying a traditional approach in which fragments are manually placed and connected (Tobias, 1967; Kimbel et al., 1984; Kimbel and White, 1988;

Kimbel et al., 2004; Caspari and Radovcic, 2006; Curnoe and Tobias, 2006) or a computer-assisted approach which uses tools of virtual anthropology (Zollikofer et al., 1998; Ponce de Leon, 2002; Gunz, 2005; Zollikofer et al., 2005; Gunz et al., 2009b; Weber & Bookstein 2011). In three dimensions, any positioning of two objects introduces six degrees of freedom, three translational and three rotational, all of which are independent. Once the object is reconstructed from volume data and converted to surfaces, virtual bones can be manually manipulated on the computer, and parts can easily be translated and rotated. In this thesis I used the software AMIRA 5.2 (Mercury Computer Systems, Chelmsford, MA) and Rapidform XOR2 (INUS Technology, Inc.) for the manipulation of fragments in a virtual environment. Examples are the anatomical reconstruction of the A.L. 444-2 mandible (4.1.1.3) and maxilla (4.1.1.4).

3.2.3.2. Mirror Imaging

One way to deal with missing or deformed anatomical structures is to restore bilateral symmetry. Using surface models, it is possible to mirror image the better preserved side entirely or just parts from one side to the other (Gunz et al., 2009b).

3.2.3.2.1. Mirroring across a best-fit midsagittal plane

Since midsagittal landmarks commonly deviate from a perfect plane, the symmetry plane has to be estimated, e.g. by a least-squares fit of a plane to the midsagittal landmarks. This can be done automatically using Rapidform XOR2 (INUS Technology, Inc.). The software computes the first three principal components of the midsagittal landmarks, projecting all landmarks onto the principal component axes (the eigenvectors), and flipping the sign of the scores on the third PC. These flipped points are then multiplied by the matrix transpose of the three eigenvectors calculated previously (Gunz et al., 2009b).

3.2.3.2.2. Reflected relabelling

Reflected relabelling (RR) is not only the essential step in the Procrustes analysis of asymmetry (see 3.2.3.5.3) but also a useful tool during the reconstruction process. For the specimen to be reconstructed, a reflected copy of the original configuration of landmarks is produced. This is done by changing the signs for one of the coordinates of all landmarks. The

paired landmarks are then relabelled by swapping the labels between left and right paired landmarks of the reflected copy. Finally, a GPA superimposes both the original configuration of landmarks and the reflected and relabelled copy (Mardia et al., 2000).

3.2.3.2.3. Beyond mirror imaging

In difficult scenarios that can appear in various fields such as paleoanthropology and forensics, simple mirror imaging cannot be applied. This is the case when a large part of the cranium is missing and there is no clue to the actual midsagittal plane. Since it is not possible to establish a midsagittal plane that could be used to mirror the existing part, bilateral symmetry cannot be restored by simple mirror imaging. A solution to this problem is introduced in this thesis by exploiting biological information based on a reference sample and quantitative methods. I estimate the position of the midsagittal plane based on a sample of reference specimens using a partial GPA, and then reconstruct the skull according to the estimated midplane using mirror imaging (for details see 3.2.2.5.5).

To show the applicability of the above described approach we use this technique for the reconstruction of the A.L. 444-2 maxilla. Since it is necessary to apply the morphological information of reference specimens, I surface-scanned high-resolution casts of A.L. 200-1 at the Naturhistoisches Museum Wien (**Figure 13**). Scanning was conducted using a Breuckmann light stripe scanner.

a)

Figure 13 Casts of A.L. 200-1

3.2.3.3. Estimation of missing data

There are many types of studies in various scientific fields for which missing values are an issue, e.g. across the social sciences (Acock, 2005). Many conventional statistical procedures using standard software like SAS or SPSS exclude incomplete cases that have any missing variable values from the analysis. Consequently, there is a loss of information in these incomplete cases. Traditional approaches deal with missing values in various ways, e.g. by listwise deletion, pairwise deletion, and mean substitution. Several classifications exist for characterizing missing values defined by Rubin (1976) including (1) missing completely at random and (2) missing at random. When values are missing completely at random they are randomly distributed, e.g. in a matrix consisting of a large data set. Data is missing at random if the likelihood of missing data on the variable is unrelated to the value of the variable, after controlling for other variables in the analysis. Data may be missing in ways that are neither of the above mentioned classifications, for example in fossil specimens. Taphonomic processes may have had a larger influence on geologically older specimens or specimens that were transported during sedimentation. Therefore different taphonomic scenarios have an influence on the amount of missing (fossilized) bone. Since morphology in GM is represented by landmarks, such regions are coded as missing: landmark locations unobservable in the respective specimen. From a statistical point of view these points can be regarded as missing data. Furthermore semilandmarks that are missing tend to cluster on forms thereby introducing spatial correlation (Gunz, 2005).

In contrast to the imputation of missing data in questionnaires in social science, we can make use of several basic principles of the skulls bauplan when reconstructing fossil specimens. We can use information about bilateral symmetry and utilize the smoothness of many parts, for example the neurocranium. Furthermore, several parts of the craniofacial complex are tightly integrated with each other, reducing the number of degrees of freedom how different parts can be placed relative to each other. Gunz (2005) tried to formalise this biological knowledge to make it available to any missing data protocol by establishing a principled way to do such reconstructions with landmark coordinate data. A basic step in the reconstruction process is completing a form by simple mirror imaging (see section 2.3.4.5.). A second source of morphological information that can be applied is allometry by regressions of Procrustes shape coordinates on Centroid Size. Morphological integration can be used to asses the uncertainty in the spatial relationship between parts in the craniofacial complex (see

section 2.3.4.3.2). Finally, curvature smoothness can be used in a geometric reconstruction (see below).

3.2.3.3.1. Geometric reconstruction

In general, the geometric reconstruction is based on the smoothness properties of the thin-plate spline. The smoothness of a transformation can be quantifed by the bending energy, the scalar measure of deformation associated with the thin plate spline interpolation (Bookstein, 1989; Bookstein, 1991b). TPS requires only a single reference form (template) which can be represented by a Procrustes mean shape of a species or one uses each specimen in the sample to create multiple reconstructions.

The first step during geometric reconstruction is the establishment of a template. This template or reference consists of a set of landmarks and semilandmarks that is tailored to the area that is missing in the specimens to be reconstructed. If the missing area is in the neurocranium, then the template has to be set up in a way that the surrounding area of the defect is densely covered with landmarks and semilandmarks. This is because the thin-plate spline is locally bent according to the existing morphology. Hence the closer the landmarks are to the defect, the better the result will be. The template is then warped onto each complete specimen cranium by iterative TPS (Bookstein, 1991a). This procedure aligns the template and target according to homologous anatomical landmarks present in both models. A TPS is invariant to position, scale and rotation of the forms and therefore does not require a previous Procrustes fitting step. When virtually damaged specimens are targets, landmarks and semilandmarks of the template in the respective missing area of the target are declared as missing so that their coordinates will be estimated during warping.

3.2.3.3.1.1. Example: Reconstructing the endocranial cavity of Cioclovina

In order to obtain an approximation of the total endocranial volume, missing parts of the cranial base were virtually reconstructed by using a modern human cranium as reference. I determined the reference by carrying out a Generalized Procrustes Analysis (GPA) and a subsequent PCA in form space (Mitteroecker et al., 2004) on 34 anatomical landmarks present in 25 modern human crania and Cioclovina. I chose the specimen that was closest to the Upper Paleolithic calvarium in terms of Procrustes distance as reference (Bookstein, 1991b) which can be regarded as a measure of geometrical closeness (**Figure 14**).

The missing area incorporates the medial part of the left cerebral fossa, the clivus, the anterior and posterior clinoid processes, parts of the dorsum sellae, the ala minor, the lamina cribrosa, and the posterior part of the orbital roof formed by the frontal bone. Using the open-source software Edgewarp3D (Bookstein and Green, 2002) and AMIRA 5.3, a 3D-template of 508 anatomical landmarks (n=34) and semilandmarks (n=474) was created to capture the geometry of the complete endocranial surface of the reference. I estimate missing data using thin plate splines (TPS; Bookstein, 1991) by warping the complete reference cranium onto the target, in this case the cranial remains of Cioclovina. This procedure aligns the reference and the target according to homologous anatomical landmarks present in both models.

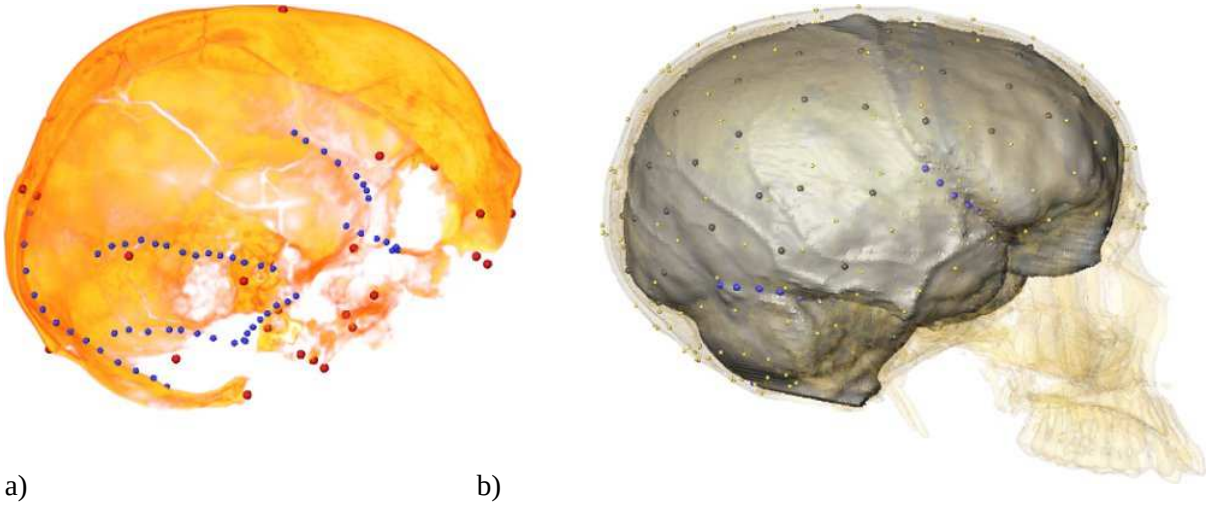

a) b)

Figure 14 a) Cioclovina with anatomical landmarks (red) and curves (blue). Lateral view into the endocranial cavity. b) Template with curve (blue) and surface (ectocranial: yellow, endocranial: gray) semilandmarks.

First, a TPS interpolation based on the anatomical landmarks was computed to warp all semilandmarks from the reference to Cioclovina. In this way, the reference and target are aligned according to the anatomical landmarks and all semilandmarks are roughly estimated according to minimum bending energy of just the landmarks. In a following step, each semi-landmark is projected onto the preserved parts of the respective endocranial surface of Cioclovina and slid along tangents to the surfaces. Landmarks on the reference that correspond to the missing area in Cioclovina were manually declared as "fully relaxed", i.e. missing, and are estimated according to the TPS algorithm. Finally, the estimated subcranial parts that are corresponding to the missing area in Cioclovina were fused with the original virtual endocast using Rapidform.

3.2.3.3.2. Statistical reconstruction

Another way to deal with missing data is to employ a statistical reconstruction, utilizing group form constraints (Weber and Bookstein, 2011), e.g. by applying a multiple multivariate regression. This approach exploits the morphological information present in a reference group or population (Gunz, 2005). Regression-based methods assume that there is an integration pattern of how morphological features covary with other anatomical traits (Bolker, 2000; Bookstein et al., 2003; Klingenberg, 2008; Mitteroecker and Bookstein, 2008). Available morphology on the damaged specimen is used to control the estimation of the missing regions, along with variation/covariation information from undamaged specimens. A disadvantage with multiple linear regression is that the linear relationship is ‘‘overfitted” in the case when the completed forms are used in the statistical analyses.

3.2.3.3.3. Knockout simulations

3.2.3.3.3.1. Beyond mirror imaging: New approaches during anatomical reconstructions

The basic steps in the study are summarized in **Figure 15** and described in detail in the following paragraphs.

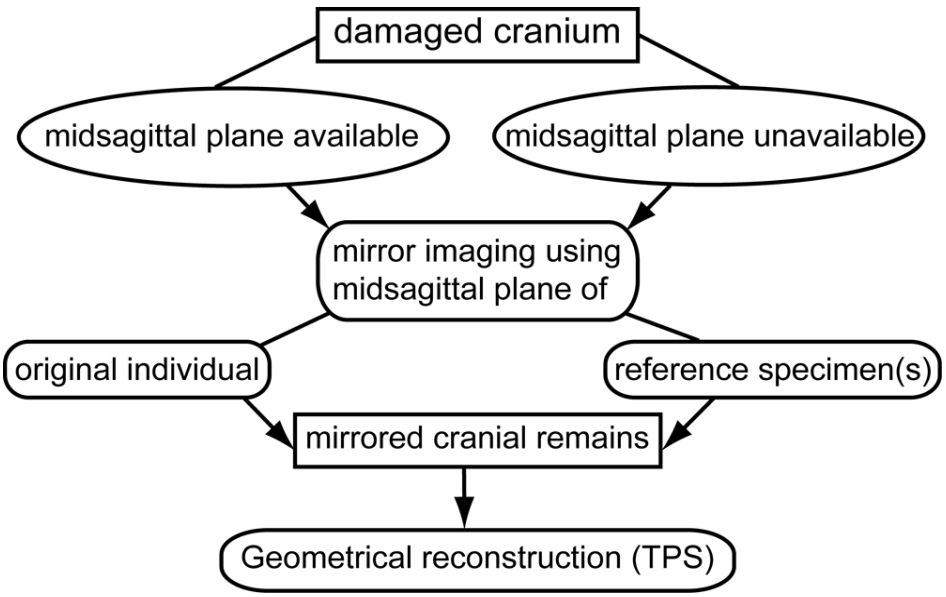

Figure 15 Individual steps during the reconstruction of the different cases; TPS=thin plate spline

Surface data

This study included computed tomography (CT) of 26 dried skulls from adult modern humans (13 females and 13 males) of mixed origin (Europe, Africa, Australia, Asia) ranging in age from 18y to 59y (**Table 1**). The CT scans were acquired at the Radiologie 2 Medizinische Universität Innsbruck, Austria, and at the Ruber clinic Madrid, Spain, via a Siemens Somatom Plus 40 (Innsbruck) and a General Electric, model GE Light Speed 16 (Madrid). All CT scans were recorded in DICOM file format at a reconstruction matrix size of 512 by 512 pixels. Pixel size ranged from 0.42 to 0.51mm and slice thickness from 0.625 to 1 mm. The half-maximum height protocol (Spoor et al., 1993) was used to reconstruct each cranial surface from the CT scans via the software package Amira 5.2 (Mercury Computer Systems, Chelmsford, MA). The procedure uses the histogram of the CT grey values to determine the appropriate border between materials (here bone and air) based on the Half Maximum Height Value. This value is then used as threshold for the generation of surfaces from CT data.

Table 1 Specimens: beyond mirror imaging (see 2.1.2)

specimens	*label*	*sex*	*age*	*origin*
Pell001	Ind1	male	18y	Europe
VA001	Ind2	female	25y	Europe
VA002	Ind3	male	45y	Europe
VA003	Ind4	male	25y	Europe
VA004	Ind5	female	30y	Europe
VA007	Ind6	male	20y	Europe
VA013	Ind7	female	20y	Australia
VA014	Ind8	female	35y	Africa
VA017	Ind9	male	30y	Australia
VA018	Ind10	male	25y	Europe
VA019	Ind11	female	20y	Europe
VA020	Ind12	male	45y	Australia
VA021	Ind13	male	45y	Europe
VA022	Ind14	male	51y	Europe
VA024	Ind15	female	20y	Africa
VA025	Ind16	male	30y	Africa
VA026	Ind17	male	35y	Asia
VA027	Ind18	male	35y	Asia
VA030	Ind19	female	23y	Europe
CSIC_OL794	Ind20	male	47y	Europe
CSIC_OL866	Ind21	female	59y	Europe
CSIC_OL1112	Ind22	male	23y	Europe
CSIC_OL1197	Ind23	female	30y	Europe
CSIC_OL1899	Ind24	female	43y	Europe
CSIC_OL1912	Ind25	female	30y	Europe
CSIC_OL1927	Ind26	female	20y	Europe

Landmark and semilandmark data

Using the open-source software Edgewarp3D (Bookstein and Green, 2002) and AMIRA 5.2 (Mercury Computer Systems, Chelmsford, MA), a 3D-template of 646 anatomical landmarks (n=79) and semilandmarks (n=567) was created to capture the geometry of the cranial surface (**Table 2, Figure 16**). The template was warped onto each complete specimen cranium by iterative thin-plate spline (TPS; Bookstein, 1991). This procedure aligns the template and target according to homologous landmarks present in both models. When virtually damaged specimens are the targets, the landmarks and semilandmarks of the template in the respective missing area of the target are declared as missing so that their coordinates will be estimated during warping.

Table 2 List of anatomical landmarks: beyond mirror imaging (see 2.1.2)

no.	*Pair landmarks*	*no.*	*Unpair landmarks*
1	Frontotemporale [a]	2	Glabella [a]
3	Frontomalare-temporale [a]	7	Nasion [a]
4	Frontomalare-orbitale [a]	15	Rhinion
5	Torus inferior [a]	24	Prosthion [a]
6	frontal - nasal - maxillary bone [a]	25	Nasospinale [a]
8	Zygotemporale inferior [a]	26	Orale [a]
9	Zygotemporale superior [a]	27	Incisivion [a]
10	Jugale [a]	28	Sutura palatina mediana & transversa [a]
11	Zygomaxillare [a]	30	Staphylion [a]
12	Foramen infraorbitale [a]	33	Bregma
13	Zygoorbitale [a]	37	Inion
14	Sutura nasomaxillaris - Apertura piriformes [a]	38	Lambda
16	M^2-M^3 [a / b]	45	Sphenobasion
17	M^1-M^2 [a / b]	46	Basion
18	M^1-P^4 [a / b]	47	Opisthion
19	P^4-P^3 [a / b]		
20	P^3-C [a / b]		
21	Canine base [a / b]		
22	C-I^2 [a / b]		
23	I^1-I^2 [a / b]		
29	Foramen palatinum majus [a]		
31	Maxillary bone - Os palatinum [a]		
32	Sutura sphenozygomatica - Fissura orbitalis		
34	Stephanion		
35	Linea temporalis posterior		
36	Auriculare		
39	Postglenoid		
40	Foramen ovale		

41	Canalis caroticus
42	Sutura occipitomastoidea - Foramen jugulare
43	Condylus occipitalis anterior
44	Condylus occipitalis posterior

[a] Facial landmarks

[b] Digitized on the alveolar process between the teeth

As substantial surface information is omitted using only traditional anatomical landmarks, we included curve and surface semilandmarks. As part of the digitization process, semilandmarks were allowed to slide along curves and surfaces to minimize the bending energy of the TPS computed between each specimen and the sample Procrustes average. This iterative procedure approximates curves by sets of chords calculated as vectors of two neighboring (semi)landmarks, and surfaces by their triangulation (Bookstein, 1997; Gunz et al., 2005b). Once relaxed, semilandmarks can be considered as homologous points.

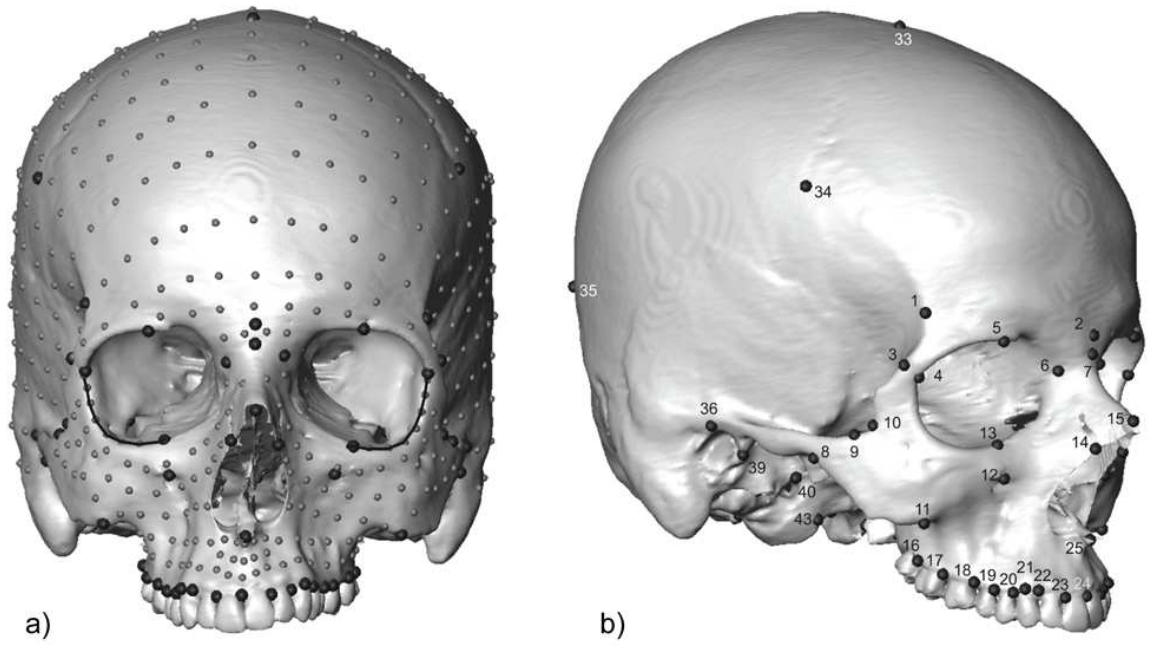

Figure 16 a) Complete template with anatomical landmarks (black; n = 79) and curve and surface semilandmarks (grey; n = 567). b) Anatomical landmarks of the template; labels are related to Table 2

Landmarks and semilandmarks were converted to shape coordinates by Generalized Procrustes Analysis (GPA) (Rohlf and Slice, 1990). This involves translating, rescaling, and rotating the configurations relative to each other so as to minimize the overall sum of squared distances between corresponding (semi)landmarks. The rescaling adjusts the landmark coordinates so that each configuration has a unit Centroid Size (CS; square root of the

summed squared Euclidean distances from all (semi)landmarks to their centroid) (Dryden and Mardi, 1998).

Knockout individuals

For the two knockout regions to be tested, we used the software Rapidform XOR2 (INUS Technology, Inc.) to cut crania along a-priori defined arbitrary planes. For the first case (mid-sagittal plane is still preserved) we took one individual (Ind1; **Table 1**) and oriented it with respect to the Frankfurt Horizontal plane (xy-plane) for better visualization (frontal view). Then, the midsagittal plane (defined as the best fit plane of 12 anatomical landmarks: prosthion, subspinale, rhinion, nasion, bregma, lambda, inion, opisthion, basion, staphylion, incisivion, orale) was defined parallel to the y-axis. The cutting plane for the first simulation was located by an anticlockwise rotation of -30° of the midsagittal plane using an axis parallel to the y-axis at nasion. After the rotation, an arbitrary translation of 3 mm along the x-axis towards zygorbitale (landmark 13) was performed. As a result, most of the left side of the cranium and significant parts of the right side were deleted, but a small portion of the left side remained which could later be used to establish the midsagittal plane (**Figure 17a**). This first knockout individual (KI-1) still featured 36 anatomical landmarks.

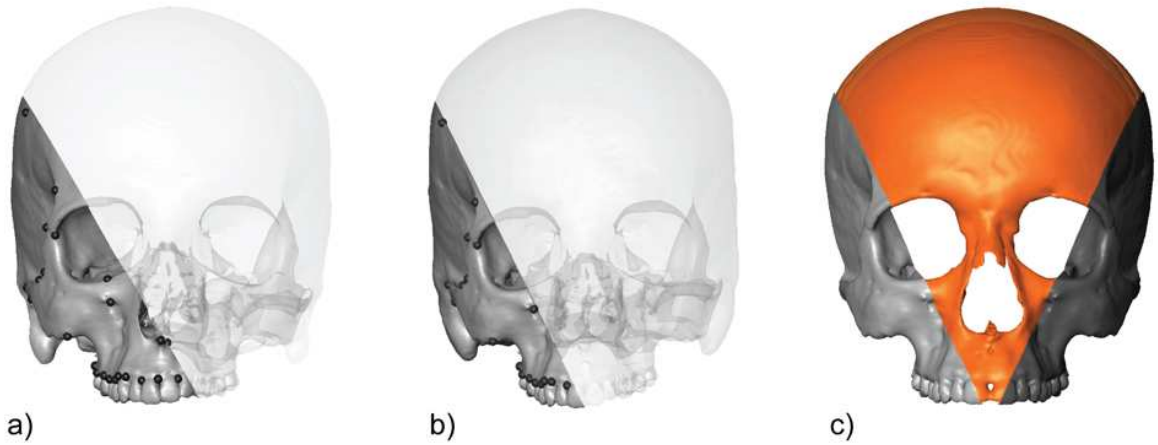

Figure 17 Knockout individuals. a) First knockout individual (KI-1) with remaining 36 anatomical landmarks. b) Second knockout individual (KI-2) with remaining 24 anatomical landmarks. c) Mirroring KI-2 along a midsagittal plane and estimating the remaining missing area using TPS (orange)

The cutting plane for the second case (no midsagittal landmarks preserved) was defined by taking the cutting plane of the first case and translating it further to the right side of the cranium (again along the x-axis) for a distance of 12 mm, and rotate it for another -6°. This second knockout individual (KI-2) completely lacks any landmarks from the midsagittal plane and features only 24 landmarks (**Figure 17b**).

Missing data estimation

Bilateral symmetry of KI-1 was restored by mirror imaging the right side along a best fit plane of the seven remaining midsagittal anatomical landmarks (prosthion, subspinale, opisthion, basion, staphylion, incisivion, orale). In the same step, each of the 36 real landmarks, that are present in the virtually cut cranium, was mirrored along the same plane, leaving out unpaired landmarks. During this procedure, a mirror-imaged model is created.

Restoring bilateral symmetry in KI-2 is a disproportionately harder task. Since there are no midsagittal landmarks that can be used to establish a midsagittal plane, we use the midsagittal plane of all the other individuals in the sample to mirror image the remaining right half of KI-2. To be able to implement this information, the individuals in the sample were superimposed via a GPA that only incorporated the 24 anatomical landmarks remaining in KI-2 (partial GPA). The position of the rest of the landmarks is calculated using the respective translation vector and rotation matrix of each individual that was computed during the GPA. The whole procedure could be referred to as a *block* GPA. This procedure was carried out via the open-source software Morpheus et al. (Slice, 1998) by "demoting" each landmark in the missing area of KI-2. As all the individuals are now superimposed according to the remaining 24 landmarks of KI-2, it is possible to compute the best fit midsagittal plane of every complete individual and mirror the surface of KI-2 relative to these midsagittal planes using Rapidform XOR2. The 24 anatomical landmarks that are present in KI-2 were included in the mirroring process, unpaired landmarks were not present. Accordingly, during this procedure we gain 28 different versions of the mirrored KI-2 (25 using each reference individual, and one in each case using the grand mean, the female mean and the male mean). Figure 3c shows the result of mirroring KI-2 according to the midsagittal plane of the Procrustes mean shape. It is worthwhile to note that GPA scales the landmarks configurations to unit CS, so any effect of size was circumvented during the computation of the midsagittal planes. By multiplying the landmark configuration and surface model of each specimen by its respective CS obtained during GPA, the superimposed landmark configurations are brought back to the space of the original specimens. This allows the usage of the original units (mm) to express the accuracy of the reconstruction.

Geometric reconstruction

After mirror imaging the knockout individuals in order to get a bilateral form (**Figure 17c**), we estimate the remaining missing data by TPS interpolation (Bookstein, 1991; Gunz, 2005a). The basic idea in the use of TPS algebra for missing data estimation is the warping of a

complete reference configuration (reference model or template) onto an incomplete target (target model), minimizing the thin plane spline's bending energy between the reference and the target (Bookstein, 1991; Gunz, 2005a).

In case of KI-1, the single surface model created during mirroring together with the available anatomical landmarks, served as target. Each complete specimen served as reference model and was warped onto the mirrored KI-1. The second knockout simulation created 25 individual models plus three models obtained by using the female, male, and grand mean as references. In this case, corresponding mirrored reconstructions and original individuals represent the target and reference respectively. That means that the complete surface model of, for example, Ind2 (**Table 1**) was used as reference and was warped onto the mirror reconstruction of KI-2 according to the midsagittal plane of Ind2.

Asymmetry

To quantify total asymmetry of a individual (object symmetry), I applied the Procrustes asymmetry assessment method from Mardia et al. (2000). The computation of total asymmetry for each individual incorporated the following steps: 1) for each individual landmark configuration of the facial bone (facial landmarks), a mirrored and appropriately relabeled form is produced; 2) each individual and its mirror are projected into shape-space using GPA; and 3) the total asymmetry is defined as the Procrustes distance between the original landmark configuration and its relabeled reflection. Since after GPA, each individual is in shape space, the Procrustes distance between each individual and its mirror is rather small. This asymmetrical variation is not necessarily biologically informative but provides additional information that could help to interpret the outcome of the reconstruction.

3.2.3.1.1.1 Comparing 3-dimensional virtual methods for reconstruction in craniomaxillofacial surgery

Fifteen skulls were selected for simulating the virtual osteotomy. The first one, a male of 31 years old, was collected at the Laboratory of Anthropology, Department of Histories and Method for the Conservation of Cultural Heritage (University of Bologna). The CT scan was carried out at the Radiology Department of Ravenna Hospital by means of the Brilliance 64-Slice CT scanner by Philips, with a slice thickness of 0.9 mm, increment 0.45 mm. The second one (**Figure 18**), belonging to a male of 18 years old, was CT scanned at the Pellegrin

Hospital, Bordeaux, with Brilliance CT 40-Slice by Philips, with a slice thickness of 0.9 mm, increment 0.45 mm.

Table 3 Specimens: comparing 3-dimensional virtual methods for reconstruction in craniomaxillofacial surgery (see 2.1.3)

specimens	*label*	*sex*	*age*	*origin*
VA001	H1	female	25y	Europe
VA003	H2	male	25y	Europe
VA006	H3	male	20y	Europe
VA013	H4	female	20y	Australia
VA020	H5	male	45y	Australia
VA024	H6	female	20y	Afrika
VA026	H7	male	35y	Asia
VA027	H8	male	35y	Asia
VA030	H9	female	23y	Europe
CSIC_OL794	H10	male	47y	Europe
CSIC_OL1112	H11	male	23y	Europe
CSIC_OL1197	H12	female	30y	Europe
CSIC_OL1899	H13			Europe
Pell001	H14	male	18y	Europe
Pico	H15	male	31y	Europe

In Rapidform XOR (INUS Technology, Inc.), left zygomatic virtual osteotomy (including segments of the maxillary bone, part of the orbital floor and the latero-orbital wall of the zygomatic bone) was simulated in the models (**Figure 18b**). This was accomplished by three virtual cutting planes passing approximately through the following sutures: zygomo-maxillary suture, fronto-zygomatc suture and temporal-zygomatic suture on the zygomatic arc.

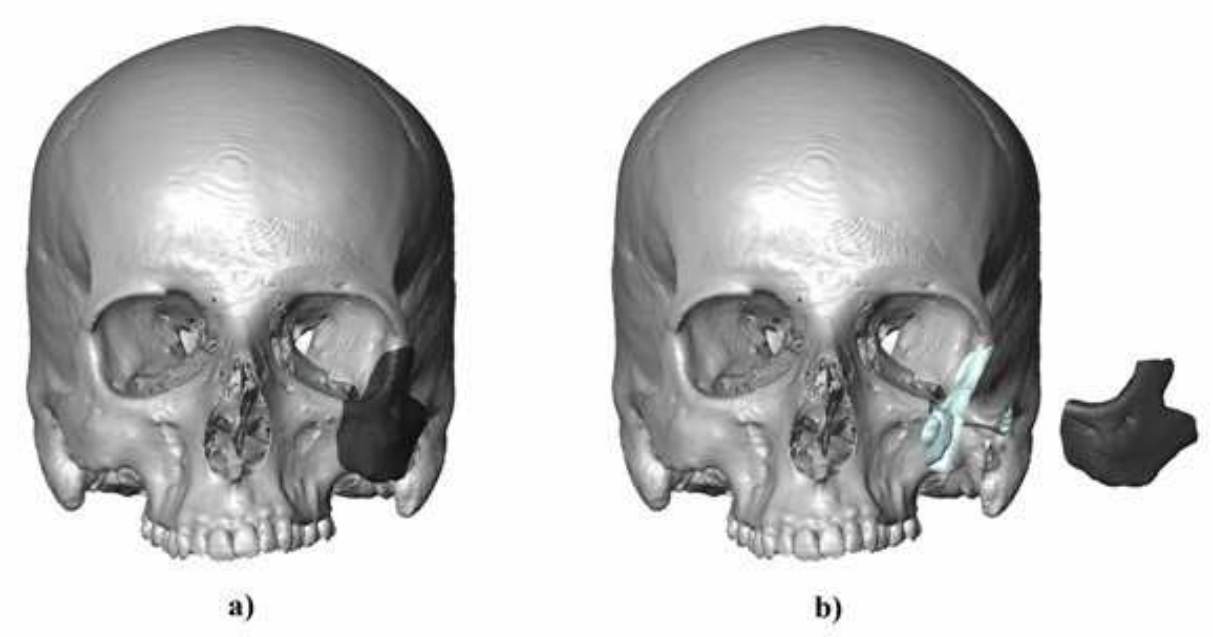

Figure 18 a) Three-dimension digital model of the cranium with the left zygomatic portion in dark gray; b) virtual osteotomy of the left zygomatic bone.

The midsagittal plane was defined as the best fit plane of 8 anatomical landmarks (prostion, subspinale, nasion, bregma, lambda, inion, opistion, staphylion). In order to test the deviation of the reconstruction to the original specimens, three virtual reconstruction techniques were tested:

1) The right unaffected hemiface was mirrored and the left missing part was directly restored by the mirrored-copy without attempting any manual or automatic alignment of the reflected part onto the left hemiface.
2) In Rapidform XOR, the right mirrored hemiface was aligned to the left osteomized hemiface using the iterative closest point function(ICP) that minimizes the distance between two point clouds applying the least squares method. Accordingly, the missing left part was replaced by the bone segment of the aligned right mirrored hemiface.
3) The mirrored cranium was molded towards the original one applying thin plate spline (TPS) warping.

Due to the restricted amount of anatomical landmarks in the maxillofacial region, which could be further reduced after osteotomy, it is necessary to include semilandmarks. In detail, a template including 16 anatomical landmarks and 187 semilandmarks was defined on the mirrored-copy of the fifteen skulls in Edgewarp 3d and Amira 5.2. A curve was digitized along the margin of each orbit and 36 semilandmarks were evenly projected on each curve (curve semilandmarks) (**Figure 19a,b; Table 4**). Additionally, 114 semilandmarks were digitized on the surface of the template (surface semilandmarks).

Table 4 Landmarks and curves: comparing 3-dimensional virtual methods for reconstruction in craniomaxillofacial surgery (see 2.1.3)

no.	*landmark*	*curves*	*Semi-lms count**
1	Articular eminence (ar-em) left	Alveolar right	9
2	Articular eminence (ar-em) right	Alveolar left	9
3	Bregma (b)	Lower zygomaticotemporal outline left	10
4	Ektomolare (ekm) left	Upper zygomaticotemporal outline left	15
5	Ektomolare (ekm) right	Temporal left	4
6	Frontotemporale (ft) left	Orbital left	14
7	Frontotemporale (ft) right	Orbital right	8
8	Frontomalare orbitale (fmo) left	Temporal right	4
9	Frontomalare orbitale (fmo) right		
10	Nasion (n)	Total semilandmarks on curves	72
11	Orale (ol)		
12	Prostion (pr)		
13	Staphylion (sta)		

14	Stephanion (st) left
15	Stephanion (st) right
16	Subspinale (ss)

*semilandmarks identified on curves

Afterwards, a corresponding set of landmarks and semilandmarks was created on the target models (the original resected craniums). After manual digitization of the 16 anatomical landmarks and the 8 curves, the 73 curve semilandmarks were automatically projected onto the respective curves digitized so far. Accordingly they can be used as fixed landmarks together with the anatomical landmarks to drive a TPS warping for constraining the 114 surface semilandmarks closer to their proper position. Since some of the surface semilandmarks could not be directly placed on the surface of the model, a further projection step was required.

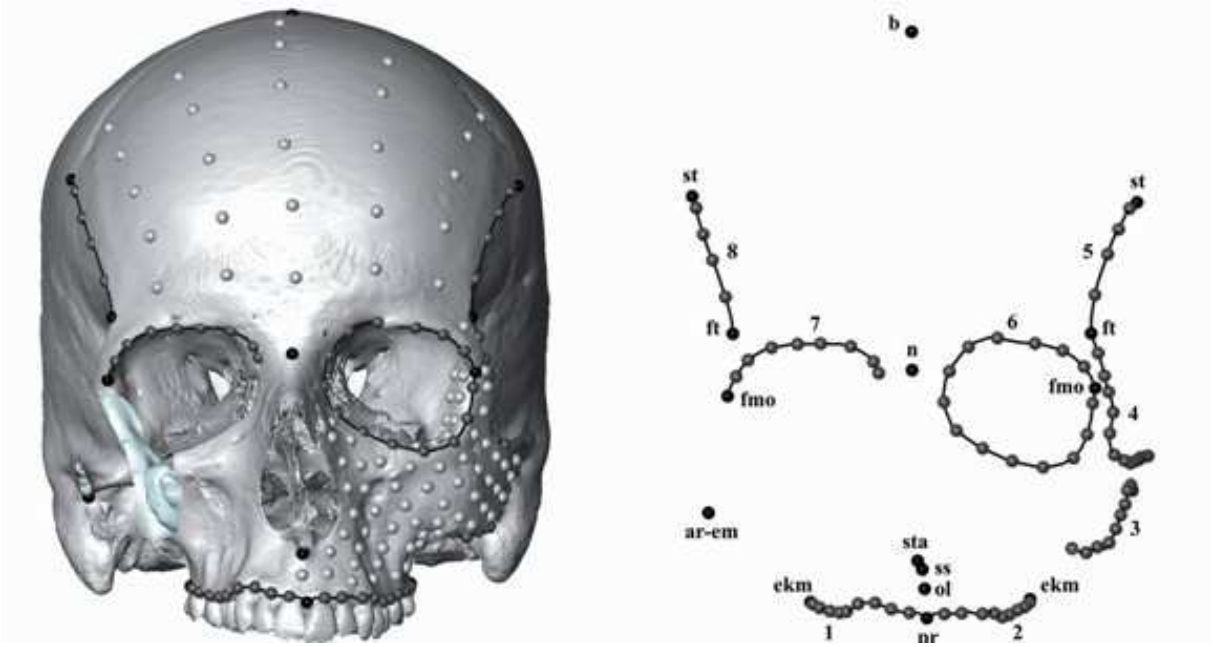

a) b)

Figure 19 a) set of landmarks and semilandmarks defined on the reference model (template); b) landmarks, curves and curves semilandmarks of the template; landmarks and curve's names are in Table I.

The 203 landmarks and semilandmarks of the reference and the target were imported into Amira 5.2. Using the "LandmarkSurfaceWarp" module, the surface of the reference was then warped onto the specimen with the missing zygoma according to the landmarks and semilandmarks of the template, using the Bookstein transformation mode based on the TPS

interpolation. This mode guarantees that all landmarks will be transformed exactly to their corresponding points, applying the nearest neighbour interpolation for resampling the final model.

The digital models obtained by TPS warping were imported in Rapidform XOR and the zygomatic segments were isolated using the cutting planes previously created for virtual zygomatic osteotomy.

In order to visualize and quantify the differences between the reconstructed models and the original osteotomized bone segments, deviation surface analyses were carried out in Rapidform XOV/Verifier (INUS Technology, Inc.). The original models were considered as the reference surface. Using the "Auto Color Bar" function, the mean and the standard deviation (SD) were automatically computed and the color scales ranging from the minimum to the maximum were created automatically displaying the color-coded onto the model's surface. In detail, negative and positive values emphasized respectively the backward and forward displacement of the reconstruction compared with the original left zygomatic bone. For each reconstruction, the value that represent the interval between the mean ±2SD (that account for 95% of the surface deviation) was used for t-test (Shapiro-Wilk test underlined that the variable are normally distributed) in order to verify if the reconstructions differ from each other in a significant way. The statistical analysis has been computed using the software PAST v. 1.90 (PAlaeontological STatistics). Finally, as an example, a more detailed description of the outcome obtained in two cases (individual H15 and H14) was provided.

3.2.3.3.3.2. Virtual reconstruction of modern and fossil hominoid crania: effects of the choice of the reference form

The study included computed tomography (CT) scans of 64 dried skulls from *Homo sapiens* (n=25), *Pan troglodytes* (n=19), and *Pongo pygmaeus* (n=20). Sexes are evenly distributed within each species sample (**Table 5**). Three CT scans of fossils are included: Sts 5 (*Australopithecus africanus*; Broom, 1947), Petralona (*Homo heidelbergensis*; Kokkoros and Kanellis, 1960), and Mladec 1 (modern *Homo sapiens*; Szombathy, 1925). The reference samples and fossils are chosen because they represent a very broad range of hominoid morphology, each characterized by its own particular mosaic of ancestral and derived features (see section 2.2.1). All of the included fossils have a good preservation status. Their small

missing areas do not affect the process of reconstruction when simulating the missing areas that are analogous to A.L. 444-2.

Table 5 Specimens: consequences of reference sample choice (see 2.2)

	collection	sex	
Homo sapiens			
VA001	Vienna	female	
VA002	Vienna	male	
VA003	Vienna	male	
VA004	Vienna	female	
VA007	Vienna	male	
VA013	Vienna	female	
VA014	Vienna	female	
VA017	Vienna	male	
VA018	Vienna	male	
VA019	Vienna	female	
VA020	Vienna	male	
VA021	Vienna	male	
VA022	Vienna	male	
VA024	Vienna	female	
VA025	Vienna	male	
VA026	Vienna	male	
VA027	Vienna	male	
VA030	Vienna	female	
OL794	CSIC	male	
OL866	CSIC	female	
OL1112	CSIC	male	
OL1197	CSIC	female	
OL1899	CSIC	unknown	
OL1912	CSIC	unknown	
OL1927	CSIC	unknown	
Pan troglodytes			
ch-25124-cr	Vienna	male	*Pan troglodytes sp*
ch-793-cr	Vienna	female	*Pan troglodytes sp*
CA14A	York	male	*Pan troglodytes sp*
S143	Senckenberg	female	*Pan troglodytes sp*
A1MMRAC10447	Toulouse	male	*Pan troglodytes schweinfurthi*
A2MMRAC286	Toulouse	male	*Pan troglodytes schweinfurthi*
A2MMRAC9576	Toulouse	male	*Pan troglodytes schweinfurthi*
A2MMRAC83006M13	Toulouse	male	*Pan troglodytes schweinfurthi*
A2MMRAC83006M17	Toulouse	male	*Pan troglodytes schweinfurthi*
S035	Senckenberg	female	*Pan troglodytes sp*
S088	Senckenberg	male	*Pan troglodytes sp*
S126	Senckenberg	female	*Pan troglodytes sp*
MRAC 83006M16	Toulouse	male	*Pan troglodytes schweinfurthi*
MRAC 9931	Toulouse	female	*Pan troglodytes schweinfurthi*
A1FMRAC10448	Toulouse	female	*Pan troglodytes schweinfurthi*
A2FMRAC8341	Toulouse	female	*Pan troglodytes schweinfurthi*
A2FMRAC8369	Toulouse	female	*Pan troglodytes schweinfurthi*
A2FMRAC9655	Toulouse	female	*Pan troglodytes schweinfurthi*
A2IMRAC11987	Toulouse	unknown	*Pan troglodytes schweinfurthi*

Pongo pygmaeus			
ZSM-1981/25	ZSM	male	*Pongo pygmaeus pygmaeus*
ZSM-1981/33	ZSM	female	*Pongo pygmaeus pygmaeus*
ZSM-1981/82	ZSM	female	*Pongo pygmaeus pygmaeus*
ZSM-1981/90	ZSM	female	*Pongo pygmaeus pygmaeus*
ZSM-1981/123	ZSM	female	*Pongo pygmaeus pygmaeus*
ZSM-1981/135	ZSM	female	*Pongo pygmaeus pygmaeus*
ZSM-1981/139	ZSM	female	*Pongo pygmaeus pygmaeus*
ZSM-1981/141	ZSM	male	*Pongo pygmaeus pygmaeus*
ZSM-1981/143	ZSM	male	*Pongo pygmaeus pygmaeus*
ZSM-1981/145	ZSM	male	*Pongo pygmaeus pygmaeus*
ZSM-1981/146	ZSM	male	*Pongo pygmaeus pygmaeus*
ZSM-1981/151	ZSM	male	*Pongo pygmaeus pygmaeus*
ZSM-1981/152	ZSM	male	*Pongo pygmaeus pygmaeus*
ZSM-1981/165	ZSM	female	*Pongo pygmaeus pygmaeus*
ZSM-1981/174	ZSM	female	*Pongo pygmaeus pygmaeus*
ZSM-1981/176	ZSM	male	*Pongo pygmaeus pygmaeus*
ZSM-1981/178	ZSM	male	*Pongo pygmaeus pygmaeus*
ZSM-1981/183	ZSM	female	*Pongo pygmaeus pygmaeus*
ZSM-1981/190	ZSM	male	*Pongo pygmaeus pygmaeus*
ZSM-1981/208	ZSM	female	*Pongo pygmaeus pygmaeus*

Using the open-source software Edgewarp3D and AMIRA 5.2, a 3D-template of 77 anatomical landmarks and 681 semilandmarks was created to capture the geometry of the complete ectocranial surface (**Table 6**, **Figure 20a**). The template was warped onto each complete specimen (target) cranium by iterative TPS. This procedure aligns the template and target according to homologous anatomical landmarks present in both models. A TPS is invariant to position, scale and rotation of the forms and therefore does not require a previous Procrustes fitting step. As traditional anatomical landmarks only capture the cranial geometry quite incompletely, we included curve and surface semilandmarks that add morphological information. As part of the digitization process, semilandmarks were allowed to slide along curves and surfaces to minimize the bending energy of the TPS computed between each reference and target specimen. This iterative procedure approximates curves by sets of chords calculated as vectors of two neighboring (semi)landmarks, and surfaces by their triangulations. Once relaxed, semilandmarks can be considered as geometrically homologous points.

In each specimen, exactly the area that is missing in A.L. 444-2 was “knocked out” (**Figure 20b,c**). Missing regions in the neurocranium incorporate large portions of the parietal and sphenoid bone, and the superior part of the temporal squama. In the midsagittal plane, approximately the middle third of the area between bregma and lambda was missing. Bilaterally, the missing area involved both parietal eminences and approached the coronal suture up to krotaphion. The sphenoid bone was almost completely missing. Missing facial

portions included parts of the upper (inferior supraorbital margin) and mid-facial skeleton (nasal bones and the maxillary bone excluding the alveolar ridge and upper dentition).

In total, 8 anatomical landmarks (2, 12, 13, 14, and 15; see Table 1) and 110 semilandmarks in the facial and 137 semilandmarks in the neurocranial region were declared as absent. Missing data was then estimated by TPS, warping:

1) all three species' consensus configurations to each "knockout" individual (n=201),
2) all the specimens in the sample
   a) onto one chosen "knockout" individual from each of the extant species that we refer to as Homo1, Pan1, Pongo1 (n=189 because Homo1, Pan1, and Pongo1 were excluded from the reference sample), and
   b) onto each of the fossils (n=192)

Warping was performed with the open-source software Edgewarp3D (Bookstein and Green, 2002a). First, a TPS interpolation based on 69 (total number of anatomical landmarks minus the missing eight anatomical facial landmarks) out of the 77 anatomical landmarks was computed to warp all semilandmarks and missing landmarks from the reference to each "knockout" individual.

Table 6 Anatomical landmarks: consequences of reference sample choice (see 2.2)

no.	*Pair landmarks*	*no.*	*Unpair landmarks*
1	Frontotemporale */**/***	2	Glabella */**/***
3	Frontomalare-temporale */***	7	Nasion */**/***
4	Frontomalare-orbitale */***	15	Rhinion */***
5	Torus inferior */**/***	24	Prosthion */**/***
6	Frontal - nasal - maxillary bone */**/***	25	Nasospinale */**/***
8	Zygotemporale inferior	26	Orale */***
9	Zygotemporale superior	27	Incisivion */**/***
10	Jugale **/***	28	Sutura palatina mediana & transversa */***
11	Zygomaxillare */**/***	30	Staphylion **/***
12	Foramen infraorbitale */**/***	33	Bregma */**/***
13	Zygoorbitale */***	36	Lambda */**/***
14	Sutura nasomaxillaris - Apertura piriformes */**/***	43	Sphenobasion */**/***
16	M2-M3 */*** (alv)	44	Basion */**/***
17	M1-M2 */*** (alv)	45	Opisthion */**/***
18	M1-P4 */*** (alv)		
19	P4-P3 */*** (alv)		
20	P3-C *** (alv)		
21	Canine base *** (alv)		
22	C-I2 */*** (alv)		
23	I1-I2 *** (alv)		
29	Foramen palatinum majus **/***		
31	Distal M3 **/***		

32	Sutura sphenozygomatica - Fissura orbitalis */**/***
34	Stephanion **/***
35	Auriculare */**/***
37	Postglenoid */**/***
38	Foramen ovale **
39	Canalis caroticus
40	Sutura occipitomastoidea - Foramen jugulare
41	Condylus occipitalis anterior */**/***
42	Condylus occipitalis posterior */**/***

*landmarks in Mladec1 (n=61), ** landmarks in Petralona (n=68), landmarks in Sts5 (n=46)
(alv) digitized on the alveolar process between the teeth

For the fossils the number of anatomical landmarks in this step was reduced (**see Table 6**) because some of them lacked landmarks even before the knock out procedure. In this way, the reference and target are aligned according to the anatomical landmarks and all semilandmarks are roughly estimated according to minimum bending energy of just the landmarks. In a following step, each semilandmark is projected onto the preserved parts of the ectocranial surface of the target and slid along tangents to its surface. Landmarks on the reference that correspond to the missing area in the target were manually declared as "fully relaxed", i.e. missing, and are estimated according to the TPS algorithm. The warping of complete reference forms from the same or a closely related species to an incomplete specimen generates an amount of reconstructions for each case that corresponds to the amount of references employed.

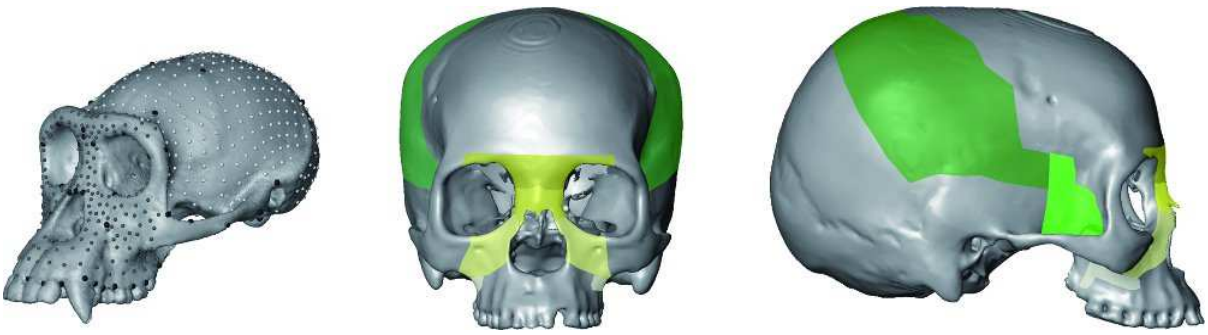

a) b) c)

Figure 20 Template and missing areas. a) Complete template with anatomical landmarks (black; n = 77) and curve and surface semilandmarks (dark grey: face, n = 225; light grey: neurocranium, n = 456). b) facial and c) neurocranial knockout regions in the style of A.L. 444-2. Subdivided regions color coded (facial: yellow, neurocranial: green).

Results for each of the reconstruction series are expressed in the form of residuals between the (semi)landmarks of the original configuration and the estimated configurations. A semilandmark carries only shape information perpendicular to the curvature; thus for the missing semilandmarks only the residual normal to the ridge curve or surface was used. We

define reconstruction accuracy as the square root of the mean squared difference between the original and the reconstruction (root mean square: RMS), which has the same units as the data (mm). The RMS was computed for each landmark and an average residual is calculated for the landmark in each individual that shows the highest RMS in each reconstruction series in each region, in the following referred to as the average of the maximum landmark RMS. Minimum and maximum distances were computed for each landmark separately and visualized in a color coded bar plot together with the maximum landmark RMS (**Figures 50 and 51**). Missing facial and neurocranial areas were subdivided to allow a more detailed visualization of the differences between the original and the reconstruction. Note that all missing data in the facial area (all its subareas together) and in the neurocranial area (all its subareas together) were estimated separately. For an improved visualization of the results, the neurocranial missing area was separated into (1) a sphenoid (n=26), (2) a parietal (n=108), and (3) a midsagittal area (n=3). The facial knockout region is subdivided into four areas: (1) superior alveolar process (n=12), (2) anterior maxillary surface (n=54), (3) nasal and interorbital area (n=14), and (4) the supraorbital region (n=30). Landmarks and semilandmarks were then converted to shape coordinates by Generalized Procrustes Analysis (GPA). This involves translating, rescaling, and rotating the configurations relative to each other so as to minimize the overall sum of squared distances between corresponding (semi)landmarks. The rescaling adjusts the landmark coordinates so that each configuration has a unit Centroid Size (CS; square root of the summed squared Euclidean distances from all (semi)landmarks to their centroid) (Rohlf and Slice, 1990). Principal Component Analysis (PCA) of the matrix of shape coordinates was carried out on the original sample. Reconstructions of the virtually fragmented fossils were subsequently projected in the same multivariate space (shape space) as the original sample so that we can evaluate the variability of the reconstructions in relation to the species' variability of the originals.

3.2.4. Statistical analyses

Several statistical procedures were carried out during the different analyses which are presented below.

3.2.4.1. Principal component analysis

During factor analysis several variables are summarized to some few factors. Factor analysis is therefore assigned to data-reducing or hypothesis-generating statistical methods (Backhaus et al., 2006). The basic idea of factor analysis is information compression. The goal is to extract a few factors from many variables with the least loss of information. A statistical analysis of the data has to highly preserve the individual variances but simultaneously condense them, so that on the one hand further computations remain manageable and on the other hand a substantive interpretation of the data is meaningful. A particularity of the factors is that the concentrated information must not be interpreted in the same way as the raw data. Factor analysis is therefore always hypothesis-generating. The extraction, here the method of principal components analysis generates factors by extracting the variance included in the variables. The factor summarizes the initially present variables and is usually multidimensional (Sachs, 2004). The correlation of a variable with one factor is represented by the factor loadings. The shorter the spatial distance between factor and variable in the factor space is, the higher is the correlation. A positive or negative factor loading indicates that the factor is positively or negatively correlated with the variables. With a factor loading of 0 the factor and the variable are stochastically independent of each other. A factor loading of 1 means that the factor perfectly correlates with the variable, hence both are identical. The eigenvalue of a factor is the total variance of all variables that explains this factor. The eigenvalue results regardless of the extraction method and is always the sum of all squared factor loadings of the factor (Backhaus et al., 2006). In this study, the extraction method is represented by a principal components analysis (PCA). The goal of this method is to extract a few valid factors from variables with many properties that are determining these factors. Through the transformation of multi-dimensional features in a vector space with new base, the correlation is minimized. The Principal Axis Transformation can be represented by a matrix, consisting of the eigenvectors of the covariance matrix. The data is then represented as a point cloud in a n-dimensional Cartesian coordinate system. Then a new coordinate system is placed in the point cloud, and this coordinate system is rotated. The first axis is defined by the point cloud, so that the variance of the data in this direction is maximized. The second axis is orthogonally on the first axis. In its direction is the second largest variance and so on. For n-dimensional data, there are n principle axes that are perpendicular to each other (Bortz, 1999).

If Procrustes shape coordintes are analyzed using a PCA, shape variations are thus represented by principal components (O´Higgins and Pan, 2004). With a principal component analysis of Procrustes shape coordinates (i.e. landmark coordinates after superimposition) differences in the mean shapes in relation to gender and age can be tested. Studies in which ontogenetic changes in size is the main source of shape variation, is it very likely "that the first principal components will adequately represent the relationship between size and shape (allometry)" (O'Higgins & Pan, 2004, p. 30). PCA of the matrix of shape coordinates augmented by a column of the natural logarithm of Centroid Size (lnCS) is corresponding to a PCA in form space (Mitteroecker et al., 2004).

To visualize the shape deformation along the principal components, the eigenvectors of the principal components need to be transformed into coordinates that will be added to the mean configuration (mean shape). The shape change represented by the eigenvectors of a particular principal component – the corresponding *relative warp* – can then be visualized as a thin plate spline deformation from the mean shape *plus* or *minus* the eigenvectors. For the first principal component, each resulting landmark configuration then corresponds to the right (plus) and left (minus) side of the PC respectively. Form changes along a principal component or a trajectory can visualized by means of surface warps analogues to the procedure in shape space. They are produced by taking the landmark coordinates of the mean shape and adding the eigenvectors, together with the exponential function of the corresponding loadings for lnCS (see **Appendix 4** for R code).

3.2.4.2. Partial least squares (PLS)

The PLS method explores the interrelations between two or more blocks of observations and is useful in examining morphological integration (Rohlf and Corti, 2000; Mitteroecker and Bookstein, 2007). Singular warps are a special case of partial least squares used to quantify and visualize the covariation of anatomical regions when all variable blocks are shape coordinates (Bookstein, 1996a; Gunz and Harvati, 2007). The blocks of variables are chosen a priori to the analysis. An advantage of this technique is that it can also be used to analyze the relationship between shape and other variables such as climatic variables or behaviours (Manfreda et al., 2006). In the approach introduced in my thesis I will estimate the orientation of the upper jaw in relation (non-shape block) to the shape of the sphenoid bone (shape block). Two-block partial least squares is based on a singular value decomposition of the between-block covariance matrix. It calculates the linear combinations of the original (shape)

variables that provide the best mutual cross-prediction between the two blocks (Rohlf and Corti, 2000; Gunz and Harvati, 2007).

3.2.4.2.1. Facial orientation and integration in the hominoid cranium

Partial least squares (PLS) is the main procedure used in these analyses. The following section introduces the methodology, while the R code used during the analysis is given in the **Appendix 5**.

3.2.4.2.1.1. Facial orientation and morphological integration with the cranial base

The data is from computed tomography (CT) scans of 81 dried skulls from *Pan troglodytes* (n=40)*, and Pongo pygmaeus* (n=41) (**Table 7**). Using the open-source software Edgewarp3D along with AMIRA 5.2, a 3D-template of 47 anatomical landmarks and 52 semilandmarks on curves was created to capture the geometry of the cranial base (anterior cranial fossa, medial portion of the middle cranial fossa, and clivus) and the face (**Table 8, Figure 21**). The number of landmarks in the *Pan* sample was reduced due to the poor preservation status of many specimens, leaving out the pre-sellar portion of the cranial base (basion) and some of the landmarks on the anterior cranial base. This will prevent a discussion of the results concerning the posterior cranial base in *Pan*, e.g. in relation to post-sellar basicranial flexion, but is unlikely to influence the outcomes concerning the association between the anterior cranial base and the face.

Table 7 Specimens: facial orientation and morphological integration with the cranial base (see 2.3.4.1)

catalogue number	***collection***	***sex***	***subspecies***
ch-793-cr	Vienna	female	unknown
A2FMRAC8341	Tervuren	female	*Pan troglodytes schweinfurthi*
A2FMRAC8369	Tervuren	female	*Pan troglodytes schweinfurthi*
A2FMRAC9655	Tervuren	female	*Pan troglodytes schweinfurthi*
MRAC 9931	Tervuren	female	*Pan troglodytes schweinfurthi*
A1FMRAC10448	Tervuren	female	*Pan troglodytes schweinfurthi*
LA886	York	female	unknown
LA1086	York	female	unknown
S035	Senckenberg	female	*Pan troglodytes verus*
S087	Senckenberg	female	*Pan troglodytes verus*
S107	Senckenberg	female	*Pan troglodytes verus*
S109	Senckenberg	female	*Pan troglodytes verus*
S122	Senckenberg	female	*Pan troglodytes verus*
S126	Senckenberg	female	*Pan troglodytes verus*

S130	Senckenberg	female	*Pan troglodytes verus*
S134	Senckenberg	female	*Pan troglodytes verus*
S135	Senckenberg	female	*Pan troglodytes verus*
S142	Senckenberg	female	*Pan troglodytes verus*
S143	Senckenberg	female	*Pan troglodytes verus*
A2MMRAC9576	Tervuren	male	*Pan troglodytes schweinfurthi*
A1MMRAC10447	Tervuren	male	*Pan troglodytes schweinfurthi*
ch-25124-cr	Vienna	male	unknown
CA14A	UCL Anatomy Collection	male	unknown
LA686	York	male	unknown
LA786	York	male	unknown
A2MMRAC83006M13	Tervuren	male	*Pan troglodytes schweinfurthi*
A2MMRAC83006M16	Tervuren	male	*Pan troglodytes schweinfurthi*
A2MMRAC83006M17	Tervuren	male	*Pan troglodytes schweinfurthi*
S088	Senckenberg	male	*Pan troglodytes verus*
S095	Senckenberg	male	*Pan troglodytes verus*
S102	Senckenberg	male	*Pan troglodytes verus*
S108	Senckenberg	male	*Pan troglodytes verus*
S110	Senckenberg	male	*Pan troglodytes verus*
S117	Senckenberg	male	*Pan troglodytes verus*
S129	Senckenberg	male	*Pan troglodytes verus*
S132	Senckenberg	male	*Pan troglodytes verus*
S137	Senckenberg	male	*Pan troglodytes verus*
S141	Senckenberg	male	*Pan troglodytes verus*
A2IMRAC11987	Tervuren	undetermined	*Pan troglodytes schweinfurthi*
1981/33	ZSM	female	*Pongo pygmaeus pygmaeus*
1981/60	ZSM	female	*Pongo pygmaeus pygmaeus*
1981/82	ZSM	female	*Pongo pygmaeus pygmaeus*
1981/84	ZSM	female	*Pongo pygmaeus pygmaeus*
1981/86	ZSM	female	*Pongo pygmaeus pygmaeus*
1981/90	ZSM	female	*Pongo pygmaeus pygmaeus*
1981/95	ZSM	female	*Pongo pygmaeus pygmaeus*
1981/101	ZSM	female	*Pongo pygmaeus pygmaeus*
1981/121	ZSM	female	*Pongo pygmaeus pygmaeus*
1981/123	ZSM	female	*Pongo pygmaeus pygmaeus*
1981/125	ZSM	female	*Pongo pygmaeus pygmaeus*
1981/135	ZSM	female	*Pongo pygmaeus pygmaeus*
1981/136	ZSM	female	*Pongo pygmaeus pygmaeus*
1981/139	ZSM	female	*Pongo pygmaeus pygmaeus*
1981/156	ZSM	female	*Pongo pygmaeus pygmaeus*
1981/165	ZSM	female	*Pongo pygmaeus pygmaeus*
1981/174	ZSM	female	*Pongo pygmaeus pygmaeus*
1981/176	ZSM	female	*Pongo pygmaeus pygmaeus*
1981/192	ZSM	female	*Pongo pygmaeus pygmaeus*
1981/208	ZSM	female	*Pongo pygmaeus pygmaeus*
1981/212	ZSM	female	*Pongo pygmaeus pygmaeus*
1981/25	ZSM	male	*Pongo pygmaeus pygmaeus*
1981/45	ZSM	male	*Pongo pygmaeus pygmaeus*
1981/47	ZSM	male	*Pongo pygmaeus pygmaeus*
1981/68	ZSM	male	*Pongo pygmaeus pygmaeus*
1981/69	ZSM	male	*Pongo pygmaeus pygmaeus*
1981/93	ZSM	male	*Pongo pygmaeus pygmaeus*
1981/99	ZSM	male	*Pongo pygmaeus pygmaeus*
1981/141	ZSM	male	*Pongo pygmaeus pygmaeus*

1981/143	ZSM	male	*Pongo pygmaeus pygmaeus*
1981/145	ZSM	male	*Pongo pygmaeus pygmaeus*
1981/146	ZSM	male	*Pongo pygmaeus pygmaeus*
1981/149	ZSM	male	*Pongo pygmaeus pygmaeus*
1981/151	ZSM	male	*Pongo pygmaeus pygmaeus*
1981/152	ZSM	male	*Pongo pygmaeus pygmaeus*
1981/164	ZSM	male	*Pongo pygmaeus pygmaeus*
1981/178	ZSM	male	*Pongo pygmaeus pygmaeus*
1981/190	ZSM	male	*Pongo pygmaeus pygmaeus*
1981/202	ZSM	male	*Pongo pygmaeus pygmaeus*
1981/203	ZSM	male	*Pongo pygmaeus pygmaeus*
1981/234	ZSM	male	*Pongo pygmaeus pygmaeus*

The template was warped onto each specimen by iterative TPS. Landmarks and semilandmarks were converted to shape coordinates by Generalized Procrustes Analysis (GPA).

In order to analyze the covariation between the rigid motion of the palate and the shape of the cranial base and upper face (represented by the orbits), the whole maxillary bone, considered as a single module, is treated as a rigid body whose position is determined by the position of its centroid and by its orientation. A rigid body is an idealization of a solid body of finite size in which deformation is neglected and a common concept in physics ("Rigid body – Wikipedia". Retrieved from http://en.wikipedia.org/wiki/Rigid_body). In rigid bodies the distance between any two given set of points remain constant, regardless of external forces exerted on it. In this context, a rigid motion is a "transformation consisting of rotations and translations which leaves a given arrangement unchanged" (Weisstein, 2012). In three dimensions this totals six degrees of freedom, three for translation and three for rotation. The following paragraph describes how the information about the degrees of freedom of the palatal rigid motion is extracted. Each step is carried out for a pooled sample (investigating evolutionary integration) and for each species separately (investigating structural integration).

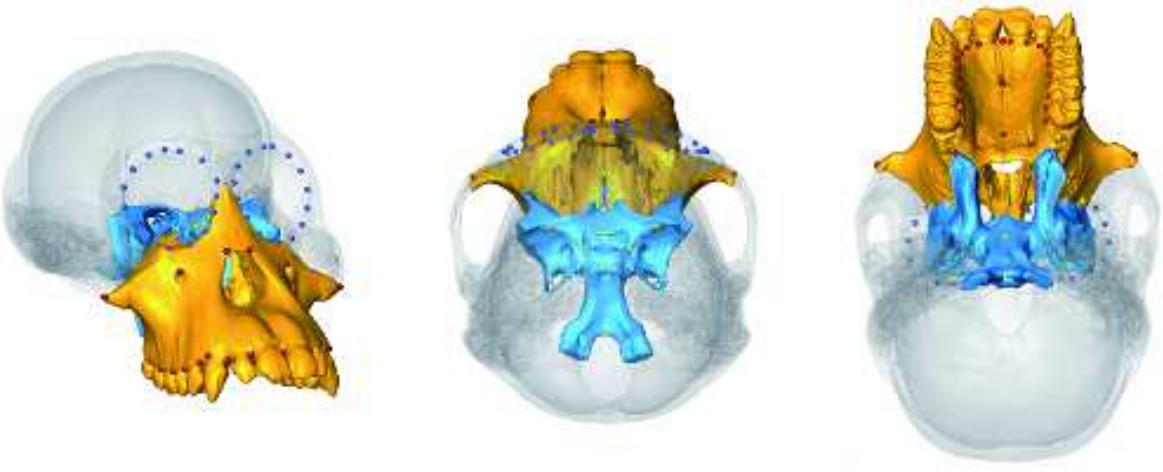

Figure 21 Template: Facial orientation and integration with the hominoid cranial base

A Generalized Procrustes Analysis of the basicranial module was carried out (block GPA). The coordinates of the maxillary block were then computed applying the rigid motions (i.e. the translation vectors and rotation matrices) obtained during the Procrustes fit of the basicranial module. In the next step, the obtained three-dimensional maxillary coordinates were projected onto the midplane. Now the rigid motion of each palate can be described by only 3 degrees of freedom - two for translation (Δx and Δy) and one for rotation (θ) - instead of six degrees of freedom in three dimensions. This assumes perfect bilateral symmetry of the skull, which is only an idealization and simplification. But since the main interest is in palatal deflection, we ignore variation in the roatation in the anterior-posterior axis of the skull. Hence, rigid motions of the maxilla during this superimposition are restricted to translations in y - and z - direction and a rotation about the x - axis. To determine the palatal rigid motion of each specimen, I extracted the vectors that are represented by the palatal line segments for each specimen. Each palatal vector is then projected on the palatal mean vector of its species and the signed angle θ is extracted. Δx and Δy are obtained by computing the centroid of five midsagittal maxillary landmarks (nasospinale, prosthion, orale, incisivion, palatine suture) for each specimen (R code is given in **Appendix 6**). In general, the set-up of the analysis resembles a 2D analysis of the ostracode Veenia in which the rigid motion of one segment is extracted applying a baseline that is restricted to the other segment (Bookstein, 1991). The "baseline" or "basis" is the basicranium and the rigid motion of the maxillary bone will be estimated according to the cranial base.

In the third step of the analysis, the covariation between the shape of the first module [a) cranial base b) cranial base and upper face] and the rigid motion of the second module (hard palate) is analysed using a Partial Least Squares analysis (PLS). The application of PLS to Procrustes coordinates is often called singular warp analysis. In this analysis there is only one set of landmarks, namely for the cranial base. PLS describes the multivariate relationship between palate rigid motion (Δx for anterior-posterior displacements, Δy for inferior-superior displacements, and θ for rotation) and the shape of the cranial base and upper face in terms of a pair of latent variables (one for shape and one for translation/orientation) that together have the highest possible covariance (predictive power). There further exists a second pair of variables that is (geometrically) orthogonal to the first pair, such that the corresponding scores, the second pair of singular warp scores, exhibit the highest covariance (which covariance equals the second singular value). The third and last pair of variables is defined analogously.

Table 8 Landmarks: facial orientation and morphological integration with the cranial base (see 2.3.4.1)

Basicranial block	18
Sphenozygomatic suture hits inferior orbital fissure (l + r)	
Sphenobasion	
Foramen ovale posterior (l + r)	
Foramen ovale anterior (l + r)	
Basion *	
Dorsum sellae midsagittal *	
Jugum sphenoidale midsagittal	
Posterior limit of the cribriform plate	
Anterior limit of the cribriform plate	
Most lateral point of ala minor (l + r) *	
Sphenofrontal suture hits cribriform plate (l + r) *	
Processus clinoideus anterior (l + r) *	
Maxillary block	29
Nasomaxillary suture hits piriform aperture (l + r)	
Infraorbital foramen (l + r)	
Nasospinale	
Zygomaxillare (l + r)	
M2-M3 ** (l + r)	
M1-M2 ** (l + r)	
M1-P4 ** (l + r)	
P4-P3 ** (l + r)	
P3-C ** (l + r)	
Canine base ** (l + r)	
C-I2 ** (l + r)	
I1-I2 ** (l + r)	
Prosthion	
Orale	
Incisivion	
Maxillary bone - Os palatinum	
Foramen palatinum majus (l+r)	

Singular warps of the shape block are linear combinations of the original shape coordinates and can be visualized either as scores (i.e., projections of the original variables onto these axes) or as deformations (Bookstein et al., 2003). We use the thin-plate spline algebra (Bookstein et al., 2003a) to deform a triangulated scanned surface of a single specimen for each species (see **Figure 12**). The landmarks and semilandmarks of this specimen are used to warp the surface points from the original configuration in Procrustes space into the same configuration after different multiples of the singular vectors are added (see Gunz and Harvati, 2007). Visualization of the singular warps was rendered in Amira 5.3 (Mercury Computer Systems S.A.).

In this way it is possible to predict the position of the palate in relation to the shape of the cranial base complex and upper face. Each dimension of the PLS describes how the rigid motion of the palate versus the normalized cranial base. This procedure estimates the

uncertainty of the modules´ position, namely the degrees of freedom of the rigid motion that are most associated with the shape of the cranial base (see **Appendix 5**). To assess the predictability of the single parameters of rigid motions vis a vis basicranial shape we use a net partial prediction, a form of PLS regression.

3.2.4.2.1.2. Facial orientation and morphological integration with the mandible

The sample consists of 31 *Pongo pygmaeus pygmaeus* and 26 *Hylobates muelleri* specimens, each one consisting of a complete cranium with mandible. All skulls belong to the Selenka Collection at the Zoologische Staatssammlung München, Germany (**Table 9**). For each specimen, 3D coordinates of 49 anatomical and 494 semi-landmarks were recorded using AMIRA (Mercury Computer Systems S.A.) and Edgewarp (Bookstein & Green, 2002; **Table 10, Figure 22**).

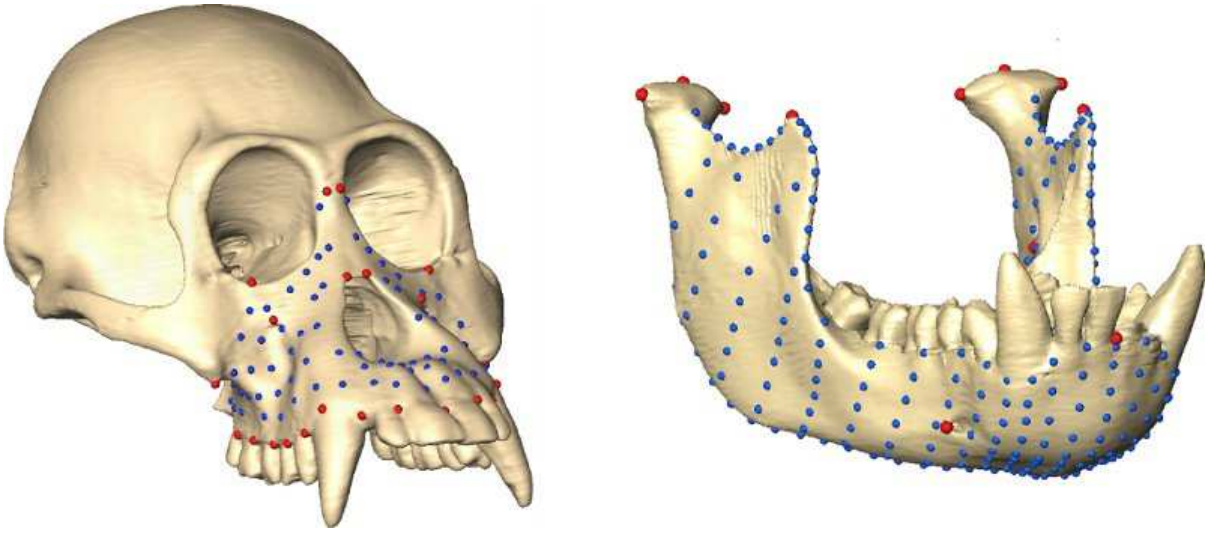

Figure 22 Template: Facial orientation and mandibular shape

Each species landmark set was separately superimposed by generalized Procrustes analysis. Procrustes shape coordinates were then used to conduct principal component analysis in Procrustes shape-space. Morphological integration of the maxilary bone and the mandible within each species was studied using singular warps (SW), a special case of symmetrical 2-block partial least squares.

Table 9 Specimens: facial orientation and morphological integration with the mandible (see 2.3.4.2)

catalogue number	collection	sex	catalogue number	collection	sex
Pongo pygmaeus pygmaeus			*Hylobates muelleri*		
1981/25	ZSM	male	1981/301	ZSM	male
1981/33	ZSM	female	1981/302	ZSM	unknown
1981/45	ZSM	male	1981/303	ZSM	unknown
1981/47	ZSM	male	1981/304	ZSM	male
1981/60	ZSM	female	1981/305	ZSM	male
1981/68	ZSM	male	1981/306	ZSM	male
1981/69	ZSM	male	1981/311	ZSM	male
1981/86	ZSM	female	1981/312	ZSM	male
1981/90	ZSM	female	1981/321	ZSM	male
1981/95	ZSM	female	1981/322	ZSM	male
1981/99	ZSM	male	1981/326	ZSM	unknown
1981/121	ZSM	female	1981/355	ZSM	female
1981/135	ZSM	female	1981/358	ZSM	female
1981/136	ZSM	female	1981/360	ZSM	female
1981/139	ZSM	female	1981/364	ZSM	female
1981/141	ZSM	male	1981/368	ZSM	female
1981/143	ZSM	male	1981/270	ZSM	male
1981/145	ZSM	male	1981/328	ZSM	female
1981/146	ZSM	male	1981/329	ZSM	male
1981/149	ZSM	male	1981/333	ZSM	male
1981/151	ZSM	male	1981/334	ZSM	female
1981/152	ZSM	male	1981/335	ZSM	male
1981/156	ZSM	male	1981/336	ZSM	female
1981/164	ZSM	male	1981/344	ZSM	male
1981/165	ZSM	female	1981/351	ZSM	male
1981/183	ZSM	male	1981/367	ZSM	female
1981/190	ZSM	male			
1981/192	ZSM	female			
1981/202	ZSM	male			
1981/203	ZSM	male			
1981/234	ZSM	male			

We corrected for sex and size by substracting the sex specific mean from females and males respectively. We used the thin-plate spline algebra to deform a triangulated scanned surface of a typical specimen for each species in order to visualize the shape changes using the program AMIRA.

Table 10 Landmarks: facial orientation and morphological integration with the mandible (see 2.3.4.2)

Mandibular block: Anatomical landmarks	8
Infradentale	
Linguale	
Mental foramen (l + r)	
Mandibular foramen (l + r)	

Tip of the coronoid (l + r)	
Top of the right condyle (l + r)	
Medial extremity of the right condyle (l + r)	
Lateral extremity of the right condyle (l + r)	
Mandibular block: Curve semilandmarks	
Midsymphysis	
Outer alveolar	
Inner alveolar	
Anterior ramus	
Coronoid	
Inferior border	
Facial block	41
Frontotemporale (l + r)	
Glabella	
Frontomalare-temporale (l + r)	
Frontomalare-orbitale (l + r)	
Torus inferior (l + r)	
Frontale/Nasale/Maxillare (l + r)	
Nasale	
Jugale (l + r)	
Zygoorbitale (l + r)	
S. nasomaxillaris/ Apertura piriformes (l + r)	
Rhinion	
Zygomaxillare (l + r)	
Foramen infraorbitale (l + r)	
Nasospinale	
Kontakt M2-3 (l + r)	
Kontakt M1-2 (l + r)	
Kontakt M1-P4 (l + r)	
Kontakt P4-P3 (l + r)	
Kontakt P3-C (l + r)	
Canine base (l + r)	
Kontakt C-I2 (l + r)	
I1_I2 (l + r)	
Prosthion	

CHAPTER 4: RESULTS

4. RESULTS

4.1. Virtual reconstructions of fossils: exemplifying the standard approaches

This section gives the detailed reconstruction protocols that were used during the reconstruction of the A.L. 444-2 fragments and the Cioclovina endocast.

4.1.1. A.L. 444-2

The following sub-sections present the result of the reconstruction of the major A.L. 444-2 fragments, as introdced in 2.1.1.1.

4.1.1.1. Mirror-imaging: the frontal bone

The left side of the frontoparietal fragment is mostly intact and minimally deformed. Plastic deformation has affected the right side of the specimen through moderate superomedial rotation of the supraorbital region and adjacent temporal surface (**Figure 23a**).

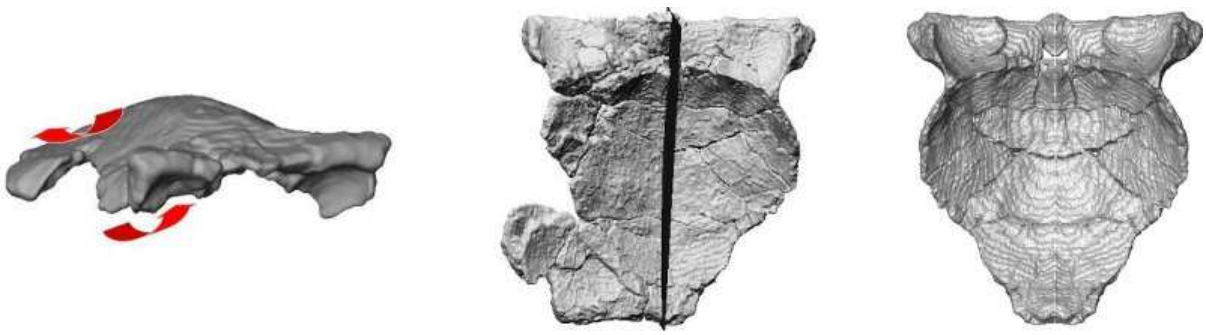

a) b) c)

Figure 23 A.L. 444-2 frontal bone

In order to restore bilateral symmetry, the right side of the frontal fragment is cut along an empirical midsagittal plane (**Figure 23b**), represented by the *crista frontalis* (see **Figure 2**) and bregma. The minimally deformed left side of the frontal bone is mirrored along this midsagittal plane. The anterosuperior fragment of right parietal that was attached to the frontal bone is omitted. The result is a perfectly symmetry frontal bone (**Figure 23c**).

4.1.1.2. Reflected relabelling: the posterior calvaria

The posterior calvaria originally consisted of three major pieces: the occipital squama with an attached fragment of the posterior right parietal bone and the two temporal bones. The right temporal was separated at the occipitomastoid suture, whereas the left temporal had broken just medial to the suture; both temporals articulate with the occipital. Because there is an offset in the midsagittal plane in the reconstructed posterior calvaria by Kimbel et al. (2004) one cannot simply estimate a best-fit plane for mirror imaging. This plane would be distorted in anterior-superior and transversal dimensions. The offset is visualized in **Figure 24**, by separating the both fragment, mirroring the left half and superimposing both fragments using a GPA with the landmarks defined below.

The goal is to establish a midsagittal plane to mirror the better preserved right occipital half. Therefore, bilateral symmetry was re-established by applying reflected relabelling. To these ends, eight bilateral anatomical landmarks of the original occipital were digitized: tip of masteoid process, auriculare, superior border of the porus acusticus internus, and the medial border of Fossa mandibularis. These landmarks are reflected (this can be automatically done in Rapidform XOR) and manually relabeled by swapping the labels.

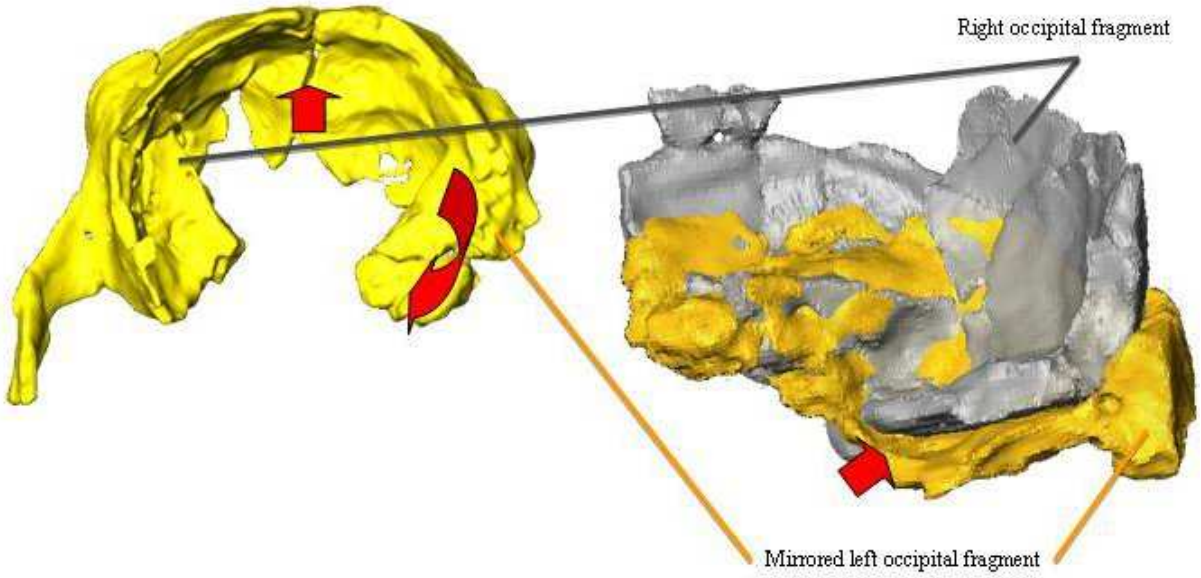

Figure 24 A.L. 444-2 original posterior calvaria and a superimposition of the half with the mirror of the left half.

In the next step a GPA on the original and mirrored configuration is carried out; the resulting consensus and the Centroid Size (149.511) are stored. Using the *landmarks surface warp* (rigid) function in Amira 5.2, I aligned the surface of the right occipital fragment (that is

better preserved) with the mean shape. Like this I was able to use the best-fit midsagittal plane of the perfectly symmetric mean shape to mirror the right occipital without the deviations introduced by the original posterior calvaria. Finally I computed a PCA of the mean landmark configuration and took the eigenvectors (n=3) to create a midsagittal plane in Rapidform XOR. At last I applied this midsagittal plane for mirror imaging the original right occipital that was earlier aligned to the consensus surface. The maximum bizygomatic breadth of the symmetrized posterior calvaria (167.15mm) is more or less identical with the value that is given by Kimbel et al. (2004; p.65) of their reconstruction (167.00mm).

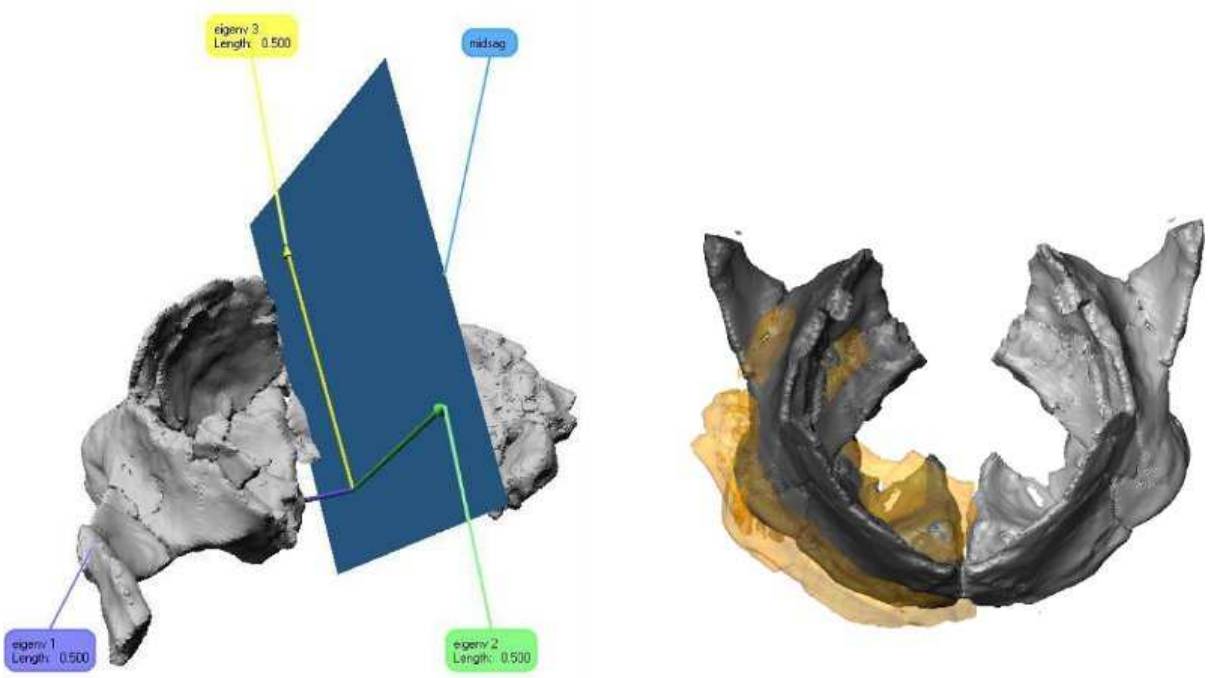

a) b)

Figure 25 A.L. 444-2 original posterior calvaria and a) the midplane obtained after reflected relabelling. b) Symmetrized posterior calvaria (grey) and original left fragment (orange).

4.1.1.3. Object manipulation in three dimensions: the mandible

The right side and anterior corpus of the mandible were recovered in three pieces, not including teeth. Since the corpus is broken along a line running from the left I2/C interdental septum diagonally to the base below the right canine (**Figure 26**).

The outer ramal part (**Figure 26a**) was rotated by the 8° clockwise around the y-axis by center on the lower border of the fragment. Then it is rotated 1° anticlockwise around x,

while centering it on most anterior point of the lower border of the outer ramal part. To align the M2 that is set too low in the mandible I created a plane on M1 on the edge between root and crown (cervical line). The same plane was created for M2 and M3. Now, the M3 plane is aligned with M2 plane, in order to approximately align the M3 with the M2 in inferior-superior direction.

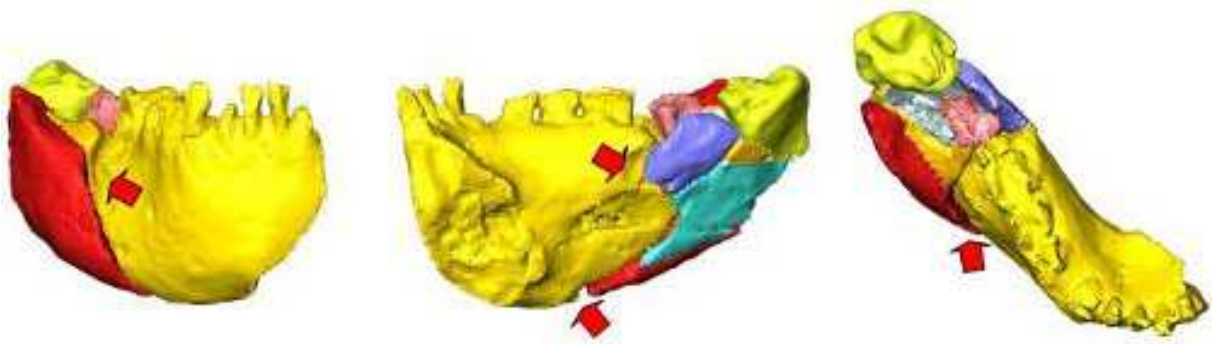

a) b) c)

Figure 26 A.L. 444-2 mandible a) lateral view, b) labial view, and c) occlusal view.

To estimate the general outline of the post-canine tooth row a reference is used. Since it is known that the postcanine teeth in *A. afarensis* are aligned in a straight line (Kimbel and Delezene, 2009) this information can be used as a rough guidance. Therefore, I created an outline A.L. 400-1 (**Figure 27a**), defined by the tooth edges in occlusal view. The A.L. 444-2 second and third molar are then placed within the area defined by the outline by moving the M2 and M3 anteriorly (**Figure 27b**).

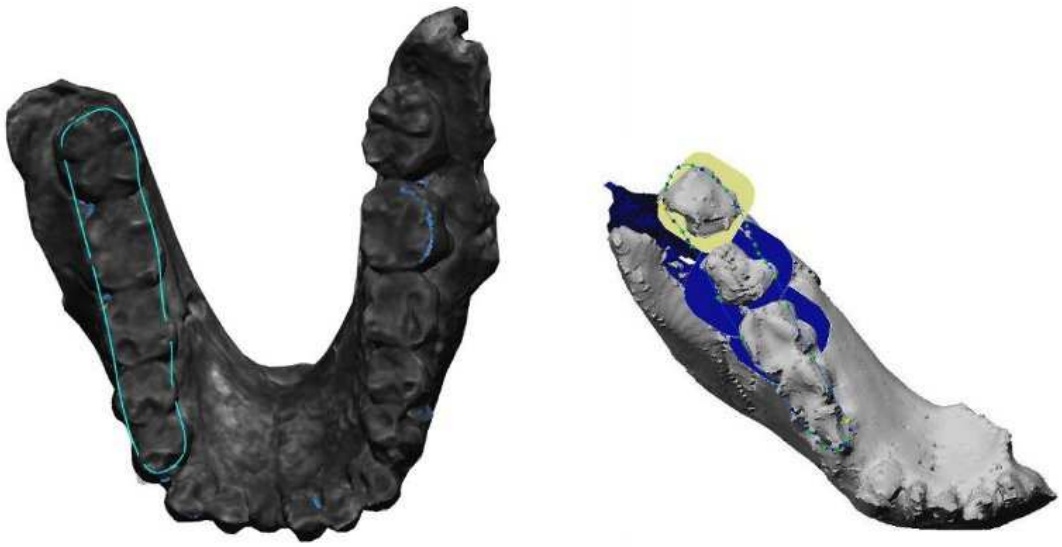

a) b)

Figure 27 a) A.L. 400-1 and b) A.L. 444-2 mandible fragment in occlusal view. The out line of A.L. 400-1 was applied as a reference to roughly guide the orientation of the displaced A.L. 444-2 second and third molar.

The labial flake at M2 (**Figure 26**, blue) is rotated 10° clockwise around the z-axis and moved 0.4mm anterior. The labial ramus part is moved 0.3mm anteriorly. The M3 together with its socket is displaced anterior to close the gap with the labial flake and moved inferior in order to get contact with labial ramus part. Afterwards, it is moved laterally for aligning it with the shared crack with labial ramus part. Doing so, the continuity of the linea mylohyoidea is restored.

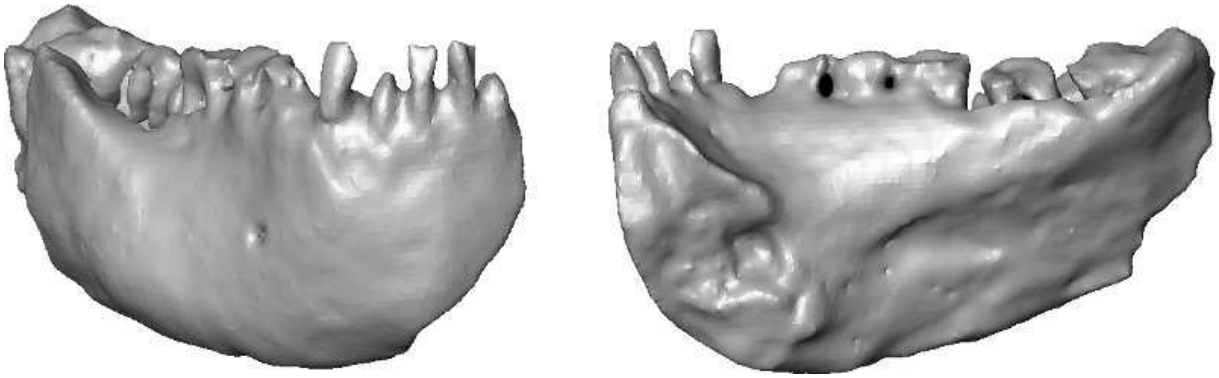

Figure 28 A.L. 444-2 mandible reconstruction

4.1.1.4. Beyond mirror imaging: the maxilla

The maxilla was recovered in three primary pieces: the entire right half, the left half anterior to the M2 position, and the alveolar bone and parts of the maxillary sinus walls. It is both plastically deformed and broken along a major crack that runs anterior-posteriorly. Although the left maxilla is somewhat more complete, it is less well preserved than the right. The palatal roof is characterized by a discrepancy in the elevation of the two sides of the palatal roof along an artificial step in the midline, the left side being higher than the right (**Figure 29**).

The main goal of this reconstruction was to restore bilateral symmetry and thus produce a retro-deformed model of the maxilla. Since the right half is in better condition it is considered as the preferred part for mirror imaging. The disadvantage that comes with this choice is that the front teeth and the bifid crest are omitted, thus some additional reconstruction steps are involved. Another problem that is arising when using the right maxillary part is that the position of the M3 is anatomically wrong. Inspecting a high resolution cast one can see interproximal wear facets on both the M2 and M3, which is giving

a hint that both teeth were in contact in vivo. To restore the anatomically correct position of the right M3 the left maxillary fragment is segmented, mirrored, and aligned with the right half using the best-fit surface alignment in Rapidform XOR (global and fine). Then the alveolar area of both parts is cut out to restrict the final surface alignment to the area of M1, M2, and M3.To obtain a reference position I cut out the left mirrored M3, that is now on the same occlusial plane like the rest of the molars. The cervical plane of the left mirrored M3 is then aligned with the cervical plane of the original right M3, that is now in a anatomically correct position.

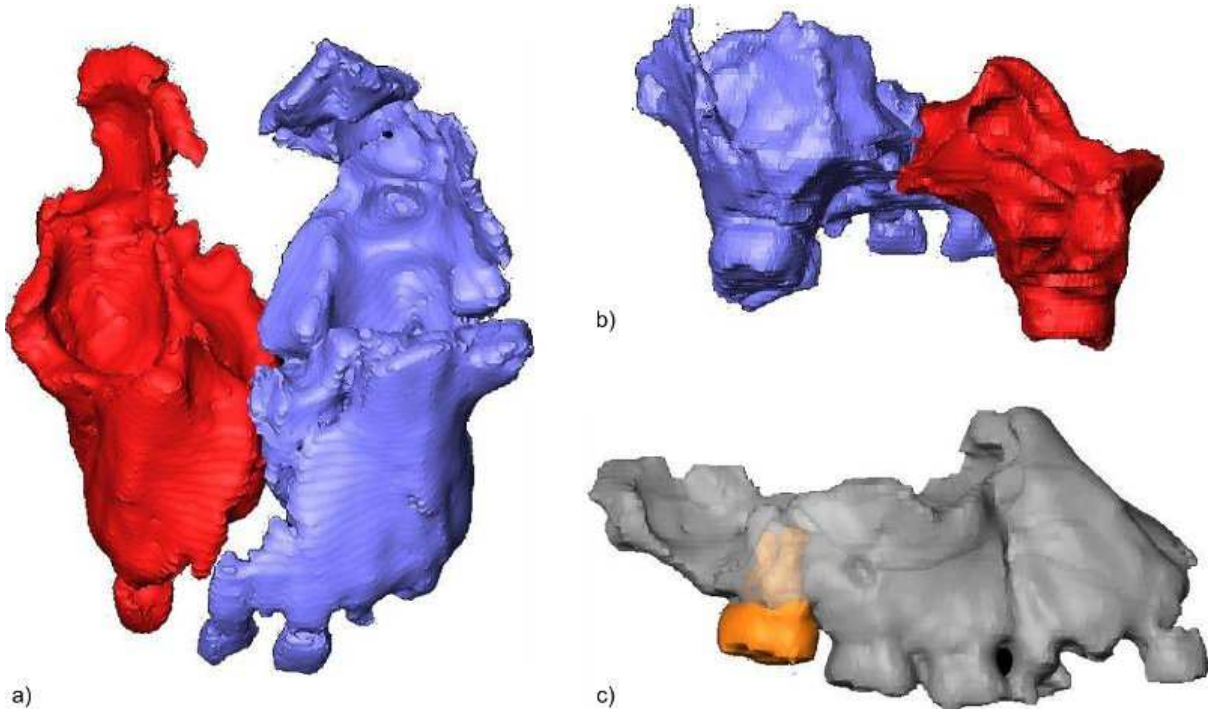

Figure 29 A.L. 444-2 maxilla, left (blue) and (red) half seperately segmented. a) fronto-dorsal view, b) posterior view (showing the offset of the two palatal halves), and c) lateral view (M3 seperately segmented, orange)

The next task is to restore bilateral symmetry. This will be done using the approach introduced above using information of midsagittal planes from reference individuals. Following landmarks are put on the reconstructed right half of A.L. 444-2 and several reference individuals: nasospinale, prosthion, C-P3, P4-M1, M1-M2, M2-M3 (on the alveolar bone, **Figure 30a**). Reference individuals are S141 (*Pan troglodytes*), one *Gorilla* specimens (Gorilla/CA9a, Vienna), Sts 51a (*Australopithecus africanus*), and A.L. 400-1 (*Australopithecus afarensis*). A GPA is conducted on these individuals and A.L. 200-1 is chosen as reference because it has the lowest Procrustes distance to A.L. 444-2 (**Figure 30b**).

To circumvent size effects that could influence the results, the original surfaces are transferred to the Procrustes shape coordinates obtained during the GPA. Both surfaces are now already aligned according to the landmarks present in both maxillae. In Rapidform XOR I compute the best-fit midplane of A.L. 200-1 (analogues to the procedures described for the occipital) and mirror the aligned A.L. 444-2 right half together with its landmarks according to this midplane. Afterwards the surfaces (original and mirror) and landmarks have to be scaled according to the Centrod Size (63.31) obtained during the GPA.

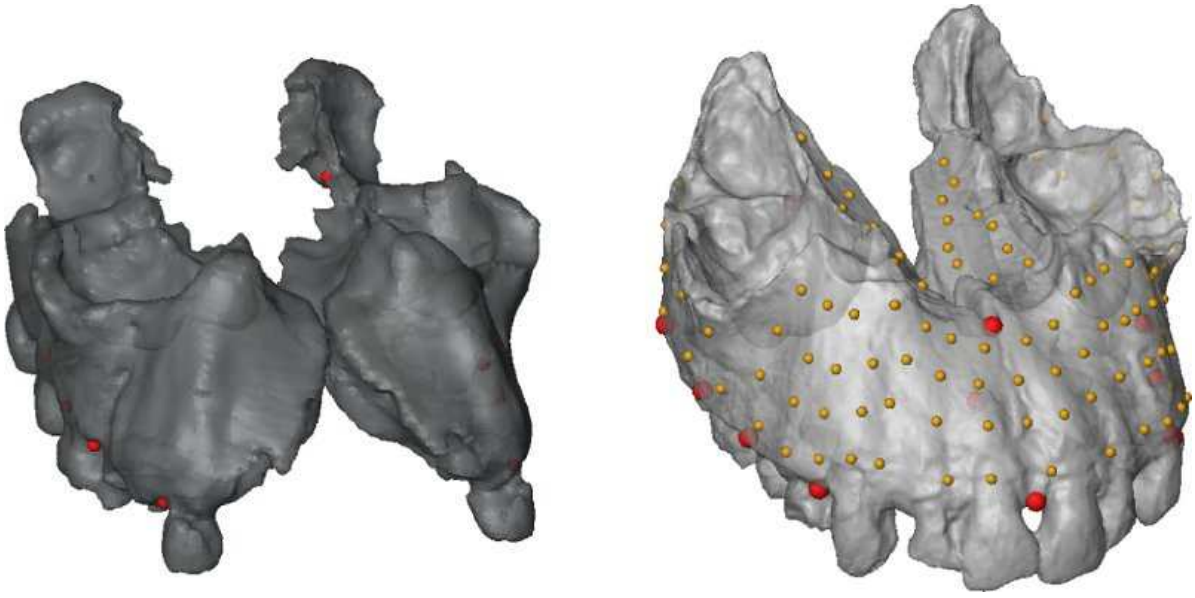

a) b)

Figure 30 a) Symmetrized A.L. 444-2 maxilla and b) A.L. 200.1 template with semilandmarks.

Now the maxilla is symmetrized, but large portions of the premaxilla and the palatal roof are missing. To estimate the missing data a geometric reconstruction using TPS is applied. The goal is to reconstruct the missing portions in the symmetrized model using the original A.L. 444-2 maxilla for the premaxilla and the palatal roof using A.L. 200-1. Therefore we have to build up a template that includes semilandmarks, in order to reconstruct parts that are not represented by anatomical landmarks like the palatal roof. Since the original A.L. 444-2 maxilla is deformed, we use the undeformed A.L. 200-1 specimens to construct a template (**Figure 30).** This template includes 13 anatomical landmarks and 107 surface semilandmarks. Bilateral landmarks are I2-C, C-P3, P4-M1, M1-M2, M2-M3, Foramen palalatinum majus, M3 distal inner alveolar margin, P4 medial inner alveolar margin, M1 medial inner alveolar margin, M2 medial inner inner alveolar margin. Midsagittal landmarks that are missing in A.L. 444-2 are: nasospinale, prosthion, and Foramen incisivum. The landmark configuration including the landmarks and semilandmarks of the original A.L. 444-

2 maxilla is warped on the symmetrized maxilla. To get the resulting surface the landmark configuration of the original maxilla from EWSH is imported to Amira 5.2. With the help of the landmark surface warp module a surface model of the original maxilla that was warped onto the symmetrized maxilla is obtained. This surface will be used to reconstruct the premaxillary part in the symmetrized maxilla. To do so, the premaxillary part and the part of nasospinale are cut out in Rapidform XOR. The orientation of the premaxillary part is almost perfect since the models are aligned in EWSH. I move the premaxilla 1mm lateral for the best junction between the two first incisors and mirror the left premaxilla (this side is better preserved) according to the midsagittal plane of A. L. 200-1. The single parts are fused in Rapidform XOR using the “fill holes” function. To incorporate the bifid crest that was omitted above I create a best fit midsagittal plane of the bifid crest in Rapidform XOR. This plane is aligned together with the midplane of AL200-1 that is the global reference plane in this configuration. The alignment of the two planes rotates it clockwise in front view. It is manually moved inferior until the right lateral surface of the crest touches the surface of the maxilla. The overlapping areas of the premaxilla and crest are cut in Rapidform XOR.

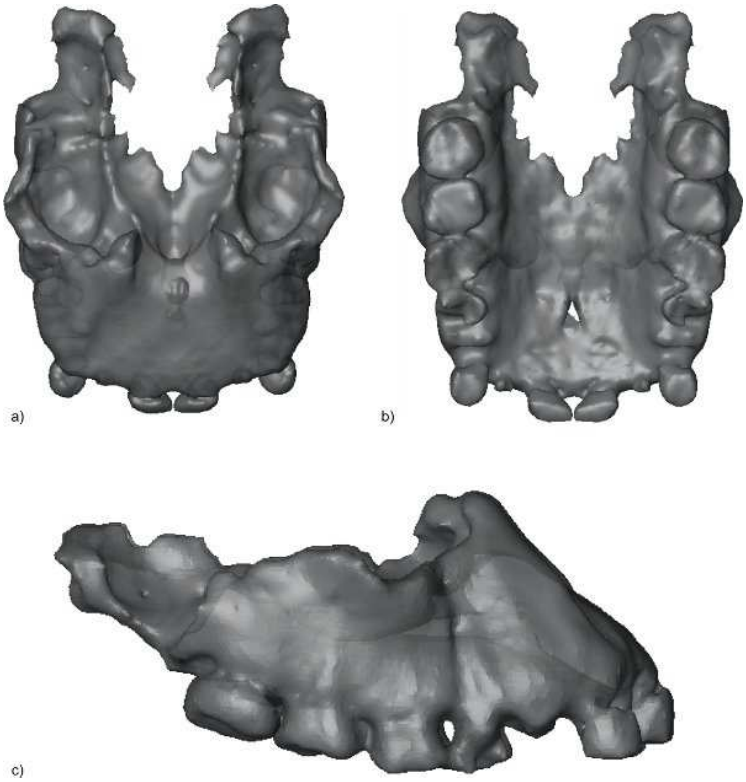

Figure 31 Reconstruction of the A.L. 444-2 maxilla. a) fronto-dorsal view, b) ventral view, c) lateral view

4.1.1.5. Geometric reconstruction: the endocranial cavity of Cioclovina

I determined the reference by carrying out a Generalized Procrustes Analysis (GPA) and a subsequent PCA in form space (Mitteroecker et al., 2004) on 34 anatomical landmarks present in 25 modern human crania and Cioclovina. I chose the specimen that was closest to the Upper Paleolithic calvarium in terms of Procrustes distance (Bookstein, 1991) which can be regarded as a measure of geometrical closeness. The specimen closest to Cioclovina was a 20 year old female of Southern African origin (VA24) with an endocranial volume of 1365.43cc (**Figure 32**).

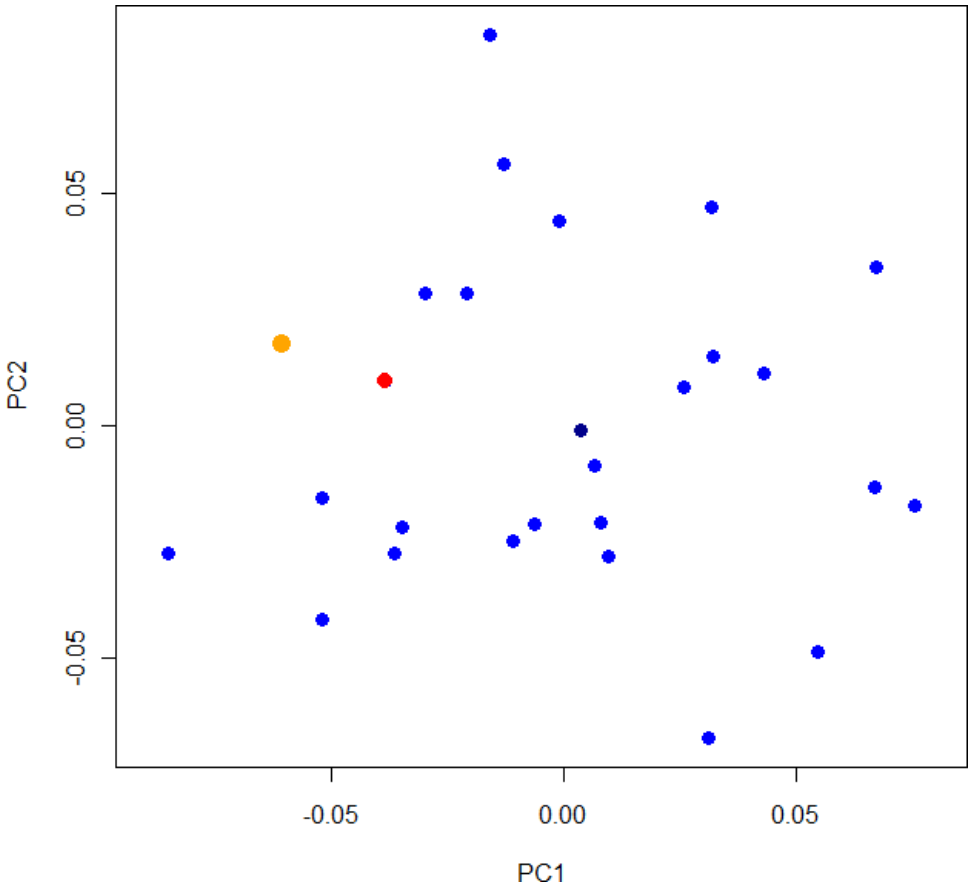

Figure 32 Form space PCA. Human reference sample (blue), Cioclovina (orange) and the reference specimen VA24 (red) that has the smallest Procrustes distance to Cioclovina

A cranial endocast is a three-dimensional replica of the endocranial cavity of the skull. Cranial endocasts allow the observation of some of the external features of the brain. Information on circulatory and nervous system of the endocranium as well as general shapes and volumes can be inferred from endocasts, and such information has been used to address the paleoneurology of fossil hominins (Connolly, 1950; Holloway, 1974, 1983; Holloway and

Kimbel, 1986; Bruner et al., 2003; Falk et al., 2005; Holloway et al., 2005; Bruner and Manzi, 2008).

Among the most commonly described features of the brain hemispheres are the petalia asymmetries (protrusions of the hemispheres producing imprints on the inner skull surface); the Yakovlenian torque (a forward "torquing" of the structures surrounding the right Sylvian fissure relative to their counterparts on the left); and the asymmetry on the occipital horns of the lateral ventricles (a deeper projection on the left occipital bone is common) (Toga and Thompson, 2003). The inferior aspect of the Cioclovina endocast allows the observation of such asymmetries. Cioclovina exhibits a protrusion of the right occipital lobe over the left which is mainly attributed to the right sinus configuration creating the impression of a occipital petalia (see **Figure 33**). When the sinus volume is accounted for, the left occipital lobe exceeds the one in depth and volume, suggesting handedness. However, a small anterior extension of the left frontal lobe over the right one is also observed.

The estimation of the total endocranial volume for the Cioclovina endocast was based on a virtual reconstruction using a modern human cranium as reference. The missing part of the basicranium was reconstructed using TPS, obtaining a total volume of the Cioclovina of approximately 1498.53 cc.

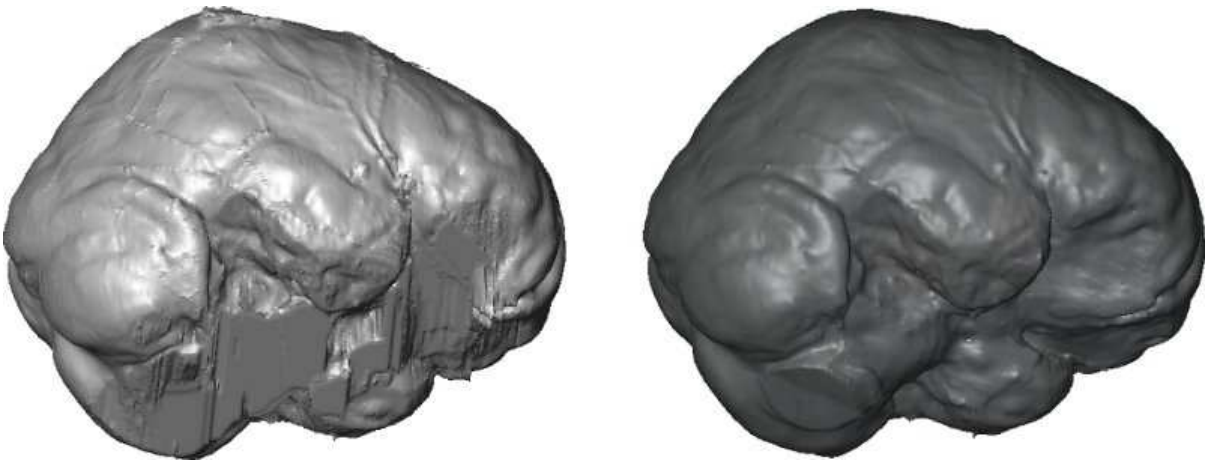

a) b)

Figure 33 a) Original endocast with missing portions. b) Reconstruction of the Cioclovina endocast using a modern human reference cranium

4.2. Beyond mirror imaging: New approaches during anatomical reconstructions

4.2.1. First and second knockout individual

Figure 34a shows a form-space PCA of the original sample (red spheres), in which the reconstructions of KI-1 (blue spheres) and KI-2 (green spheres) are projected. **Figure 34b** displays a magnified view of the above form-space PCA in the proximity of the original individual (Ind1 = black sphere). Figure 4c shows form differences in the modern human sample for the first three eigenvectors facilitating the interpretation of the resulting reconstructions in the light of human cranial variation. The first three PCs explain ~ 64% of total variation. PC1 (40.16 %) represents dolicocephalic (negative scores) versus brachycephalic (positive scores) form differences. Individuals on the left side (negative PC1 scores) of the PCA plot are characterized by a narrow and high vaulted neurocranium with a broader and higher face. In contrast, individuals on the right side of the PCA plot show a broad and stout neurocranium and a narrower and shorter face (**Figure 35**). From the lateral view (not shown), negative PC1 scores are related to a more protrusive maxillary bone, the nasal clivus is less steep and the zygomas are more prominent. Negative PC2 (14.83 %) scores generally correspond to narrow faces with a lesser interorbital breadth and a narrow nasal aperture. Nasal bones are projected anteriorly and the maxilla is rotated ventrally. Positive PC2 scores are related to a broader face with a higher interorbital breadth, a wide nasal aperture, nasal bones that are posteriorly positioned, with a maxillary bone that is more dorsally rotated. Negative PC3 (8.77 %) scores correspond to a flat frontal shape, the zygomatic bones are relatively superior and more flaring, the orbital shape is more squared, and the neurocranium is generally broader. Positive PC3 scores correspond to a rounded frontal shape, the face is less broad and the orbital shape is more rounded.

The highest variation for the produced reconstructions is along PC1, reflecting the influence of the breadth of the cranium on the outcome of the reconstruction, though the degree of variation is much higher for KI-2 (green line; **Figure 34a,b**). Mean reconstructions for both cases (light blue and light green spheres respectively; see **Figure 34b**) plot close to the original individual (Ind1). Results of each simulation are discussed in the following sections.

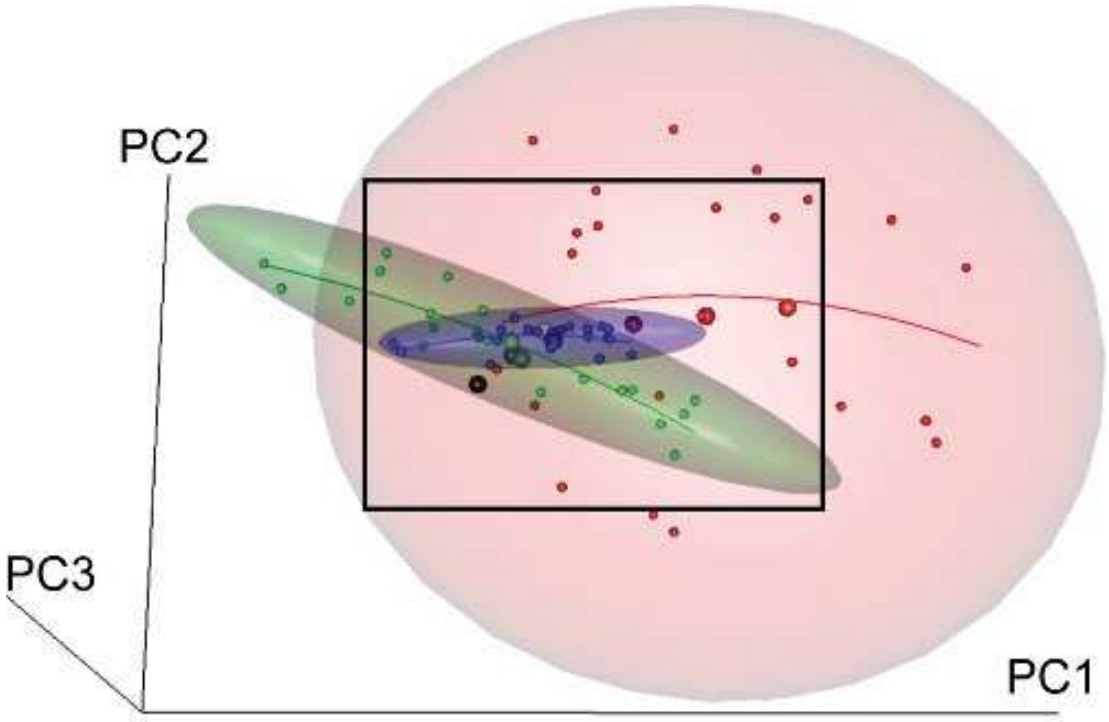

a)

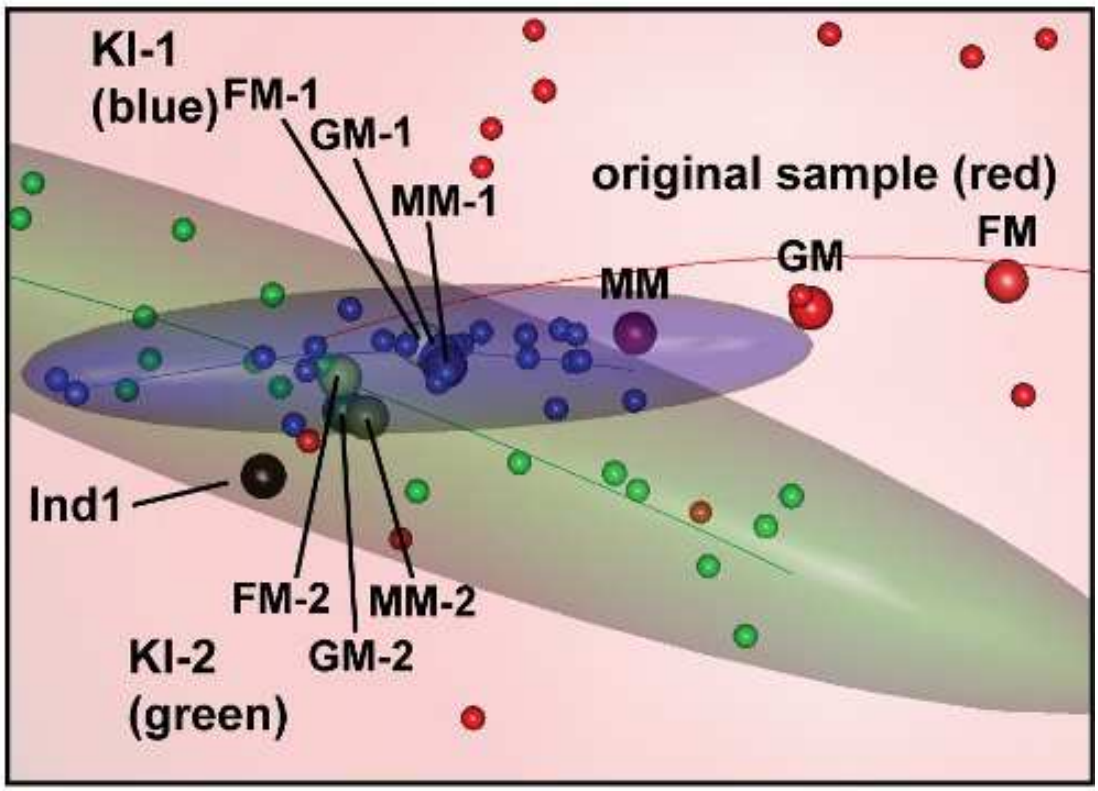

b)

Figure 34 a) Form-space PCA of the first three eigenvectors and 95% confidence intervals. Original sample (red), reconstructions of KI-1 (blue), reconstructions of KI-2 (green). The black sphere is the original individual that was reconstructed during the simulations. Quadratic regression lines for the original sample (red), KI-1 (blue), and KI-2 (green). b) Magnified view of the form-space PCA in the proximity of the original Ind1 (black sphere), Male mean (MM), female mean (FM) and the grand mean (GM).

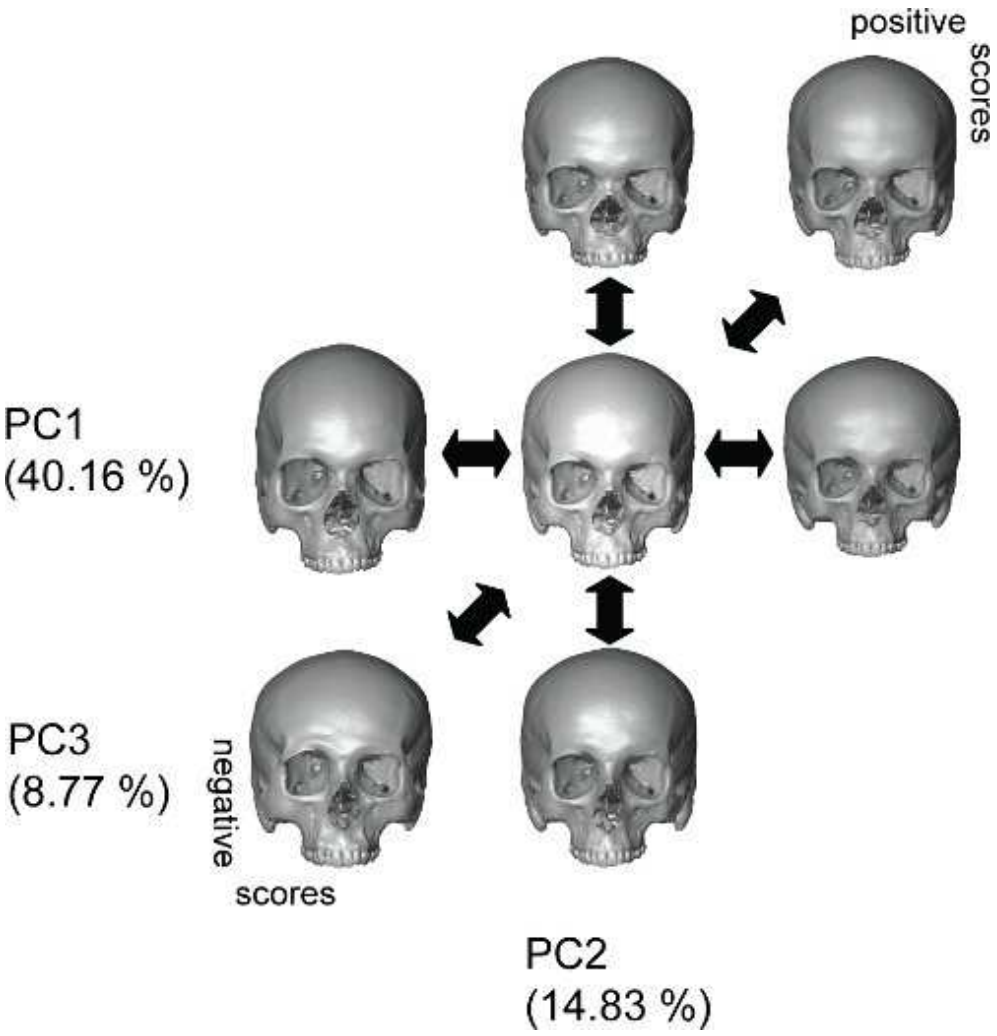

Figure 35 Form changes along the first three principal components.

4.2.2. First knockout individual (KI-1)

In the first knockout individual (KI-1) most of the left side of the cranium and significant parts of the right side were deleted, but a small portion of the left side remained which could later be used to establish the midsagittal plane (**Figure 17a**).

4.2.2.1. Accuracy

Figure 36 shows form changes along the quadratic regression line (minimum to maximum; see **Figure 34a** for quadratic regression line) for reconstructions of the first case. Reference crania that are characterized by a relatively higher cranial vault (left side of PC1; see **Figure 35**) produce reconstructions with a high vaulted neurocranium (**Figure 36**). On the other

hand, template craniums that are broader (right side PC1) produce less vaulted neurocrania. Facial differences are less influenced by the reference crania because facial breadth of KI-1 is determined during mirror imaging; the missing facial area is small compared to the missing area of the cranial vault. Besides the height of the neurocranium, form changes related to the orbital shape and the height of the nasal aperture are most obvious.

Figure 36 Form changes in the space of the first three PCs in the first knockout simulation. From negative to positive PC1 scores. Ranging from reconstructions with a higher vaulted (left) to a flatter () neurocranium

While dolichocephalic individuals produce reconstructions that are characterized by superior-inferior elongated orbits and nasal apertures (negative PC2 scores; **Figure 35**), brachycephalic templates produce orbits and nasal apertures that are less high in the superior-inferior dimension (positive PC2 scores). The mean shapes (female, male, and grand mean) produced reconstructions that (together with Ind2 and Ind14) are closest in form to the original Ind1 in terms of accuracy as well as Procrustes distance (**Table 10**). The male mean did not produce a better outcome in relation to accuracy or Procrustes distance than the female or grand mean.

The accuracy from the original individual to each reconstruction after missing data estimation ranges from 2.39mm to 2.81mm for the mirroring and 2.13mm to 9.75mm for missing data estimated by TPS (**Table 11**). The variation in the values for MD-MIRROR is due to the TPS procedure. Semilandmarks on MD-MIRROR slide during the estimation of the MD-TPS, so different templates produce slightly different landmark configurations on MD-MIRROR as well. The RMS of landmarks in the MD-MIRROR area vary between 0.05mm for landmarks positioned on the nasal clivus to 8.21mm for landmarks on the lateral alveolar process. The RMS of landmarks in the MD-TPS area vary between 0.24mm for landmarks in the supraorbital region just above the orbits to 9.73mm for rhinion. Using a color-coded deviation map (**Figure 37**), we highlight the shape differences between the original individual 1 and the reconstruction (using the grand mean as reference specimen). In this case the accuracy of MD-MIRROR was between 2.48mm and 2.65mm for MD-TPS. The highest

negative values (*i.e.*, when the reconstruction is smaller than the original) were found in the infraorbital region, the orbital wall, and cranial vault. Positive values were associated with landmarks in the maxillozygomatic area, supraorbital margin, on the lower portion of the parietal bone, and in the temporal region.

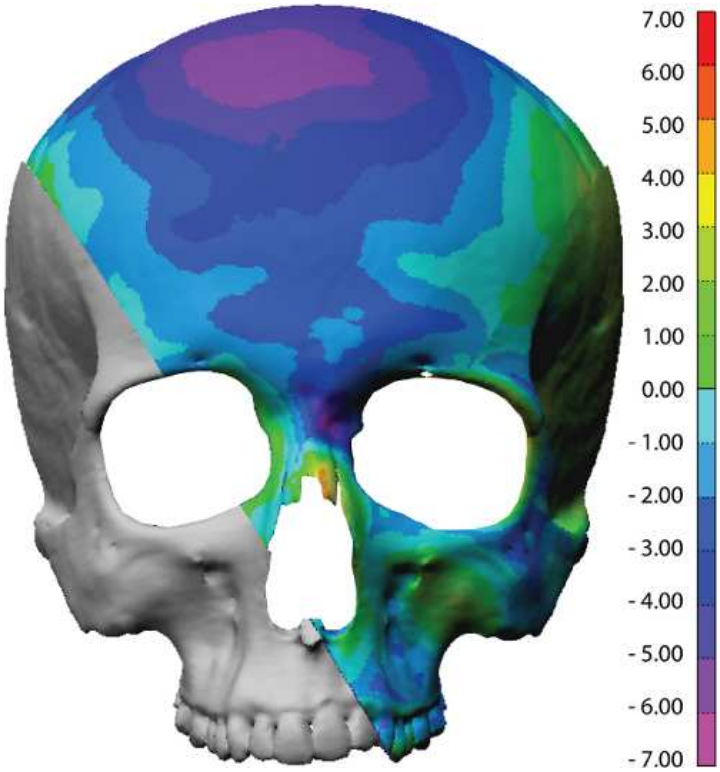

Figure 37 KI-1 reconstructed grand mean shape. Surface deviation between Ind1 and the reconstruction of the missing data in MD-MIRROR and MD-TPS obtained using the grand mean as reference specimen. Signed color-coded deviation map ranging from -7mm to 7mm

Landmarks that are situated on the mirror image generally show a smaller RMS than landmarks that were estimated using TPS. Nevertheless, landmarks estimated by TPS which are situated in the immediate vicinity of remaining “bone” have a small RMS comparable to MD-MIRROR.

4.2.2.2. Sexual dimorphism

The mean male form tends to be rather dolichocephalic (**Figure 35**, left side of the plot, higher scores for CS) while the mean female is rather brachycephalic (**Figure 35**, left side of the plot, lower scores for CS). Males and females tend to separate on PC1, for which lnCS has the highest loading, illustrating sexual size dimorphism.

Table 11 KI-1: accuracy of the reconstruction (mm)

label	*MD-MIRROR*	*MD-TPS*	*label*	*MD-MIRROR*	*MD-TPS*	*label*	*MD-MIRROR*	*MD-TPS*
ind2	2.49	2.13	ind12	2.52	5.48	ind22	2.5	3.72
ind3	2.57	6.65	ind13	2.49	4.62	ind23	2.41	2.72
ind4	2.43	2.9	ind14	2.58	2.31	ind24	2.52	3.58
ind5	2.42	3.78	ind15	2.53	5.77	ind25	2.51	7.05
ind6	2.44	6.21	ind16	2.59	4.2	ind26	2.39	9.75
ind7	2.51	5.01	ind17	2.59	7.26	grand mean	2.48	2.65
ind8	2.59	3.89	ind18	2.81	7.21	female mean	2.47	2.3
ind9	2.64	7.23	ind19	2.53	2.76	male mean	2.49	3.07
ind10	2.56	2.56	ind20	2.45	2.94			
ind11	2.49	5.39	ind21	2.53	5.65			

While male and female mean shapes do not differ significantly (p-value=0.82, number of permutations = 10,000), their mean forms (form is shape *and* size) do differ significantly (p-value < 0.001). That underscores a long known fact, namely that size is an important factor for sexual dimorphism. Sexual size dimorphism was confirmed by a permutation test on male and female CS (p-value < 0.001, number of permutations = 10,000). Nevertheless, the results suggest that sex of the reference cranium has not much influence on the accuracy of the reconstruction (**Figure 38**).

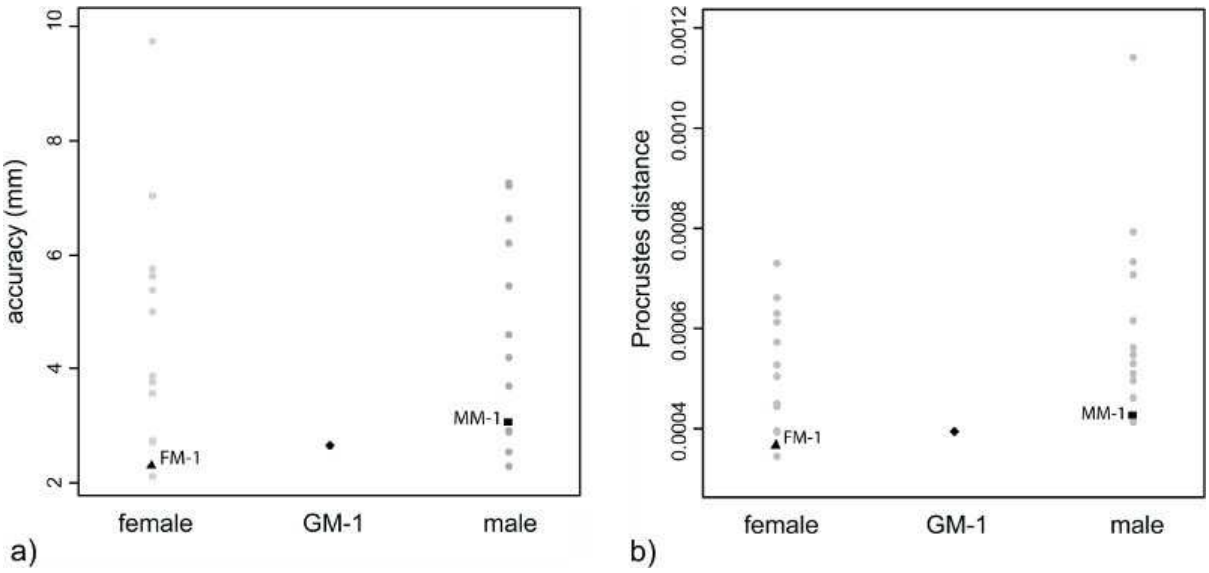

Figure 38 KI-1. a) Sex versus accuracy in the MD-TPS area (131 missing landmarks). b) Procrustes distance between the facial landmark configuration (n=385; see Statistical analyses) of each reconstruction and the original Ind1. Male mean (MM-1), female mean (FM-1) and the grand mean (GM-1)

In fact, the female mean provides a reconstruction that is even a bit closer to the original knockout individual (a male) as the one reconstructed by the male mean, both in terms of accuracy and Procrustes distance. **Figure 38** illustrates the distribution of reconstructions obtained by templates of different sex in terms of accuracy and Procrustes distance. Permutation tests (number of permutations = 10,000) show that there is no significant difference in the mean of the female and male reconstructions in terms of accuracy or Procrustes distance (p-value > 0.92). Furthermore, the variance within the female and male group is not significantly different (p-value > 0.68, number of permutations = 10,000).

4.2.2.3. Asymmetry

Table 12 contains the values of object asymmetry for each individual in the sample. Smallest values can be found for the Procrustes mean shape (grand mean) and for the sex specific mean shapes.

In KI-1, asymmetry did not influence the final outcome. There is no correlation between the values of facial asymmetry of the individual used as reference for the reconstruction (**Table 12**) and the accuracy or Procrustes distance from the respective reconstruction to the original Ind1 (see **Figure 39a,b**) r = -0.03, b) r = 0.06), all are highly significant at a $P<0.01$. This means that less asymmetric templates did not yield better results than more asymmetric individuals and vice versa. In general, the symmetrized male, female, and grand mean shape produce reconstructions with the highest accuracy.

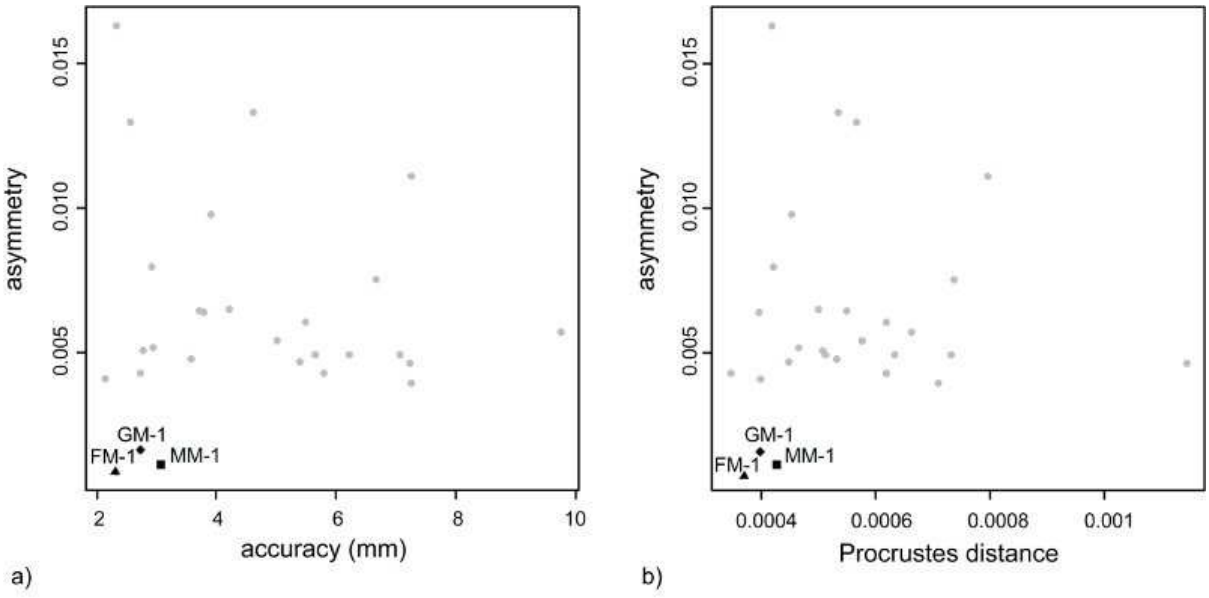

Figure 39 KI-1. a) Asymmetry versus accuracy in the MD-TPS area. b) Procrustes distance between the complete landmark configuration of each reconstruction and the original Ind1. Male mean (MM-1), female mean (FM-1) and the grand mean (GM-1)

Table 12 Total asymmetry for each individual in the sample (*10-3)

Ind1 [a]	7.245	Ind11	4.683	ind21	4.933
ind2	4.122	Ind12	6.063	ind22	6.464
ind3	7.539	Ind13	13.344	ind23	4.286
ind4	7.996	Ind14	16.313	ind24	4.77
ind5	6.404	Ind15	4.283	ind25	4.922
ind6	4.937	Ind16	6.515	ind26	5.742
ind7	5.432	Ind17	3.95	grand mean	1.502
ind8	9.806	Ind18	4.627	female mean	0.848
ind9	11.099	Ind19	5.101	male mean	1.095
Ind10	12.995	ind20	5.186		

[a] Knockout individual

4.2.3. Second knockout individual (KI-2)

The second knockout individual (KI-2) completely lacks any landmarks from the midsagittal plane and features only 24 landmarks (**Figure 17b**).

4.2.3.1. Accuracy

In contrast to the first case, KI-2 reconstructions vary in direction of the first three PCs, reflecting that the variability in the second case is higher. Using the midsagittal plane of different individuals during the first step of the reconstruction (mirror imaging) produced 28 different models that vary in facial and neurocranial size. The resulting variation in cranial form exceeds the variation in the human reference sample as some reconstructions are not within the 95% confidence interval of the human sample (**Figure 34a**). **Figure 40** shows the form changes along the static allometric trajectory (green) of the second knockout simulation illustrated in **Figure 34a**.

Figure 40 KI-2. Form changes associated with the first PC of the second knockout simulation, from negative to positive scores. Ranging from reconstructions with a narrow (left) to a broad (right) neurocranium

Even though we used the shape space configurations of the templates to circumvent problems that would have been imposed by the templates' size, obvious differences in the breadth of the resulting reconstructions can be observed. Templates characterized by a less broad cranium (dolichocephalic) produce reconstructions that are also narrow and have a more protrusive maxilla (**Figure 40**). Individuals with a broader neurocranium (brachycephalic) and a broader face produce broader reconstructions.

Reconstruction accuracy of the missing facial area for each individual ranged from 2.28mm to 10.36 mm for MD-MIRROR and 2.65mm to 9.48mm for MD-TPS. Variation of the values for MD-MIRROR is much higher than in the first knockout simulation (**Table 13**).

Table 13 KI-2: accuracy of the reconstruction (mm)

label	*MD-MIRROR*	*MD-TPS*	*label*	*MD-MIRROR*	*MD-TPS*	*label*	*MD-MIRROR*	*MD-TPS*
ind2	2.64	2.65	ind12	6.57	6.3	ind22	2.47	3.25
ind3	3.29	6.14	ind13	7.33	6.05	ind23	9.63	6.36
ind4	7.93	5.83	ind14	6.19	4.23	ind24	6.8	3.39
ind5	10.36	6.36	ind15	4.37	5.99	ind25	7.34	4.98
ind6	8.67	7.25	ind16	5.15	5.27	ind26	9.35	9.48
ind7	5.15	5.04	ind17	4.27	5.34	grand mean	2.46	2.78
ind8	2.27	3.99	ind18	4.23	7.14	female mean	2.48	2.78
ind9	2.28	6.99	ind19	2.55	3.16	male mean	2.8	3.52
ind10	5.14	4.6	ind20	4.37	4			
ind11	5.17	4.98	ind21	6.35	5.03			

The RMS of MD-MIRROR landmarks varies from 1.25mm for landmarks positioned on the zygomatic bone including the lateral orbital rim to 11.3mm for landmarks on the alveolar ridge. The RMS of MD-TPS landmarks varies from 0.62mm mm for landmarks in the supraorbital region to 10.42mm for rhinion. The color-coded deviation map in **Figure 41** illustrates the shape differences between the original knockout individual and the reconstruction of KI-2 using the grand mean (GM) as reference. The accuracy for MD-MIRROR was 2.46mm and 2.78mm for MD-TPS (**Table 13**). Therefore missing data estimation using the grand mean as a template performs comparably in both simulations. Negative deviation values (*i.e.*, the reconstruction is smaller than the original) are found in the infraorbital region, medial orbital wall, and cranial vault, while positive deviation values occur both in the mirrored side and in a portion of the left parietal bone.

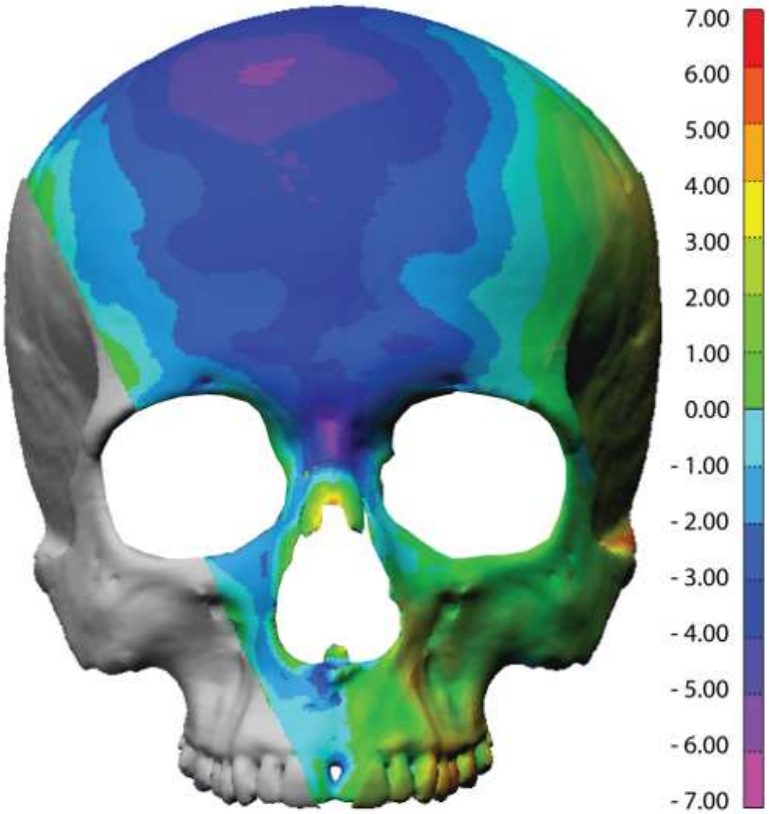

Figure 41 KI-2 reconstructed using the Procrustes mean shape (GM). Surface deviation between Ind1 and the reconstruction using the grand mean as reference specimen for MD-MIRROR and MD-TPS. Signed color-coded deviation map ranging from -7mm to 7mm. Highest distances from the original are in the superior cranial vault and the left alveolar region

4.2.3.2. Sexual dimorphism

The mean landmark configuration for reconstructions created from female and male references do not differ significantly in terms of accuracy or Procrustes distance (number of permutations = 10,000, p-value > 0.43). Likewise, female and male variances are not significantly different (number of permutations = 10,000, p-value > 0.21) in terms of accuracy or Procrustes distance. The female mean reconstruction is as close to the original knockout individual as the male mean reconstruction. In general, the grand mean performs better than any single reference specimen (**Figure 42**).

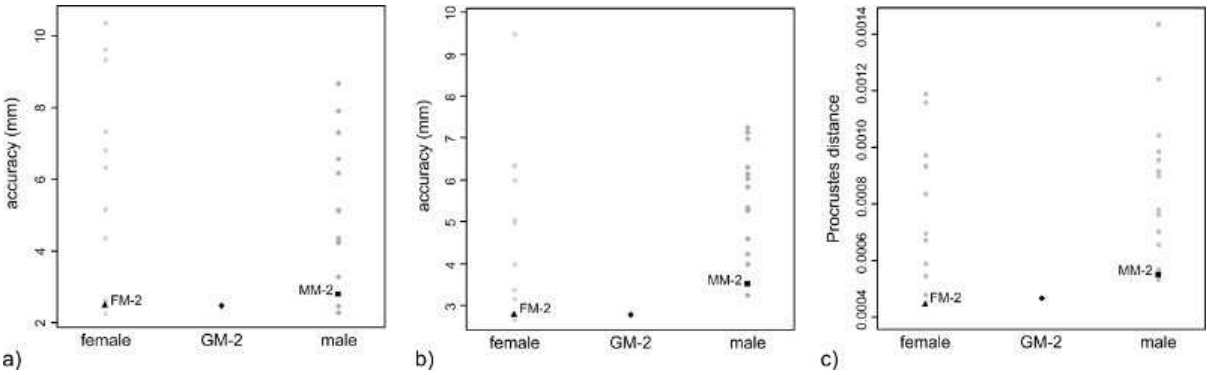

Figure 42 KI-2. a) sex versus accuracy in the MD-MIRROR area (113 landmarks) b) sex versus accuracy in the MD-TPS (159 landmarks) c) Procrustes distance between the complete facial landmark configuration (n=385; see Statistical analyses) of each reconstruction and the original Ind1. Male mean (MM-2), female mean (FM-2) and the grand mean (GM-2)

4.2.3.3. Asymmetry

We found a low correlation between the amount of facial asymmetry in the reference (**Figure 43**) and resulting accuracy of the respective reconstruction. Also the Procrustes distance of the respective reconstruction to original Ind1 and the corresponding values for asymmetry show only a low correlation (see **Figure 43**: a) r = 0.146, b) r = 0.203, c) r = 0.37), all are highly significant at a $P<0.01$. As for case 1, less asymmetric templates did not necessarily yield better results than more asymmetric individuals and vice versa. In general, the male, female, and grand mean shape produce reconstructions with the highest accuracy.

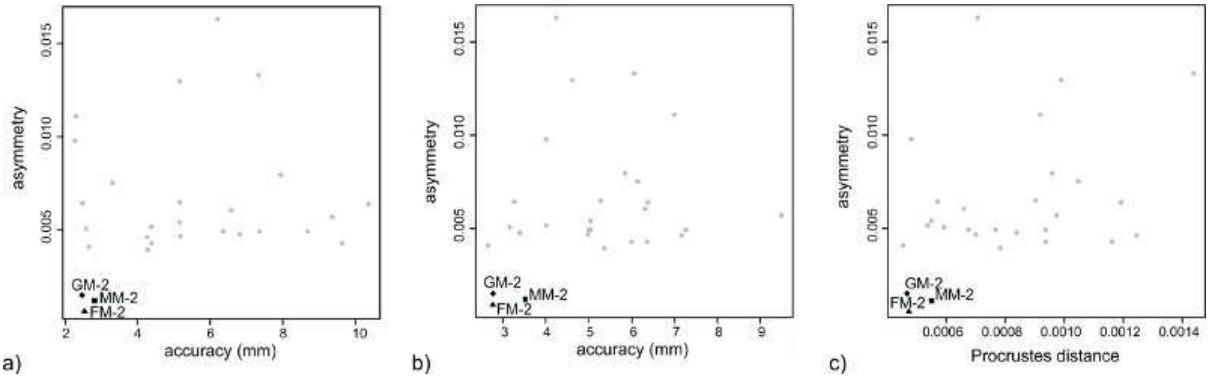

Figure 43 KI-2. asymmetry versus accuracy. a) MD-MIRROR b) MD-TPS c) Procrustes distance between the complete landmark configuration of each reconstruction and the original Ind1. Male mean (MM-2), female mean (FM-2) and the grand mean (GM-2)

4.3. Comparing 3-dimensional virtual methods for reconstruction in craniomaxillofacial surgery

The mean and standard deviation (SD) between the reconstructed surfaces and the original surface of the 15 original resected zygomatic bones are shown in **Table 14**. Small mean values and attendant reduced SD establish the criteria for the success of correct reconstructions.

Table 14 Mean, standard deviation (SD) and absolute value between the mean ± 2SD (measurements in mm)

			Mirror	
Cases	Mean	SD	Mean-2SD	Mean+2SD
H1	-0.497	0.903	-2.304	1.310
H2	-0.557	1.411	-3.379	2.265
H3	0.317	1.105	-1.894	2.527
H4	-0.249	1.204	-2.656	2.159
H5	-0.847	1.282	-3.412	1.717
H6	-0.453	1.425	-3.303	2.397
H7	-0.033	0.815	-1.663	1.597
H8	0.078	1.125	-2.171	2.328
H9	0.352	1.551	-2.749	3.454
H10	1.308	0.478	0.352	2.264
H11	-0.861	0.918	-2.697	0.976
H12	1.602	0.669	0.263	2.940
H13	-0.772	0.718	-2.209	0.664
H14	-1.458	2.085	-5.628	2.711
H15	-0.352	0.843	-2.038	1.335
			Mirror registered	
Cases	Mean	SD	Mean-2SD	Mean+2SD
H1	-0.032	0.482	-0.996	0.933
H2	0.101	0.902	-1.702	1.905
H3	0.166	0.535	-0.904	1.235
H4	-0.047	0.502	-1.051	0.957
H5	-0.186	0.970	-2.127	1.754
H6	-0.467	1.254	-2.975	2.041
H7	0.142	0.767	-1.391	1.675
H8	0.605	0.836	-1.067	2.277
H9	0.071	0.628	-1.185	1.327
H10	0.179	0.465	-0.751	1.110
H11	-0.113	0.395	-0.904	0.678
H12	-0.268	0.633	-1.534	0.998
H13	-0.089	0.361	-0.811	0.633
H14	-0.715	0.993	-2.701	1.272
H15	-0.044	0.579	-1.203	1.115
			TPS warping	
Cases	Mean	SD	Mean-2SD	Mean+2SD
H1	-0.142	0.453	-1.048	0.763

H2	-0.385	0.429	-1.244	0.474
H3	-0.679	0.514	-1.707	0.350
H4	0.387	0.402	-0.418	1.192
H5	0.342	0.766	-1.190	1.874
H6	-0.108	0.714	-1.535	1.319
H7	0.481	0.499	-0.518	1.480
H8	0.072	0.622	-1.173	1.317
H9	-0.254	0.781	-1.816	1.307
H10	-0.011	0.429	-0.870	0.847
H11	0.133	0.352	-0.571	0.837
H12	0.034	0.387	-0.739	0.807
H13	-0.041	0.307	-0.655	0.573
H14	-0.295	0.627	-1.549	0.960
H15	-0.280	0.746	-1.772	1.211

The mirror method shows the larger mean and SD values when compared to the others methods (**Table 14**), even if the difference of the means between paired groups is not statistically significant ($p>0.05$). Nevertheless, while method 1 provides large interval value when mean±2SD is computed, these distances are reduced with method 2 and further with method 3. In fact, this interval is statistically significant when method 1 is compared either to method 2 ($p<0.002$) or method 3 reconstruction respectively ($p<0.001$). When the comparison involves methods 2 and methods 3, the results is near to the statistical significant level ($p=0.059$), meaning that the reconstruction based on TPS interpolation functions provides in general more reliable results than the other methods.

4.3.1. First example: individual H15

By mirroring the unaffected side without attempting any further correction of the mirrored model position, deviation between the original and the mirrored surface range between +1mm and -1.5 mm (**Table 14**, **Figure 44a,b**). In the frontal and temporal process of the zygomatic bone, the reconstructed model is slightly backward positioned compared to the original (between -0.5/-1.0mm and -1.0/-1.5mm respectively). Similar results were obtained for the anterior rim of the orbit (between -1.0/-1.5mm).

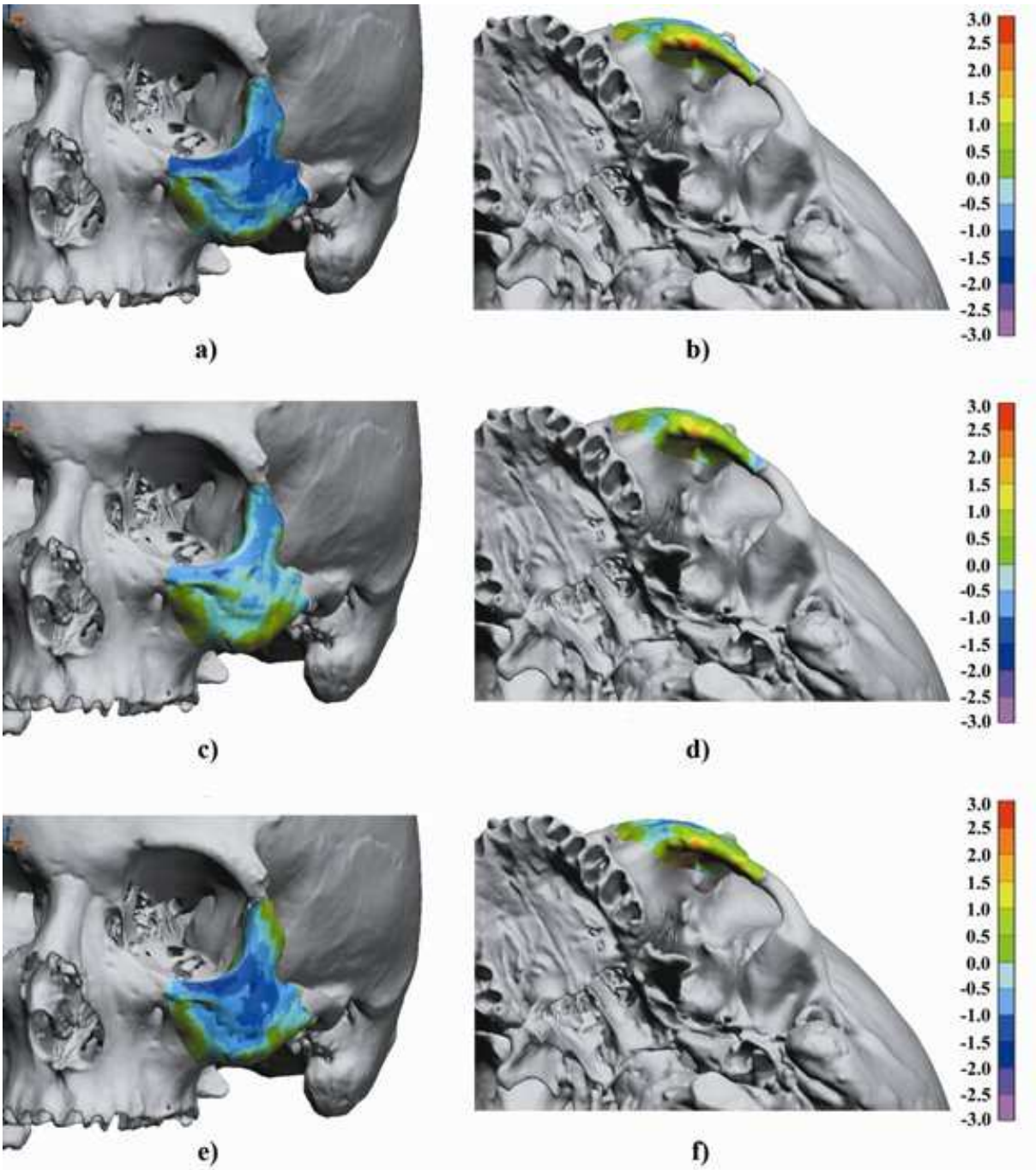

Figure 44 Individual H15. The color map underlines the distance between the reconstruction and the original model; a, b) reconstruction based on method 1; c, d) reconstruction based on method 2; e, f) reconstruction based on method 3. The color-bar scale is in millimeter.

The deviation measured in the maxillary region and in the lower aspect of the zygomatic bone (between-0.5/+1mm) could be related to the somewhat larger size of the mirrored model in those specific areas. This is supported by the results obtained from the second method, when an alignment between the two hemifaces was performed before isolating the zygomatic segment (**Figure 44c,d**). In fact, the maxillary and the lower zygomatic region of the reconstructed model are slightly larger than the original one.

Notwithstanding, the result is improved since the mean and the standard deviation are clearly reduced (**Table 14**). It is worthwhile to note the better position of the reconstructed bone with regard to critical areas like the temporal process of the zygomatic bone, the lateral orbital wall and the lower orbital rim when compared to the former reconstruction. The results did not improve significantly when the reconstruction is carried out by TPS interpolating functions (**Table 14**, **Figure 44c**). Nevertheless, it is worthwhile to note that the continuity between the reconstruction and the original bone near the resected areas are correctly reproduced.

4.3.2. Second example

Unsatisfactory results were obtained with the mirroring tool for individual H14. This is certainly due to the natural asymmetry of the cranium and the impossibility to define an unambiguous midsagittal plane. Consequently, the frontal process of the zygomatic segment deviates more than 4mm backward from the original bone, while the latero-orbital floor is more than 4mm upward. A backward position of the virtual reconstruction is also displayed in the lower orbital rim as well as in the temporal process. In the last case, the temporal process is positioned so backward that the deviation computed by the software is related to the posterior surface of the original temporal process. For this reason it is colored in green (**Figure 45a,b**).

The mean distances between the reconstruction and the original decrease when method 2 is used (**Figure 45c,d**). The surface deviation between the two compared models is reduced both in the lateral orbital wall (less than -2mm) and in the temporal process (about -1mm) of the zygomatic bone. Similarly, the deviation is decreased in the latero-orbital floor (less than +2.5mm). Nevertheless, differences with the original bone still persist, as for example in the inferior margin of the zygomatic (**Figure 45c,d**).

The best outcome was clearly provided by means of method 3 (**Figure 45e,f**). The deviation is generally reduced between -0.5/+0.5mm (about +1mm in the latero-orbital floor) and a smooth continuity was reached in the contact area between the reconstruction and the original cranium. The latter is one of the major contributions provided by the TPS based reconstruction: in fact, for all the 15 individuals (and hence not limited to individual H14 and H15), the contact areas between the reconstructed and the original bone is always better than those provided by the mirror or mirror-registered tool.

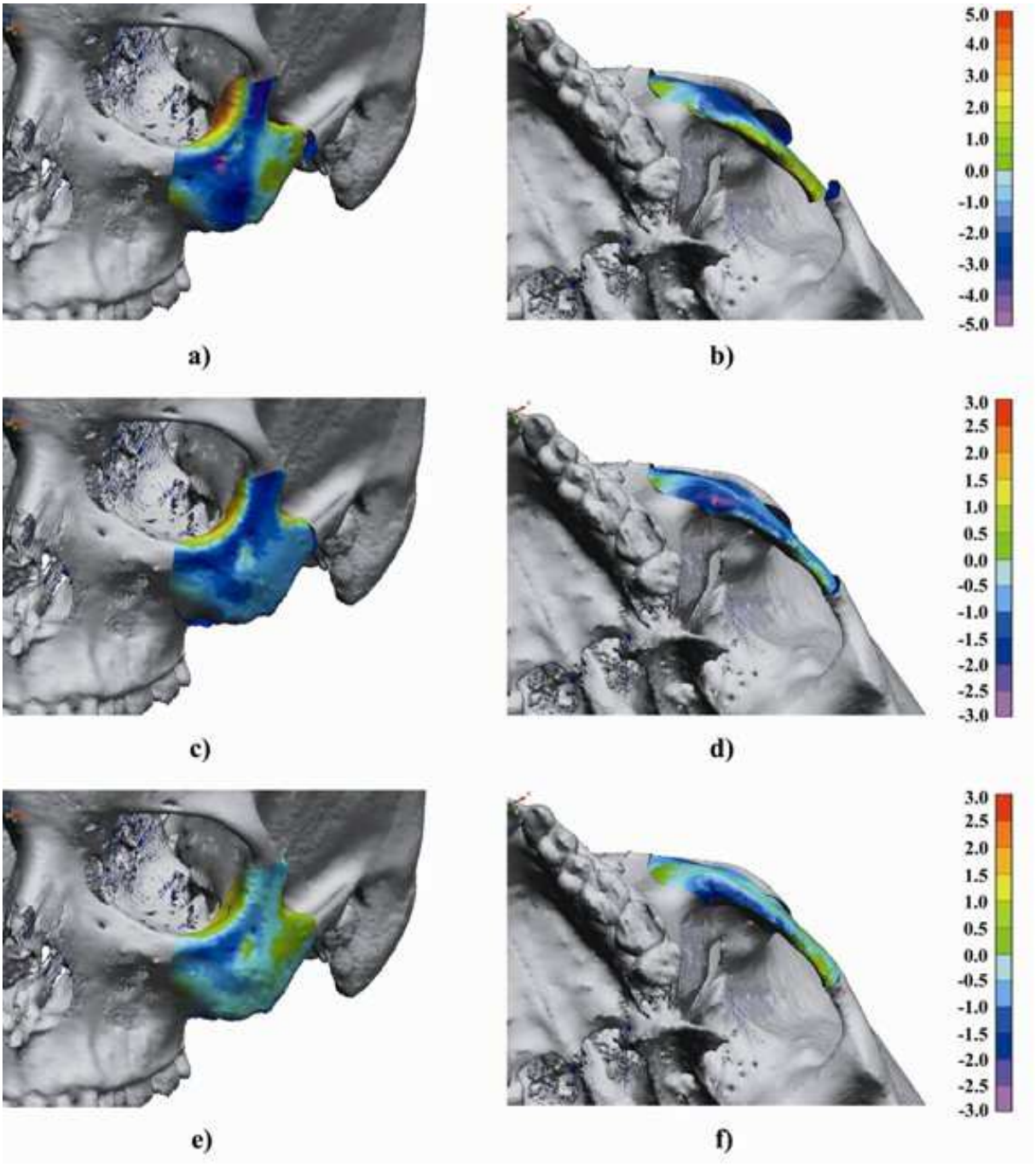

Figure 45 Individual H14. The color map underlines the distance between the reconstruction and the original model; a, b) reconstruction based on method 1; c, d) reconstruction based on method 2; e, f) reconstruction based on method 3. The color-bar scale is in millimeter.

4.4. Virtual reconstruction of modern and fossil hominoid crania: effects of the choice of the reference form

4.4.1. Reconstructions using the Procrustes mean shape

The results showed that for reconstructions within species (e.g., *Homo* mean shape for *Homo*), average RMS for individuals ranged between 1.11mm (0.18) and 1.32mm (0.43) for the face. On the smoothly curved braincase (*the* domain of TPS) results were between 0.71mm (0.22) and 1.17mm (0.39) (**Table 15**).

Table 15 Reconstruction of one individual by Procrustes mean shapes: RMS for landmarks: mean and SD (in mm)*

			face			
	Homo (n=25)	*Pan* (n=19)	*Pongo* (n=20) reconstructed by	Mladec1	Petralona	Sts5
Homo (mean shape)	1.21 (0.28)	3.4 (0.75)	2.93 (0.58)	1.82	2.33	2.89
Pan (mean shape)	3.54 (0.45)	1.32 (0.43)	1.82 (0.41)	3.76	4.23	1.47
Pongo (mean shape)	3.54 (0.50)	1.71 (0.42)	1.11 (0.18)	3.3	3.54	1.33
			neurocranium			
Homo (mean shape)	1.17 (0.39)	1.53 (0.35)	2.14 (0.32)	1.34	2.54	1.5
Pan (mean shape)	1.69 (0.43)	0.71 (0.22)	1.18 (0.20)	1.63	2.32	1.04
Pongo (mean shape)	1.87 (0.48)	1.29 (0.26)	0.79 (0.14)	1.59	2.12	0.97

*average of the RMS of individuals in the respective knockout round

For facial reconstructions between species the lowest average RMS for individuals was 1.71mm (0.42) when the *Pan* sample is reconstructed by the Procrustes mean shape of *Pongo.* Not surprisingly, the highest average RMS of 3.54mm (0.45 for *Pan*, 0.50 for *Pongo*) was obtained by estimating missing landmarks in the *Homo* sample with the Procrustes mean shape of *Pan* and *Pongo* (**Table 15**). Facial reconstructions of Mladec1 and Petralona show the lowest RMS when using the Procrustes mean shape of *Homo* (1.82mm and 2.33mm) as reference. The lowest RMS in the facial reconstruction of Sts 5 can be observed using *Pan* or *Pongo* as reference (1.47mm and 1.33mm).

In the neurocranium the lowest average RMS for individuals was 1.18mm (0.20) when the *Pongo* sample is reconstructed by the Procrustes mean shape of *Pan.* The highest average RMS for individuals of 2.14mm (0.32) was obtained by estimating missing landmarks in the *Pongo* sample with the Procrustes mean shape of *Homo* (**Table 15**). In the estimation of missing data in fossil specimens the lowest RMS can be found when using the Procrustes

mean shape of *Homo* for the reconstruction of Mladec 1 and the Procrustes mean shape of *Pan* or *Pongo* for the reconstruction of Sts 5. When reconstructing Petralona, lowest values can be found when taking the Procrustes mean shape of *Pongo* as reference, though the differences in the accuracy between the three species´ Procrustes mean shape is only marginally.

4.4.2. Reconstructions using each specimen in the sample

In intrapecies reconstructions the average RMS for individuals ranged between 1.52mm (0.18) and 2.08mm (0.31; Mladec 1) in the face and between 0.79mm (0.26) and 1.32mm (0.19) for the braincase (**Table 16**).

Table 16 Reconstrcuction of one individual by complete sample: RMS for landmarks: mean and SD (in mm)*

			face			
	Homo1	Pan1	Pongo1	Mladec1	Petralona	Sts5
			reconstructed by			
Homo (n=25)	1.86 (0.40)	4.52 (0.47)	3.33 (0.5)	2.08 (0.31)	2.73 (0.47)	2.94 (0.52)
Pan (n=19)	2.85 (0.46)	1.75 (0.35)	2.05 (0.44)	3.71 (0.38)	4.36 (0.61)	1.65 (0.33)
Pongo (n=20)	2.77 (0.33)	3.08 (0.27)	1.52 (0.23)	3.42 (0.24)	3.92 (0.49)	1.52 (0.18)
			neurocranium			
Homo (n=25)	1.32 (0.19)	1.85 (0.27)	1.90 (0.45)	1.60 (0.28)	2.45 (0.42)	1.64 (0.31)
Pan (n=19)	2.58 (0.31)	0.79 (0.26)	0.99 (0.23)	1.87 (0.36)	2.28 (0.44)	1.10 (0.25)
Pongo (n=20)	2.55 (0.31)	0.83 (0.22)	0.93 (0.24)	1.83 (0.32)	2.15 (0.45)	1.05 (0.22)

*average of the RMS of individuals within the respective knockout round

For facial reconstructions between species the lowest average RMS for individuals was 1.52mm (0.18) when Sts 5 was reconstructed by the *Pongo* sample, a value comparable to the intraspecies reconstruction of Pongo1 (1.52mm (0.23)). Reconstructing the missing facial area in Sts 5 with the sample of *Pan* yields a similar average RMS (1.65mm (0.33), while the employment of the *Homo* sample as reference shows an average RMS that is almost twice as high (2.94 (0.52)).

As it is the case in the facial reconstruction using the Procrustes mean shape, the highest average RMS was received when estimating missing landmarks in Pan1 and Pongo1

using the *Homo* sample (Pan1: 4.52mm (0.47), Pongo1: 3.33mm (0.50)). Estimating missing facial landmarks in Petralona performs best when taking the *Homo* sample as reference (2.73mm (0.47)), but still showing a rather high average RMS that is comparable to the reconstruction of Homo1 by *Pan* and *Pongo*. Reconstructing Petralona´s missing facial area with the samples of *Pan* and *Pongo* respectively, high average RMS are observed (4.36mm (0.61) and 3.92mm (0.49)) that are approximately twice as high as the average intraspecies RMS. This also applies for Mladec 1 (using the *Pan* sample as reference: 3.71mm (0.38); using the *Pongo* sample as reference: 3.42mm (0.24)), illustrating the general inability of the *Pan* and *Pongo* references to estimate missing facial data in the *Homo* genus and vice versa.

In the neurocranium the lowest average RMS was obtained when Pan1 was reconstructed by the sample of *Pongo* (0.83mm (0.22)) and vice versa (0.99mm (0.23)). These values consequently lie in the lower range of intraspecies reconstructions (*Homo*: 1.32mm (0.19), *Pan*: 0.79 (0.26), *Pongo*: 0.93 (0.24)). Compared to the intraspecies reconstructions of *Pan* and *Pongo* the average RMS for *Homo* is rather high and reflects the high variability of the human neurocranial form. Remarkable to note are the average RMS in the reconstruction of Sts 5 by *Pan* and *Pongo* (1.10mm (0.25) and 1.05mm (0.22) that lie well within the above mentioned range of intraspecies reconstructions. The highest average RMS was received by estimating missing landmarks in Homo1 with the sample of *Pan* (of 2.58mm (0.31)) and *Pongo* of (2.55mm (0.31)) and in the reconstruction of Petralona. Surprisingly, employing the *Pan* and *Pongo* sample as reference in the estimation of missing neurocranial data in this specimens slightly lower average RMS (*Pan*: 2.28mm (0.44), *Pongo*: 2.15mm (0.45)) than taking *Homo* as reference (2.45mm (0.42)) are obtained.

As expected, intraspecies reconstructions produce the lowest average RMS. Nevertheless, interspecies reconstructions of Sts 5 using the *Pongo* sample show average RMS close to the ones obtained during intraspecies reconstructions for both regions and are therefore considered as acceptable.

Moreover, average RMS for the neurocranium is lower than for the face. **Figure 46** illustrates the accuracy in interspecies reconstructions in terms of (average) RMS of individuals between all possible combinations in the knockout simulation (excluding Mladec 1 because it belongs to the *Homo sapiens* sample) according to **Table 15**.

4.4.3. An example of interspecies reconstruction in 2D

To illustrate the dependencies between resulting reconstruction on the one hand and the amount of missing data and choice of reference form on the other, I switch to a simple 2D case and consider only landmarks in the midsagittal plane (effects would be similar in 3D but harder to visualize in print). **Figure 47** shows the estimation of missing data using TPS for the knockout configuration in two dimensions using Edgewarp2D (Bookstein and Green, 2002). The orientation of each skull in the images is according to the Frankfurt plane. In **Figure 47a** and **b**, Pongo1 is reconstructed by Pan1.

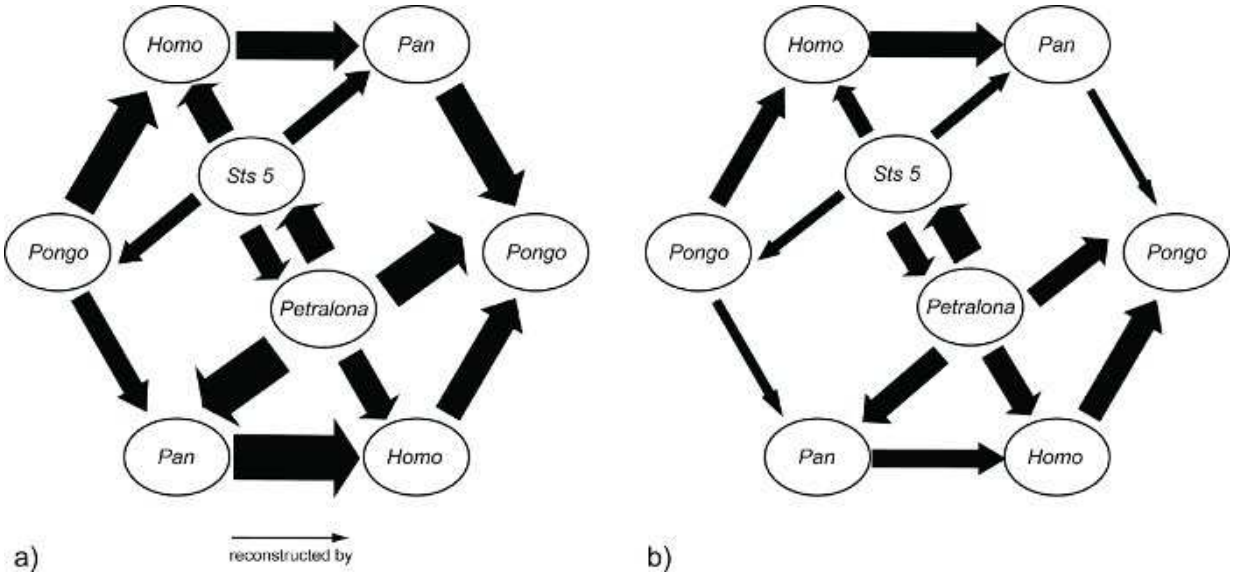

Figure 46 Accuracy in interspecies reconstructions in terms of (average) RMS of individuals. Thickness of arrows corresponds to reconstruction error. a) Facial knockout region. b) Neurocranial knockout region. Thickness of arrows corresponds to values in Table 2

In the first simulation, the estimated surface semilandmarks in the neurocranium perfectly follow the bony surface of the original individual. Estimated landmarks in the facial region show a higher deviation from the original. Note that the reconstructed supraorbital area in the reconstructed individual does not show a supraorbital torus. In the second simulation (**Figure 47b**), surface semilandmarks in the direct vicinity of the area that was declared as missing were deleted. Accordingly, the TPS interpolation in this region is only guided by the real landmarks closest to the missing area (bregma and lambda), which results in a higher deviation from the original (but still being close to the original bony surface).

In **Figure 47c** and **d**, Pongo1 is reconstructed by Homo1. Note that when surface semilandmarks are present in the direct vicinity of the missing area, the estimated surface semilandmarks also follow the original bony surface more or less perfectly. Estimated landmarks in the facial region show a high deviation from the original and illustrate that a human shaped nasal region is introduced into the reconstruction of the orangutan. When surface semilandmarks in the direct vicinity of the missing midsagittal portion are eliminated, the accuracy decreases considerably. This is because the spline in this region is bent according to the original shape of the reference.

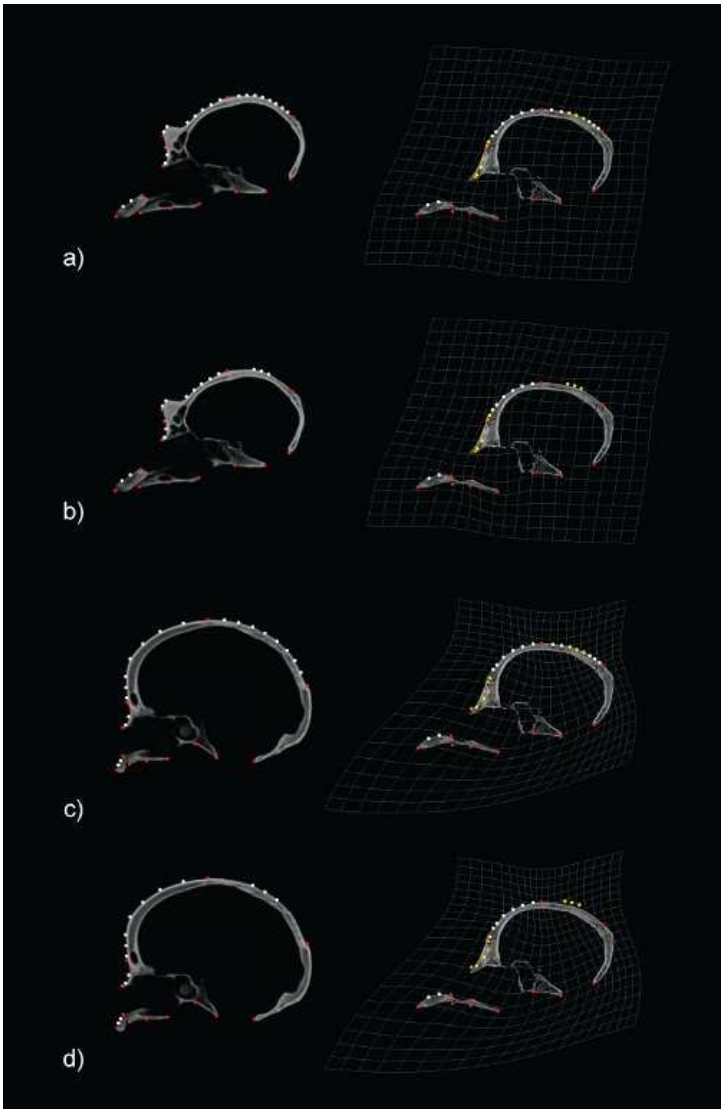

Figure 47 Estimating missing data in the midsagittal plane according to the knockout region defined above. Real landmarks are in red, surface semilandmarks are white, estimated real landmarks are orange, and estimated semilandmarks are yellow. a) Pan1 on Pongo1, complete set of surface semilandmarks, b) Pan1 on Pongo1, surface semilandmarks in the vicinity of the area declared as missing, c) Homo1 on Pongo1 , complete set of surface semilandmarks, and d) Homo1 on Pongo1, surface semilandmarks in the vicinity of the area declared as missing

Generally, a local spline between two anatomical landmarks will more or less maintain the curvature from the reference, depending on the distance between the landmarks and the form of the reference. The larger the distance between the two anchoring points, the more the spline will trace the shape of the reference in this area. In addition, the more differing the form of the reference to the target, the less accurate the estimation of missing data will be.

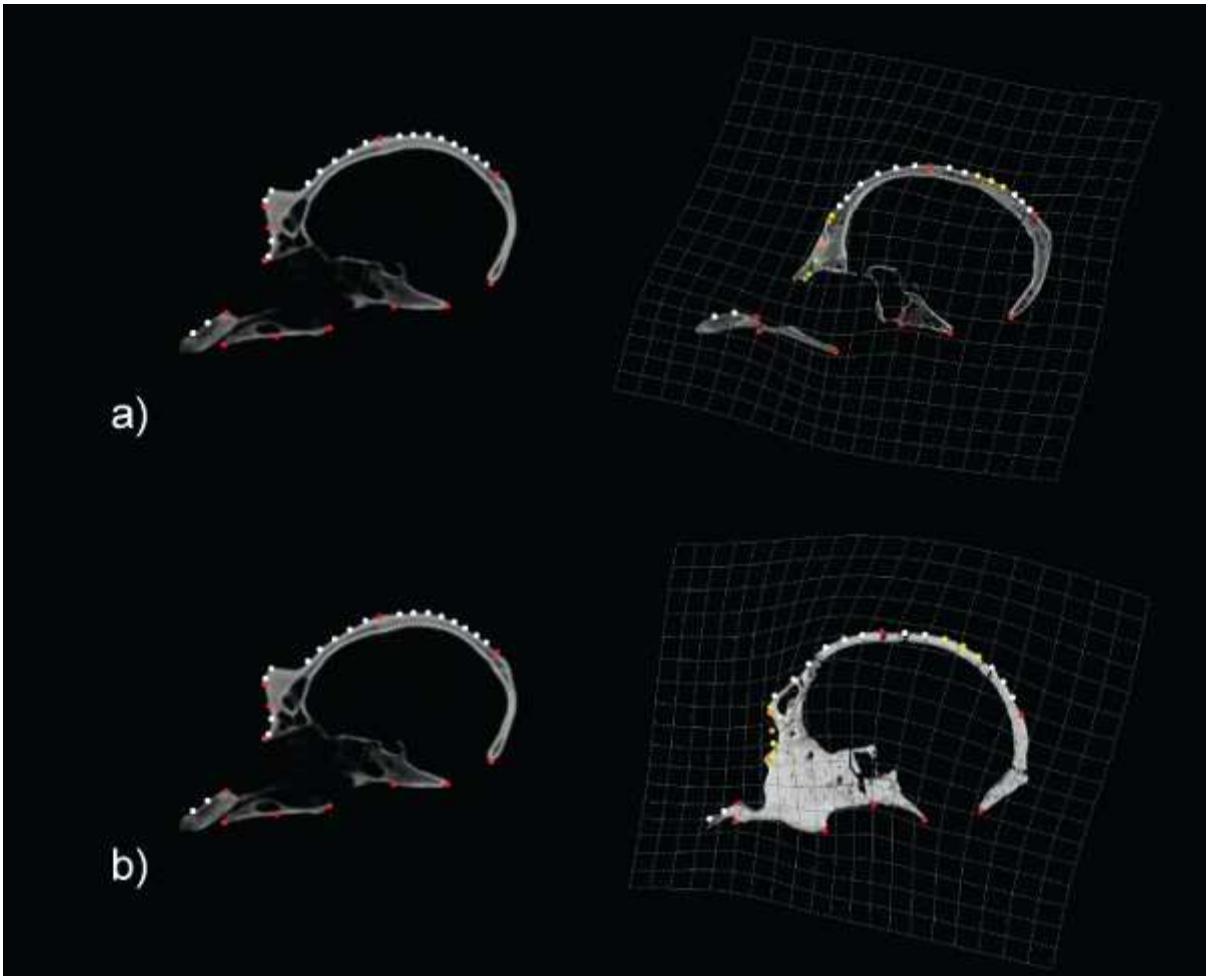

Figure 48 Estimating missing data in the midsagittal plane according to the knockout region defined above. Prosthion erased to show if the missing maxillary landmark in Sts 5 affects the outcome of the TPS missing data estimation. a) Pongo1 reconstructed by Pan1, c) Sts 5 reconstructed by Pan1

The estimated positions of the missing landmarks lie on a spline that is anchored by the real landmarks of the target (in this case bregma and lambda). Since the shape of the human cranium is more globular than those of apes, the spline in this area is rather globular as well and accordingly more curved than the surface of Pongo1. **Figure 48** illustrates the consequences when an anatomical landmark that would otherwise guide the TPS is missing, in this case *prosthion*, a landmark placed between the first incisors on the alveolar bone. This scenario is used to be sure that the missing landmarks in Sts 5 do not affect the outcome of

missing data estimation. As visulazied in **Figure 48a** the outcome is more or less identical to the reconstruction in **Figure 47a**, in which prothion is available.

4.4.4. Example of the "surface" of RMS reconstruction standard deviation

At first, I want to illustrate a pecularity of the reconstruction standard error to put its interpretation in perspective. **Figure 49** is an exploratory visualization of the spatial pattern generated by the reconstructions. The rendering of this surface was performed by a combination of two tools in "R" (R Development Core Team), the "interp" command for referring the normal SD at each semilandmark to a regular grid on the projection plane, and the "contour" command to supply the isocontours that make the resulting figure legible. Rendered thus, the diagram shows a mathematical "surface" as reconstructed inside an oval boundary that is, in fact, the edge of the parietal region colored dark green in **Figure 20** - the margin of the missing calvarial region. We are viewing it in a convenient "map projection" as if from this side of this skull as oriented in a Frankfurt plane.

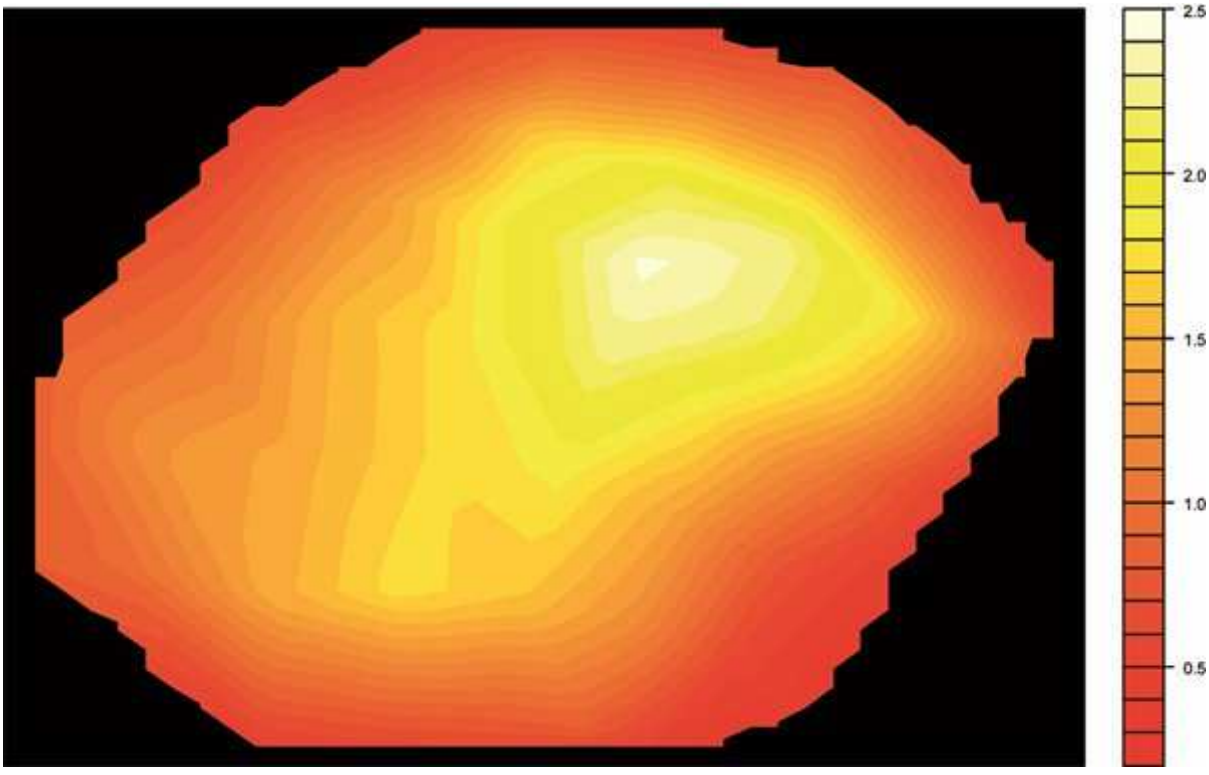

Figure 49 Example of the "surface" of RMS reconstruction standard deviation: Sts 5 reconstructed by Pongo. The underlying patch for this surface is the calvarial region coded in dark green color in Figure 20 (see text)

What is represented is not the surface of that reconstructed form but the derived surface of reconstruction standard error, in the direction perpendicular to the derived surface

itself. This surface is, as it must be, fixed at the value of zero (no uncertainty) all around its boundary, where the reconstruction leaves all the original data unchanged (black), and rises to a single well-defined interior maximum (yellow) by gradients that are very nearly linear in every traversal inwards from the boundary. Note, too, that neighboring contours are nearly parallel everywhere except upon that central dome. The location of this maximum is eccentric within the knockout region as a consequence of the large-scale structure of integration within the reference sample. This figure justifies the decision to restrict the numerical content of comparative reports to the single value at the peak of this surface; an average value would be greatly biased by the zero deviations along the boundary.

4.4.5. Facial reconstructions

Figure 50 illustrates the minimum and maximum distances as well as the average landmark RMS for each region in the facial knockout area according to Homo1, Pan1, Pongo1, Petralona, and Sts 5. The missing area in the face was subdivided into four regions for a detailed visualization of the results, but missing data in the face (as well as in the neurocranium) was estimated for the whole missing region at once, not for each region separately.

Maximum distances for interspecies reconstruction in the superior alveolar process reached values up to 6.5mm when reconstructing Homo1 by *Pongo* (**Figure 50a**). Interspecies reconstruction performed best (in terms of maximum distances that are in the range of intraspecies reconstructions) if the sample of *Pan* was used to reconstruct the missing data in Homo1 (maximum distance of 3.85mm) and Sts 5 (maximum distance of 4.35mm).

In the anterior maxillary surface maximum distances for interspecies reconstruction reached values up to 10.64mm when using *Homo* as reference for the reconstruction of Pan1 (**Figure 50b**). Except for Petralona, reconstructions involving *Homo* always performed worse. Using *Pongo* as reference for the reconstruction of Pan1, the maximum distance of 5.25mm showed comparable values to the intraspecies reconstruction of Pan1 (maximum: 4.90mm). The best results were achieved by taking *Pan* as reference for the reconstruction of Sts 5, showing a maximum distance of 4.44mm, hence showing a maximum distance that is lower than in intraspecies reconstrcutions.

The average RMS and maximum distances for intra- and interspecies reconstructions in the interorbital and nasal region were the highest observed in the facial region (**Figure 50c**). The lowest values were found for intraspecies reconstructions of *Pongo* with an average

RMS of less than 1.10mm and a maximum distance from the original to the reconstruction of 7.19mm. In contrast, the average RMS for the distance between the reconstruction and the original in *Homo* was approximately two times higher, reaching maximum values of up to 13.05mm. Highest values were always found at rhinion which situated in the middle of the missing area and therefore showing the highest deviation. Interspecies reconstructions using the *Pan* sample to estimate missing data in Pongo1 and *vice versa* showed maximum values of 11.62mm and 10.79mm respectively, thus exceeding maximum distances that were found in intraspecies reconstructions (*Pan*: 8.99mm, *Pongo*: 7.19mm). Remarkably, the lowest maximum distance was found when reconstructing Sts 5 with the *Pongo* sample (6.22mm), showing a lower value than found in intraspecies reconstructions. Like in anterior maxillary surface interspecies reconstructions involving *Homo* always performed worse, also in the nasal area of Petralona (rhinion was not considered in this specimen). Maximum distances up to 25.35mm were observed when reconstructing Pan1 with the *Homo* sample. The high variability in human nasal morphology is also reflected by a maximum distance of 13.05mm in intraspecies reconstructions. Note that the maximum distance when reconstructing Homo1 with the *Pongo* sample is lower than the intraspecies reconstruction. Maximum distances when reconstructing Homo1 with the *Homo* sample can be due to a more inferior, superior, anterior, and posterior position of the reconstructed nasal region, hence the high variation and maximum distance. In contrast, maximum distances when using *Pongo* as reference is always due to a more inferior position of the reconstructed area around rhinion, with only slight variation in antero-posterior position.

Average RMS for landmarks in the supraorbital region shows values similar to those in the anterior maxillary surface (**Figure 50d**). The intraspecies reconstruction of Pan1 shows the lowest maximum distances (3.69mm) and average RMS of landmarks (0.70mm (0.21)), Homo1 the highest (maximum distance: 5.53mm; average RMS: 0.80mm (0.34)). The highest accuracy in interspecies reconstruction can be observed when reconstructing Pongo1 using the *Pan* sample as reference (maximum distance: 5.28mm, average RMS of 0.83mm). Maximum distances that are in the range of values for the intraspecies reconstruction of Homo1 were found for Sts 5, either using *Pongo* (maximum distance: 5.50mm) and Homo (maximum distance: 5.69mm). Reconstructing the prominent supraorbital region of Petralona, the *Homo* reference sample showed the lowest maximum distance (5.89mm). In contrast, reconstructing the supraorbital region of Pan1 with *Homo*, the highest maximum values and average RMS of landmarks can be found (maximum distance: 11.32mm, average RMS of 2.45mm).

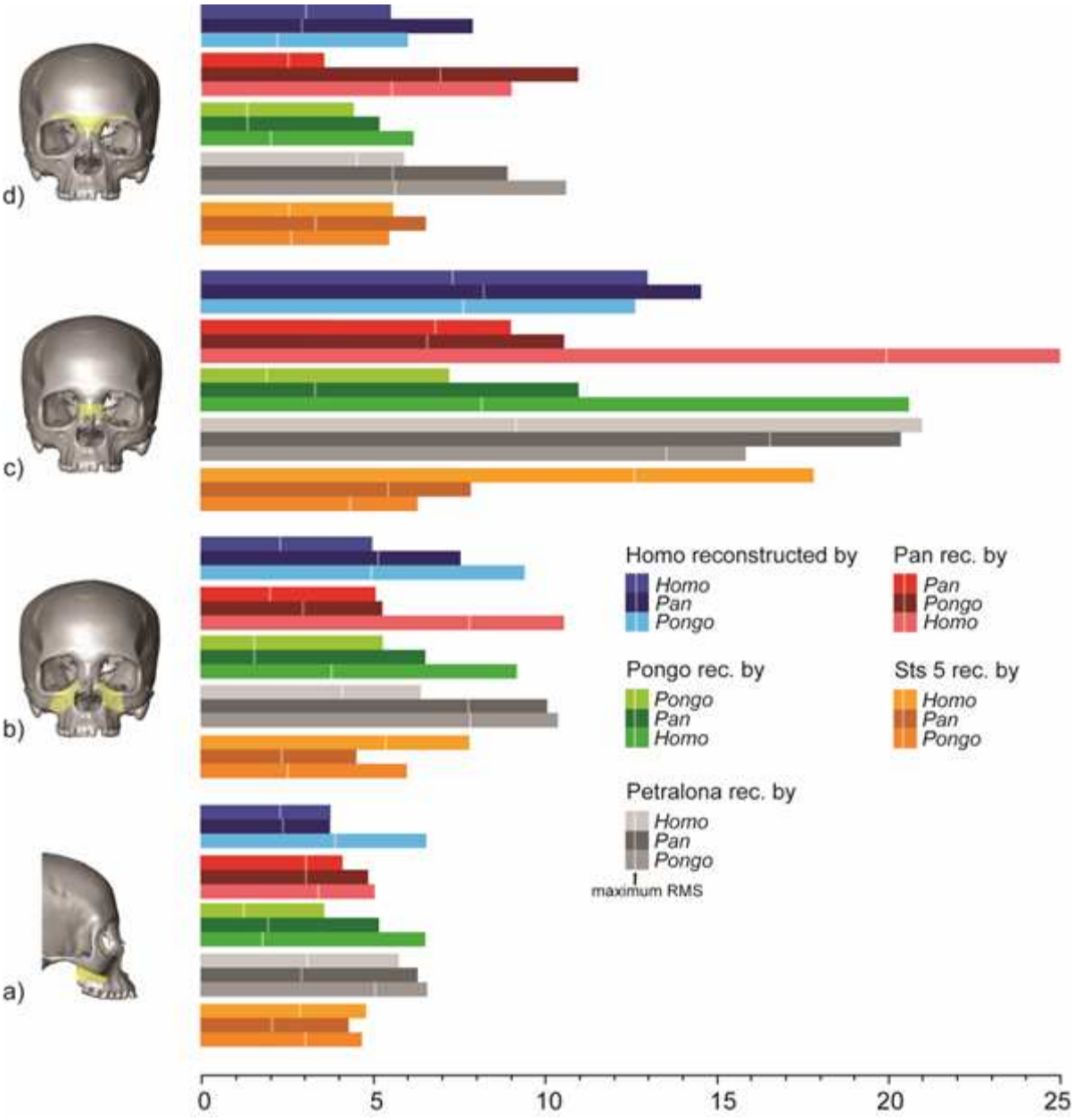

Figure 50 Minimum and maximum distances each region in the facial knockout area. Average maximum RMS (white vertical line within each bar) according to the reconstruction of Homo1, Pan1, Pongo1, Petralona and Sts 5. a) superior alveolar process, b) anterior maxillary surface, c) nasal and interorbital area and d) supraorbital region

The average maximum RMS in the supraorbital region shows values similar to those in the anterior maxillary surface (**Figure 50d**). The highest accuracy in interspecies reconstruction can be observed when reconstructing Pongo1 using the *Pan* sample as reference (1.33mm). However, the highest averaged maximum RMS was found when using *Pongo* as reference for the reconstruction of Pan1 (6.97mm), indicating that a reference of similar form does not always performs best.

Considering the fossils, the reconstruction of Sts 5 performed best when using *Pan* or *Pongo* as references, depending on the region to reconstruct. Estimating missing data in Petralona always performed best when the *Homo* sample was employed as reference. The pattern observed in the reconstruction of Mladec 1was very similar to Homo1.

4.4.6. Neurocranial reconstructions

Figure 51 illustrates the minimum and maximum distances and average RMS for each region in the neurocranial knockout area according to the reconstructions of Homo1, Pan1, Pongo1, Petralona, and Sts 5. Missing regions in the neurocranium were subdivided into three regions for better visualization of the results. For neurocranial reconstructions within species the average RMS did not exceed 1.42mm (0.12) (estimating missing data in the midsagittal area of Homo1).

Using *Pan* or *Pongo* as reference in the reconstruction of Homo1 (maximum distances of 2.73mm and 2.23) performed better than reconstructing Homo1 with *the Homo* sample, reaching maximum values up to 4.21mm (**Figure 51a**). Although the midsagittal missing area is rather small, the high variability in human neurocranial form leads to bad results when using *Homo* references of differing form. Lowest maximum distances were observed when reconstructing Pan1 with the *Pongo* sample (maximum distance: 1.30mm), performing as good as the intraspecies reconstruction of Pan1 itself (maximum distance: 1.38mm). In contrast to Homo1, estimating missing data in Petralona using the Homo reference sample show the lowest maximum distance (2.08mm), while *Pan* and *Pongo* show much higher values (3.82mm and 3.50). Reconstructing the midsagittal area in Sts 5 with the extant reference species yields homogenous results, *Pongo* showing slightly better results in terms of average RMS (0.26mm (0.07)) and maximum distance (1.42mm) than *Homo* and *Pan*.

In the parietal, maximum distances for interspecies reconstruction reached values up to 12.94mm when using *Pan* as reference for the reconstruction of Homo1 (**Figure 51b**). Highest values were typically found in the middle of the missing area that is farthest away from existing bone that could guide the TPS based reconstructed. In general, reconstruction of Homo1 always performed worse. The highest accuracy was achieved by using *Pongo* as reference for the reconstruction of Pan1 (maximum distance: 3.37mm), showing a very similar maximum distance compared to the reconstruction of Pan1 with the *Pan* sample (3.41mm). Estimating missing parietal data in Petralona, no reference reached an accuracy that is comparable to intraspecies reconstructions. Maximum distances ranged from 7.00mm

(*Homo* as reference) to 8.10 (*Pongo* as reference). But, concerning the average RMS *Pan* (1.05mm (0.62)) and *Pongo* (1.05mm (0.60)) performed slightly better than *Homo* (1.41mm (0.52)). In contrast, the maximum distance when reconstructing Sts 5 with the *Pan* sample (4.54mm) is comparable to the values obtained for the intraspecies reconstruction of *Homo* (4.43mm).

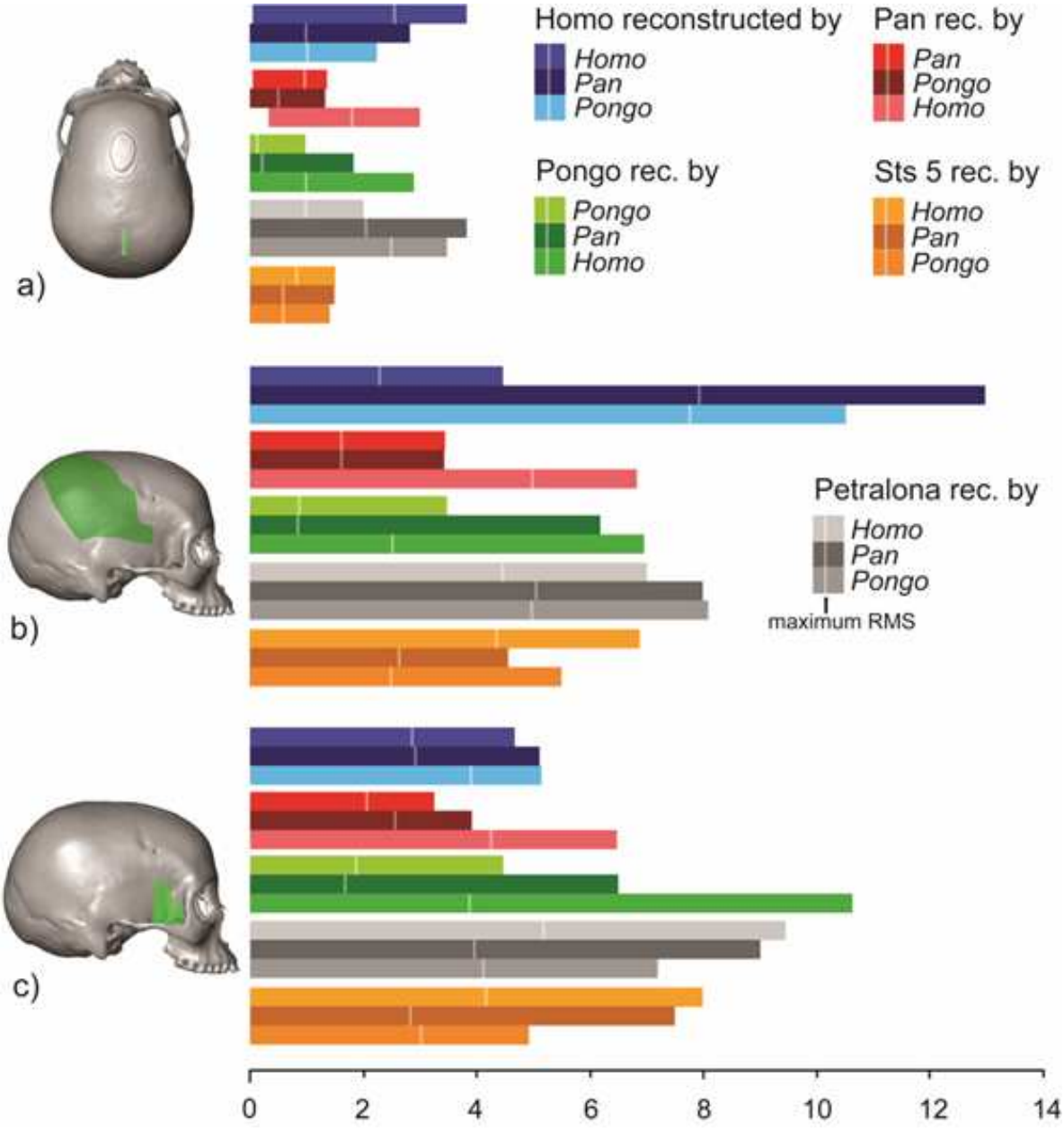

Figure 51 Minimum and maximum distances and average maximum RMS for each region in the neurocranial knockout area. According to the reconstruction of Homo1, Pan1, and Pongo1. a) midsagittal area, b) parietal, and c) sphenoid

Lowest maximum distances in intraspecies reconstructions of the sphenoid area were found in the reconstruction of Pan1 (maximum distance 3.38mm). Estimating missing data in

the sphenoid of Pan1, the lowest maximum values and average RMS of landmarks could be found when using the *Pongo* sample as reference (maximum distance: 3.85mm, average RMS of 0.62mm). The maximum distance is hence lower than in intraspecies reconstructions of *Homo* (4.70mm) and *Pongo* (4.44mm) respectively. In Petralona as well as Sts 5 taking *Pongo* as reference yielded the best results, but maximum distances in Petralona (7.29mm) are much higher than in Sts 5 (4.83mm). Maximum distances for interspecies reconstruction reached values up to 11.38mm when reconstructing Pongo1 with the *Homo* sample (**Figure 51c**). Since the sphenoid is characterized by a more or less high concavity which represents a more complex topography to reconstruct, maximum distances in intra – and interspecies reconstruction is comparable to the parietal area, even though the missing area is much smaller.

4.4.7. Visualizing regional effects concerning the choice of the reference

Figure 52 shows the interspecies reconstructions of Sts 5, showing the reconstructions that show the highest and lowest average maximum RMS for each region respectively. Consequences of the choice of the reference are less obvious in the area of the superior alveolar process (**Figure 52a**). In contrast, consequences of reference choice were obvious in the area of the inferior sphenoid, where the variation in the reconstructions of *Homo* (blue) is much higher than *Pongo* (green). The same is true in the anterior maxillary surface, where *Homo* shows maximum values up to twice those of the *Pan* sample, which performs best in this area (**Figure 52b**). In the lower parietal and upper sphenoid area the *Pongo* reference sample performs best, estimating the neurocranial curvature of Sts 5 much better than the *Homo* sample. First, the reconstructions of *Homo* show a much higher variation in the sphenoidal region; second the outline in the middle of the missing area is shifted medially in the *Homo* reconstructions. *Pongo* also outperforms the other reference species in reconstructing the interorbital area. Both interorbital breath and the posterior/anterior dimension of the nasal region were reconstructed reasonably (**Figure 52c**). The difference in the performance of different references is also obvious in the parietal, especially in the center of the missing area where the deviation from the original is highest (**Figure 52d**).

The reconstructions of *Homo* resemble the human neurocranial shape characterized by a straighter and flatter lateral neurocranial outline compared to the great apes. In contrast, reconstructions of the *Pan* sample follow the parietal curvature of Sts 5 much better, even though this region is characterized by a huge defect, lacking information of preserved

proximate morphology that could guide the TPS during missing data estimation. Reconstructions in the glabellar area using *Pongo* as reference also outperform reconstructions by *Homo*, though neither reference choice is able to reconstruct the prominent glabellar area in Sts 5 appropriately.

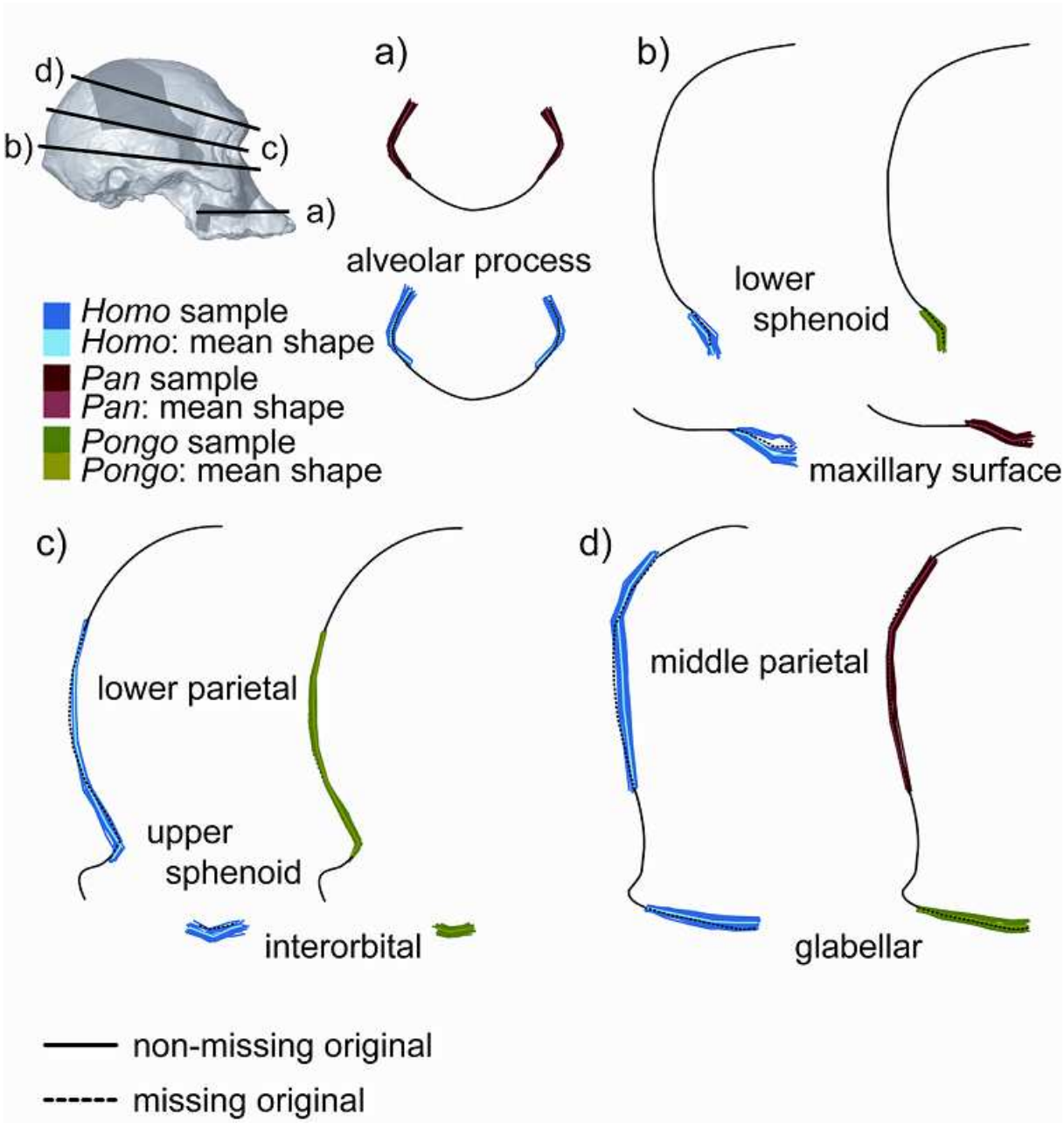

Figure 52 Sts 5 reconstructed by Homo (blue), Pan (red), and Pongo (green). Original outline (black; missing area: dashed line) of Sts 5 and the estimates based on TPS. Comparison of the reference with the lowest (bottom or left) and highest (top or) accuracy in terms of maximum distance from the original (see Figure 50 and 51); a) reconstruction of the superior alveolar process, b) the lower sphenoid and anterior maxillary surface, c) inferior parietal, superior sphenoid, and interorbital area, and d) the superior parietal and glabellar area

4.4.8. Visualizing the variation of the reconstructions

In **Figure 53** the fossil reconstructions of Mladec 1 (dark blue), Petralona (black), and Sts 5 (yellow) as well as the reconstruction of Homo1 (aquamarine blue), Pan1 (dark red), and Pongo1 (dark green) are projected in the form space spanned by the landmarks of the three reference species (*Homo*: blue, *Pan*: red, *Pongo*: green). The color of the 95% ellipsoid corresponds to the species that was used during reconstruction.

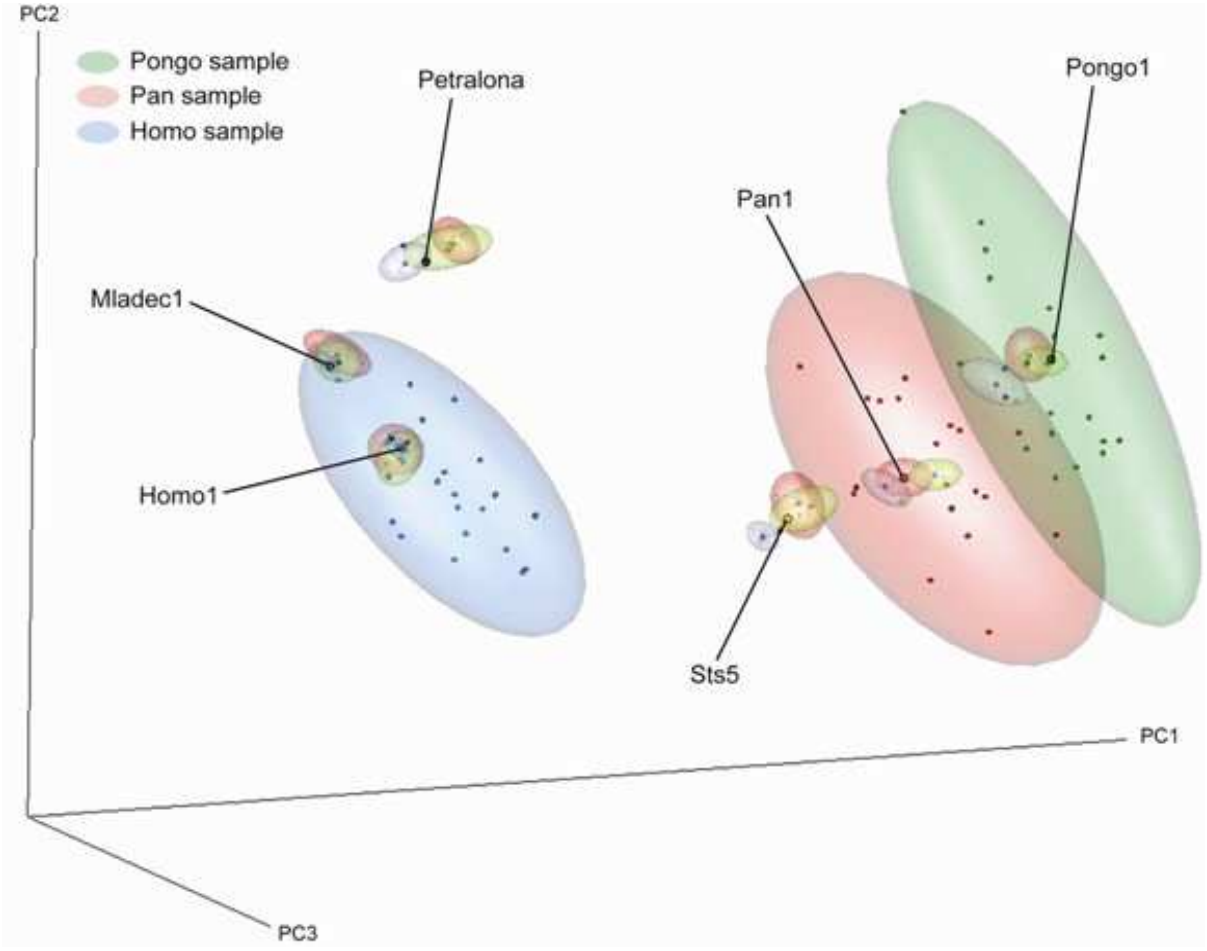

Figure 53 Form space PCA (PC1: 77.2%, PC2: 13.10%, PC3: 2.83%). Individual cases (small colored spheres) and 95% confidence ellipsoids (the large ones) for the Homo (blue), Pan (red), and Pongo (green) sample used. Original Mladec1 (dark blue), Petralona (black), and Sts5 (yellow) together with their reconstructions (blue: reconstruction by Homo, red: reconstruction by Pan; green: reconstruction by Pongo). The small 95% confidence ellipsoids correspond to the reconstruction of each case (color according to intraspecies ellipsoids)

Within this subspace of highest explained Procrustes shape variance, the variation within each group of alternate reconstructions is rather low compared to the variation within species. The anatomical reconstruction of the *Paranthropus boisei* specimens OH5 (Benazzi

et al. 2011) in comparison, showed a much higher variation compared to the TPS based reconstructions in **Figure 53**. If we merely use information from the PCA plot to choose the reference, e.g. to reconstruct Sts 5, the decision will be rather difficult to make at this largest scale precisely because the reconstructions using *Pan* and *Pongo* are so widely overlapping. As we showed in a detailed look at specific reconstructed regions, a level of detail not available from the preceding diagram, different reference samples perform better in different regions. Since we are missing detailed information about variation in fossil species, only this small scale inspection of the consequences in applying different references would permit a conclusion as to whether any choice of reference sample is appropriate at all. Nevertheless, some general guidelines can be drawn from these experiments that might be helpful to decide when one reference sample might be less inappropriate than another.

4.4.9. Guiding the choice of the reference sample

We can consider the resulting bending energy of the TPS as a criterion of performance in the process of reconstruction. **Figure 54** shows a scatterplot of the bending energy values against the Procrustes distance from the original to the corresponding reconstruction, in this example for Pan1. In this case, we find a correlation of 0.94 (**Figure 54**). Generally, the highest correlations between each pair (reconstruction - original) can be found within the extant species (Pearson's product-moment correlation: $r_{Homo1}=0.88$, $r_{Pan1}=0.94$, $r_{Pongo1}=0.91$). The high concordances suggest that bending energy can be used to estimate the performance of the reconstruction and thus provides a guideline for choosing an appropriate reference group. Correlations for the fossil reconstructions are lower ($r_{Mladec\ 1}=0.71$, $r_{Petralona}=0.65$, $r_{Sts\ 5}=0.75$). As shown in **Figure 54**, if we reconstruct Pan1, some reconstructions based on *Pongo* specimens show a similar accuracy as those using *Pan* specimens. The graph shows also that the variability for the reconstructions using *Pongo* is smaller than for the reconstructions using either *Pan* or *Homo*.

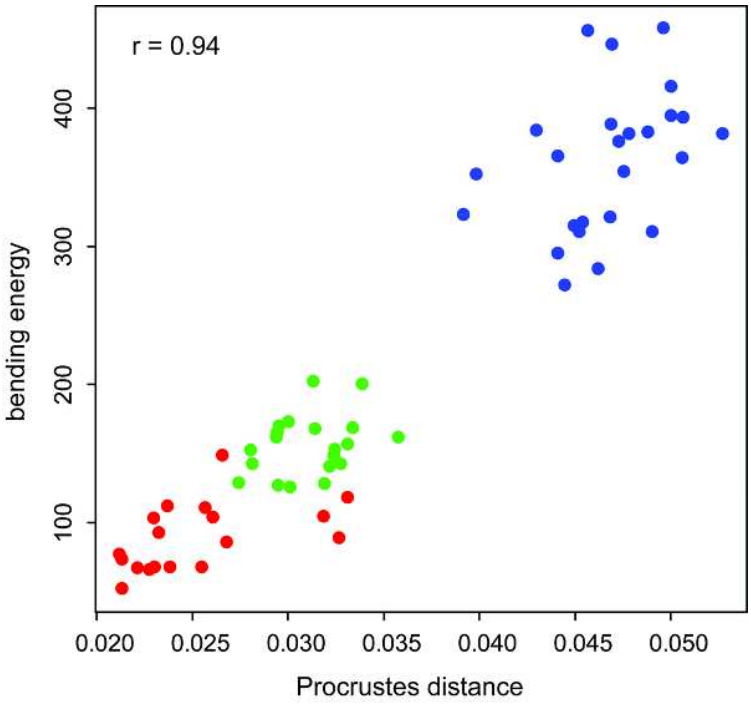

Figure 54 Correlation between bending energy and the Procrustes distance from Pan1 to each corresponding reconstruction. Pan1 reconstructed by Pan (red), Homo (blue), and Pongo (green)

4.5. Facial orientation and integration in the hominoid cranium

Figure 55 represents the two different Procrustes superimposition set-ups that were used during the analyses. The first set-up only includes the basicranial landmarks in the Procrustes fit (**Figure 55a**). In the second set-up the orbits were included in the superimposition and PLS analysis (**Figure 55b**). Note the difference in palate orientation between *Pan* and *Pongo* in **Figure 55a**, while in the second set-up, the angle describing the difference in palatal angle is smaller. Variation in the basicranial landmarks in the second set-up is higher after the Procrustes superimposition. The overlap and variation in palate orientation between and within the two species is obvious in both scenarios.

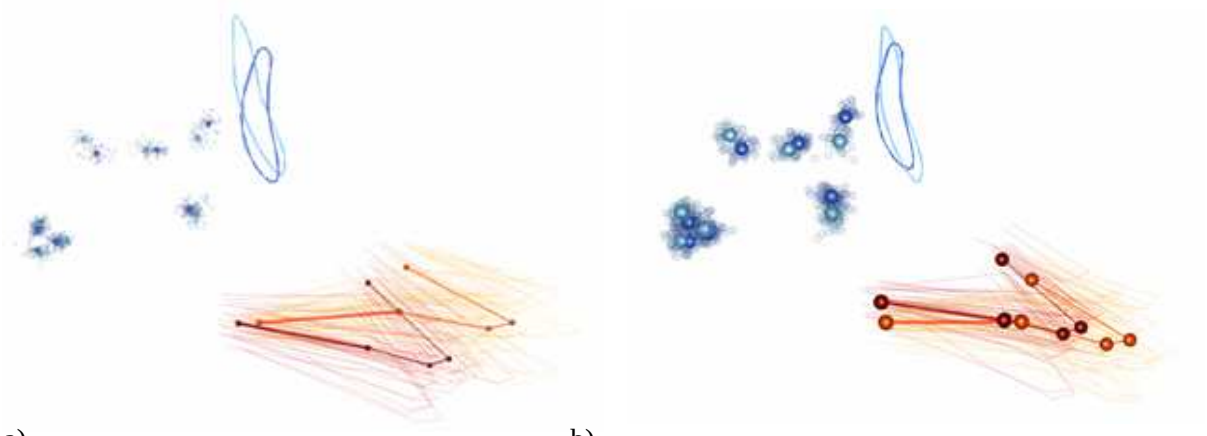

a) b)

Figure 55 Pan and Pongo sample pooled. a) Procrustes superimposition on sphenoid landmarks only b) Procrustes superimposition on landmarks of sphenoid and orbits. Mean sphenoid and orbital landmark configurations and variation around the mean for the sphenoid (dark blue: Pan, light blue: Pongo). Mean palatal (big spheres) and maxillary landmarks (small spheres) configurations for Pan (darkred) and Pongo (orange) as well as the variation of maxillary orientation in each species (Pan; red, Pongo, yellow).

4.5.1. Pooled sample PLS

To assess the covariation of maxillary rigid motions and basicranial/orbital shape, we performed a PLS analysis of the Procrustes shape coordinates against the three variables of rigid motion (Δx and Δy, and θ): a) only cranial base b) basicranial and orbital landmarks.

The first singular warp (the first dimension of the PLS analysis) in both analyses accounts for 54% of the total squared covariance between the shape coordinates and the variables of rigid motion (**Figure 56**). In both cases the first two singular warps span about 89% of the total squared covariance pattern. The correlation between the first pair of PLS scores (shape vs. rigid motion) is 0.39 (Procrustes fit: cranial base) and 0.49 (Procrustes fit: cranial base and orbits); between the second pair 0.29 and 0.49 respectively. In the first set-up both species largely overlap but do not show the same trajectory for the first singular warp. Including the orbits in the superimposition and PLS, the trajectories are parallel but shifted along SR1. Loadings on the first and second singular vector for the rigid motion are reported in **Table 17**.

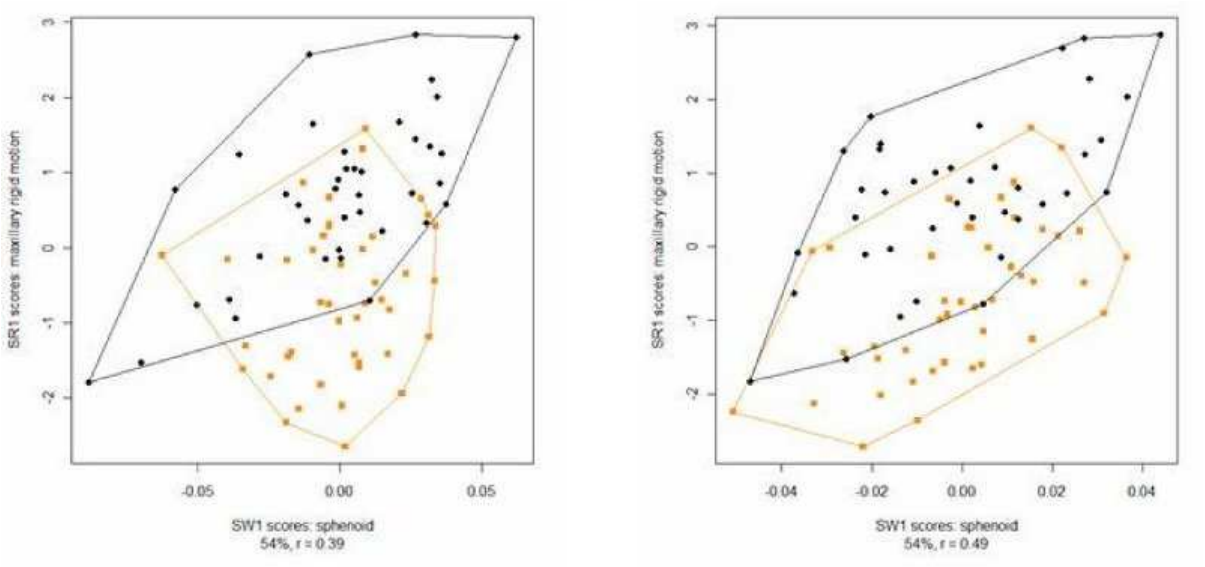

Figure 56 Pooled sample. Pan (black) and Pongo (orange). Singular warp 1 scores of the coordinate block and orientation block plotted against each other. a) Procrustes fit on basicranial landmarks, b) Procrustes fit on basicranial and orbital landmarks

The estimations of uncertainty in palate orientation can be expressed as palatal angles relative to the mean palatal orientation of both species that serves as basis, i.e. 0°. For the Procrustes superimposition that only takes landmarks on the sphenoid into account palatal angles for *Pan* range from -28.8° (negative sign corresponds to downward rotation relative to mean of both species) to 6.9° (positive sign corresponds to upward rotation relative to mean of both species), with a species mean of -8.4°. Palatal orientation for *Pongo* ranges from -3.4° to 18.3°, with a species mean for the orangutan sample of 7.1° (see also **Figure 55a**). Considering the Procrustes superimposition on sphenoidal and orbital landmarks, palatal angles for *Pan* range from -28.3° to 10.4°, with a species mean of -5.4° (i.e ventrally rotated). Palatal orientation for *Pongo* ranges from -7.8° to 16.7°, with a species mean of 4.1° (i.e dorsally rotated; see also Figure 55b).

Table 17 Loadings of the first two singular vectors for the translation/orientation variables

	cranial base		*cranial base & orbits*	
Variables	pooled sample			
	Singular vector 1	Singular vector 2	Singular vector 1	Singular vector 2
θ	-0.38	0.21	-0.45	0.21
Δx	0.72	0.67	0.72	0.66
Δy	-0.57	0.71	-0.52	0.75

4.5.2. Within species PLS

Procrustes fit on basicranial landmarks (see **Figure 55a**). The first singular warp explains 52% (*Pan*) and 55% (*Pongo*) of the total squared covariance between basicranial shape palate rigid motion. The first two singular warps span 87% (*Pan*) and 89% (*Pongo*) of the total squared covariance pattern. The correlation between the first pair of PLS scores (shape vs. rigid motion) is 0.58 (*Pan*) and 0.6 (*Pongo*); between the second pair 0.49 (*Pan*) and 0.73 (*Pongo*). Loadings on the first and second singular vector for the rigid motion are reported in **Table 18**.

Table 18 Loadings of the first two singular vectors for the translation/orientation variables

	Procrustes fit on basicranial landmarks		Procrustes fit on basicranial&orbital landmarks	
Variables	Singular vector 1	Singular vector 2	Singular vector 1	Singular vector 2
		Pan		
θ	-0.18	0.69	0.65	-0.01
Δx	0.66	-0.44	-0.61	0.59
Δy	0.73	0.57	0.45	0.81
		Pongo		
θ	0.53	0.22	0.6	-0.2
Δx	-0.62	0.76	-0.48	-0.87
Δy	-0.58	-0.61	-0.64	0.45

Procrustes fit on basicranial and orbital landmarks (see **Figure 55b**). The score-plots show how well the position and orientation of the palate can be predicted by the shape and spatial relationship of the basicranium and orbits (**Figure 57**). The first singular warp explains about 10% more of the total squared covariance between basicranial shape palate rigid motion (*Pan*: 68%, *Pongo*: 66%) than in the former set-up. The first two singular warps span 89% (*Pan*) and 91% (*Pongo*) of the total squared covariance pattern. The singular warp scores are highly correlated (0.8 for both *Pan* and *Pongo*); between the second pair 0.67 (*Pan*) and 0.7 (*Pongo*), though for *Pan* the correlation will not be considered because of the outlier (**Figure 57**). Loadings on the first and second singular vector for the rigid motion are reported in **Table 18**. In *Pongo*, the direction of the singular vectors is the same for both set-ups. In the *Pan* sample, SW1 has high loadings on Δx and Δy, the displacement of the centroid in

anterior-posterior direction; θ loads high SW2. When including the orbits into the Procrustes fit and PLS, θ (palate orientation) has the highest loading on SW1.

Figure 58 and **59** visualize the corresponding shape differences as predicted by the loadings of the first singular vector for the shape variables of the sphenoid and orbits and orientation variables for the palate. In both species, the shape features that are associated with high scores along the first singular warp, and that thus correspond to a more dorsally deflected palate, include an inferior-superior inflation of the sphenoid body at the height of the dorsum sellae and a decrease of relative orbital height.

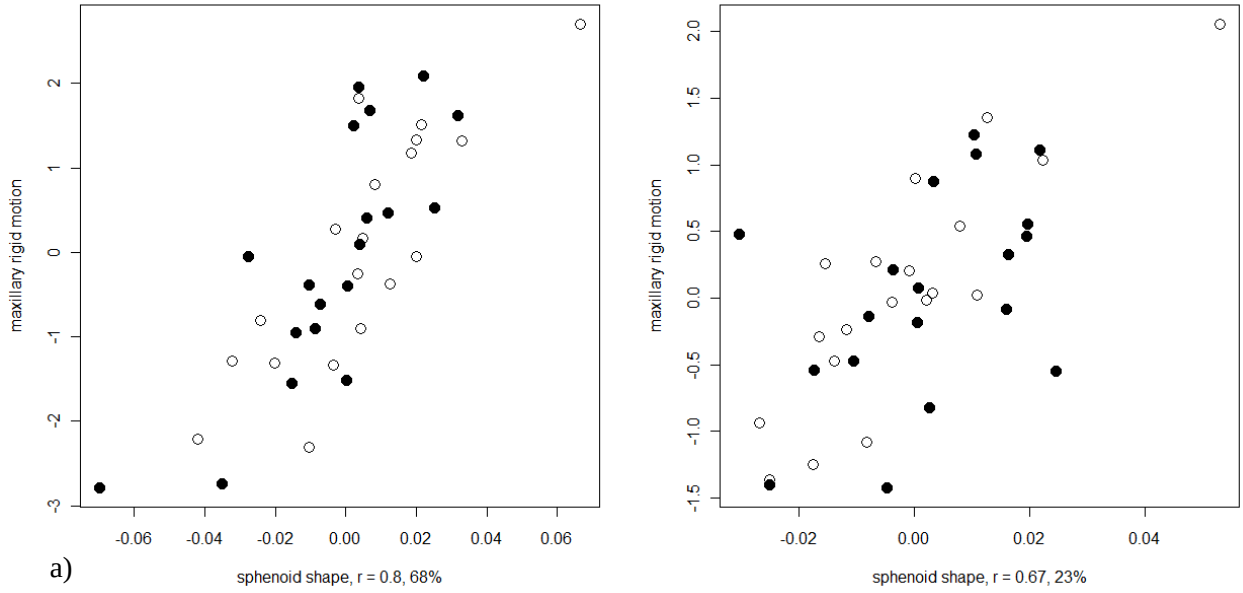

a)

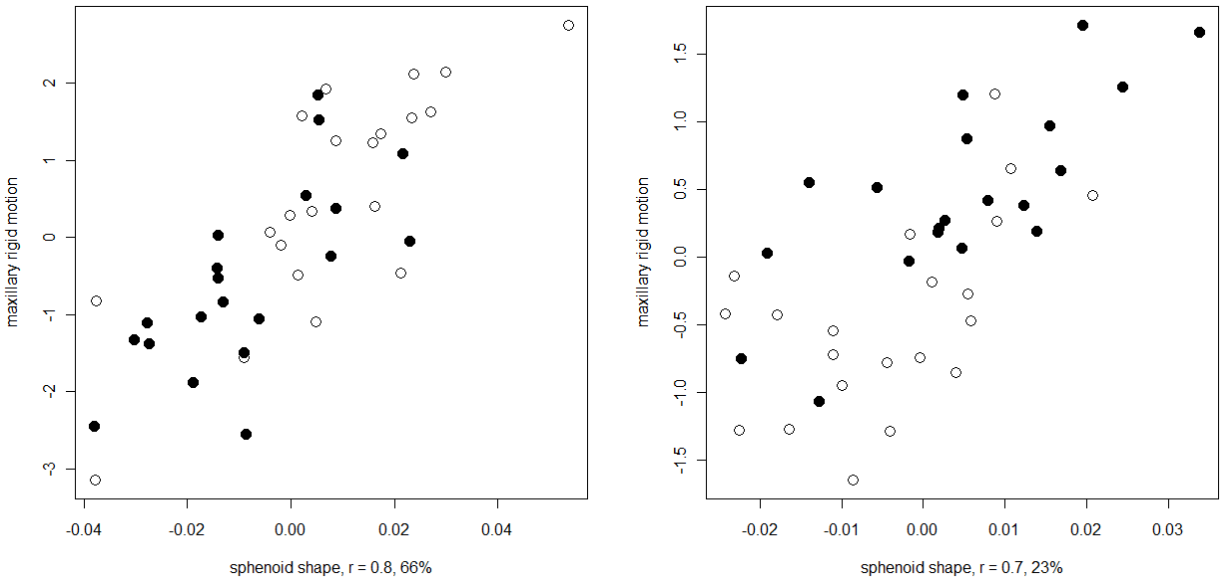

b)

Figure 57 Singular warp 1 () and 2 (left) scores of the coordinate block and orientation block plotted against each other. a) Pan sample,b) Pongo sample. Filled circles: males, open circles females

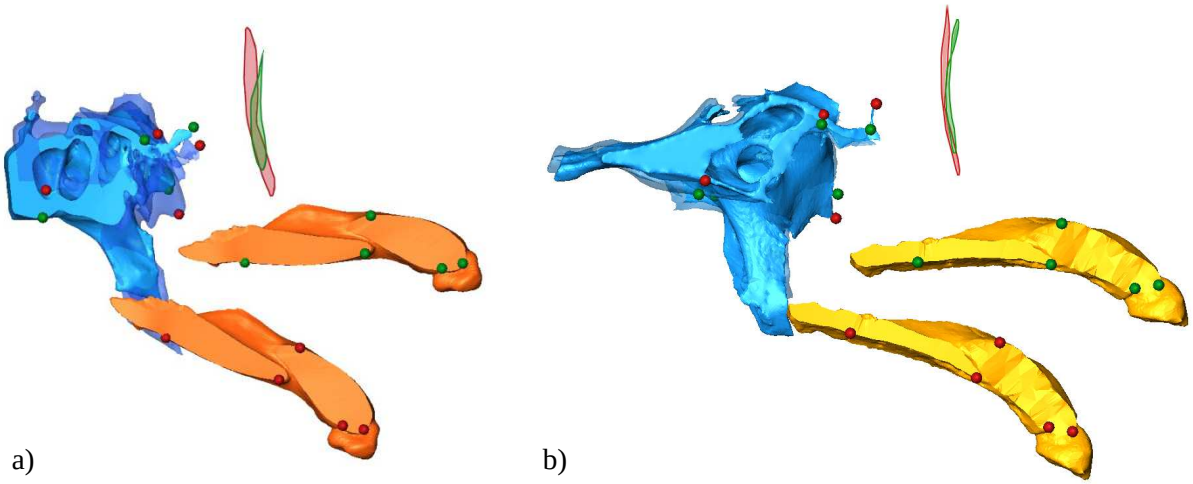

a) b)

Figure 58 Singular warp 1 for Pongo (a) and Pan (b). Minimum (red landmarks) and maximum (green landmarks) SW1 scores for each species. Midline section of the palate, lateral aspect of the temporal surface of the greater wings of sphenoid bone, the anterior and posterior end of the cribriform plate, and sphenion

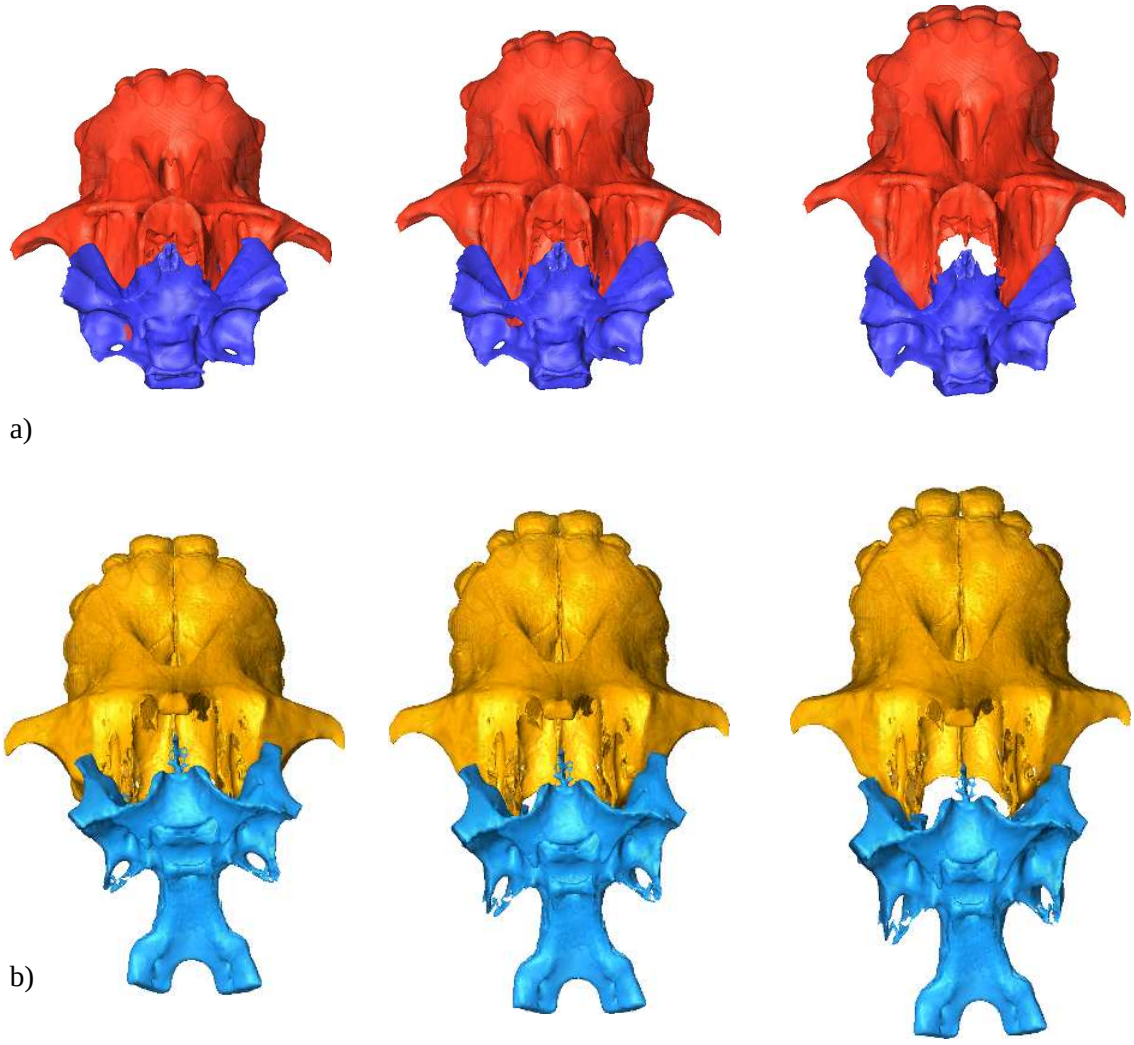

a)

b)

Figure 59 Dorsal view: Singular warp 1 for Pongo (a) and Pan (b). Minimum SW1 (left), consensus shape (middle) and maximum () SW1 scores for each species.

For SW1 in *Pongo*, a ventrally rotated palate covaries with a shortened planum sphenoideum associated with a steeper orientation of the cribriform plate and an anterior-posteriorly elongated cranial base with longer medial middle cranial fossae. In *Pan* a ventral deflection of the palate does not covary with a shortened planum sphenoideum and but rather is associated with a less steep orientation of the cribriform plate for SW1. Furthermore, a dorsal deflection of the palate in chimpanzees involves an anticlockwise rotation of the inferior border of the sphenoid.

In the lateral aspect of the temporal surface of the greater wings of sphenoid bone and the cribriform plate, one sees that there is a substantial difference in the shape changes that accompany the reorientation of the palate between *Pan* and *Pongo*. In *Pongo*, a dorsal deflection of the palate is accompanied by an inferior displacement of the anterior border of the temporal surface of the greater wings of sphenoid bone and a superior displacement of the anterior border of the cribriform plate. In contrast, a more dorsally oriented palate in chimpanzees covaries with a concerted anterior displacement of the anterior border of the temporal surface of the greater wings of sphenoid bone and anterior border of the cribriform plate.

The second dimension loads highly on the anterior-posterior positioning of the maxilla, thus differentiating specimens that have an anteriorly-posteriorly longer cranial base combined with a more anteriorly placed maxilla than the others. In *Pongo*, an anteriorly placed maxillary bone covaries with an anteriorly-posteriorly elongated sphenoid, a clockwise rotation of the inferior border of the sphenoid body and a more superior-anteriorly placed dorsum sellae. Additonally, an anteriorly placed maxilla covaries with an increased breath at the posterior border of the cribriform plate. In individuals that are characterized by a more anteriorly placed maxilla, the middle cranial fossa is elongated accompanied by an anterior-posteriorly elongation of the temporal surface of the greater wings of sphenoid bone. SW2 of *Pan* are not described here since the pattern that can be seen in **Figure 57** is mostly due to the outlier showing the minimum SW2 score.

We use a net partial predictior in order to investigate the covariation between the single variables of palate position (Δx: anterior - posterior, Δy: superior - inferior) and orientation (θ), i.e. predict Δx, Δy, and θ separately from basicranial and orbital shape (**Table 18**).

Table 19 correlation for predicting palatal position (Δx, Δy) and orientation (θ) with basicranial/orbital shape

Variables	cranial base	cranial base & orbits	orbits
		Pan	
θ	0.48	0.74	0.7
Δx	0.45	0.75	0.7
Δy	0.53	0.67	0.59
		Pongo	
θ	0.43	0.71	0.64
Δx	0.58	0.77	0.68
Δy	0.58	0.72	0.56

4.6. Facial orientation and mandibular shape: integration in the hominoid cranium

Figure 60 and **Figure 61** present the results of the PC analysis of the centered Procrustes shape coordinates (relative warps). In both species, either the maxillary PC1 or PC2 are representing shape changes related to facial orientation, though the variation is more pronounced in *Pongo*. Mandibular PC1 or PC2 are related to shape changes in the orientation of the ramus and mandibular length.

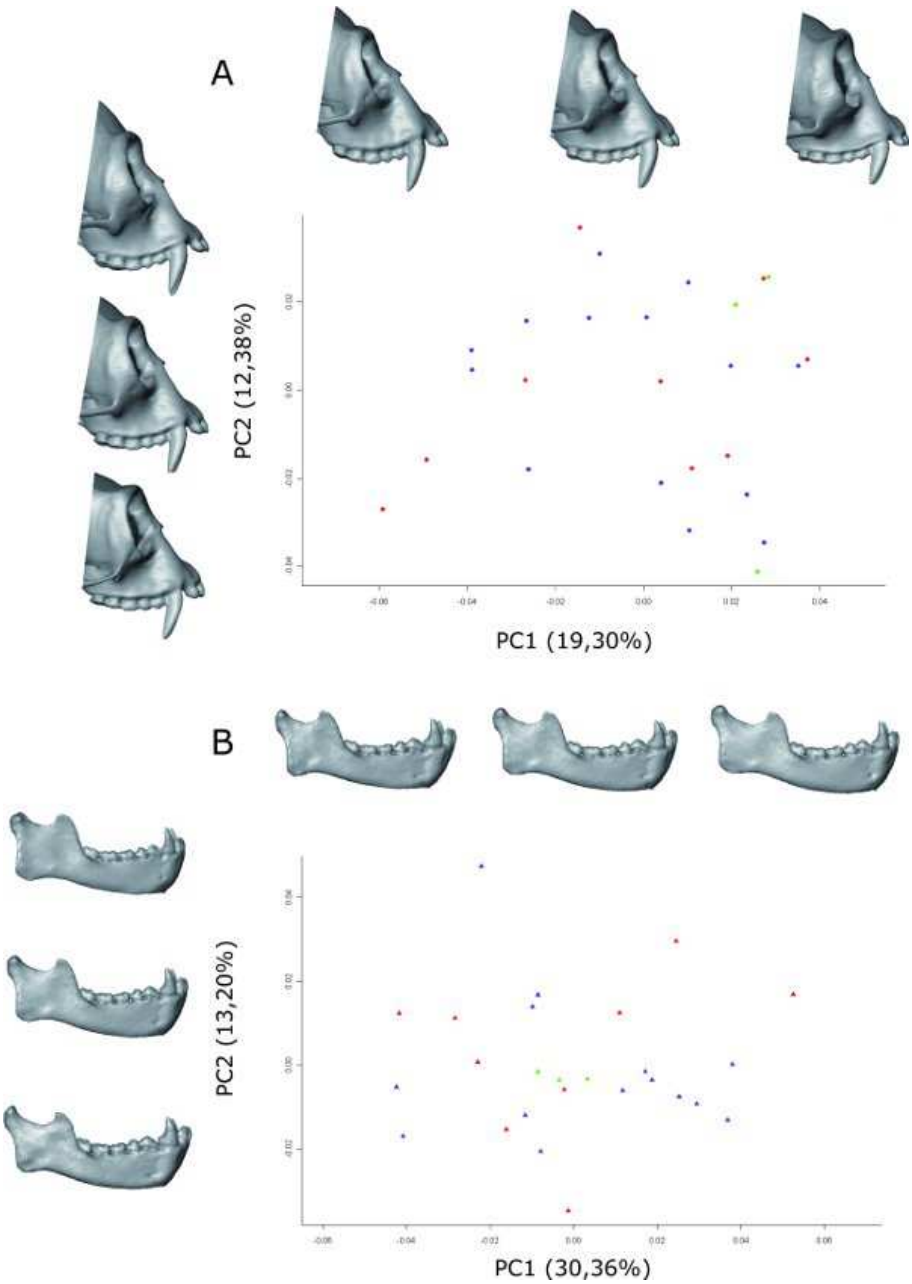

Figure 60 Shape space PCA. (A) Maxilla. (B) Mandible. Females (red), males (blue), and individuals of unnown sex (green). Surface morphs along PC1 and PC2

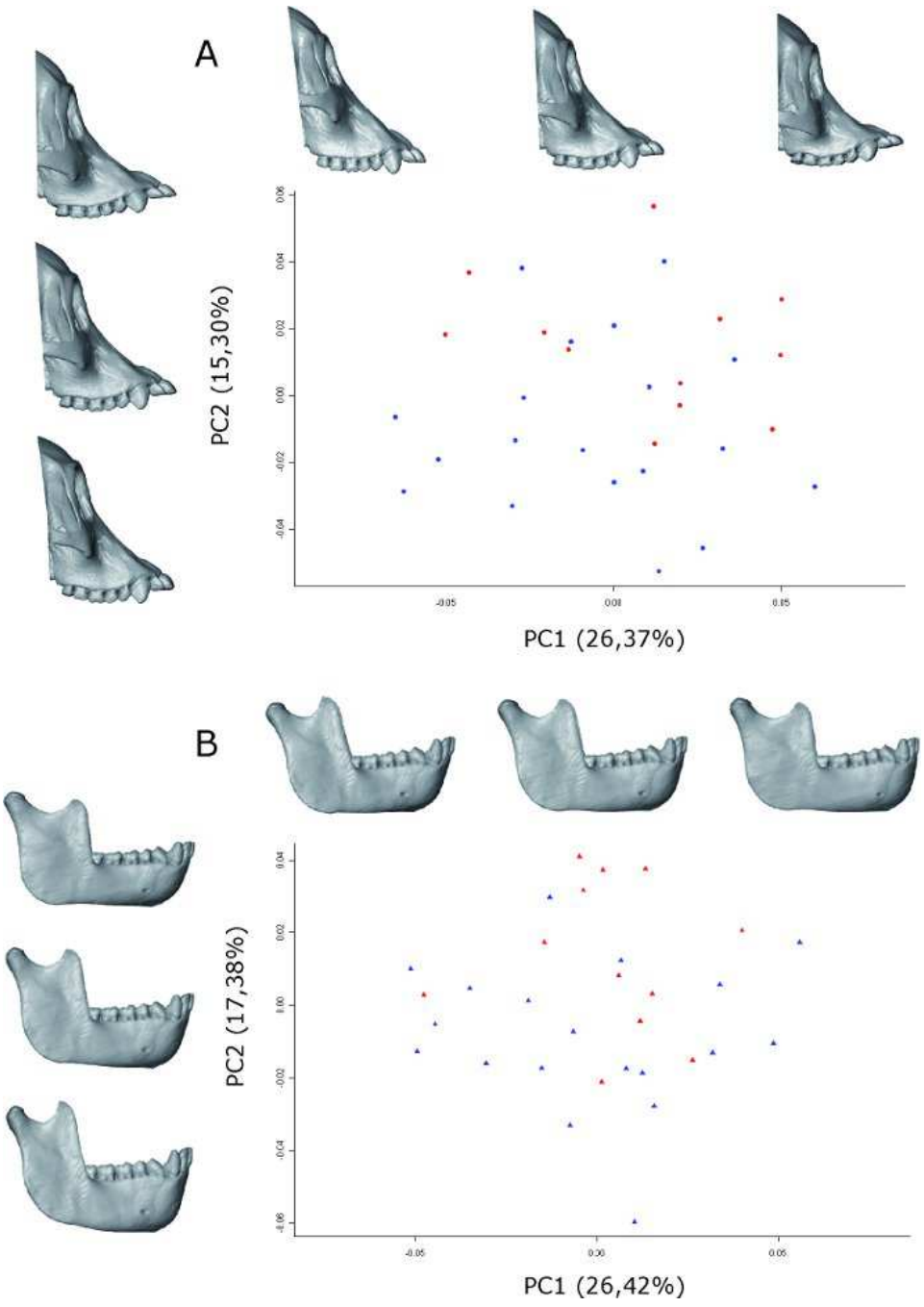

Figure 61 Shape space PCA. (A) Maxilla. (B) Mandible. Females (red), males (blue), and individuals of unnown sex (green). Surface morphs along PC1 and PC2

Concerning patterns of covariation, in *Pongo* a downward deflection of the premaxilla is correlated (r > 0.71) with an increase of the angle between mandibular corpus and ramus, and a relatively higher symphysis (**Figure 63**). On the contrary, a dorsal flexion of the midface covaries with a more vertical ramus orientation and lower symphysis. In *Hylobates*, a downwardly deflected premaxilla also covaries with a backwardly inclined ramus, a higher symphysis, but also a rounded inferior border of the anterior corpus (**Figure 62**). Correcting for sex and size, we find that SW1 and SW2 scores do not correlate (r < 0.3) with Centroid Size in both species.

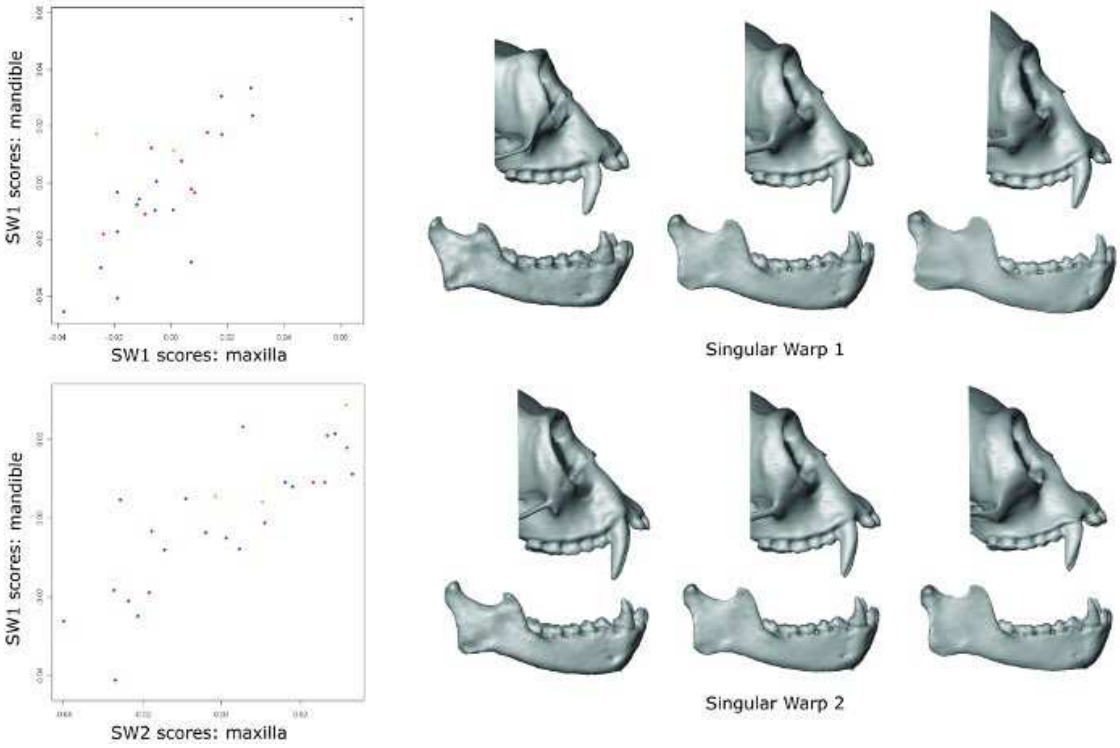

Figure 62 Hylobates. SW scores of the two coordinate blocks plotted against each other (left). SW1 (top) and SW2 (bottom). Visualizing the shape dimensions associated with the plotted scores

The first singular warp (18.02%) contrasts a less inclined and a steeper inclined premaxilla associated with a smaller and wider mandibular ramus respectively. SW1 scores are highly correlated (r = 0.79). The second singular warp (14.14%) contrasts a less deflected with a steeper upwardly rotated premaxilla associated with a lower and a higher coronoid process respectively. SW2 scores are highly correlated (r = 0.82).

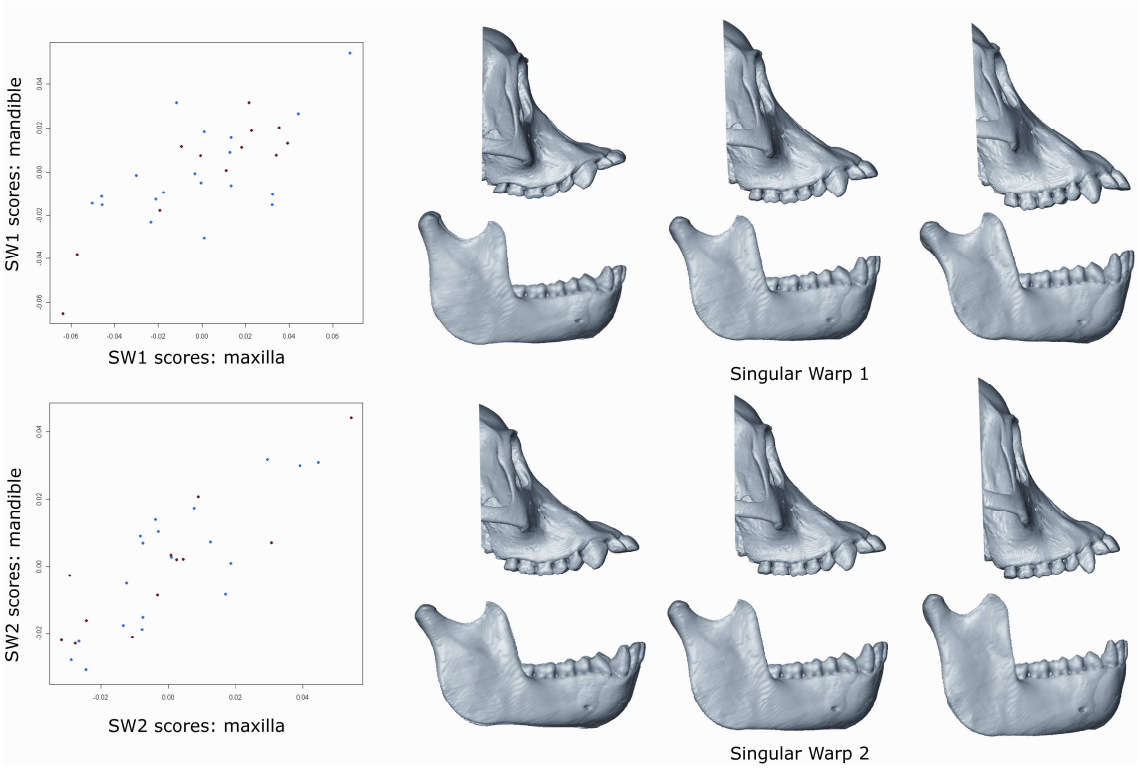

Figure 63 Pongo. SW scores of the two coordinate blocks plotted against each other (left). SW1 (top) and SW2 (bottom). Visualizing the shape dimensions associated with the plotted scores ()

The first singular warp (21.30%) contrasts a dorsally deflected with a ventrally rotated maxilla associated with an orthogonal and obtuse ramal angle respectively. Correlation of SW1 scores r = 0.71. The second singular warp (14.39%) contrasts an elongated maxilla with a shorter middle face associated with a lower and higher ramus respectively. SW2 scores are highly correlated (r = 0.83).

CHAPTER 5: DISCUSSION

5. DISCUSSION

5.1. Virtual reconstructions

Some forms need to be reconstructed before analyzing and visualizing the gross morphology. Using a virtual approach instead of reconstructing the real specimen has a number of advantages, foremost the introduction of guidelines that make the reconstruction reproducible. Any reconstruction can be regarded as solving a 3d jigsaw puzzle including a variety of decisions, and thereby potentially introducing various failures and subjective influences. Every reconstruction will only be an approximation of the original state, showing a level of uncertainty that is influenced by its preservation status and the amount of missing data (Weber and Bookstein, 2011). The following sections will discuss the outcome of the various reconstruction scenarios that were part of my thesis.

5.1.1. Reconstruction of fossils

Applying the toolkit of Virtual Anthropology and Geometric Morphometric several part of the *Australopithecus afarensis* specimen A.L. 444-2 and the endocast of Cioclovina were reconstructed. The following sections use methods that are part of the standard procedure during virtual reconstruction, others were developed to solve problems that come along with large missing areas.

One important advantage in using virtual methods to reassemble fossil fragments and estimate missing data is that the precious original specimen is not jeopardized by physical attempts to glue together parts or to substitute missing parts with plaster (Weber and Bookstein, 2011). If original fossil fragments are already glued together, as it is the case for the A.L. 444-2 posterior calvaria, a virtual approach allows the separation of the single parts without harming the fossilized bone. Furthermore, virtual representations of fossil remains can be inspected by employing visualization tools like color gradients (**Figure 2**). Such color-coding can provide additional information about preservation and morphology by visually identifying localized distortions, e.g., breaks and dents (Gunz et al., 2009b). It also helps during the identification of superficial anatomical structures like temporal lines, crests, or sulci. Another visualization tool that is helpful during the visualization of volume data is volume texturing (see **Figure 4**). While the visualization of surfaces can disguise internal

structures, using volume texturing it is possible to reveal differences in bone density which is of help during the identification of cracks or sutures.

5.1.1.1. Mirror-imaging: the frontal bone of A.L. 444-2

In primates, the frontal bone consists of two parts - the squama frontalis, corresponding to the region of the forehead, and an orbital portion, which contributes to the formation of the roofs of the orbital and nasal cavities. The internal surface of the squama frontalis of the frontal bone is concave and shows a vertical groove, the sagittal sulcus, in the midline. The edges unite inferiorly and form a ridge, the frontal crest. The sagittal sulcus lodges the superior sagittal sinus, while its margins and the crest provide attachments to the falx cerebri.

Morphological information represented by the *crista frontalis* and bregma were used to estimate a best-fit midline. Using this plane, the better preserved left frontal side was mirrored in order to restore bilateral symmetry. Doing so, the anterosuperior fragment of the right parietal is omitted. Since this fragment was flattened and plastically deformed and much of its endocranial surface is destroyed, this is regarded as acceptable and negligible for potential subsequent steps. By restoring bilateral symmetry I corrected for the plastic deformation that has affected the right side of the specimen through superomedial rotation of the supraorbital region and adjacent temporal surface. The frontal squama that was elevated on the right side is now in one plane with the right portion of the frontal.

Though this rather straightforward reconstruction is a good example for the advantages of virtual reconstruction methods, it also demonstrates the limits that are given for any reconstruction. Since the glabellar region is significantly damaged, morphological information about the supraglabellar region in this specimen remains inaccesible. Moreover, the cortical bone has been abraided from most surfaces, both internally and externally, reducing thickness by 0.5–1.0 mm (Kimbel et al., 2004). Estimating bone thickness without a precise knowledge of intraspecific variation within *Australopithecus afarensis* renders any effort foredoomed.

5.1.1.2. Reflected relabelling: the posterior calvarium of A.L. 444-2

The posterior calvarium in A.L. 444-2 comprises the occipital squama and both temporal bones. Most of the squamous part and the right pars lateralis are preserved in the occipital bone and a short segment of the foramen magnum margin just anterior to opisthion is present bilaterally. While opisthion itself is missing, about 6.0 mm on the left and 10.5 mm on the right foramen magnum margin are present (Kimbel et al., 2004). Both temporals were originally glued to the occipital at the height of the occipitomastoid suture. According to Kimbel et al. (2004) both temporals articulate with the occipital. Because a thorough inspection of the volume data revealed no artificial shift in the areas where the fragments were glued together no attempt was undertaken in the reconstruction to separate the temporals from the occipital. The two halves of the occipital are originally broken along a sagittally oriented fault that approximates the midline. Both parts were compressed toward the midline during taphonomy, resulting in an overlapping of the nuchal plane. Kimbel et al. (2004) separated and reattached the occipital fragments along this break in their "proper position", which still left a vertical offset of 2 to 3 mm in the nuchal plane in their reconstruction. When superimposing the both halves by mirror imaging of the left occipital fragment it becomes obvious that the right occipital fragment is elevated compared to its counterpart. Even if part of this deviation is an artefact of the GPA (because there is no medial landmark that could restrict the superimposition medially) one has to take a pronounced deformation of the nuchal plane into account.

To correct the vertical offset in the nuchal plane, bilateral symmetry was restored by reflected relabelling. Several steps included the digitization of landmarks, reflected relabelling, computation of the best-fit midsag plane, and mirror imaging to produce a symmetrized posterior calvaria. Comparing the maximum bizygomatic breadth of the symmetrized posterior calvaria (167.15mm) with the value that is given by Kimbel et al. (2004; p.65) for their reconstruction (167.00mm), it is remarkable that the values are very similar. In **Figure 25b** the symmetrized posterior calvaria and the reconstruction from Kimbel et al. (2004) are superimposed according to the right half. In the symmetrized reconstruction the petrous portions of the temporal bone are medio-laterally closer than in the original reconstruction which would theoretically lead to a decreased maximum bizygomatic breadth. There are several explanations for the more or less identical values in the two different reconstructions: (1) the deviation of the estimated midplane from a "perfect" midplane in the virtual reconstruction is high, thus creating an artificially narrow or broad (depending on the

direction of the deviation) anterior aspect of the posterior calvaria at the zygomatic root in the temporal. (2) Both zygomatic processes are broken at their roots, and the left zygomatic process is plastically deformed. If Kimbel at al. (2004) joined the left zygomatic process in a way that the root is artificially placed medially, a similar maximum bizygomatic breadth compared to the symmetrized reconstruction could result.

The main assumption of this procedure involves bilateral symmetry, thus the resulting form is symmetrized whereas the original cranium shows directional asymmetry in the nuchal crest. Omitting this information could be a major problem when investigating head posture and locomotion, but would not affect an inspection of gross morphology when joining the single fragments to an overall craniofacial reconstruction. This example contrasts the dilemma in virtual reconstruction – on the one hand incorporating as much information as possible from the specimen to be reconstructed and on the other hand restoring its morphology and thereby potentially omitting important individual characteristics. However, the advantage of this approach is that it can be applied in cases where traditional approaches would fail due to the complex reconstruction protocol. On the other hand each of these steps involves an uncertainty of estimation itself and the sum of this uncertainty can lead to an error propagation concerning the whole reconstruction. A solution to this approach is producing several reconstructions, each one basing on different assumptions and approaches. While this may be possible for some incomplete specimen, the preservation of other cases may prevent the realization of this premise.

5.1.1.3. Object manipulation in three dimensions: the mandible of A.L. 444-2

Working in a virtual environment has more advantages than just protecting the original fossil remains. Using the traditional approach, the reconstruction is exposed to gravity. This affects the process of reassembling the fragments but also the drying in case clue or plaster is used. Hence, the position of the placed fragments can change during reconstruction. Another disadvantage is that is more or less impossible to keep the minutes, including the precise measure of object translation and rotation.

The mandibular corpus of A.L. 444-2 is broken along a line running from the left second incisor/canine interdental septum diagonally to the base below the right canine. To restore the fragments´ integrity, several steps of manual alignment were carried out. The reconstruction protocol comprises the alignment of the second and third molar, the rotation of the outer ramal part, using a reference tooth row outline using A.L. 400-1, manual alignment

of the labial flake, and reestablishment of the continuity of the mylohyoid line. Even though each step is based on certain assumptions (continuity of curvature and muscle attachments or occlusion), several uncertainties are introduced. Therefore the reconstructed semi-mandible is only one of several possible solutions. However, the published reconstruction protocol of this specimen reads as follows: “The gap between the posterior two fragments of the right mandible corpus was eliminated on a cast by detaching the displaced posterior piece and properly realigning it with the more anterior segment along the fracture line. This eliminated the artificial gap between the M1 and M2 positions” (Kimbel et al., 2004; page 19). While the virtual reconstruction introduced here is still far from being perfect, it exceeds former attempts in formalizing a reconstruction protocol that can be verified or falsified by other scientists. This is of major interest when the reconstruction is employed in subsequent analysis, e.g. for the investigation of facial height or prognathism.

5.1.1.4. Beyond mirror imaging: the maxilla of A.L. 444-2

The maxilla was recovered in three primary pieces: the entire right half, the left half anterior to the M2 position, and the alveolar bone and parts of the maxillary sinus walls. It is characterized by plastic deformation and a major crack that runs anterior-posteriorly. Although the left portion is more complete, it is less well preserved than the right. The palatal roof shows an elevation of the two sides of the palatal roof along an artificial step in the midline. Section 4.1.1.4 provides the reconstruction protocol that included several steps including mirror-imaging using the midplane of a complete reference specimen (A.L. 200-1) and geometric reconstruction. The reconstruction in this case required a combination of the introduced methods: object manipulation (placement of the molar), anatomical reconstruction using the midplane of a complete reference specimen, and geometric reconstruction for the estimation of missing data. Because of the combination of these factors, the uncertainty in any reconstruction will be high, even though only one reconstruction is presented in this thesis. This combination will lead to an error propagation over the whole reconstruction, but the effects of the propagation of uncertainty is hardly investigated and a potential source of future work.

5.1.1.5. Geometric reconstruction: the endocranial cavity of Cioclovina

Using tools of Virtual Anthropology, it is possible to access information that would otherwise remain inaccessible without destroying the specimens under consideration. The visualization of internal structures using volume data became common use in medical imaging and offers an invaluable tool in the investigation of fossil remains. One example for the application of modern visualization methods in anthroplogy is the segmentation of virtual endocasts. They can provide evidence on size and shape characteristics, blood supply trajectories and neurological features of the brain, allowing comparative analyses crucial to our understanding of human brain evolution. Neubauer et al. (2004) reconstructed the endocranium of MLD 37/38, an incomplete but well-preserved *Australopithecus africanus* cranium. Using the segmentation methods and geometric reconstruction, the authors were able to estimate the total endocranial volume of this specimen and described endocranial morphological details that were physically inaccessible before.

Using a referenced based geometric reconstruction, I reconstructed the endocast of the Cioclovina Upper Paleolithic calvarium, one of the earliest reliably dated European modern human fossils. The missing area incorporates large parts of the cranial base, preventing a reliable estimation of endocranial volume. The estimation of the total endocranial volume for the Cioclovina endocast was based on a virtual reconstruction using a modern human cranium as reference, yielding a total volume of Cioclovina of approximately 1498.53 cc. This is only one of several examples that illustrates the advantage of working with digital representations in the form of volume data. Another example is the volume rendering of the inner ear to visualize, e.g. using high-resolution magnetic resonance data, clinically suspected inner ear abnormalities in patients (Klingenbiel et al. 2002).

5.1.2. Beyond mirror imaging

During cranial reconstruction, mirror imaging exploits information about bilateral symmetry of the skull. In this study we compared cranial reconstructions for cases in which the midsagittal plane was partly preserved (thus mirroring could be directly applied, KI-1), to cases where midsagittal planes were not available and had to be estimated from a reference sample (KI-2).

The second simulation showed a larger variability than the first one. However, it is worth noting that the grand mean shape of the reference sample produces results that are very similar to the original individual for both simulations, with an average error less than 3mm

(Table 3, 5). Furthermore, we found no differences between reconstructions using the male or the female mean. Therefore, we conclude that the grand mean can be regarded as a good resource for reconstructions in cases where mirror imaging can not be applied immediately.

As in every reconstruction process, we have to accept that we can never achieve a truly accurate craniofacial reconstruction. Any reconstruction is an approximation towards the original because missing data has to be estimated using assumptions and information derived from other individuals or samples. One such assumption in the process, symmetry, neglects information about asymmetry in the individual. Other small-scale characteristics of the facial skeleton, for example the form of the nasal bones, that for example could influence the biomechanics of the model or help in the identification of the remains of a victim, are omitted as well. On the other hand, this approach provides a reproducible method to reconstruct the entire cranium when the midsagittal plane is missing, a major advantage that was not existing using traditional manual approaches. As shown in **Figures 37** and **41**, the overall deviation from the original specimen to the reconstructed one in the middle and upper face is rather moderate. The highest deviation always appeared at the apex of the cranium (thus in the region farthest from the preserved parts in the experiments). In forensic cases this might be of less importance (the individual hair style in a reconstruction will mask this region in many cases) but has to be considered in other applications.

Human craniofacial shape ranges from dolicocephaly (long, narrow head form) with a leptoprosopic (long, narrow, protrusive) face to brachycephaly (wide, short globular head forms) with a euryprosopic (broad, flat, less protrusive facial form) face (Bastir and Rosas, 2005). The results confirm Enlow's (1990) hypothesis that males tend to represent the dolicocephalic head form, where females exhibit a more brachycephalic cranial form. We investigated patterns of normal phenotypic variability in the sample in order to evaluate which reference individuals produce reconstructions that are geometrically closest to the original individual. Visualizing form changes within the original sample as well as in both reconstruction samples, we can see that templates which resemble the knockout individual in general viscerocranial form (either long and narrow or broad and flat) yield better results than reference individuals that are of the opposite head form. But, since there is a continuous phenotypic transition between the extremes, only a general conclusion can be drawn from the results. Analyzing covariation patterns between neurocranial and facial shape or between single craniofacial characters could help to determine which cranial features accompany others (Bastir and Rosas, 2005; Mitteroecker and Bookstein, 2008a).

A shortcoming of this approach is that there is no definitive a-priori choice of the template to be used. Individuals that have the lowest Procrustes distance when comparing only a small part of the face (the part that is preserved in the knock-out individual) are finally not closest to the original individual after the reconstruction.

I apply Procrustes mean shapes of females and males, on the one hand to take sexual differences into account and on the other hand to circumvent population biases. Differences between male and female skulls become discernible at puberty when male skulls develop features that reflect sites of increased muscle attachment, whereas female skulls tend to retain more gracile features, though inter-population differences make general descriptions complicated (Acsadi and Nemeskeri, 1970; Ferenbach et al., 1980; Buikstra and Ubelaker, 1994). Therefore, the outcome of every reconstruction will be influenced by the sex of the chosen template. We showed that using a template that is of the same sex as the individual to be reconstructed does not provide better results than the grand mean shape in the sample. This may be due to the fact that the sample comprises individuals of various origins. Since patterns of sexual dimorphism vary between human populations, pooling the specimens of the same sex in the sample may have deleted population affinities. During the reconstruction process it is therefore preferable to employ a reference sample of the same origin and sex. Nevertheless, in cases where the sex cannot be determined, the grand mean shape is a good starting point for reconstruction. In general, the more information about the individual is available, the higher is the probability for an accurate reconstruction, even though it will represent only an approximation of the actual cranial anatomy. A geometric morphometric approach for the classification of crania for forensic scientists is the program 3D – ID (Slice and Ross, 2009). It aims to aid in the assessment of the sex and/or ancestral affiliation of unknown cranial remains and could be a helpful first step in the reconstruction process, since it also accounts for missing data.

I investigated facial asymmetry because it is well known that neither skulls nor faces are perfectly symmetric (Klingenberg et al., 2002; Willmore et al., 2005; Schaefer et al., 2006). However, we found no correlation between asymmetry and accuracy of the reconstruction: asymmetric crania provide RMS as high or low as more symmetric individuals. Nevertheless, some further considerations are required. First, no mirroring approach can perfectly reconstruct the original cranium since asymmetry will be omitted. Secondly, a technical problem arises using a midsagittal plane defined by a limited number of midsagittal points. The resulting reconstruction will be directly affected by the deviation of this plane to a hypothetical perfect midsagittal plane. This will consequently produce an

artificially narrow or broad face, depending on the dimension of the deviation. The resulting mirror image for KI-1 stresses this conclusion. Mirror imaging the right side using the midsagittal plane of only inferiorly situated landmarks does not yield satisfactory results (RMS of about 2.52mm for MD-MIRROR; Table 3). Even if more superiorly situated landmarks can be incorporated in the computation of the midsagittal plane, intrinsic asymmetry cannot be overcome. The midsagittal plane of an asymmetric individual will always be shifted around the x- and/or y-axis. This shortcoming becomes even more obvious for the second simulation. The error of mirroring is magnified by superimposing individuals only according to the anatomical landmarks that are available in KI-2. The asymmetry of the reference individual is added to the asymmetry of KI-2, which can result in reconstructions that are artificially narrow or broad. In spite of all these limitations, some combinations yielded results that are comparable to the outcomes obtained using the individuals' own mirroring plane. But since asymmetry is not the only factor influencing the outcome of the reconstruction since also the form of the reference plays an important role, individuals that show a comparable low level of asymmetry than the grand mean do not necessarily produce reconstructions of high accuracy. Generally, the Procrustes mean shape is less asymmetric than any individual in the sample and therefore asymmetry as a source of error is reduced, allowing for similar results in both simulations.

Uncertainties in the reconstruction due to the references´ asymmetry could be decreased by including an existing mandible into the reconstruction process. The bicondylar breadth of the jaw could be employed as a guide as to how far apart the temporomandibular joints should be positioned relative to each other. Also the orientation of the mirrored model could be verified in this way, overcoming even the problems that are imposed by a midsagittal mirror plane that is affected by asymmetry. Furthermore, even the midsagittal plane of the mandible itself could be used to correct for deviations of the cranial midsagittal plane, as far as it is possible to align the mandible with the cranial remains, *i.e.* by centric occlusion of the upper and lower dentition. The interactions between asymmetry of the reference used during the reconstruction and the resulting asymmetry of the reconstruction needs to be approached in future studies.

Most hominin cranial fossils are incomplete, whereas many conventional analyses of gross morphology require that specimens be complete. We introduce a new combination of tools from Virtual Anthropology and geometric morphometric methods (GMM) for the reconstruction of severely damaged crania in which the midsagittal cranial plane was no longer available. In such cases, a three-dimensional reconstruction applying a traditional

manual approach would be almost impossible to apply. Even if the variability of these reconstructions is larger compared with those obtained using the original midsagittal plane, we have shown that the Procrustes mean shape of both simulations provide similar results in terms of accuracy. Using the Procrustes mean shape of the reference sample is therefore a good resource for the entire reconstruction of the cranium, circumventing negative effects introduced by the asymmetry of a single reference specimen. Finally, we emphasize that the methods introduced here for cranial reconstruction could find potential applications the reconstruction of any bilateral

5.1.3. Virtual reconstruction in surgery

Function and aesthetic restoration are the basic goals of cranio-maxillofacial reconstruction (Schmelzeisen et al., 2004; Kokemueller et al., 2008). As mentioned by some researches that deal with attractiveness (Komori et al., 2009b, 2009a) and in regard to the general idea followed by the surgeons, the restoration of a symmetric shape could improve the outward appearance and hence provide a remarkable contribution to the quality of life. It is also obvious that functional restoration does not depend on this assumption, because it is possible to restore functionality without following strict symmetric intentions. Aesthetic, to the contrary, is to some point associated to symmetry. I am aware that human craniofacial anatomy is characterized by a certain degree of asymmetry (both skeletal and soft tissue). More precisely, there is a high degree of inter-individual variation. This concept is fundamental for reconstruction purposes.

In general, I have verified that the mirroring tool is not always the correct solution for zygomatic bone reconstruction, and more precise outcomes are provided either by a registration of the mirrored unaffected hemiface on the affected hemiface or by TPS warping of the mirrored cranium on the original one. There is not one solution for bone reconstruction, so that the more reliable outcome depends on the specific case under study. In fact, as shown above, individual H15 (**Figure 44**) is a typical example in which the midsagittal plane can be fairly well determined and the unaffected hemiface could be directly used as a reference for replacing the defect of the affected side. However, as shown in **Figure 45c,d**, a preliminary alignment between the two models is suggested before isolating the replacement segment in order to deal with potential errors produced during mirroring the model due to the imperfect position of the midsagittal plane.

In the second example (individual H14), the degree of asymmetry was larger, and the mirroring tool failed to provide a reliable solution for reconstruction. This was evident during

the definition of the midsagittal plane due to the deviation of the 8 anatomical “midsagittal” landmarks from the best fitting plane, and was confirmed in the surface deviation analysis. Even if the effects of an incorrect mirroring procedure could be reduced by carrying out an alignment between the two models, the result is still unsatisfactory. Accordingly, restoring symmetry is not a suitable solution because not only the virtual osteotomized part was asymmetric, but also the surrounding regions displayed a fair amount of asymmetry. Restoring, or better, creating symmetry would required a more virtual invasive surgery that must also remove these surrounding regions.

In order to restore function and deal with aesthetic appearance on the one hand, but also limiting the surgery to the defected areas without involving the unaffected bones, a reliable alternative could be the thin plate spline (TPS) warping. In all the virtual simulations, the models reconstructed by TPS functions displayed small mean deviation and reduced SD with respect to the original osteotomized model and an adequate continuity with the original surrounding bone (**Figure 45e,f**).

The approach based on TPS interpolation functions was for example used in paleoanthropology for fossil reconstruction (Gunz et al., 2005b), in forensic anthropology for the reconstruction of a fragmented skull (Benazzi et al., 2009b) and was recently employed in physical anthropology for the virtual reconstruction of missing condyles (Benazzi et al., 2009a). Unlike the mirroring procedure, TPS interpolation functions warp the reference shape to the target shape based on a set of corresponding landmarks/semilandmarks. Since symmetry between the two hemifaces is not relevant, the reconstructed model will be somewhat asymmetric compared to the reference. The amount of asymmetry depends both on morphometric features of the target shape, and on the size of the area that has to be reconstructed. Whereas the former is obvious (the more asymmetric is the target shape, the more asymmetric the reconstruction will be), the latter point requires a further explanation. As mentioned above, TPS interpolation function was used to establish geometric homology between two sets of semilandmarks (reference and target) in order to estimate the position of the missing landmarks. The TPS functions bends the spline near existing landmarks, and the estimation of the missing data is best in the proximity of the preserved part, in which landmarks are supposed to be placed. Consequently, increasing the size of the osteotomy will reduce the probability to find anatomical landmarks useful to bend the spline in the vicinity of the missing data, then the TPS grid is almost square (Gunz et al., 2005b). In other words, the further the location of the estimated landmarks from the preserved surface, the closer they resemble the reference shape.

In the virtual reconstruction of the zygomatic segment, the area surrounding the osteotomy was marked by several landmarks onto which the TPS function bend the spline, allowing a fair prediction of the missing data. Accordingly, regarding the amount of surface deviation between the reconstruction and the original zygomatic bone (**Table 13**), by TPS interpolation functions the continuity between reconstruction and original bone near the resected area is correctly restored. Based on this information, if the osteotomy had involved wider portion of one hemiface so that less landmarks were preserved, the reconstruction using TPS function would have resembled the reference shape. Obviously, the approach based on TPS warping is more time consuming compared to the mirror-registered one, and the usefulness of the method requires a careful evaluation of the specific problem.

Finally, it is also worthwhile to emphasize that the method could be also useful if the defect is not limited to one hemiface, but involves more or less extensively both the hemifaces. As shown in Benazzi et al. (2009), an external reference shape, morphometrically similar to the face that has to be reconstructed, can be warped to the target shape. In order to deal with this scenario, a "virtual skull database" for selecting the best reference shape should be available. It is evident that the same limitations mentioned above still persist: the fewer landmarks are used to bend the spline near the missing data, the more the reconstruction will be similar to the reference shape.

By means of CAPP for surgical simulation, surgeons have the possibility to test different reconstruction approaches in a 3D virtual space that allows a precise visualization of the simulated outcome. The mirroring procedure is one of the possible alternatives useful in reconstruction, may not always be the optimum solution, i.e. when the hemifaces are considerably asymmetric. In this pilot study, either the mirror-registered approach or the thin plate spline (TPS) technique achieved better results, overcoming the primary limits of the mirroring approach.

Up to now the TPS technique was used for reconstruction in anthropology and paleoanthropology, where the limits of the mirroring approach are well known. Therefore, it is important to emphasize that TPS has the potential to become a valuable tool in cranio-maxillofacial surgery, providing improvement in the accuracy of bone reconstruction.

5.1.4. The choice of the reference

In this study I investigated in detail how the choice of the reference sample in thinplate spline based reconstructions influences the uncertainty in terms of reconstruction accuracy.

Although previous work has touched this topic (Gunz et al., 2009b; Neeser et al., 2009), a comprehensive description of effects resulting from the choice of reference, particularly if drawn from different species, was not yet available. Additionally, I introduced a potential way to guide the choice of the reference sample in interspecies reconstructions in terms of bending energy.

In contrast to Gunz et al. (2009), I focused on TPS based reconstructions that involve large cranial areas (~50% of the face and 30% of the neurocranium) instead of rather restricted anatomical regions such as the glabellar area. I described the resulting deviations in intraspecies (for: *Homo sapiens*, *Pan troglodytes*, *Pongo pygmaeus*) and interspecies (for: *H. sapiens, H. heidelbergensis, P. troglodytes*, *P. pygmaeus*, and *A. africanus*) reconstructions from each one specimen of five different species rather than focusing on a single specimen. This allowed the assessment of the arising uncertainty when employing the same species during reconstruction for the extant species, as well as the consequences of the choice of reference during interspecies reconstructions for all species. Compared to Neeser et al. (2009) missing data in the knock-out regions was represented by numerous landmarks and semi-landmarks rather than a single landmark. The inclusion of semilandmarks allowed the consideration of whole surface patches that would otherwise have remained unattended. I also avoided an arbitrary definition of missing areas by randomly knocking out landmarks because data in case of fragmented fossils might not be missing at random. For instance, delicate and thinner bones break more easily. From the plethora of potential cases where specific cranial areas are missing, I have chosen one concrete and difficult real scenario that includes both facial and neurocranial parts, i.e. the knockout scenario analogous to A.L. 444-2.

Not unexpectedly, using reference specimens of similar shape produced the highest accuracy, both for facial and neurocranial reconstructions. Surprisingly though, we observed that a reference sample of similar form does not necessarily yield the highest accuracy, e.g. reconstructing the alveolar process of *Pongo* using *Homo* as reference sample yields better results than employing *Pan*. However, missing data estimation in certain regions that represent derived characters of the species cannot be reconstructed reliably, e.g. the glabellar region in Petralona and Sts5. In contrast to Neeser et al. (2009) we found that TPS based reconstructions are quite well-suited to estimate missing data in large defects, both within species (e.g. *Pongo*) and between species (*Pan* and *Pongo*), for example in the parietal area where a maximum average RMS of less than 2mm occurred.

In the knockout configuration applied here, the resulting posterior variance in neurocranial reconstructions is lower than in the face. The better performance in neurocranial

(interspecies) reconstruction is due to the fact that the thin-plate spline is based on the smoothness properties of the area surrounding the region to reconstruct (cf. Gunz et al. 2009). The thin-plate spline is usually explained as a "smoothing" or "interpolation" function. Indeed it minimizes overall bending of the map in the class of all maps consistent with the given landmarks (Bookstein, 1991b). But variation in the relative position of any two closely spaced landmarks leads to large variations in the positions of estimated semilandmarks (Bookstein and Green, 1993). The effect can even be more dramatic if the spline is used to predict areas lying outside the convex hull of those landmarks used for the interpolation, or to put it to the extreme, if one tries to estimate landmarks on the maxilla when only occipital landmarks are present. However one may find the case that even "inside" a system of the knockout area, the spline will distort the estimated area (Bookstein, 1991b; Bookstein and Green, 1993). In the context of reconstruction, this effect will be present whenever there is considerable variation of curvature right at the edge of the simulated "knockout region". This effect was most obvious in the sphenoidal area owing to different degrees of postorbital constriction among species. The degree of constriction is comparable between *Pan*, *Pongo*, and perhaps also *Australopithecus africanus*, but it is significantly reduced in *Homo* which leads to an increased uncertainty of reconstruction in this area.

Reconstructing specimens of similar neurocranial shape, e.g. between *Pan* and *Pongo*, showed the lowest uncertainties. Reconstructing specimens of differing shape, e.g. the great apes (oval) and humans (globular), the lowest accuracies were observed. Furthermore, the homologous neurocranial area missing in *Homo* has a much larger area than in *Pan* or *Pongo*, an obvious effect of the size increase and globularisation of the human cranium. Therefore highest maximum average RMS could be found when *Homo* was reconstructed by *Pan* or *Pongo*. Because the endocranial capacity and neurocranial shape of the great apes is similar to Australopithecines, they are generally more qualified as a reference for a target of similar cranial shape such as Sts 5. *Pongo* and *Pan* are defined by cranial capacities less than 500 cc. Australopithecines have a capacity between 428 and 550 cc, while *H. sapiens* is defined by a capacity larger than 1100 cc (Strait et al., 1997; Aiello and Dean, 2002).

Splines in a missing region are bent according to the original shape of the reference, and according to the preserved morphology of the specimen under reconstruction (see e.g., the sphenoidal area). For example, the sagittal profile of Petralona is not much different in size but is quite differently shaped compared to *Homo* - it is much less globular, and thus the reconstruction is worse using *Homo* templates than *Pan* or *Pongo*. In the lateral missing area, however, the accuracy taking *Homo* as reference is higher, those from *Pan* and *Pongo* worse.

Another factor that is influencing neurocranial reconstructions is degree of postorbital constriction, which is influenced by the position of the orbits relative to the neurocranium, the expansion of the brain and the temporalis muscle. The degree of postorbital constriction of the cranium, defined by an index of minimum frontal breadth (posterior to the supraorbital torus) divided by maximum upper facial breadth (bi-frontomalare temporal), is comparable between *Pan* (0.70), *Pongo* (0.66) and *Australopithecus* (0.66). However, in *Homo* an absolutely reduced postorbital constriction with an index of 0.92 is observed, due primarily to expansion of the brain (see Cameron and Groves, 2004 for summary). The degree of postorbital constriction is correlated with the shape of the greater wings of the sphenoid, being more concave in species with a lower index. Since the greater wings of sphenoid are completely missing in this simulation, the estimated missing data in this region will to a certain point reflect the morphology of the reference. Reconstructing the great apes with *Homo*, a less concave temporal surface will be implemented in the reconstruction, together with a lesser degree of postorbital constriction. Reconstructing *Homo* with *Pan* or *Pongo*, the degree of postorbital constriction will be higher in the produced reconstruction. Generally, estimating missing data in the area of the alae majores performs better when reconstructing *Homo* with the great apes than vice versa. Since semilandmarks on the temporal face of the zygomatic are acting as an anterior anchorage, the TPS is guided in the lateral dimension.

One cannot expect any reference specimen from another taxon to deliver good results in all regions. Interspecies reconstructions are a compromise in response to a lack of alternatives. As mentioned, reconstructions in facial regions generally perform worse than in neurocranial regions. The facial topography with its locally dramatically changing curvature (e.g. in the nasal region) is much more complex. TPS in the face implements the morphology of the missing area from the reference sample into the target. If the specimen to be reconstructed and the reference specimens are similar in gross morphology with regard to facial shape (i.e. prognathic vs. orthognathic), the average maximum RMS for interspecies reconstructions are similar to reconstructions within the species, as shown for *Pan* and *Pongo*. Why, then, does reconstruction of great apes sometimes perform comparably well when taking *Homo* as a reference, e.g., in the superior alveolar and supraorbital area? In these experiments this is because both regions lie in the direct vicinity of preserved morphology. As introduced in **Figure 49**, the estimation of missing data naturally performs better at the edges than towards the center of the missing area. This effect of large reconstruction errors is obvious in the interorbital and nasal knockout regions, which were characterized by a complete lack of bone in their neighborhood. The distinct features of the human nasal

morphology add to the higher uncertainty, leading to maximum average RMS up to 8.20mm (Homo1 reconstructed by *Pan*) and 7.60mm (Homo1 reconstructed by *Pongo*). When reconstructing the great apes with the *Homo* sample, maximum average RMS was twice as high (19.98mm). In those cases a human-shaped nasal roof was introduced to the reconstructions, which renders missing data estimation in this region pointless. Furthermore, the interorbital breadth, defined by an index of mid-interorbital breadth divided by orbital height, of the reference is implemented in the specimens to reconstruct. The orbital cavities of the chimpanzee are more widely separated by the ethmoid bone than are those of the orangutan (Aiello and Dean, 2002). A narrow interorbital is observed in *Pongo* with a mean index of 0.32, *Pan* exhibits an intermediate condition with a mean index of 0.46, while Australopithecus has a mean of 0.63 (Cameron and Groves, 2004). *H. sapiens* has a mean index of 0.65, while Petralona has an extremely broad interorbital. Since this part of the facial skeleton is completely missing in this scenario, the interorbital breadth of the reconstruction is predetermined by the reference, introducing a narrow interorbital breadth when taking *Pongo* as reference and more widely separated orbital cavities when *Pan* or *Homo* is the reference. Additionally, medial orbital shape will be determined by the reference. Orbital shape is affected by numerous processes, including cranial base angulation (Shea, 1985, 1988), facial height and breadth considerations (Rak, 1983), and capsular requirements (Enlow and Hans, 1996). This feature is thus rather complex and considered to be of developmental, functional, and phylogenetic interest (Cameron and Groves, 2004). In *Pongo* orbits are higher than broad, while circular-rhomboid shaped orbits are observed in *Pan*, and all hominins preserving this feature (see Tobias, 1991; Wood, 1991; M.G. Leakey et al., 2001). Since in the knockout configuration the lateral orbital margin is available, a guide for the TPS is provided. The shape of the medial orbital margin, as well as the interorbital breadth is accordingly determined by the configuration of the reference employed. Finally the shape of the pyrifom aperture between the three species is different. While *Pongo* is characterized by an ovoid outline, the piriform aperture in *Pan* is rather rounded (Vogel, 1966). Consequently, estimating the shape of the nasal aperture in *Pongo* with the sample of *Pan* will introduce a rounded aperture in the reconstruction.

This confirms results by Gunz et al. (2009) which stated that “the posterior distribution of the reconstructions reflects the shape differences among the reference crania that served as the prior distribution used to impute the missing data” [p.56]. TPS reconstructions cannot be a perfect solution, but for scientific problems at the very largest spatial scales, their accuracy might be sufficient, for instance, when reconstructed specimens are incorporated in further

ontogenetic or phylogenetic studies (Gunz et al., 2009a; Gunz et al., 2009b; Gunz et al., 2010) or for visualization purposes (Kranioti et al., 2011). As **Figure 53** showed, the variation in reconstructions might prove smaller than any hypothetic intraspecies variation of the fossil specimens (if one assumes a similar range of variation as seen in the extant species). In the morphometric subspace of the first three PCs, those reconstructions have only a small posterior variance, i.e. the distribution of the reconstructions is smaller than intraspecies variation. But since this is the variance of the reconstruction for only a single specimen, one would have to add an additional matrix that is quite a bit larger, the matrix corresponding to (estimated) intraspecific covariance (as shown in **Figure 53** for *Homo*, *Pan*, and *Pongo*). In **Figure 53**, the variance due to choice of the reference specimens is very small because the distance function here, Procrustes distance, is not sensitive to restricted local changes like the introduction of a humanoid nasal roof in the reconstruction of the great apes. But other kinds of computation are based on other distance functions, which could be distorted in reference to the Procrustes distance. If those reconstructions would be used further, for instance in biomechanical analyses, it is possible that distributions of strain energy in the middle face would differ, in spite of being limited to only a small neighborhood in shape space. This is the main reason why the full posterior variance of those reconstructions has to accompany the image of those reconstructions, e.g. when exported for any further biomechanical computations like finite element analyses. I also argue that any use of a reconstruction later in the data flow of any scientific project needs to be accompanied by the maximum of the RMS differences, and also its geometrical representation (as a vector perpendicular to the surface), in order to convey the actual uncertainty of the hypothetical form claimed to have been reconstructed. Further analyses, e.g., modeling experiments are needed to obtain deeper insights about the effects of minor and major morphological changes in skull shape on the distribution of stress and strain (Weber et al., 2011).

Another interesting case with regard to the consequences of the reference choice is the reconstruction of the supraorbital region. *Pan troglodytes* exhibits a strong, barlike supraorbital torus separated from the frontal squama by a transverse depression identified as the sulcus supratoralis (Shea, 1988). Since the supraorbital torus is very weakly developed in orangutans, one would assume that a more or less pronounced torus is introduced when using a chimpanzee as reference. However, the non-missing semilandmarks that were situated anteriormost in Pan1 are projected on the supraorbital ridge of Pongo1 (**Figure 47**). Therefore the spline in this area is locally bent downward and the estimated missing landmark configuration in the supraorbital region does not show any sign of a sulcus supratoralis. In

contrast, when using *Pongo* as reference for the reconstruction of Pan1, the resulting reconstructions are missing a supraorbital torus and a frontal squama, thus showing a much higher deviation from the original specimens. The missing landmarks in the interorbital area maintain the same configuration as in the reference, both concerning the shape and the interlandmark distances. If also the superior portion of the supraorbital region would be missing, thus lacking a surface in the target to guide the TPS, a torus in the missing area would be introduced as well, since the local landmark configuration of the reference would be maintained. Since Sts 5 is characterized by the absence of this sulcus intervening between the frontal squama and the forward-jutting supraorbital element (Schwartz and Tattersall, 2002a), the highest accuracy is achieve in facial reconstruction using *Pongo* as it lacks a supraorbital torus as well. However, none of the references was able to reconstruct the bulging glabellar area of Sts 5 accurately, since none of the references has this trait. This also applies to the thick supraorbital tori in Petralona; all the reference species failed to reconstruct the morphology adequately, the *Homo* sample came closest. Another disadvantage, likewise inherent to every reconstruction process, is the inability to reconstruct individual characteristics and (syn)apomorphies of the craniofacial skeleton of the respective fossil in interspecies reconstructions. In this example, the form of the nasal bones or the thickness of the supraorbital tori, that characterizes the individual specimens are omitted. Nevertheless, I argue that the accuracy and precision of this approach reproduces the gross morphology adequately enough to include the reconstructed specimens in analyses of onto- and phylogeny.

These findings confirm prior considerations that morphological characteristics of the reference specimen(s) will be introduced into the reconstructions (Zollikofer and Ponce de Leon, 2005; Gunz et al., 2009b). But in which way? I could exemplify the degree to which anatomical characteristics of the reference are incorporated into the reconstruction (see **Figure 52**). Besides illustrating these relationships in a quantitative way, I could also show that a higher reconstruction accuracy (in terms of Procrustes distance from the original to the reconstruction) is associated with smaller bending energy values. This leads to an approach for choosing appropriate reference specimens for the species used in the sample. In the experiment described above, the bending energy and Procrustes distance show the highest correlations within the extant species ($r > 0.88$). Correlations for the fossil reconstructions are lower (r between 0.65 - 0.75). These results show that for the reconstruction of a fossil specimen it would of course be best to select specimens from the same species. As this is not possible in many cases due to the scarcity of material, I propose, at least for the fossil species that we incorporated in the sample (*Australopithecus africanus*, *Homo heidelbergensis*), to

choose from another species that shows the lowest average bending energy vis-a-vis the target (*P. troglodytes* as reference for *A. africanus, H. sapiens* for *H. heidelbergensis*). By estimating missing data in fossil specimens that have been virtually "damaged", we showed that the uncertainty of fossil reconstructions (in terms of the reconstruction accuracy) is in certain regions comparable to intraspecies reconstruction of extant specimens. This information and the high correlation between reconstruction accuracy and bending energy leads us to the recommendation to use a *Pan* sample for the reconstruction of Australopithecines, except for the glabellar area (should not be considered for interspecies reconstruction). Continuative studies are needed to explore if these recommendations also hold for other species. The goal is to establish a list of potential references for interspecies reconstruction. However, the disadvantage of this method is that it can only be verified if (almost) complete fossil specimens are available. Besides selecting the reference cautiously it is also important to incorporate as much morphological information from the specimen to be reconstructed as possible (individual form constraints; see Weber and Bookstein, 2011). The accuracy of estimation, especially when employing a reference sample from different species, depends on the number of missing coordinates, the geometry of the missing part, its variability in the reference population, and last but not least the point spacing and distribution of the coordinates on the non-missing parts. In this context the crucial resource is the presence of semilandmarks that cover the still existing morphology appropriately. I argue, in contradiction to Neeser et al. (2009) who stated that "morphological similarity appears to be of less importance than large reference-samples (p. 16)" that morphological similarity in terms of geometrical closeness is crucial for the choice of the reference sample, especially when using TPS as a reconstruction method. Considering the discussed constraints and guidelines, interspecies reconstruction is able to reconstruct the missing areas in some cases with only a small error, as shown for Sts 5.

5.2. Facial orientation and integration in the hominoid cranium

The following sections discuss the results obtained from the analyses concerning patterns of integration in the hominoid cranium and their potential relevance for virtual reconstructions.

5.2.1. Facial orientation and basicranial shape: an approach via rigid motions

The orientation of the facial skeleton, also described as facial kyphosis, has been investigated in a number of studies, starting with analyses of dissected primate crania by German anatomists (Hofer, 1952b; Kummer, 1952; Biegert, 1957; Vogel, 1966; Angst, 1967; Thenius, 1970). The aim of this study was to investigate 3D patterns of covariation between basicranial and orbital shape and midfacial position and orientation. The findings confirm observations of earlier authors that described the variation and overlap in midfacial orientation both within *Pan* and *Pongo* (Angst, 1967; Leslie, 2010). Considering the Procrustes fit on the basicranial landmarks only (**Figure 55a**), it is obvious that the orientation of the splanchnocranium relative to the neurocranium is different between *Pan* (klinorhynch) and *Pongo* (airorhynch). This confirms oberservation from Shea (1985) who hypothesized that the orangutan face primarily differs from *Pan* in its position relative to the braincase. In contrast to earlier studies, this is the first to statistically quantify patterns of morphological association. This new approach introduced here predicts the position and orientation of the midface according to the shape of the cranial base and upper face, thus providing essential information for the interpretation of hypotheses concerning facial orientation and integration. Finally, these findings may also be of use in reconstructions of fragmented specimens. Because the results provide estimations of uncertainty of palate orientation, i.e. the degree of freedom of its rigid motion, they deliver valuable information in the case these models are used in continuative studies, e.g. in biomechanics.

I showed that in contrast to *Pan*, variation in midfacial orientation in *Pongo* may not strictly follow the predictions proposed by the "facial block" (see below). This questions the hypothesis that anthropoids are characterized by stringent angular invariance between the back of the face and the top of the face, which is also the bottom of the anterior cranial base. In the last decade the cooperation of developmental genetics on experimental animals and morphometrics yielded deeper insights in the mechanisms of structural interactions in the craniofacial complex (López et al., 2008; Martínez-Abadías et al., 2011). The method introduced in this chapter may be of help in this synthesis by delivering a quantitative approach to analyze covariation patterns in the face and cranial base.

Studies of midfacial orientation usually focus on topographic relationships between the splanchnocranium and neurocranium. Traditional methods for the anaylsis of the orientation of the midface require the use of reference planes for registration. A variety of

reference planes have been used to assess spatial relationships among different components of the skull. Most studies on the external cranium employed the nasion-basion plane (e.g., Schultz, 1950, 1955; Vogel, 1966, 1968) while radiographic studies used the anterior cranial base/planum sphenoideum (e.g. Biegert, 1957; Angst, 1967), the cerebral surface of the posterior cranial base/basioccipital clivus (e.g., Biegert, 1957; Angst, 1967; Ross and Ravosa, 1993), the pharyngeal surface of the basioccipital (e.g., Hofer, 1952; Biegert, 1957; Angst, 1967), the Frankfurt horizontal (e.g., Ashton, 1957; Biegert, 1957; Suwa, 1981), or the vestibular horizontal (Delattre and Fenart, 1956). Leslie (2011) used multiple reference planes to potentially strengthen the assessment of facial orientation by providing multiple lines of support. But the use of multiple reference planes potentially obscures signals when there is variation in the orientation of the reference planes relative to each other, e.g. between the clivus and anterior cranial base.

Investigating 3D patterns of covariation between basicranial and orbital shape and midfacial position and orientation on the other hand overcomes most of the above mentioned problems in the study of integration pattern in the craniofacial complex. Morphological integration in a general sense refers to the connections or relationships among morphological elements. While functional integration describes interactions among components that affect an organism´s performance, developmental integration (both genetic and epigenetic) describes interactions of compartments during growth and development. The combination of genetic and epigenetic integration permits modules to fit and work together during ontogeny (Lieberman, 2011). Since genes vary in populations, genetic integration leads to evolutionary integration, the coordinated evolution of morphological traits (Cheverud, 1996). In analyses pooling all the adult specimens of the two species, most of the variation and covariation is due to the mean species differences. Accordingly, the first dimensions of PLS describes evolutionary integration - how the face and the cranial base covary across the species means (Mitteroecker and Bookstein, 2008a). Differences of integration among *Pan* and *Pongo* can be identified in plots of the SW scores for midfacial orientation against those for the cranial base (and orbits). **Figure 56** shows these plots for the two different Procrustes superimposition set-ups that were used. If developmental and evolutionary integration were identical, all specimens would lie close to a straight line in the plots. According to **Figure 56a**, basicranial shape versus midfacial orientation, *Pan* and *Pongo* do not share a common pattern of integration. Moreover, the degree of integration in *Pongo* is much lower compared to *Pan*. Including the orbits in the Procrustes fit, the pattern of integration is similar between the species, the trajectories are parallel. In both species, individuals with an upwardly rotated

palate show a decrease in relative orbit height. In contrast, individuals with a downwardly rotated palate have a relative orbit height that is increased. However the results from the pooled PLS have to be treated with caution. Since the supraorbital morphology between the two species is differing, the superimposition including the orbits "rotates" the chimpanzee maxillae dorsally since the supraorbital torus in *Pan* projects anteriorly compared to *Pongo* (see **Figure 55a**). This increases the variation in the superimposed basicranial landmarks, influencing the outcome of the analysis in the pooled sample. The difference in the superimposition manifests itself in the palatal angles that express the orientation of each specimens´ palate in relation to the mean palatal angle of both species. Variation in the first superimposition set-up (only basicranial landmarks are superimposed) is much higher than in the superimposition that includes the cranial base and the orbits.

Integration in the skull is manifested both developmentally and functionally. At a simple, structural level, integration is evident from shared walls and spaces. Changes to the form or function of any component of the skull will affect the form and function of others (Lieberman, 2011). We investigate patterns of functional integration separately within each species, because in the pooled sample intraspecific differences may be blurred. However, one has to be careful when interpreting differences in integration patterns between based on separate PLS analyses. The results indicate a moderate integration among the shape of the cranial base and the relative position of the middle face in *Pan* and *Pongo*. But when including the orbits, we found a tight morphological integration between basicranium, upper face, and facial orientation that is evident in the high correlations (0.8) between the singular warp scores. A significant correlation of palate and orbit orientation across all primates was already reported by Ravosa (1991): "… as the anterior aspect of the palate becomes more dorsally rotated relative to the cranial base (airorhynchy), there is a corresponding dorsal rotation of the orbital aperture and axis". We found that both orbit orientation *and* shape covary with midfacial orientation. **Figure 58** shows for both species that individuals with an upward rotated palate show a decreased relative orbit height (round orbital aperture) and a clockwise rotated superior orbital aperture. In contrast, klinorhynch individuals have a relative orbit height that is increased (elliptical orbital shape) and an anticlockwise rotation of the superior orbital aperture. This integrational pattern was not only found to be tight, but was also shared between chimpanzees and orangutans (as shown in the pooled PLS). Differences in orbit orientation were also observed for SW2 in *Pongo*, individuals with a more anteriorly placed maxilla showing inclined orbits. SW2 represents allometric changes associated with basicranial length and the anterior-posterior position of the midface in *Pongo*. Smaller

individuals show an anteriorly-posteriorly shortened cranial base that is covarying with a posterior translation of the midface. Males tend to cluster on the positive scale of singular warp 2, showing a longer cranial base and a maxillary centroid that is anteriorly placed. Lieberman (2008) already showed that relatively larger faces are associated with more extended cranial bases. But concerning midfacial orientation, we only found a moderate correlation between palate orientation and facial Centroid Size ($p<0.5$) in both species (allometric model; Ravosa, 1991).

This analysis investigates spatial and structural relationships between orbit and midfacial orientation and is thus able to yield information concerning hypotheses about a (indirect) influence on palate orientation through the integration of palate and orbits (Ravosa, 1988; Ravosa & Shea, 1994). But I did not investigate the integration of the palate within the maxilla which, as hypothesized by several authors are part of an integrated unit denoted as the "facial block" (Weidenreich, 1941; Delattre and Fenart, 1956; Moss and Young, 1960; Biegert, 1963; McCarthy and Lieberman, 2001). Likewise it is unknown and untested whether many of the craniofacial differences between the African and Asian great apes, including torus morphology, frontal sinus development and nasal floor topography are structurally correlated with variation in facial orientation across the taxa as many authors claimed (Shea, 1985; Brown and Ward, 1988; Shea, 1988). Furthermore, Biegert (1957) suggested a number of functional correlates of facial orientation (i.e., dietary specializations and enlarged laryngeal sacs). For orangutans Biegert (1963) noted the extreme development of the laryngeal sacs and hypothesized that this divergent skull topography of *Pongo*, compared with *Pan* and *Gorilla*, is determined almost completely by this evolutionary specialization of the laryngeal sacs.

Variation in primate facial orientation also has been proposed to be correlated with variation in the angulation of the cranial base (Biegert, 1963; Enlow and Azuma, 1975; Sirianni and Swindler, 1979; Enlow, 1990; Ross and Ravosa, 1993). Singular warps 1 for *Pongo* do not show any basicranial shape change that could be attributed to a change in the relative orientation of the pre- and post-sellar segments relative to one another. Interestingly however, the inflation of the sphenoid body could potentially fake a correlation between the angular relationship of the clivus and the planum sphenoideum and midfacial orientation when applying traditional morphometric methods using angles (Ross and Ravosa, 1993).

Several comparative investigations were testing associations among various factors including relative brain size, cranial base flexion, supraorbital structures, orbital orientation, and midfacial orientation among primates (Ross and Ravosa, 1993; Ross and Henneberg,

1995; Lieberman et al., 2000a). Ross and Ravosa (1993) reported a significant positive correlation between increasing ventral deflection of the palate and increasing brain size relative to basicranial length across primates and across the haplorhines. However, no correlation between these variables was found within the non-human hominoids, within modern and archaic humans, or within the catarrhines (Ross and Ravosa, 1993; Ross and Henneberg, 1995). Ross and Ravosa (1993) furthermore suggested that the significant correlations observed in their bivariate comparisons between palate orientation and cranial base angulation are merely due to palate orientation tracking orbital axis orientation. We did not quantify orbital axis orientation but found that the prediction of midfacial orientation is high using orbit shape exclusively (0.7 for *Pan*, 0.64 for *Pongo*; **Table 18**). Adding information of the cranial base improves the prediction only slightly (0.75 for *Pan*, 0.71 for *Pongo*). This is an argument for the hypothesis that midfacial shape is only indirectly, or secondarily, affected by the shape of the anterior cranial base and that palate and orbits are tightly integrated.

Even though we found a shared pattern in both species - a dorsally deflected palate covaries with an inflation of the posterior sphenoid body and a decrease in relative orbit height - several differences in covariation patterns among the species were observed. In *Pongo*, a dorsal deflection of the palate covaries with an *inferior* displacement of the anterior border of the temporal surface of the greater wings of the sphenoid bone and a *superior* displacement of the anterior border of the cribriform plate. In contrast, a more dorsally oriented palate in chimpanzees covaries with an anterior displacement of both the anterior border of the temporal surface of the greater wings of sphenoid bone and anterior border of the cribriform plate (**Figure 58**). These findings do not support results from McCarthy and Lieberman (2001) who hypothesized that the top and back of the face appear to form an integrated unit ("facial block") in anthropoids (see Lieberman et al. 2000 for summary). The notion of the "facial block" predicts that as the anterior cranial base flexes relative to the posterior cranial base, the posterior maxillary plane (PM plane; describes the back of the face) flexes accordingly, rotating the posterior and upper portions of the face underneath the anterior cranial fossa (klinorhynchy). In contrast, extension of the anterior cranial base will rotate the posterior and upper portions of the face dorsally (airorhynchy). In *Pongo* we found that a ventrally rotated (more flexed relative to the posterior cranial base) anterior cranial base covaries with airorhynchy (and a ventrally rotated orbit). According to the prediction of the "facial block" hypothesis a more flexed anterior cranial base should covary with

klinorhynchy. Though this is true for *Pan*, the results show that for *Pongo* the hypothesis of the “facial block” does not hold.

Montagu (1943) described orangutans as having a uniquely shortened ethmoid and cribriform plate compared to the other apes and hypothesized that the observed fronto-nasal-ethmoidal stenosis in *Pongo* resulted in the ethmoid complex being pushed downwards and backwards. Based on Montagu´s (1943) observations, Shea (1985) stated that the orientation of the cribriform plate in *Pan* is steeper than in *Pongo*, and hypothesized that this structural difference may account for the airorhynchy of orangutans. The results show that cribriform plate and midfacial orientation are covarying, though the pattern of integration is different between *Pan* and *Pongo* (**Figure 58**). A more dorsal orientation of the palate in *Pongo* covaries with an *inferior* position of the anterior edge of the cribriform plate. In *Pan*, a dorsally deflected palate covaries with a more *superior* position of the anterior cribriform plate.

The tight morphological integration between basicranial and orbit shape and midfacial orientation is evident in the correlations (0.8) between the singular warp scores. These correlations can either be caused by direct individual interactions of the bones via synchondrosal and sutural growth (Ma and Lozanoff, 1996; Cendekiawan et al., 2010; Jimenez et al., 2012) or are spurious correlations because all bones are directly or indirectly affected by numerous factors like brain size and shape (Jeffery, 2003; López et al., 2008), and masticatory forces dependent on food properties (Hohl, 1983; Tang and Mao, 2006; Menegaz et al., 2010).

Synchondroses act as growth centers and are the last sites in the cranium to terminate growth. A premature or delayed ossification of the synchondroses can result in a shortening or lengthening of the base of the skull and thus to underdevelopment of the middle face or acromegaly respectively (Schumacher, 1997). The role of the cranial base in midfacial development has further been demonstrated in animal experimentation studies that indicate that normal development of the cranial base is necessary for establishing the position of the midface (Hoyte, 1991) and for normal palatal closure (Long et al., 1973; Brinkley and Vickerman, 1978; Kjaer, 1992). But facial orientation is a complex feature and is not likely to have a single input influencing its variation within and between species. One potential factor accounting for variation in midfacial orientation at an evolutionary scale may be based on length variations in tandemly repeated sequences that are hypothesized to be a major source of morphological variation (Fondon and Garner, 2004). In a comparative genomic study of repetitive elements in developmental genes of 92 breeds of dogs Fondon and Garner (2004)

found a moderate correlation between the degree of palate dorsiflexion and total allele length of Runx-2 which is involved in the differentiation of osteoblasts and influences craniofacial development. A similar mechanism could be responsible for the morphological change that was observed in a sample of St. Bernard dogs, younger breeds showing a tilting of the palate and upper jaw (Drake and Klingenberg, 2008). Generally, alterations in genetically controlled developmental processes play a major role in craniofacial development and in generating morphological variation. Martinez-Abadias et al. (2010) showed that mutations in the fibroblast growth factor receptor 2 (FGFR2) influence not only the coronal suture, which was already well-known for the Apert syndrome, but also facial sutures and bones of the face, e.g. the palate. Because of the difficulties that arise when quantifying the variation in midfacial orientation using traditional morphometrics, these results have to be treated with cautiousness. Nevertheless, they have the potential to offer new insights about the multifactorial inputs in facial shape variation.

Examining the findings in the light of the above described genetical inputs on craniofacial development complicates the discussion about modularity, a concept which has been used to address some of the most fundamental and interesting questions in morphological evolution, including evolvability and constraints on morphological variation, and the production of morphological diversity (Goswami, 2006; Goswami and Polly, 2010). Polanski and Franciscus (2006) hypothesized that a modularization or developmental ‘‘uncoupling’’ between the face and neurocranium theoretically could have permitted different extrinsic selective pressures (e.g. ecological variation, group composition, and subsistence energetics and behavior) to operate independently on both the face and the neurocranium in hominoids. Alternatively, natural selection may have operated primarily on only one of the modules, with the other responding passively as part of a coevolved set of ontogenetically and evolutionary interdependent or integrated structures (Polanski and Franciscus, 2006). The data does support neither of these hypotheses, because we did find a weak to moderate degree of integration between basicranial shape and midfacial orientation in *Pan* and *Pongo*. Consequently, the cranial base has some influence on palatal orientation but is not the dominating factor accounting for the observed variation within each species. According to Raff (1996), modularization is based on morphological dissociation, where individual traits or functional units acquire a degree of genetic and developmental independence such that traits in different modules evolve independently, while traits in the same module change in a concerted manner (Winther, 2001; Schlosser, 2002). Contrary to this exclusive definition of modularity, in being spatially and developmentally connected to

the anterior cranial base and thus influenced by the growth at the spheno-ethmoidal synchondrosis (Cendekiawan et al., 2010) or frontoethmoidal suture (Rice, 2008), facial orientation may still be influenced by other factors such as mastication (Menegaz et al., 2010) or respiratory behaviors (Shapiro, 1988) contributing to the variation in the midfacial orientation.

Stuctural integration in the skull is obvious since the palate is also the floor of the nasal cavity and hence the growth of the upper jaw is stimulated to a large extent by the growth of the nasal cavity (Lieberman, 2011). The nasal cavity in turn shares bony walls with the orbits, which are affected by the growth and development of the eyes and the brain (mediated by the anterior cranial fossa). By sharing walls of bone, growth in one region can accommodate growth in a neighboring region and vice versa and many interactions are both direct and indirect (Lieberman, 2011). Variations in these interactions are a potential source of the huge variation of midfacial orientation we observed in *Pan* and *Pongo*. And slight changes in the patterns of integration may be responsible for the differences concerning anterior cranial fossa orientation and midfacial orientation we observed between the two species. But the organization of the head and the ways in which modules interact also impose many constraints (Lieberman 2011). Ross and Henneberg (1995) for example suggested that there must be functional constraints on how far back the hard palate can be positioned without occluding the airways.

Besides Biegert (1957), another German anatomist, Angst (1967) stated that *Gorilla* and *Pongo* demonstrate sexual dimorphism in the expression of midfacial orientation - larger bodied males showing more dorsally oriented upper jaws than their female counterparts (Biegert, 1957; Angst, 1967). Furthermore, Shea (1986) hypothesized that orangutan males are more airorhynchous than females, providing space for the large throat sacs mature males develop. Winkler et al. (1988) investigated sexual dimorphism in exocranial and endocranial dimensions in *Pongo*. The authors radiographed each one male and female orangutan, and one male gorilla and measured the “expression of airorhynchy” as the “endocranial base-hard palate angle” for these specimens. Within *Pongo* they found the female orangutan had a more dorsally rotated palate than the male gorilla. This study does not find a sexual dimorphism in midfacial orientation in *Pan* or *Pongo*, thus the explanation that throat sac development is responsible for airorhynchy in *Pongo* seems disproved.

Finally the findings may be of use in reconstructions of fragmented specimens because with this method we are able to predict midfacial position with basicranial and orbital shape. This provides estimations of uncertainty of palate orientation, i.e. the degree of freedom of its

rigid motion that may among other things help reconstructions of hominid cranial fossils. Determining the uncertainty of the position of a cranial structure, i.e. the degrees of freedom of a rigid motion, is especially of interest in biomechanical studies, where virtual reconstructions of fossil hominids are serving as models (Laitman, 2005). One application for interpreting morphology in fossils is finite element analysis (FEA), for example in biting simulations in which the response of cranial structures to an applied load is investigated (Ross et al., 2002; Strait et al., 2002; Preuschoft and Witzel, 2004; Witzel et al., 2004; Marinescu et al., 2005; Richmond et al., 2005; Ross, 2005; Strait et al., 2008). In FEA, it is necessary to define the attachment locations of the masticatory muscles and the temporal ligament in accordance with the anatomical data that is represented by the FE - model of the reconstructed fossil. The geometry of the model influences the estimated muscle length, which directly influences the muscle force through the force – length relationship, affecting the computed internal forces and deformations. In addition, a slightly more anteriorly placed maxilla will react differently to a specific loading regime than the same maxilla placed more posteriorly. In general, the geometry and position of the jaws and the mandibular fossa will influence the applied bite force and thereby the outcome of the analysis. That is why the uncertainty of the estimated position of a bone will strongly influence the uncertainty of the biomechanics: the equations that are applied incorporate the geometry of the object directly. If one considers the large variability of palatal orientation into account (see **Figure 55a,b**), one has to be extremely careful to use virtual reconstructions of models, whose upper jaw lacked a connection to the rest of the skull and whose maxillary position and orientation was therefore estimated. Even though the observed intraspecies variation observed in this study depends on the superimposition, both species show a range of palatal orientation from the mean around 15°. Surely every biomechanical study will suffer from such an amount of uncertainty, but also the quality of ontogenetic and phylogenetic analyses will surely decrease and become a point of contact for criticism.

Even though we have to be extremely careful when directly apply these observed extant patterns of covariation in the reconstruction of fossil hominid species, we obtain futher information of how living morphologies vary. By better comprehending the complex interactions of different components of the craniofacial complex, we are given a potential tool that is useful to estimate the position of a bone and the uncertainty of its rigid motion – delivering valuable information during the reconstruction process and for continuative research using these models.

5.2.2. Patterns of covariation between facial and mandibular shape

Earlier studies suggest that the orientation of the anterior cranial base affects the orientation of the upper face directly, and that it indirectly influences palate orientation through the integration of palate and orbits (Ravosa, 1988; Ravosa & Shea, 1994). In addition, any positional modification of the nasomaxillary complex is connected to developmental adjustments of the mandibular components (Enlow & Hans, 1996). *Pongo* is characterized by a high degree of intraspecific variation in facial orientation. In this pilot study I found that in orangutans, and to a lesser degree in *Hylobates*, a downward deflection of the (pre)maxilla is highly correlated with an increase of the angle between mandibular corpus and ramus, and a relatively higher symphysis. This indicates that the structural accommodation of keeping the upper and lower dentition in occlusion is accomplished by altering the ramal and symphyseal orientation in relation to the deflection of the hard palate. In *Hylobates*, the (pre)maxillary orientation seems to be connected with the curvature of the inferior border of the mandibular corpus posterior to the canine area. These findings are in line with previous studies that show patterns of jaw integration in humans and chimpanzees that interpreted their finding in the light of the counterpart analysis principle (Bastir & Rosas, 2004). One key idea of the counterpart concept is that the main structural and functional purpose of the ramus is to provide occlusion while bridging the pharyngeal space (Enlow et al., 1982; Bhat and Enlow, 1985; Enlow and Hans, 1996). The assumption was corroborated by Smith and Josell (1984), and the covariation patterns and the moderate correlation ($r \sim 0.7$) found in this study between the midface and mandible is likely may be a further indication of this structural function of the ramus.

These findings are of potential use in the reconstruction of fragmented specimens by delivering information about how two distinct characteristics, facial orientation and mandibular shape, vary together. Imagining a hypothetical case in which a skull is found whose upper jaw is separated from the rest of the skull and whose manibular fossae are deteriorated. In this case an alignement of the maxilla according to the articulating mandible and cranial base is prevented. But combing the above described information about the covariation of sphenoid shape (section 5.2.1.) and mandibular shape (5.2.2.) with facial orientation will potentially increase the possibility to estimate the orientation of the maxilla with less uncertainty. Either way, by underlying the decision of where to place a fragmented bone on quatitative basis makes the process reproducible and accessible for discussion why one reassembled the fragments in a particular way – one premise of virtual anthropology. In

contrast, using traditional methods there is more or less no alternative then to place a fragement that is missing any connection to the surrounding bone arbitrarily to some extent. Both introduced approaches (5.2.1. and 5.2.2.) describe patterns of how cranial modules vary together, and are therefore a helpful source of information during the reconstruction of incomplete specimens.

CHAPTER 6: CONCLUSIONS

6. CONCLUSIONS

The completeness of a skull is a fundamental requirement for many types of analyses. Different approaches for the estimation of missing data emerged in the last decade and found applications in various fields such as anthropology, craniomaxillofacial surgery, forensics, bioarchaeology, and paleontology. Any reconstruction requires assumptions that derive, for instance, from functional constraints, integration, symmetry, species affinity or taphonomy (Gunz et al., 2009b; Weber and Bookstein, 2011). As Gunz et al. (2009b) stated, "different assumptions and algorithms lead to different estimations" and this is why "there exists no ´all-purpose´ reconstruction" (p. 61). One part of this thesis is therefore dedicated to the question how different reference based approaches will influence the outcome of reconstructions. Since the uncertainty of the shape of a reconstructed bone is influencing the uncertainty of continuative applications, my findings represent a valuable source of information for scientists working with (virtual) reconstructions. Furthermore, I introduce new approaches for the reconstruction of incomplete specimens that are characterized by large portions of missing bone or the complete separation of cranial fragments that show no broken edges that connect those parts.

Reconstructions can never provide a perfect solution, but for scientific problems at larger spatial scales (e.g., gross morphology of a skull), their accuracy might be sufficient. The reconstruction process in this context can be regarded as a heuristic approach (Weber & Bookstein 2011), characterized by combining various VA and GMM methods and evaluating the results in the light of earlier reconstructions. One example for the advantages of a virtual approach is the reconstruction of OH 5 (Benazzi et al., 2011), the holotype of Paranthropus boisei. The original reconstruction using traditional methods from Tobias (1967) showed a skewed position of the upper calvariofacial fragment and an uncertainty in the relative position of the neurocranium to the face. Using three-dimensional digital data, Geometric Morphometric methods and computer-aided design (CAD) techniques, Benazzi et al. (2011) were able to produce a symmetrical craniofacial reconstruction while taking the reconstructions´ uncertainty into account by producing a series of alternative models.

I introduced a new combination of tools from Virtual Anthropology and geometric morphometric methods (GMM) that contributes to the toolkit of procedures for the anatomical reconstruction. It aims at the reconstruction of severely damaged crania in which the midsagittal cranial plane was no longer available. In such cases, a three-dimensional reconstruction applying a traditional manual approach would be almost impossible to apply.

Even if the variability of the reconstructions is larger compared with those obtained using the original midsagittal plane, I have shown that the Procrustes mean shape of both simulations provide similar results in terms of accuracy. Using the Procrustes mean shape of the reference sample is therefore a good resource for the entire reconstruction of the cranium, circumventing negative effects introduced by asymmetry of a single reference specimen. The introduced method could find potential applications in the reconstruction of any bilateral symmetric bone, e.g. the pelvis, and can be applied in various fields such as forensics, (paleo)anthropology, and paleontology.

A scientifical field in which virtual reconstructions are recently incorporated is pre-operative planing in surgery. By means of CAPP (computer-assisted preoperative planning) for surgical simulation, surgeons have the possibility to test different reconstruction approaches in a three-dimensional virtual space that allows a precise visualization of the simulated outcome. In the study presented in this thesis, virtual reconstructions of digital osteomized zygomatic bones were simulated by means of different reconstruction techniques. Mirror imaging is one possible alternative widely used in reconstruction, but may not always be the optimal solution, i.e. when the hemifaces are considerably asymmetric. In this pilot study I showed that a best fit registration of the mirrored unaffected hemiface combined with TPS warping achieved better results, overcoming the evident limits of the mirroring approach. Up to now the TPS technique was used for reconstruction in anthropology and paleoanthropology, where the limits of the mirroring approach are well known. Therefore, it is important to emphasize that the TPS technique has the potential to become a valuable tool in cranio-maxillofacial surgery, providing improvement in the accuracy of bone reconstruction.

Another new approach that may be of potential use in the reassembly of bony fragments is represented by the investigation of rigid relationships in the craniofacial complex. If there are no anatomical clues or constraints that guide the re-assembly of isolated fragments, e.g. broken edges that would clearly connect two parts, the result will show a high degree of matching uncertainty. A way to estimate this positional uncertainty of anatomical structures or modules, for example facial parts relative to the basicranium, is to investigate the integrational pattern of rigid relationships between these cranial modules in extant species and apply this information during the reassembly of cranial fossil fragments. Beside estimations of uncertainty concerning the orientation of cranial modules relative to each other, this approach reveals patterns of covariation between midfacial orientation and basicranial shape. This approach overcomes most of the disadvantages of traditional approaches such as the

employment of reference planes for registration and allows the visualization of covariation patterns in relation to facial orientation in three dimensions. The position and orientation of the midface is predicted according to the shape of the cranial base, thus providing essential information for the interpretation of hypotheses concerning facial orientation and for reconstruction of fragmentary specimens. The observed pattern of morphologic covariation in this comparative sample (*Pan* and *Pongo*) may theoretically help to estimate the morphologic covariation in fossil specimens. However, this is only valid under the assumption that the morphological integration in extinct hominoid species is equal to the one observed in extant hominoids, which is most often an inadequate generalization (Ackermann, 2002; Ackermann, 2003). Nevertheless we can assume that basic patterns of craniofacial integration are conserved during hominoid evolution and that patterns of variation and covariation are similar among related primate populations, as it is the case for African apes and humans (Ackermann and Krovitz, 2002, Mitteroecker and Bookstein, 2008). Applying information about the morphologic covariation in closely related species, so to speak as surrogate models, for the anatomical reconstruction of fossil specimens could therefore be potentially of immense value. Since the applicability of this approach is disputed, the main goal in this thesis is merely the determination of the degrees of freedom of a rigid motion of a cranial structure. Evaluating the range of variation in facial orientation yields a meaure of uncertainty that is of interest for reconstructions used in biomechanical studies, where the uncertainty of the position of a bone will strongly influence the uncertainty of the biomechanics.

The second major issue that is discussed in this thesis is the geometrical reconstruction of severly damaged crania. Most hominin cranial fossils are incomplete, requiring reconstruction prior to deployment in subsequent analyses. However, complete reference crania from the same taxon are often absent for fossils. I studied the consequences of intraspecies and interspecies reconstructions by estimating missing data in several virtually fragmented models of hominoid crania (extant and fossil). Using a reference sample of *Homo*, *Pan*, *Pongo* and several fossils, I investigated the posterior distribution and uncertainty of the generated multiple intraspecies and interspecies reconstructions. Although previous work has touched this topic (e.g., Gunz et al. 2009, Neeser et al. 2009), a comprehensive description of effects resulting from the choice of reference, particularly if drawn from other species, was not yet available. Defining the accuracy of a reconstruction as the maximum RMS error normal to the true surface, and relying throughout on data resources comprising many hundreds of landmarks and semilandmarks, I have shown that TPS based reconstructions in many cases lead to reasonable results for large cranial defects in both the face and the

neurocranium. I showed that the accuracy in interspecies reconstruction often show very similar errors - even outperforming intraspecies reconstructions in some cases, e.g., among *Pan* and *Pongo* and *Pan*/*Pongo* and Sts 5. Finally, I introduced a potential guideline for the decision which reference sample should be chosen for interspecies reconstructions.

In summary, this thesis contributes to the the toolkit of virtual anthropology and geometrics morphomtrics by introducing new approaches and findings that are useful for the virtual reconstruction of fragmented specimens.

CHAPTER 7: OUTLOOK

7. OUTLOOK

The main goal for future work will be the establishment of a semi-automatic reference-based toolkit of procedures for the anatomical reconstruction of fragmented specimens, using tools from Virtual Anthropology and geometric morphometrics. However, before the methods introduced above (together with some other approaches to be developed) can be fused into a standardized set of procedures (for example in the form of a software package), a detailed and extended investigation of the reconstruction methods introduced has to be carried out.

In the section "Beyond mirror imaging: New approaches during anatomical reconstructions", the sample size has to be increased in order to account for the large craniofacial variability in humans. Furthermore, the approach has to be broadened, i.e. each hominoid species has to be included to circumvent possible pitfalls and false conclusions that are always an issue when dealing with small sample sizes. The method can be extended to the anatomical reconstruction of the cranial base, a cranial module that is characterized by bilateral symmetry and crucial for the estimation of cranial volume. Finally, a detailed investigation of the influence of asymmetry on the reconstruction uncertainty is needed, since this approach is using bilateral symmetry as the main assumption during the reconstruction process. In general, the latter two points also matter for the comparison of "three-dimensional virtual methods for reconstruction in craniomaxillofacial surgery". Establishing a large data base that includes various reconstruction scenarios will provide a useful tool for many potential application areas and, for instance, minimize the time of pre-operative planning in cases where time expenditure is crucial.

This thesis contributes to virtual reconstruction by delivering a quantitative and reproducible way of positioning maxillary fragments and a measure for the uncertainty when reassembling these fragments during the anatomical reconstruction. One potential field of application for this approach is the reassembly of cranial fossil fragments. Exploiting the information about the covariation between cranial bones in a reference sample allows the placement of cranial fragments in a reproducible way, in this case the maxilla that completely lacks connections to any other bone. Since the placement is based on the covariation pattern observed in a reference sample, it will not be the anatomical knowledge of a physical anthropologist that guides the anatomical reconstruction, but the morphological information inherent in the particular reference sample. Together with the standard error of the position of the respective fragment, this study delivers a quantitative measure that describes the uncertainty of positioning and reassembling cranial fossil fragments. In this thesis I laid the

foundations for this approach by advancing the subject of cranial integration and facial orientation from a different angle, providing further insight in the spatial relationships of the hominoid cranium. In order to substantiate the results and identify the observed patterns of covariation (relative orbit height and palatal orientation) as a general hominoid characteristic, the sample size as well as the number of included species has to be increased. Then, the justification of the potential use of this method in the reconstruction of fossil hominoids would be strengthened. Further information about craniofacial patterns of covariation is needed particularly between a) maxillary shape and palatal orientation, and b) maxillary orientation and palatal orientation. If there is a tight integration between maxillary shape and palatal orientation, i.e. if one can estimate midfacial orientation from maxillary shape, an additional source of information would be available, decreasing the degrees of freedom of the positioning of the face relatice to the orbits and cranial base. Investigating the pattern of integration between maxillary orientation and palatal orientation would help to test the hypothesis concerning the "facial block" by analizing the relationship between the posterior maxillary plane, the orbits, and the anterior cranial fossa. This approach could also be helpful to evaluate the dimension of error propagation in the reassembly of cranial fragments. One could use the position of the cranial base and all the estimated positions of the maxilla after the partial GPA as continuative "bases" for the estimation, e.g., of the position of the frontal bone. By doing so, the positioning of the frontal bone will depend on the uncertainty of the maxillary position, which increases the uncertainty of positions the frontal could occupy in a reconstruction. The discrepancy from the actual position of the frontal then yields the standard error.

Crucial future work that lacked attention so far concerns the "consequences of reference sample choice" of internal cranial structures. To my knowledge there is no investigation concerning the uncertainties that are arising when reconstructing virtual endocasts, cranial fossae or sinuses. As I have shown in "Reconstructing the endocranial cavity of Cioclovina", reconstructions can be crucial for the estimation of endocranial volume, together with the visualization of internal structures. Furthermore, for biomechanical studies it can be mandatory to include cranial sinuses in the model. This is a difficult task both in terms of choosing the approapriate reference and superimposing this reference according to internal reference points. This finally leads to the three-dimensionl geometric analysis of sinus variability itself, an undertaking that is extremely difficult to achieve because of the lack of anatomical landmarks.

8. REFERENCES

Ackermann R. 2002. Patterns of covariation in the hominoid craniofacial skeleton: implications for paleoanthropological models. Journal of Human Evolution 43:167-187.

Ackermann R, Cheverud JM. 2002. Discerning evolutionary processes in patterns of tamarin (genus Saguinus) craniofacial variation. American Journal of Physical Anthropology 117:260-271.

Ackermann RR. 2003. Using extant morphological variation to understand fossil relationships: A cautionary tale. South African Journal of Science 99:255-258.

Ackermann RR, Cheverud JM. 2000. Phenotypic covariance structure in tamarins (genus Saguinus): a comparison of variation patterns using matrix correlation and common principal component analysis. American Journal of Physical Anthropology 111:489-501.

Ackermann RR, Cheverud JM. 2004. Morphological integration in primate evolution. In: Pigliucci M PK, editor. Phenotypic Integration: Studying the Ecology and Evolution of Complex Phenotypes. Oxford: Oxford University Press. p 302-319.

Acock AC. 2005. Working With Missing Values. Journal of Marriage and Family 67:1012-1028.

Acsadi GY, Nemeskeri J. 1970. History of human life span and mortality. Budapest: Akademiai Kiado.

Adams D, Rohlf FJ, Slice D. 2004. Geometric morphometrics: Ten years of progress following the “revolution”. Italian Journal of Zoology 71:5-16.

Aiello L, Dean C. 2002. An Introduction to Human Evolutionary Anatomy: Academic Press.

Angst R. 1967. Beitrag zum Formenwandel des Craniums der Ponginen. Z. Morph. Anthropol. 58:109-151.

Ashton EH. 1957. Age changes in the basicranial axis of the Anthropoidea. Proc Zool Soc Lond 129:61-74.

Auerbach BM, Raxter MH. 2008. Patterns of clavicular bilateral asymmetry in relation to the humerus: variation among humans. Journal of Human Evolution 54:663-674.

Auerbach BM, Ruff CB. 2006. Limb bone bilateral asymmetry: variability and commonality among modern humans. Journal of Human Evolution 50:203-218.

Backhaus K, Erichson B, Plinke W, Weiber R. 2006. Multivariate Analysemethoden. Eine anwendungsorientierte Einführung. Berlin-Heidelberg-New-York: Springer-Verlag.

Bajnóczky I, Királyfalvi L. 1995. A new approach to computer-aided comparison of skull and photograph. International Journal of Legal Medicine 108:157-161.

Bastir M, O'Higgins P, Rosas A. 2007. Facial ontogeny in Neanderthals and modern humans. Proceedings of the Royal Society B: Biological Sciences 274:1125-1132.

Bastir M, Rosas A. 2004. Facial heights: Evolutionary relevance of postnatal ontogeny for facial orientation and skull morphology in humans and chimpanzees. Journal of Human Evolution 47:359-381.

Bastir M, Rosas A. 2005. Hierarchical nature of morphological integration and modularity in the human posterior face. American Journal of Physical Anthropology 128:26-34.

Bastir M, Rosas A. 2006. Correlated variation between the lateral basicranium and the face: A geometric morphometric study in different human groups. Archives of Oral Biology 51:814-824.

Bastir M, Rosas A, Kuroe K. 2004. Petrosal orientation and mandibular ramus breadth: Evidence for an integrated petroso-mandibular developmental unit. American Journal of Physical Anthropology 123:340-350.

Bastir M, Rosas A, Lieberman DE, O'Higgins P. 2008. Middle Cranial Fossa Anatomy and the Origin of Modern Humans. The Anatomical Record: Advances in Integrative Anatomy and Evolutionary Biology 291:130-140.

Bastir M, Rosas A, Stringer C, Manuel Cuétara J, Kruszynski R, Weber GW, Ross CF, Ravosa MJ. 2010. Effects of brain and facial size on basicranial form in human and primate evolution. Journal of Human Evolution 58:424-431.

Begun DR. 2007. Fossil Record of Miocene Hominoids. In: Henke W, Tattersall I, editors. Handbook of Paleoanthropology, Volume II: Primate Evolution and Human Origins. Berlin: Springer-Verlag. p 921-977.

Benazzi S, Bertelli P, Lippi B, Bedini E, Caudana R, Gruppioni G, Mallegni F. 2010. Virtual anthropology and forensic arts: the facial reconstruction of Ferrante Gonzaga. Journal of Archaeological Science 37:1572-1578.

Benazzi S, Bookstein FL, Strait DS, Weber GW. 2011a. A new OH5 reconstruction with an assessment of its uncertainty. Journal of Human Evolution 61:75-88.

Benazzi S, Fiorenza L, Kozakowski S, Kullmer O. 2011b. Comparing 3D Virtual Methods for Hemimandibular Body Reconstruction. The Anatomical Record: Advances in Integrative Anatomy and Evolutionary Biology 294:1116-1125.

Benazzi S, Senck S. 2011. Comparing 3-Dimensional Virtual Methods for Reconstruction in Craniomaxillofacial Surgery. Journal of Oral and Maxillofacial Surgery 69:1184-1194.

Benazzi S, Stansfield E, Kullmer O, Fiorenza L, Gruppioni G. 2009a. Geometric Morphometric Methods for Bone Reconstruction: The Mandibular Condylar Process of Pico della Mirandola. The Anatomical Record: Advances in Integrative Anatomy and Evolutionary Biology 292:1088-1097.

Benazzi S, Stansfield E, Milani C, Gruppioni G. 2009b. Geometric morphometric methods for three-dimensional virtual reconstruction of a fragmented cranium: the case of Angelo Poliziano. International Journal of Legal Medicine 123:333-344.

Bhat M, Enlow DH. 1985. Facial variations related to headform type. Angle Orthod 55:269–280.

Biegert J. 1957. Der Formwandel des Primatenschädels und seine Beziehungen zur ontogenetischen Entwicklung und den phylogenetischen Spezialisationen der Kopforgane. Ggbrs. Morph. Jahrb 98:77-199.

Biegert J. 1963. The evaluation of characteristics of the skull, hands and feet for primate taxonomy. In: Washburn SL, editor. Classification and Human Evolution. Chicago: Aldine. p 116-145.

Bilsborough A, Rae TC. 2007. Hominoid Cranial Diversity and Adaptation. In: Henke W, editor. Handbook of Paleoanthropology. Berlin, Heidelberg: Springer.

Björk A. 1969. Prediction of mandibular growth. Am. J. Orthod. 55:585-599.

Bolker JA. 2000. Modularity in Development and Why It Matters to Evo-Devo. American Zoologist 40:770-776.

Bookstein F. 1989. Principapl warps:thin-plate splines and the decomposition of deformations. IEEE Trans Pattern Anal Mach Intell 11:567−585.

Bookstein FL. 1991. Morphometric Tools for Landmark Data: Geometry and Biology. Cambridge Cambridge University Press.

Bookstein F, Schäfer K, Prossinger H, Seidler H, Fieder M, Stringer C, Weber GW, Arsuaga J-L, Slice DE, Rohlf FJ, Recheis W, Mariam AJ, Marcus LF. 1999. Comparing frontal cranial profiles in archaic and modern Homo by morphometric analysis. The Anatomical Record 257:217-224.

Bookstein FL. 1996a. A standard formula for the uniform shape component in landmark data. In: Marcus LF, Corti M, Loy A, Naylor JP, Slice DE, editors. Advances in morphometrics: NATO ASI Ser. p 153–168.

Bookstein FL. 1996b. Combining the tools of geometric morphometrics. In: Marcus LF, Corti M, Loy A, Naylor JP, Slice DE, editors. Advances in morphometrics: NATO ASI Ser. p 131-151.

Bookstein FL. 1997. Landmark methods for forms without landmarks: morphometrics of group differences in outline shape. Medical Image Analysis 1:225-243.

Bookstein FL, Green WDK. 1993. A feature space for edgels in images with landmarks. Journal of Mathematical Imaging and Vision 3:231-261.

Bookstein FL, Green WK. 2002. Edgewarp 3D. Available from: ftp://brainmap.stat.washington.edu/pub/fred/ewsh3.19.man/.

Bookstein FL, Gunz P, Mitteroecker P, Prossinger H, Schæfer K, Seidler H. 2003. Cranial integration in Homo: singular warps analysis of the midsagittal plane in ontogeny and evolution. Journal of Human Evolution 44:167-187.

Brinkley LL, Vickerman MM. 1978. The mechanical role of the cranial base in palatal shelf movement: an experimental re-examination. J. Embryol. exp. Morph. 48:93-100.

Broom R. 1947. Discovery of a new skull of the South African Ape-man, Plesianthropus. Nature 159:672.

Brown B. 1997. Miocene hominoid mandibles: Functional and phylogenetic perspectives. In: Begun DR, Ward CV, Rose MD, editors. Function, phylogeny and fossils: Miocene hominoid evolution and adaptations. New York, London: Plenum Press. p 153–171.

Brown B, Ward SC. 1988. Basicranial and facial topography in Pongo and Sivapithecus. In: JH S, editor. Orang-utan Biology. London: Oxford University Press. p 247-260.

Brown KA. 1982 The identification of Linda Agostini. The significance of dental evidence in the Albury 'pyjama girl' case. A case report. Forensic Science International 20:81-86.

Bruner E, Manzi G. 2008. Paleoneurology of an “early” Neandertal: endocranial size, shape, and features of Saccopastore 1. Journal of Human Evolution 54:729-742.

Bruner E, Manzi G, Arsuaga JL. 2003. Encephalization and allometric trajectories in the genus Homo: Evidence from the Neandertal and modern lineages. Proceedings of the National Academy of Sciences 100:15335-15340.

Buikstra JE, Ubelaker DH. 1994. Standards for Data Collection from Human Skeletal Remains. Fayetteville: Arkansas Archaeological Survey Press.

Cameron DW, Groves CP. 2004. Bones, Stones and Molecules. “Out of Africa” and Human Origins Elsevier Inc.

Caspari R, Radovcic J. 2006. New reconstruction of Krapina 5, a male Neandertal cranial vault from Krapina, Croatia. American Journal of Physical Anthropology 130:294-307.

Cattaneo C. 2007. Forensic anthropology: developments of a classical discipline in the new millennium. Forensic Science International 165:185-193.

Cendekiawan T, Wong RWK, Rabie ABM. 2010. Relationships Between Cranial Base Synchondroses and Craniofacial Development: A Review. The Open Anatomy Journal, 2:67-75.

Cheverud JM. 1982. Phenotypic, genetic, and environmental morphological integration in the cranium. Evolution 36:499-516.

Cheverud JM. 1988. A comparison of genetic and phenotypic correlations. Evolution 42:958–968.

Cheverud JM. 1995. Morphological integration in the Saddle Back Tamarin (Saguinus fuscicollis) cranium. American Naturalist 145:63-89.

Cheverud JM. 1996. Developmental Integration and the Evolution of Pleiotropy. Amer. Zool. 36:44-50.

Claes P, Vandermeulen D, De Greef S, Willems G, Clement JG, Suetens P. 2010. Computerized craniofacial reconstruction: Conceptual framework and review. Forensic Science International 201:138-145.

Claes P, Vandermeulen D, De Greef S, Willems G, Suetens P. 2006. Craniofacial reconstruction using a combined statistical model of face shape and soft tissue depths: Methodology and validation. Forensic Science International 159:S147-S158.

Clement JG, Marks MK. 2005. Computer-graphic facial recontruction. Amsterdam: Elsevier Academic Press.

Connolly JC. 1950. External Morphology of the Primate Brain. Springfield, Illinois Charles C. Thomas.

Curnoe D, Tobias PV. 2006. Description, new reconstruction, comparative anatomy, and classification of the Sterkfontein Stw 53 cranium, with discussions about the taxonomy of other southern African early Homo remains. Journal of Human Evolution 50:36-77.

Dean MC. 1984. Comparative myology of the hominoid cranial base. I. The muscular relationships and bony attachments of the digastric muscle. Folia Primatol 43:234–248.

Delattre A, Fenart R. 1956. Analyse morphologique du splanchnocrane chez les primates et ses rappots avec le prognathisme. Mammalia 20:169-323.

Drake AG, Klingenberg CP. 2008. The pace of morphological change: historical transformation of skull shape in St Bernard dogs. Proceedings of the Royal Society B: Biological Sciences 275:71-76.

Dryden I, Mardi KV. 1998. Statistical Shape Analysis. New York: JohnWiley & Sons.

Enlow DH. 1990. Facial Growth, 3rd ed. Philadelphia: Saunders.

Enlow DH, Azuma M. 1975. Functional growth boundaries in the human and mammalian face. In: Bergsma D, Langman J, editors. Morphogenesis and Malformation of Face and Brain: The First International Conference on Morphogenesis and Malformation. New York: Alan R Liss. p 217-230.

Enlow DH, Hans MG. 1990. Handbook of Facial Growth. Philadelphia, London, New York: W.B. Saunders Company.

Enlow DH, Hans MG. 1996. Essentials of facial growth. Oxford: Elsevier

Enlow DH, McNamara JA. 1973. The neurocranial basis for facial form and pattern. Am. J. Orthod. 43:256-270.

Enlow DH, Moyers RE, Hunter WS, McNamara JAJ. 1969. A procedure for the analysis of intrinsic facial form and growth. Am J Orthod Dentofacial Orthop 56:6–23.

Falk D, Hildebolt C, Smith K, Morwood MJ, Sutikna T, Brown P, Jatmiko, Saptomo EW, Brunsden B, Prior F. 2005. The Brain of LB1, Homo floresiensis. Science 308:242-245.

Ferenbach D, Schwidetzky I, Stloukal M. 1980. Recommendations for age and sex diagnosis of skeletons. Journal of Human Evolution 9:517–550.

Le Floch-Prigent N., Moschidou-Polizois A. 1991. The Petralona cranium: C.T. Scan findings. Bull. Geol. Soc. Greece, 25 (2): 437-452.

Fondon JW, Garner HR. 2004. Molecular origins of rapid and continuous morphological evolution. Proceedings of the National Academy of Sciences 101:18058-18063.

Gateno J, Xia JJ, Teichgraeber JF, Christensen AM, Lemoine JJ, Liebschner MAK, Gliddon MJ, Briggs ME. 2007. Clinical Feasibility of Computer-Aided Surgical Simulation (CASS) in the Treatment of Complex Cranio-Maxillofacial Deformities. Journal of oral and maxillofacial surgery : official journal of the American Association of Oral and Maxillofacial Surgeons 65:728-734.

Gawlikowska A, Szczurowski J, Czerwiński F, Miklaszewska D, Adamiec E, Dzięciołowska E. 2007. The fluctuating asymmetry of mediaeval and modern human skulls. HOMO - Journal of Comparative Human Biology 58:159-172.

Gerasimov MM. 1971. The Face Finder. London: Hutchinson & Co.

Glaister J, Brash JC. 1937. Medico-legal Aspects of Ruxton Case Edinburgh: Harcourt Brace/Churchill Livingstone.

Goswami A. 2006. Cranial modularity shifts during mammalian evolution. American Naturalist 168:270-280.

Goswami A, Polly PD. 2010. The Influence of Modularity on Cranial Morphological Disparity in Carnivora and Primates (Mammalia). PLoS ONE 5:e9517.

Grine FE, Gunz P, Betti-Nash L, Neubauer S, Morris AG. 2010. Reconstruction of the late Pleistocene human skull from Hofmeyr, South Africa. Journal of Human Evolution 59:1-15.

Grün R. 1996. A re-analysis of electron spin resonance dating results associated with the Petralona hominid. J. Human Evol. 30:227–241.

Gunz P. 2005. Statistical and geometric reconstruction of hominid crania: reconstructing australopithecine ontogeny: Ph.D. thesis, University of Vienna.

Gunz P, Bookstein FL, Mitteroecker P, Stadlmayr A, Seidler H, Weber GW. 2009a. Early modern human diversity suggests subdivided population structure and a complex out-of-Africa scenario. Proceedings of the National Academy of Sciences.

Gunz P, Mitteroecker P, Bookstein FL. 2005a. Semilandmarks in Three Dimensions. Modern Morphometrics in Physical Anthropology:73-98.

Gunz P, Mitteroecker P, Bookstein FL. 2005b. Semilandmarks in three dimensions. In: Slice DE, editor. Modern Morphometrics in Physical Anthropology. New York: Kluwer Academic/Plenum Publishers. p 73-98.

Gunz P, Mitteroecker P, Bookstein FL, Weber GW. 2004. Computer aided reconstruction of incomplete human crania using statistical and geometrical estimation methods. Enter the Past: Computer Applications and Quantitative Methods in Archaeology, BAR International Series:92-94.

Gunz P, Mitteroecker P, Neubauer S, Weber GW, Bookstein FL. 2009b. Principles for the virtual reconstruction of hominin crania. Journal of Human Evolution 57:48-62.

Gunz P, Neubauer S, Maureille B, Hublin J-J. 2010. Brain development after birth differs between Neanderthals and modern humans. Current Biology 20:R921-R922.

Gunz, P. and K. Harvati (2007). "The Neanderthal "chignon": Variation, integration, and homology." Journal of Human Evolution 52(3): 262-274.

Hallgrímsson B, Lieberman DE, Liu W, Ford-Hutchinson AF, Jirik FR. 2007. Epigenetic interactions and the structure of phenotypic variation in the cranium. Evolution & Development 9:76-91.

Harvati K, Gunz P, Grigorescu D. 2007. Cioclovina (Romania): affinities of an early modern European. Journal of Human Evolution 53 732-746.

Hassfeld S, Mühling J. 2001. Computer assisted oral and maxillofacial surgery – a review and an assessment of technology. International Journal of Oral and Maxillofacial Surgery 30:2-13.

Hennig GJ, Herr W, Weber E, Xirotiris NI. 1981. ESR-dating of the fossil hominid cranium from Petralona Cave, Greece. Nature 292:533-536.

Henry M M. 1991. Sexual dimorphism inAustralopithecus afarensis. Journal of Human Evolution 20:21-32.

Herries AIR, Shaw J. 2011. Palaeomagnetic analysis of the Sterkfontein palaeocave deposits: Implications for the age of the hominin fossils and stone tool industries. Journal of Human Evolution 60:523-539.

Hershkovitz P. 1970. Notes on Tertiary platyrrhine monkeys and description of a new genus from the late Miocene of Colombia. Folia Primatol. 13:213-240.

Hofer H. 1952. Der Gestaltwandel des Schädels der Säugetiere und der Vögel, mit besonderer Berücksichtigung der Knickungstypen und der Schädelbasis. Verh. Anat. Ges. 99:102-126.

Hofer H. 1960. Studien zum Problem des Gestaltwandels des Schaedels der Saeugetiere insbesondere der Primaten, I. Die medianen Kruemmungen des Schaedels und ihre Erfassung nach der Methode von Landzert. Z. Morph. Anthropol. 50:299-316.

Hofer H, Spatz W. 1963. Studien zum Problem des Gestaltwandels des Schädels der Säugetiere, insbesondere der Primaten. II. Über die kyphosen Fetaler und neonater Primatenschädel. Z Morphol Anthropol. 53:29–52.

Hofer HO. 1954. Die cranio-cerebrale Topographie bei den Affen und ihre Bedeutung fuer die menschliche Schädelform. HOMO - Journal of Comparative Human Biology 5:52-72.

Hohl TH. 1983. Masticatory Muscle Transposition in Primates: Effects on Craniofacial Growth. J. max.-fac. Surg. 11 149-156.

Hohlweg-Majert B, Schön R, Schmelzeisen R, Gellrich N-C, Schramm A. 2005. Navigational Maxillofacial Surgery Using Virtual Models. World Journal of Surgery 29:1530-1538.

Holloway RL. 1974. The casts of fossil hominid brains. Scientific American 231:106-115.

Holloway RL. 1983. Cerebral brain endocast pattern of Australopithecus afarensis hominid. Nature 303:420-422.

Holloway RL, Broadfield DC, Yuan MS. 2005. Brain Evolution and Endocasts: Introduction. In: The Human Fossil Record: John Wiley & Sons, Inc. p 1-26.

Holloway RL, Kimbel WH. 1986. Endocast morphology of Hadar hominid A.L. 162-28. Nature 321:536.

Hoyte D. 1991. The cranial base in normal and abnormal skull growth. Neurosurgery Clinics of North America 2:515-537.

Hublin JJ. 1984. The fossil man from Salzgitter Lebenstedt (FRG) and its place in human evolution during the Pleistocene in Europe. Zeitschrift für Morphologie und Anthropologie 75:45-56.

Huxley TH. 1863. Evidence as to Man's Place in Nature. New York: D. Appleton and Company.

Iscan MY, Helmer RP. 1993. Forensic Analysis of the Skull: Craniofacial Analysis, Reconstruction, and Identification. New York: Wiley-Liss.

Iscan MY, Solla HE, McCabe BQ. 2005. Victim of a dictatorial regime: Identification of Mr. Roberto Gomensoro Josman. Forensic Science International 151:213-220.

Jeffery N. 2003. Brain expansion and comparative prenatal ontogeny of the non-hominoid primate cranial base. Journal of Human Evolution 45:263-284.

Jimenez P, Martinez-Insua A, Franco-Vazquez J, Otero-Cepeda XL, Santana U. 2012. Maxillary changes and occlusal traits in crania with artificial fronto-occipital deformation. American Journal of Physical Anthropology 147:40-51.

Kanellis A, Savva A. 1964. Craniometric study of the Homo neanderthalensis of Petralona. Aristot. Panep. Thess. 9:65-92.

Kendall DG. 1984. Shape-manifolds, Procrustean metrics and complex projective spaces. Bull. London Math. Soc. 16:81-121.

Kimbel W, Rak Y, Johanson D. 2004. The Skull of Australopithecus afarensis. Oxford: Oxford University Press.

Kimbel WH, Delezene LK. 2009. “Lucy” redux: A review of research on Australopithecus afarensis. American Journal of Physical Anthropology 140:2-48.

Kimbel WH, White TD. 1988. A Revised Reconstruction Of The Adult Skull Of ustralopithecus afarensis. Journal of Human Evolution 17:545-550.

Kimbel WH, White TD, Johanson DC. 1984. Cranial Morphology of Australopithecus-Afarensis - a Comparative-Study Based on a Composite Reconstruction of the Adult Skull. American Journal of Physical Anthropology 64:337-388.

Kjaer I. 1992. Human prenatal palatal shelf elevation related to craniofacial skeletal maturation. The European Journal of Orthodontics 14:26-30.

Klingenberg CP. 2008. Morphological Integration and Developmental Modularity. Annual Review of Ecology Evolution and Systematics 39:115-132.

Klingenberg CP, Barluenga M, Meyer A. 2002. Shape analysis of symmetric structures: quantifying variation among individuals and asymmetry. Evolution 56:1909-1920.

Klingebiel R, Thieme N, Kivelitz D, Enzweiler C; Werbs M, Lehmann R 2002. Three-dimensional Imaging of the Inner Ear by Volume-Rendered Reconstructions of Magnetic Resonance Data. Arch Otolaryngol Head Neck Surg. 2002;128(5):549-553.

Klug C, Schicho K, Ploder O, Yerit K, Watzinger F, Ewers R, Baumann A, Wagner A. 2006. Point-to-Point Computer-Assisted Navigation for Precise Transfer of Planned Zygoma Osteotomies from the Stereolithographic Model into Reality. Journal of oral and maxillofacial surgery : official journal of the American Association of Oral and Maxillofacial Surgeons 64:550-559.

Koelmeyer TD. 1982. Videocamera superimposition and facial reconstruction as an aid to identification. The American Journal of Forensic Medicine and Pathology 3:45-48.

Kokemueller H, Tavassol F, Ruecker M, Gellrich N-C. 2008. Complex Midfacial Reconstruction: A Combined Technique of Computer-Assisted Surgery and Microvascular Tissue Transfer. Journal of oral and maxillofacial surgery : official journal of the American Association of Oral and Maxillofacial Surgeons 66:2398-2406.

Kokkoros P, Kanellis A. 1960. Découverte d´un crane d´homme paléolithique dans peninsule Chalcidique. Anthropologie 64:132-147.

Komori M, Kawamura S, Ishihara S. 2009a. Averageness or symmetry: Which is more important for facial attractiveness? Acta Psychologica 131:136-142.

Komori M, Kawamura S, Ishihara S. 2009b. Effect of averageness and sexual dimorphism on the judgment of facial attractiveness. Vision Research 49:862-869.

Kranioti EF, Holloway R, Senck S, Ciprut T, Grigorescu D, Harvati K. 2011. Virtual Assessment of the Endocranial Morphology of the Early Modern European Fossil Calvaria From Cioclovina, Romania. The Anatomical Record: Advances in Integrative Anatomy and Evolutionary Biology 294:1083-1092.

Krogman WM. 1931. Studies in growth changes in the skull and face of anthropoids. IV. Growth changes in the skull and face of the chimpanzees. Am J Anat 47:325-342.

Krogman WM, İşcan MY. 1986. Human Skeleton in Forensic Medicine, 2nd edition ed. Illinois: Springfield: Charles C. Thomas Publisher.

Kummer B. 1952 Untersuchungen ueber die Entstehung der Schaedelbasisform bei Mensch und Primaten. Verh. Anat.Ges. 99:122-126.

Laitman JT. 2005. A microscope on vertebrate form and function: The power of finite element analysis. Anatomical Record Part a-Discoveries in Molecular Cellular and Evolutionary Biology 283A:251-252.

Lebedinsky NG. 1938. Über die funktionelle Bedeutung der verschiedenen Höhe des Ramus ascendens mandibulae bzw. des Unterkiefergelenkes bei Säugetieren. Vjsehr. naturf. Ges. Zürich Beiblatt 83:217 — 224.

Leslie ER. 2010. Phylogenetic Patterning of Facial Orientation in the Hominoids In: Department of Cell and Molecular Biology. Chicago, Illinois Northwestern University.

Leutenegger W, Shell B. 1987. Variability and sexual dimorphism in canine size of Australopithecus and extant hominoids. Journal of Human Evolution 16:359-367.

Lieberman D, Ross CF, Ravosa MJ. 2000a. The primate cranial base: Ontogeny, function, and integration. American Journal of Physical Anthropology 113:117-169.

Lieberman DE. 2011. Evolution of the Human Head. Harvard Harvard University Press.

Lieberman DE, Hallgrímsson B, Liu W, Parsons TE, Jamniczky HA. 2008. Spatial packing, cranial base angulation, and craniofacial shape variation in the mammalian skull: testing a new model using mice. Journal of Anatomy 212:720-735.

Lieberman DE, Krovitz GE, McBratney-Owen B. 2004. Testing hypotheses about tinkering in the fossil record: The case of the human skull. Journal of Experimental Zoology Part B-Molecular and Developmental Evolution 302B:284-301.

Lieberman DE, McBratney BM, Krovitz G. 2002. The evolution and development of cranial form in Homo sapiens. Proceedings of the National Academy of Sciences 99:1134-1139.

Lieberman DE, McCarthy RC. 1999. The ontogeny of cranial base angulation in humans and chimpanzees and its implications for reconstructing pharyngeal dimensions. Journal of Human Evolution 36:487-517.

Lieberman DE, Pearson OM, Mowbray KM. 2000b. Basicranial influence on overall cranial shape. J Hum Evol 38:291–315.

Lockwood CA, Richmond BG, Jungers WL, Kimbel WH. 1996. Randomization procedures and sexual dimorphism inAustralopithecus afarensis. Journal of Human Evolution 31:537-548.

Long SY, Larsson KS, Lohmander S. 1973. Cell proliferation in the cranial base of A/J mice with 6-AN-induced cleft palate. Teratology 8:127-138.

López EKN, Stock SR, Taketo MM, Chenn A, Ravosa MJ. 2008. A novel transgenic mouse model of fetal encephalization and craniofacial development. Integrative and Comparative Biology 48:360-372.

Ma W, Lozanoff S. 1996. Morphological deficiency in the prenatal anterior cranial base of midfacially retrognathic mice. J. Anat. 188:547-555.

Manfreda E, Mitteroecker P, Schaefer K. 2006. Functional and evolutionary anatomy of the primate atlas: A geometric morphometric approach. American Journal of Physical Anthropology:124-125.

Mardia K, Bookstein F, Moreton I. 2000. Statistical assessment of bilateral symmetry of shapes. Biometrika 87:285-300.

Marinescu R, Daegling DJ, Rapoff AJ. 2005. Finite-element modeling of the anthropoid mandible: The effects of altered boundary conditions. Anatomical Record Part a-Discoveries in Molecular Cellular and Evolutionary Biology 283A:300-309.

Marroig G, Cheverud JM. 2001. A comparison of Phenotypic Variation and Covariation Patterns and the role of Phylogeny, Ecology, and Ontogeny during Cranial Evolution and New World Monkeys. Evolution 55:2576-2600.

Martin R, Saller K, 1957. Lehrbuch der Anthropologie. Gustav Fischer, Stuttgart. pp. 488–490.

Martínez-Abadías N, Percival C, Aldridge K, Hill CA, Ryan T, Sirivunnabood S, Wang Y, Jabs EW, Richtsmeier JT. 2011. Beyond the Closed Suture in Apert Syndrome Mouse Models: Evidence of Primary Effects of FGFR2 Signaling on Facial Shape at Birth. Developmental Dynamics 240:spcone-spcone.

McCarthy RC, Lieberman DE. 2001. Posterior maxillary (PM) plane and anterior cranial architecture in primates. The Anatomical Record 264:247-260.

McCollum MA. 1999. The Robust Australopithecine Face: A Morphogenetic Perspective. Science 284:301-305.

Menegaz RA, Sublett SV, Figueroa SD, Hoffman TJ, Ravosa MJ, Aldridge K. 2010. Evidence for the Influence of Diet on Cranial Form and Robusticity. The Anatomical Record: Advances in Integrative Anatomy and Evolutionary Biology 293:630-641.

Metzger MC, Hohlweg-Majert B, Schön R, Teschner M, Gellrich N-C, Schmelzeisen R, Gutwald R. 2007. Verification of clinical precision after computer-aided reconstruction in craniomaxillofacial surgery. Oral surgery, oral medicine, oral pathology, oral radiology, and endodontics 104:e1-e10.

Mischkowski RA, Zinser MJ, Kübler AC, Krug B, Seifert U, Zöller JE. 2006. Application of an augmented reality tool for maxillary positioning in orthognathic surgery – A feasibility study. Journal of Cranio-Maxillofacial Surgery 34:478-483.

Mitteroecker P, Bookstein F. 2007. The conceptual and statistical relationship between modularity and morphological integration. Systematic Biology 56:818-836.

Mitteroecker P, Bookstein F, Badyaev A. 2008. The Evolutionary Role of Modularity and Integration in the Hominoid Cranium. Evolution 62:943-958.

Mitteroecker P, Gunz P. 2009. Advances in Geometric Morphometrics. Evolutionary Biology 36:235-247.

Mitteroecker P, Gunz P, Bernhard M, Schaefer K, Bookstein FL. 2004. Comparison of cranial ontogenetic trajectories among great apes and humans. Journal of Human Evolution 46:679-698.

Montagu MFA. 1943. The mesethmoid-presphenoid relationships in the primates. American Journal of Physical Anthropology 1:129-141.

Moore WJ, Lavelle CLB. 1974. Growth of the Facial Skeleton in the Hominoidea. London: Academic Press.

Moss ML. 1997a. The functional matrix hypothesis revisited. 1. The role of mechanotransduction. American Journal of Orthodontics and Dentofacial Orthopedics 112:8-11.

Moss ML. 1997b. The functional matrix hypothesis revisited. 2. The role of an osseous connected cellular network. American Journal of Orthodontics and Dentofacial Orthopedics 112:221-226.

Moss ML. 1997c. The functional matrix hypothesis revisited. 3. The genomic thesis. American Journal of Orthodontics and Dentofacial Orthopedics 112:338-342.

Moss ML. 1997d. The functional matrix hypothesis revisited. 4. The epigenetic antithesis and the resolving synthesis. American Journal of Orthodontics and Dentofacial Orthopedics 112:410-417.

Moss ML, Young RW. 1960. A functional cranial approach to craniology. Am J Phys Anthropol 18:281-292.

Neeser R, Ackermann RR, Gain J. 2009. Comparing the accuracy and precision of three techniques used for estimating missing landmarks when reconstructing fossil hominin crania. American Journal of Physical Anthropology 140:1-18.

Neubauer S, Gunz P, Mitteroecker P, Weber GW. 2004. Three-dimensional digital imaging of the partial Australopithecus africanus endocranium MLD 37/38. Canadian Association of Radiologists journal 55:271-278.

O'Higgins P. 2000. The study of morphological variation in the hominid fossil record: biology, landmarks and geometry. Journal of Anatomy 197:103-120.

O´Higgins P, Pan RL. 2004. Advances in the analysis of form and pattern: facial growth in African colobines. In: Anapol F, German, R. Z. & Jablonski, N. G., editor. Shaping primate evolution. Cambridge: Cambridge University Press. p 24 - 44.

O'Higgins P, Cobb SN, Fitton LC, Gröning F, Phillips R, Liu J, Fagan MJ. 2011. Combining geometric morphometrics and functional simulation: an emerging toolkit for virtual functional analyses. Journal of Anatomy 218:3-15.

Ogihara N, Nakatsukasa M, Nakano Y, Ishida H. 2006. Computerized restoration of nonhomogeneous deformation of a fossil cranium based on bilateral symmetry. American Journal of Physical Anthropology 130:1-9.

Olariu A, Skog G, Hellborg R, Stenström K, Faarinen M, Persson P, Alexandrescu E. 2005. Dating of two Paleolithic human fossil bones from Romania by accelerator mass spectrometry. In: Olariu A, Stenström K, Hellborg R, editors. Applications of High-Precision Atomic and Nuclear Methods. Bucharest: Editura Academiei Romaine. p 222-226.

Olson EC, Miller RL. 1958. Morphological integration. Chicago: University of Chicago Press.

Pham AM, Rafii AA, Metzger MC, Jamali A, Strong BE. 2007. Computer modeling and intraoperative navigation in maxillofacial surgery. Otolaryngology -- Head and Neck Surgery 137:624-631.

Plavcan JM, Lockwood CA, Kimbel WH, Lague MR, Harmon EH. 2005. Sexual dimorphism in Australopithecus afarensis revisited: How strong is the case for a human-like pattern of dimorphism? Journal of Human Evolution 48:313-320.

Polanski JM, Franciscus RG. 2006. Patterns of craniofacial integration in extant Homo, Pan, and Gorilla. American Journal of Physical Anthropology 131:38-49.

Ponce de Leon MS. 2002. Computerized paleoanthropology and Neanderthals: The case of Le Moustier 1. Evolutionary Anthropology 11:68-72.

Ponce De León MS, Zollikofer CPE. 1999. New evidence from Le Moustier 1: Computer-assisted reconstruction and morphometry of the skull. The Anatomical Record 254:474-489.

Prag J, Neave R. 1997. Making Faces: Using Forensic and Archaeological Evidence. London: British Museum Press.

Preuschoft H, Witzel U. 2004. Functional structure of the skull in hominoidea. Folia Primatologica 75:219-252.

Prossinger H, Seidler H, Wicke L, Weaver D, Recheis W, Stringer C, Müller GB. 2003. Electronic removal of encrustations inside the Steinheim cranium reveals paranasal sinus features and deformations, and provides a revised endocranial volume estimate. The Anatomical Record Part B: The New Anatomist 273B:132-142.

Radinsky LB. 1968. A new approach to mammalian cranial analysis, illustrated with examples of prosimian primates. Journal of Morphology 124:167-180.

Raff RA. 1996. The shape of life: genes, development, and the evolution of animal form. Chicago: University of Chicago Press.

Rak Y. 1983. The Australopithecine face. New York: Academic Press.

Ravosa MJ. 1991. Interspecific perspective on mechanical and nonmechanical models of primate circumorbital morphology. American Journal of Physical Anthropology 86:369-396.

Ravosa MJ, Shea BT. 1994. Pattern in craniofacial biology: Evidence from the Old World Monkeys (Cercopithecidae). Int J Primatol 15:801-822.

Reno PL, Meindl RS, McCollum MA, Lovejoy CO. 2005. The case is unchanged and remains robust: Australopithecus afarensis exhibits only moderate skeletal dimorphism. A reply to. Journal of Human Evolution 49:279-288.

Rice DP. 2008. Developmental Anatomy of Craniofacial Sutures. In: Rice DP, editor. Craniofacial Sutures: Development, Disease and Treatment. Basel: Karger. p 1-22.

Richmond BG, Jungers WL. 1995. Size variation and sexual dimorphism in Australopithecus afarensis and living hominoids. Journal of Human Evolution 29:229-245.

Richmond BG, W BW, Grosse L, Dechow PC, Ross CF, Spencer MA, Strait DS. 2005. Finite element analysis in functional morphology. Anatomical Record Part a-Discoveries in Molecular Cellular and Evolutionary Biology 283A:259-274.

Richtsmeier J, Deleon V, Lele S. 2002. The promise of geometric morphometrics. American Journal of Physical Anthropology 119:63-91.

Rohlf FJ, Corti M. 2000. Use of Two-Block Partial Least-Squares to Study Covariation in Shape. Systematic Biology 49:740-753.

Rohlf FJ, Slice D. 1990. Extensions of the Procrustes Method for the Optimal Superimposition of Landmarks. Systematic Biology 39:40-59.

Rohlf JF, Marcus LF. 1993. A revolution morphometrics. Trends in ecology & evolution (Personal edition) 8:129-132.

Rolian C, Willmore K. 2009. Morphological Integration at 50: Patterns and Processes of Integration in Biological Anthropology. Evolutionary Biology 36:1-4.

Rosas A, Bastir M. 2004. Geometric morphometric analysis of allometric variation in the mandibular morphology of the hominids of Atapuerca, Sima de los Huesos site. The Anatomical Record Part A: Discoveries in Molecular, Cellular, and Evolutionary Biology 278A:551-560.

Ross C, Henneberg M. 1995. Basicranial flexion, relative brain size, and facial kyphosis in Homo sapiens and some fossil hominids. American Journal of Physical Anthropology 98:575-593.

Ross C, Strait D, Richmond B, Spencer M. 2002. In vivo bone strain and finite-element modeling of the anterior root of the zygoma of Macaca. American Journal of Physical Anthropology:133-133.

Ross CF. 2005. Finite element analysis in vertebrate biomechanics. Anatomical Record Part a-Discoveries in Molecular Cellular and Evolutionary Biology 283A:253-258.

Ross CF, Ravosa MJ. 1993. Basicranial flexion, relative brain size, and facial kyphosis in nonhuman primates. American Journal of Physical Anthropology 91:305-324.

Rubin DB. 1976. Inference and missing data. Biometrika 63:581-592.

S.-H L. 2005. Patterns of size sexual dimorphism in Australopithecus afarensis: Another look. HOMO - Journal of Comparative Human Biology 56:219-232.

Sachs L. 2004. Angewandte Statistik. Anwendung statistischer Methoden. Berlin-Heidelberg-New-York: Springer Verlag.

Schaefer K, Lauc T, Mitteroecker P, Gunz P, Bookstein FL. 2006. Dental Arch Asymmetry in an Isolated Adriatic Community. American Journal of Physical Anthropology 129:132-142.

Schlosser G. 2002. Modularity and the units of evolution. Theory in Biosciences 121:1-80.

Schmelzeisen R, Gellrich NC, Schoen R, Gutwald R, Zizelmann C, Schramm A. 2004. Navigation-aided reconstruction of medial orbital wall and floor contour in cranio-maxillofacial reconstruction. Injury 35:955-962.

Schumacher GH. 1997. Principles of skeletal growth. In: Dixon AD, Hoyte DA, Rönning O, editors. Fundamentals of craniofacial growth. Boca Raton & New York: CRC Press. p 1 – 23.

Schwartz JH, Tattersall I. 2002a. Craniodental Morphology of Early Hominids (Genera Australopithecus, Paranthropus, Orrorin), and Overview (Volume 4). Hoboken, New Jersey: Wiley-Liss.

Schwartz JH, Tattersall I. 2002b. The Human Fossil Record, Terminology and Craniodental Morphology of Genus Homo: I (Europe): John Wiley & Sons.

Schwartz, J. H. and I. Tattersall (2010). "Fossil evidence for the origin of Homo sapiens." American Journal of Physical Anthropology 143(S51): 94-121.

Scott JE, Stroik LK. 2006. Bootstrap tests of significance and the case for humanlike skeletal-size dimorphism in Australopithecus afarensis. Journal of Human Evolution 51:422-428.

Selenka E. 1898. Menschenaffen (Anthropomorphae) : Studien über Entwickelung und Schädelbau. Erste Lieferung: Rassen, Schädel und Bezahnung des Orang Utan. Sitz Königl Preuss Akad Wissens Berlin 16:1–92.

Seth D D. 2005. Are the differences between Stw 431 (Australopithecus africanus) and A.L. 288-1 (A. afarensis) significant? Journal of Human Evolution 49:143-154.

Shea BT. 1985. On aspects of skull form in African apes and orangutans, with implications for hominoid evolution. American Journal of Physical Anthropology 68:329-342.

Shea BT. 1986. On Skull Form and the Supraorbital Torus in Primates. Current Anthropology 27:257-260.

Shea BT. 1988. Phylogeny and skull form in the hominoid primates. In: Schwartz JH, editor. Orang-utan Biology. Strasbourg Oxford University Press.

Sirianni JE, Swindler DR. 1979. A review of postnatal craniofacial growth in Old World monkeys and apes. Yrbk Phys Anthropol 22:80-104.

Slice DE. 1998. Morpheus et al.: software for morphometric research. In, Revision 1-30-98-beta ed. Department of Ecology and Evolution, State University of New York, Stony Brook.

Slice DE. 2001. Landmark coordinates aligned by Procrustes analysis do not lie in Kendall's shape space. Syst. Biol. 50:141–149.

Slice DE. 2005. Modern morphometrics. In: Slice DE, editor. Modern Morphometrics In Physical Anthropology. New York: Kluwer Acad./Plenum. p 1–45.

Slice DE, Ross A. 2009. 3D-ID: geometric morphometric classification of crania for forensic scientists. In. p Version 1.0 (16.01.2010), http://www.2013d-id.org

Slice DE, BooksteinMarcus LF. 2009b. A Glossary for Geometric Morphometrics, http://life.bio.sunysb.edu/morph/glossary/gloss1.html.

Soficaru A, Petrea C, Dobos A, Trinkaus E. 2007. The Human Cranium from the Pestera Cioclovina Uscata, Romania. Curr. Anthropol. 48:611-619.

Solla HE, Iscan MY. 2001. Skeletal remains of Dr. Eugenio Antonio Berríos Sagredo. Forensic Science International 116:201-211.

Spatz WB. 1968. Die Bedeutung der Augen für die sagittale Gestaltung der Schädels von Tarsius (Prosimiae, Tarsiiformes). Folia Primatol 9:22-40.

Spoor F, Zonneveld F, Macho GA. 1993. Linear measurements of cortical bone and dental enamel by computed tomography: applications and problems. American Journal of Physical Anthropology 91:469−484.

Starck D. 1953. Morphologische Untersuchungen am Kopf der Säugetier besonders der Prosimier, ein Beitrag zum Problem des Formwandels des Säugerschädels. Z Wiss Zool 157:169-219.

Starck D. 1979. Vergleichende Anatomie der Wirbeltiere, II. Berlin: Springer Verlag.

Strait D, Richmond B, Ross C, Spencer M. 2002. Finite element analysis of a macaque skull: applications for functional morphology. American Journal of Physical Anthropology:149-149.

Strait DS, Grine FE, Moniz MA. 1997. A reappraisal of early hominid phylogeny. Journal of Human Evolution 32:17-82.

Strait DS, Grosse IR, Dechow PC, Smith AL, Wang Q, Weber GW, Neubauer S, Slice DE, Chalk J, Richmond BG, Lucas PW, Spencer MA, Schrein C, W BW, Byron C, Ross CF. 2010. The Structural Rigidity of the Cranium of Australopithecus africanus: Implications for Diet, Dietary Adaptations, and the Allometry of Feeding Biomechanics. The Anatomical Record: Advances in Integrative Anatomy and Evolutionary Biology 293:583-593.

Strait DS, Ross CF. 1999. Kinematic data on primate head and neck posture: Implications for the evolution of basicranial flexion and an evaluation of registration planes used in paleoanthropology. American Journal of Physical Anthropology 108:205-222.

Strait DS, Weber GW, Neubauer S, Chalk J, Richmond BG, Lucas PW, Spencer MA, Schrein C, Dechow PC, Ross CF, Grosse IR, W BW, Constantino P, Wood BA, Lawn B, Hylander WL, Wang Q, Byron C, Slice DE, Smith AL. 2009. The feeding biomechanics and dietary ecology of Australopithecus africanus. Proceedings of the National Academy of Sciences.

Strait DS, W BW, Richmond BG, Ross CF, Dechow PC, Spencer MA, Wang Q. 2008. Craniofacial Strain Patterns During Premolar Loading: Implications for Human Evolution. Developments in Primatology-Progress and Prospects: 173-198.

Stringer CB. 1985 Middle Pleistocene hominid variability and the origin of Late Pleistocene humans. New York: Alan R. Liss.

Szombathy J. 1900. Un crâne de la race Cro-Magnon trouvé en Moravie. 12th Int. Cong. Anthropol. Préhist. Archaeol. 1900:133-140.

Szombathy J. 1925. Die diluvialen Menschenreste aus der Fürst-Johannes-Höhle bei Lautsch in Mähren Eiszeit 2:1-34.

Tang M, Mao J. 2006. Matrix and gene expression in the rat cranial base growth plate. Cell and Tissue Research 324:467-474.

Tattersall I, Sawyer GJ. 1996. The skull of "Sinanthropus" from Zhoukoudian, China: a new reconstruction. Journal of Human Evolution 31:311-314.

Taylor KT. 2001. Forensic Art and Illustration. New York: CRC Press.

Thenius E. 1970. Zum problem der Airorynchie des Saeugetierschaedels: Ein Deutungsversuch. Zool Anz 185:159-172.

Thompson DAW. 1917. On growth and form. Cambridge: Cambridhe University Press.

Tobias PD. 1967. Olduvai Gorge Vol. 2: The cranium and maxillary dentition of Australopithecus (Zinjanthropus) boisei. Cambridge: Cambridge: University Press.

Toga AW, Thompson PM. 2003. Mapping brain asymmetry. Nat Rev Neurosci 4:37-48.

Ubelaker DH, Bubniak E, O'Donnell G. 1992. Computer-assisted photographic superimposition. Journal of Forensic Sciences 37:750–762.

Vandermeulen D, Claes P, Loeckx D, De Greef S, Willems G, Suetens P. 2006. Computerized craniofacial reconstruction using CT-derived implicit surface representations. Forensic Science International 159:S164-S174.

Vogel C. 1966. Morphologische Studien am Gesichtsschädel catarrhiner Primaten. Bibl. Primatol. 4:1-226.

Voss PJ, Leow AM, Schulze D, Metzger MC, Liebehenschel N, Schmelzeisen R. 2009. Navigation-guided resection with immediate functional reconstruction for high-grade malignant parotid tumour at skull base. International Journal of Oral and Maxillofacial Surgery 38:886-890.

Watson PJ, O'Higgins P, Fagan MJ, Dobson CA. 2011. Validation of a Morphometric Reconstruction Technique Applied to a Juvenile Pelvis. Proceedings of the Institution of Mechanical Engineers, Part H: Journal of Engineering in Medicine 225:48-57.

Weber, G, Gunz, P, Mitteroecker, P, Thackeray, F, and Bookstein, F (2003). Skull Reference Models (SRM) and the ontogeny of A-africanus. AMERICAN JOURNAL OF PHYSICAL ANTHROPOLOGY(Suppl. 36):221-222.

Weber GW, Bookstein FL. 2011. Virtual Anthropology: A guide to a new interdisciplinary field. Berlin, Heidelberg, New York: Springer.

Weber GW, Bookstein FL, Strait DS. 2011. Virtual anthropology meets biomechanics. Journal of biomechanics 44:1429-1432.

Weber GW, Gunz P, Mitteroecker P, Stadlmayr A, Bookstein FL, Seidler H. 2006. External geometry of Mladec neurocrania compared with anatomically modern humans and Neanderthals. In: Teschler-Nicola M, editor. Early modern humans at the Moravian gate: The Mladec caves. Wien: Springer. p 453-471.

Weidenreich F. 1941. The brain and its role in the phylogenetic transformation of the human skull. Trans Am Philos Soc Phila 31:321-442.

Weisstein EW. 2012. "Rigid Motion." In: MathWorld--A Wolfram Web Resource. http://mathworld.wolfram.com/RigidMotion.html

White TD, Folkens PA, 1991. Human Osteology. Academic Press, San Diego.

Wild EM, Teschler-Nicola M, Kutschera W, Steier P, Trinkaus E, Wanek W. 2005. Direct dating of Early Upper Palaeolithic human remains from Mladec. Nature 435:332-335.

Wilkinson C. 2004. Forensic Facial Reconstruction. Cambridge Cambridge University Press.

Wilkinson C, Neave R. 2001. Skull re-assembly and the implications for forensic facial reconstruction. Science & justice : journal of the Forensic Science Society 41:233-234.

Wilkinson CM. 2006. Facial Anthropology and Reconstruction. In: Thompson T, Black S, editors. Forensic Human Identification: An Introduction. Boca Raton: Florida: Taylor & Francis Group. p 231 - 254.

Willmore KE, Klingenberg CP, Hallgrímsson B. 2005. The relationship between fluctuating asymmetry and enviromental variance in rhesus macaque skulls. Evolution 59:898-909.

Winkler L. 1988. Sexual dimorphism in exocranial and endocranial dimensions. In: Schwartz J, editor. orangutan biology. New York: Oxford university Press. p 225-232.

Winkler L. 1991. Morphology and variability of masticatory structures in the orangutan. International Journal of Primatology 12:45-65.

Winther RG. 2001. Varieties of modules: kinds, levels, origins, and behaviors. J Exp Zool 291:116–129.

Witzel U, Preuschoft H, Sick H. 2004. The role of the zygomatic arch in the statics of the skull and its adaptive shape. Folia Primatologica 75:202-218.

Wolpoff MH, Frayer DW, Jelínek J. 2006. Aurignacien female crania and teeth from the Mladec Caves, Moravia. In: Teschler-Nicola M, editor. Early modern humans at the Moravian gate: The Mladec caves. Wien: Springer. p 273-340.

Wong T-Y, Fang J-J, Chung C-H, Huang J-S, Lee J-W. 2005. Comparison of 2 methods of making surgical models for correction of facial asymmetry. Journal of Oral and Maxillofacial Surgery 63:200-208.

Xia JJ, Gateno J, Teichgraeber JF, Christensen AM, Lasky RE, Lemoine JJ, Liebschner MAK. 2007. Accuracy of the Computer-Aided Surgical Simulation (CASS) System in the Treatment of Patients With Complex Craniomaxillofacial Deformity: A Pilot Study. Journal of oral and maxillofacial surgery : official journal of the American Association of Oral and Maxillofacial Surgeons 65:248-254.

Yoshino M, Matsuda H, Kubota S, Imaizumi K, Miyasaka S, Seta S. 1997. Computer-assisted skull identification system using video superimposition. Forensic Science International 90:231-244.

Zelditch ML, Swiderski DL, Sheets HD, Fink WL. 2004. Geometric Morphometrics for biologists. Amsterdam/Boston/Heidelberg: Elsevier Academic Press.

Zingeser MR. 1973. Dentition of Brachyteles arachnoides with reference to alouattine and ateline affinites. Folia Primatol 20:351-390.

Zollikofer CPE, De Leon MSP, Martin RD. 1998. Computer-assisted paleoanthropology. Evolutionary Anthropology 6:41-54.

Zollikofer CPE, Ponce de Leon MS. 2005. Virtual Reconstruction: A Primer in Computer-Assisted Paleontology and Biomedicine. Hoboken, New Jersey: John Wiley & Sons Inc.

Zollikofer CPE, Ponce de León MS. 2002. Visualizing patterns of craniofacial shape variation in Homo sapiens. Proceedings of the Royal Society of London. Series B: Biological Sciences 269:801-807.

Zollikofer CPE, Ponce de Leon MS, Lieberman DE, Guy F, Pilbeam D, Likius A, Mackaye HT, Vignaud P, Brunet M. 2005. Virtual cranial reconstruction of Sahelanthropus tchadensis. Nature 434:755-759.

Zollikofer CPE, Ponce de Leon MS, Martin RD, Stucki P. 1995. Neanderthal computer skulls. Nature 375:283-285.

9. APPENDICES

Appendix 1 R-script: Generalized Procrustes Analysis (GPA; the R package "shapes" is mandatory; adapted from Dr. S. Katina)

```
Library(shapes)
"GPAcorrected" <- function(ARRAY) { # ARRAY of row coordinates
k <- dim(ARRAY)[1]
d <- dim(ARRAY)[2]
n <- dim(ARRAY)[3]
data.gpa <- procGPA(ARRAY) # GPA
data.psc <- data.gpa$rotated # Procrustes shape coordinates
data.CS <- data.gpa$size     # Centroid size (CS)
data.psccor1 <- array(0,c(k,d,n))
CS <- rep(0,n) # centroid size
for (i in 1:n){
CS[i] <- sqrt(sum((data.psc[,,i] - rep(1,k)%*%t(apply(data.psc[,,i],2,mean)))^2))
data.psccor1[,,i] <- data.psc[,,i]/CS[i]  # correction of the scaling step
}
data.gpa.cor <- procGPA(data.psccor1)
data.psccor2 <- data.gpa.cor$rotated # Procrustes shape coordinates
data.mean <- data.gpa.cor$mshape # Procrustes mean shape
data.CScor2 <- data.gpa.cor$size     # Centroid size (CS)
results <- list(ProcrustesShapeCoordinates = data.psccor2, CScor = data.CScor2, CS = data.CS,
ProcrustesMeanShape = data.mean)
return(results)
}
```

Appendix 2 Anatomical landmarks and definitions (Martin and Saller, 1957; White and Folkens, 1991)

Cranial landmarks	Definitions
Midline	
Inion	Point at which the superior nuchal lines merge in the midline. Located below the external occipital protuberance
Lambda	The apex of the occipital bone at its junction with the parietals, in the midline – where the lambdoidal and sagittal sutures meet
Opisthion	Midline point at the posterior margin of the foramen magnum – taken on rim of the foramen or the lower edge of the margin of the foramen
Basion	On the anterior border of the foramen magnum (opposite opisthion), in the midline
Sphenobasion	Median sagittal point taken on basio - spehno synchorodrosis
Staphylion	Point on the interpalatal suture where a line between the deepest parts of the notches at the rear of the palate crosses the midline
Sutura palatina mediana & transversa	Anterior most point on the midline of transverse palatine bone
Bregma	Posterior border of the frontal bone in the median plane
Glabella	Point on median sagittal plane, between the supercillary arches. It serves as most protruding forward point at the head in ear - eye level. Most anterior midline point on the frontal

	bone
Nasion	Intersection of the fronto‐nasal suture and the median plane
Rhinion	Midline point at the inferior free end of the internasal suture
Nasiospinale	Thin projection of bone on the midline at the inferior margin of the nasal aperture
Prosthion	Median sagittal (antero‐inferior) most forward projecting portion of premaxilla
Alveolare	midline point at the inferior tip of the bony septum between the upper central incisors – below prosthion
Incision	Point on the occlusal surface between the central incisors
Incisivion	Midpoint on posterior end of foramen
Orale	The point at the anterior edge of the hard palate located on the posterior edge of the alveoli of the two upper central incisors, connecting line intersects the midsagittal
Dorsum sellae midsagittal	Midsagittal point on the dorsum sellae between posterior clinoid processes
Jugum sphenoidale midsagittal	Most posterior midsagittal point on the jugum sphenoidale between anterior clinoid processes
Posterior limit of the cribriform plate	Posterior limit of the cribriform plate at the intersection with the planum sphenoidale
Anterior limit of the cribriform plate	Anterior limit of the cribriform plate
Bilateral	
Condylus occipitalis posterior	Posterior apex (midpoint) on occipital condyle – taken on the condyle
Condylus occipitalis anterior	Anterior apex (midpoint) on occipital condyle – taken on the condyle
Jugular foramen Ant	Taken on the anterior most point of the foramen, on the occipital bone.
Postglenoid	Most inferior point on the postglenoid process – could be below mid‐point in mandibular fossa
Foramen ovale	Lateral point on the foramen
Auriculare	Point vertically above the center of the external auditory porus at the root of the zygomatic process, a few millimeters above porion
Zygotemporale inferior	Anteroinferior point of zygomaticomaxillary suture, in antero‐lateral view
Zygotemporale superior	Anterosuperior point of zygomaticomaxillary suture
Frontomalare temporale	The most lateral point of the frontozygomatic suture. The point is located where the lateral surface of the zygomatic process of frontal bone is descending into the frontal process of the zygomatic bone
I1‐I2 inter‐alveolar septum	Point of contact – on the alveolar bone – between the incisors
I2‐canine contact	Point of contact between 2nd incisor and canine – taken on the alveolar bone
Canine‐P3 septum	Point of contact between Canine‐P3 – on alveolar bone
P3‐P4 septum	Point of contact between P3‐P4 – on alveolar bone
P4‐M1 septum	Point of contact between P4‐M1 – on the alveolar bone
M2‐M3 septum	Point of contact between M2‐M3 – on the alveolar bone
M1‐M2 septum	Point of contact between M1‐M2 – on the alveolar bone
Distal M3	Midpoint on distal margin of M3 – point taken on alveolar bone
Zygomaxillare	Most inferior point on the zygomaticomaxillary suture
Foramen infraorbitale	Midpoint on superior edge of foramen
Jugale	The point in the depth of the notch between the temporal and frontal processes of the zygomatic
Stephanion	Point where the coronal suture crosses the temporal line

Frontotemporale	The point where the temporal line reaches its most anteromedial position on the frontal bone
Frontomalare-orbitale	The one point on the lateral orbital rim at the juxtaposition with the suture frontozygomatic.
Torus inferior	Point on inferior margin of supraobrital torus roughly at the middle of the orbit
Frontal - nasal - maxillary bone	Point where the frontonasal crosses the frontomaxillary suture
Zygoorbitale	Zygomaticomaxillary suture impinges the orbital rim
Sutura nasomaxillaris - Apertura piriformes	Nasomaxillary suture impinges piriform aperture
Foramen palatinum majus	The point on the posterior edge of the greater palatine foramen
Sutura sphenozygomatica - Fissura orbitalis	Sphenozygomatic suture hits the inferior orbital fissure
Canalis caroticus	Posterolateral point on carotid canal
Sutura occipitomastoidea - Foramen jugulare	Most poterio‑lateral point on the foramen, taken on the occipital end of the suture
Most lateral point of ala minor	Most lateral point of ala minor
Sphenofrontal suture hits cribriform plate	Sphenofrontal suture hits cribriform plate
Processus clinoideus anterior	Tip of the anterior clinoid processus
Mandibular	
Infradentale	The apex of the septum between the mandibular central incisors
Linguale	intersection between the curves Sy and IA
Mental foramen	intersection of a centerline (the middle of the canal) with the conceptual extension of the surface
Mandibular foramen	point on the mandibular foramina, under the lingula mandibulæ.
Tip of the coronoid	extreme of the curves AR and Co merged together
Top of the condyle	point where the surface normal of the condyle is perpendicular to a best fit plane formed by the tip of the coronoid, medial extremity of the condyle and laterl extremity of the condyle
Medial extremity of the condyle	point where the surface normal of the condyle is perpendicular to the symmetry plane
Lateral extremity of the condyle	point where the surface normal of the condyle is perpendicular to the symmetry plane
Midsymphysis	points on the plane curve cut by the midsaggital plane (Sy)
Right outer alveolar	points along the outer alveolar ridge (OA)
Right inner alveolar	points along the inner alveolar ridge (IA)
Right anterior ramus	points along the anterior ramus ridge (AR)
Right coronoid	points along the coronoid ridge (Co)
Right inferior border	points along the inferior and posterior borders of the ramus (IB)

Appendix 3 Thin plate splines and sliding semilandmarks

Below are the standard TPS formulas according to Bookstein (1997). In three dimensions, let U be the function $U(\sim r) = |r|$, and choose a reference shape with a set of landmarks $P_i = (x_i, y_i, z_i)$, $i = 1,\ldots, k$. For three dimensional data, let U be $U_{ij} = U(P_i - P_j)$, and arrange the matrices

$K = \begin{pmatrix} 0 & U_{12} & \cdots & U_{1k} \\ U_{21} & 0 & \cdots & U_{2k} \\ \vdots & \vdots & \ddots & \vdots \\ U_{k1} & U_{k2} & \cdots & 0 \end{pmatrix}, Q = \begin{pmatrix} 1 & x_1 & y_1 & z_1 \\ 1 & x_2 & y_2 & z_2 \\ \vdots & \vdots & \vdots & \vdots \\ 1 & x_k & y_k & z_k \end{pmatrix}$, $L = \begin{pmatrix} K & Q \\ Q^t & O \end{pmatrix}$ in which O is a 4×4 matrix of zeros. The thin-plate spline $f(P)$ with values (heights) h_i at points $P_i = (x_i, y_i, z_i)$, $i = 1,\ldots, k$, is the function $f(P) = \sum_{i=1}^{k} w_i U(P - P_i) + a_0 + a_x x + a_y y + a_z z$ where w=($w_1,\ldots,w_k$, a_0, a_x, a_y, a_z)^t=L^{-1}h with h=($h_1,\ldots,h_k$,0,0,0,0)^t. Then $f(P_i) = h_i$ follows for all i: f interpolates the heights h_i at the landmarks P_i. Futhermore, the function f has the minimum bending energy $\iiint_{R^3} \sum \sum_{i,j=1,2,3} \left(\frac{\partial^2 f}{\partial x_i \partial x_j} \right)^2$ of all functions that interpolate heights h_i. This integral is proportional to $-W^t h = -h_k^t L_k^{-1} h_k$, in which L_k^{-1} (bending energy matrix) is the $k \times k$ submatrix of L^{-1}. h_k is the corresponding k-vector of the corresponding heights (h_1,h_2,…,h_k). This procedure is applied to each Cartesian coordinate of the target following: ($h = (x_1',\ldots, x_k', 0,0,0,0)$, $h = (y_1',\ldots, y_k', 0,0,0,0)$, and $h = (z_1',\ldots, z_k', 0,0,0,0)$).

For the estimation sliding semilandmarks on a tangent plane for every specimen with k landmarks in three dimensions, coordinates of anatomical and semilandmarks are order coordinatewise as the vector $Y^0 = (Y_{1x}\ldots Y_{kx}, Y_{1y}\ldots Y_{ky}, Y_{1z}\ldots Y_{kz})$, where $Y_{i_j} = Y_{i_j}^0 + T_j^1 \times v_j + T_j^2 \times w_j = Y_{i_j}^0 + T_j^1(v_{jx}, v_{jy}, v_{jz}) + T_j^2(w_{jx}, w_{jy}, w_{jz})$. The resulting matrix of directional constraints for the surface can be expressed as:

$$U(3k \times 2m): \begin{matrix} U_{i_j,j} = v_{jx} \\ U_{k+i_j,j} = v_{jy} \\ U_{2k+i_j,j} = v_{jz} \\ U_{i_j,j+m} = w_{jx} \\ U_{k+i_j,j+m} = w_{jy} \\ U_{2k+i_j,j+m} = w_{jz} \end{matrix}$$

, in which $j = 1,\ldots,k$, while all other elements are zero. The minimization of the two equations is $-Y^t \begin{pmatrix} L_k^{-1} & 0 & 0 \\ 0 & L_k^{-1} & 0 \\ 0 & 0 & L_k^{-1} \end{pmatrix} Y \equiv -Y^t L_k^{-1} Y$, and $T = -(U^t L_k^{-1} U)^{-1} U^t L_k^{-1} Y^0$ is solved by $U(3k \times 2m)$, analogues to $U(3k \times m)$ for curve semilandmarks.

Appendix 4 R-script: Principal component analysis and visualization of the shape deformation in the direction of the first principal component (PC1).

```
data.GPAt <- GPAcorrected(data.array[,,])          #GPA of the raw coordinates
LnCS<-log(data.GPAt$CS)                            #Log of Centroid Size
```

```
PSC.array <- data.GPAt$ProcrustesShapeCoordinates #Array of Procrustes shape coordinates
PSCmean <- data.GPAt$ProcrustesMeanShape          # Matrix of the consensus coordinates

k<-600 # number of landmarks
d<-3 # number of dimensions
n<-25 # number of specimens

####PCA in shape space
PSC.matrix <- matrix (0,n,k*d)
for (i in 1:n){
PSC.matrix [i,] <- c(PSC.array [,,i])
}

# Mean-centered data matrix
PSC.matrix.centered <- matrix (0,n,k*d)
for(i in 1:(k*d)){
PSC.matrix.centered [,i] <-scale(PSC.matrix [,i],center = T, scale = F)
}

S.estimate<-var(PSC.matrix.centered)   # variance-covariance matrix of the mean-centered data matrix
Eigen.Estimate<-eigen(S.Estimate)      # singular value decomposition
PCscores <- PSC.matrix.centered %*%Eigen.Estimate$vectors #Computation of the PC scores

# Example of visualization along PC1
Eigen1<-cbind(Eigen.Estimate$vectors[1:k,1], Eigen.Estimate$vectors[(k+1):2*k,1],
Eigen.Estimate$vectors[((2*k)+1):d*k,1])          #eigenvectors of the shapes coordinates
PC1.plus<- PSCmean + a*Eigen1                     # shape deformation along PC1, right side, “a” is a
magnification factor
PC1.minus<- PSCmean - a* Eigen1
```

Appendix 5 R-script: PLS function, visualization of shape changes along the first singular warp (SW1), and extraction of rigid motions

```
pls.centered <- function(M1, M2){  # M1 and M2: left and right data block, adapted from
„Morphometrics With R“ By J. Claude
  M1 <- scale(M1,scale = FALSE)   #  subtract mean from matrix
  M2 <- scale(M2,scale = TRUE)
  p1<-dim(M1)[2]; p2<-dim(M2)[2]; n<-dim(M1)[1]
  sM12<-svd(var(cbind(M1,M2))[1:p1, (p1+1):(p1+p2)])  # singular value decomposition
  vM12<-var(cbind(M1,M2))[1:p1, (p1+1):(p1+p2)]
  vM21<-var(cbind(M1,M2))[(p1+1):(p1+p2), 1:p1]
  v11<-var(M1)
  v22<-var(M2)
  D<-sM12$d; F1<-sM12$u; F2<-sM12$v
  Rv<-sum(diag(vM12%*%vM21))/sqrt(sum(diag(v11%*%v11))*sum(diag(v22%*%v22)))
  list(Rv=Rv, F1=F1, F2=F2, D=D, M1.center=M1, M2.center=M2)}

pan.sphe_max.PLS <- pls.centered(pan.sphenoid, pan.palate)   # pls on data matrix; sinlge species

# percent of variance expressed on each singular warp
pan.sphe_palate.SVperc <- round(pan.sphe_max.PLS $D/sum(pan.sphe_max.PLS $D),4)*100

panSW1.left <- t(pan.sphe_palate.PLS$F1)[1,]  # Loadings of the first singular vector, left block
panSW1.right <- t(pan.sphe_palate.PLS$F2)[1,]  # Loadings of the first singular vector, right block
```

```
panSW2.left <- t(pan.sphe_palate.PLS$F1)[2,]  # Loadings of the second singular vector, left block
panSW2.right <- t(pan.sphe_palate.PLS$F2)[2,]  # Loadings of the second singular vector, right block
panLVx1 <- pan.sphe_palate.PLS$M1.center %*% panSW1.left  #first singular warps, left block
panLVy1 <- pan.sphe_palate.PLS$M2.center %*% panSW1.right  #first singular warps, right block
panLVx2 <- pan.sphe_palate.PLS$M1.center %*% panSW2.left    #second singular warps, left block
panLVy2 <- pan.sphe_palate.PLS$M2.center %*% panSW2.right  # second singular warps, right
block

# correlation of the 2 blocks on the first SW1
pan.40Ind_coef1<-cor.test(panLVx1.40Ind ,panLVy1.40Ind , method="pearson")  # Pearson's
product-moment correlation

#Plot SW scores
par(mfrow=c(1,2))
SW1scores <- cbind(panLVx1 [,1],panLVy1 [,1])
plot(SW1scores,type="n",xlab="sphenoid shape, r = 0.61", ylab="palate rigid motion")
points(SW1scores[(males),1],SW1scores[(males),2], pch=19, cex=1.5)
points(SW1scores[(females),1],SW1scores[(females),2], pch=1, cex=1.5)
SW2scores <- cbind(panLVx2 [,1],panLVy2 [,1])
plot(SW2scores,type="n",xlab="sphenoid shape, r = 0.67", ylab=" palate rigid motion")
points(SW2scores[(males),1],SW2scores[(males),2], pch=19, cex=1.5)
points(SW2scores[(females),1],SW2scores[(females),2], pch=1, cex=1.5)

###Export shapes for visualization in AMIRA: Singular warps 1 (SW1)

# mean shapes
pan_sample_mean_sphenoid <- pan_meanshape[sphe.lms,]
pan_sample_mean_maxilla <- pan_meanshape[max.lms,]    ## the PMS for the warping in AMIRA
has to have lateral lms, otherwise the warping will fail

### SPHENOID SHAPES. shapes at min and max for SW1 values: sphenoid

SW1.target.left.min <- consensus + min(SW1scores[,1])*matrix(panSW1.left,12,3,byrow=F)
SW1.target.left.max <- consensus + max(SW1scores[,1])*matrix(panSW1.left,12,3,byrow=F)


### PALATE RIGID MOTION. Rigid motion at min and max for SW1 values: palate

## predict palate rigid motion (theta, x, and y) from from sphneoid SW1 scores (one by one)
## = regress theta, x, and y of pan on SW1.sphe scores
## no quadratic regression becasue this PLS is linear
## use centered values
#n<- number of individuals

## theta
pan.max_angles.centered <- matrix(0,n,1)
for (i in 1:n) {
pan.max_angles.centered [i,]<- pan.max_angles[i]-mean(pan.max_angles)
}
regr.theta.SW1sphe<-lm(pan.max_angles.centered~panLVx1)     # Formula for the regression
summary(regr.theta.SW1sphe)
#get the theta according to min SW1.scores
min.SW1_sphe.score<-min(panLVx1)
theta.at.min.SW1_sphe.score<
regr.theta.SW1sphe$coefficients[[1]]+regr.theta.SW1sphe$coefficients[[2]]*min.SW1_sphe.score
#-10.07950  ← negative angle: ventrally rotated
```

```
#get the theta according to max SW1.scores
max.SW1_sphe.score<-max(panLVx1)
theta.at.max.SW1_sphe.score<-
regr.theta.SW1sphe$coefficients[[1]]+regr.theta.SW1sphe$coefficients[[2]]*max.SW1_sphe.score
#6.869657  <-- positive angle: dorsally rotated


## centroid x
pan_.max_centx.centered <- matrix(0,40,1)
for (i in 1:n) {
pan_.max_centx.centered [i,]<- pan_s.max_centroids[i,1]-mean(pan_s.max_centroids[,1])
}
regr.x.SW1sphe<-lm(pan.max_centx.centered~panLVx1)      # Formula for the regression
summary(regr.x.SW1sphe)
#get the x according to min SW1.scores
min.SW1_sphe.score<-min(panLVx1)
x.at.min.SW1_sphe.score<-
regr.x.SW1sphe$coefficients[[1]]+regr.x.SW1sphe$coefficients[[2]]*min.SW1_sphe.score
#get the x according to max SW1.scores
max.SW1_sphe.score<-max(panLVx1)
x.at.max.SW1_sphe.score<-
regr.x.SW1sphe$coefficients[[1]]+regr.x.SW1sphe$coefficients[[2]]*max.SW1_sphe.score


## centroid y
pan_.max_centy.centered <- matrix(0,40,1)
for (i in 1:n) {
pan_.max_centy.centered [i,]<- pan_s.max_centroids[i,2]-mean(pan_s.max_centroids[,2])
}
regr.y.SW1sphe<-lm(pan.max_centy.centered~panLVx1)      # Formula for the quadratic regression
summary(regr.y.SW1sphe)
#get the y according to min SW1.scores
min.SW1_sphe.score<-min(panLVx1)
y.at.min.SW1_sphe.score<-
regr.y.SW1sphe$coefficients[[1]]+regr.y.SW1sphe$coefficients[[2]]*min.SW1_sphe.score
#get the y according to max SW1.scores
max.SW1_sphe.score<-max(panLVx1)
y.at.max.SW1_sphe.score<-
regr.y.SW1sphe$coefficients[[1]]+regr.y.SW1sphe$coefficients[[2]]*max.SW1_sphe.score


## get 3d coordinates for SW1: palate rigid motion

meanshape.palate <- Pan_meanshape[palate.mid.lms,]

# 3d rotation matrices  -> rotation about y-axis
rot.mat.3d.min.Ay <- rbind(c(cos(rad.theta.min ),0,sin(rad.theta.min )),c(0,1,0),c(-sin(rad.theta.min
),0,cos(rad.theta.min )))
rot.mat.3d.max.Ay <- rbind(c(cos(rad.theta.max ),0,sin(rad.theta.max )),c(0,1,0),c(-sin(rad.theta.max
),0,cos(rad.theta.max )))

# 3d translation <- keep org y-coords (because from the rotated bGPA coords I took the x and z-coords
[c(1,3)])
meanshape3d.trans.min <- (cbind((meanshape.palate[,1]+centx.min),meanshape.palate
[,2],(meanshape.palate [,3]+centy.min)))
```

```
meanshape3d.trans.max <- (cbind((meanshape.palate[,1]+centx.max),meanshape.palate
[,2],(meanshape.palate [,3]+centy.max)))

# export
palate_pos.SW1.min <- meanshape3d.trans.min%*%rot.mat.3d.min.Ay
palate_pos.SW1.max <- meanshape3d.trans.max%*%rot.mat.3d.max.Ay
```

Appendix 6 R-script: Generalized Procrustes Analysis, obtaining the final rotation matrix of each specimen (programmed together with Michael Coquerelle; adapted from „Morphometrics With R“ By J. Claude)

```
### full Procrustes superimposition of one individual (M1) onto another individual (M2)
fPsup<-function(M1, M2)
  {k<-ncol(M1)
  Z1<-trans1(centsiz(M1)[[2]])   #scaled LM configuration
  Z2<-trans1(centsiz(M2)[[2]])
  sv<-svd(t(Z2)%*%Z1)
  V<-sv$v; U<-sv$u; Delt<-sv$d
  sig<-sign(det(t(Z2)%*%Z1))
  Delt[k]<-sig*abs(Delt[k]) ; V[,k]<-sig * V[,k]
  Gam<-V%*%t(U)     # rotation matrix
  beta0<-sum(Delt)
  list(Mp1=beta0*Z1%*%Gam,Mp2=Z2,rotation=Gam,scale=beta0,DF=sqrt(1-beta0^2))}

### full GPA
p<-dim(A)[1]; k<-dim(A)[2]; n<-dim(A)[3]
fgpa2<-function(A)
  {p<-dim(A)[1]; k<-dim(A)[2]; n<-dim(A)[3]      #information about the size of an array
  temp2<-temp1<-array(NA, dim=c(p,k,n))          #empty array
  Siz<-numeric(n)
  for (i in 1:n)                    #translate and scale configurations to unit size → coords / CS
        {Acs<-centsiz(A[,,i])
         Siz[i]<-Acs[[1]]                  #CS of ind
         temp1[,,i]<-trans1(Acs[[2]])}   #scaled and then translated (= minus coords of centroid)
  iter<-0; sf<-NA  #intialize & set the type of objects that are going to be used for the iteration
  M<-temp1[,,1]    #use the first configuration as reference for the first superimposition
  for (i in 1:n)
     {temp1[,,i]<-fPsup(temp1[,,i],M)[[1]]}
 M<-mshape(temp1)                          #define a new consensus
 Qm1<-dist(t(matrix(temp1,k*p,n)))       #define quantaty Qm that must be minimized. Here
Qm is the sum of Proc distances between configs; calculate the square root of the sum of
squared diffeences
  Q<-sum(Qm1); iter<-0
  sc<-rep(1,n)                          #set the scaling factor to 1
  Z1.new<-array(0,c(p,k,n))    # set new array to collect the single individual rotation matrices
  V<-array(0,c(k,k,n))
  U<-array(0,c(k,k,n))
  DIAG<-matrix(0,n,k)
  phi.new<-array(0,c(k,k,n))
```

```
  beda<-rep(0,n)
  cum.rot.mat<-array((diag(x = 1, k, k)),c(k,k,n))      #creates an identity matrix for every
individual according to the dim(A); used for the start in the computation of the final rotation
matrix (product of all rotations)
  while (abs(Q)>0.00001){          #start the loop
     for (i in 1:n){                    #rotate and scale the configuration to the current consensus
       Z1.new[,,i]<-temp1[,,i]
       V[,,i]<-svd(t(M)%*%Z1.new[,,i])$v      #SVD of of new consensus and the individuals
after the first fPsup
       U[,,i]<-svd(t(M)%*%Z1.new[,,i])$u
       DIAG[i,]<-svd(t(M)%*%Z1.new[,,i])$d
       sig<-sign(det(t(Z1.new[,,i])%*%M))
       DIAG[i,k]<-sig*abs(DIAG[i,k])
       V[,k,i]<-sig*V[,k,i]
       phi.new[,,i]<-V[,,i]%*%t(U[,,i])     # rotation matrix: I need the final phi for every new
Z1<-temp1[,,i]
       beda[i]<-sum(DIAG[i,])         # overwritting function; should be n dimensions, e.g. list
       temp1[,,i]<-X<-sc[i]*Z1.new[,,i]%*%phi.new[,,i]}     # temp1 = rotated specimens
     M<-mshape(temp1)                                        #define a new consensus
     for (i in 1:n)                  #compute the rescaling factor and rescale superimposed configs
      {sf[i]<-sqrt(sum(diag(temp1[,,i]%*%t(M)))
        /(sum(diag(M%*%t(M)))*sum(diag(temp1[,,i]
        %*%t(temp1[,,i])))))
      temp2[,,i]<-sf[i]*temp1[,,i]}
     M<-mshape(temp2)          #compute a new consensus, new scale factors, and the
differece between the square roots of the sum of paired suared diffeences
     sc<-sf*sc
     Qm2<-dist(t(matrix(temp2,k*p,n)))
     Q<-sum(Qm1)-sum(Qm2)                          #until Q is not below the tolerence,
reiterate 6 and 7
     Qm1<-Qm2
     iter=iter+1
     temp1<-temp2
     for (i in 1:n) {
     cum.rot.mat[,,i]<-(cum.rot.mat[,,i])%*%(phi.new[,,i])}}   # cumulated rotation matrices of
all iterations
  list(rotated=temp2,iterationnumber=iter,Q=Q,intereuclidean.dist=Qm2,
mshape=centsiz(mshape(temp2))[[2]],
cent.size=Siz,rotation.mat=cum.rot.mat,translated.mat=temp1)}


##final roatation matrix of the specimens
rot.mat<-fgpa2(data)$rotation.mat    # final rotation matrix

#compute radiants
radiants.matrix<-matrix(0,(n+1),1)
for (i in 1:(n+1)) {
radiants.matrix[i,]<-acos(rot.mat[1,1,i])
}

#compute angles → used to extract the rigid motions
angles.matrix<-matrix(0,(n+1),1)
```

```
for (i in 1:(n+1)) {
angles.matrix[i,]<-(180/pi)*radiants.matrix[i,]
}
```

German summary p. 18 ff

Dipl. –Biol. Sascha Senck
Rauscherstrasse 7/6
1200 Vienna
Austria

Mobile phone: 0043660 1471025
E-mail: sascha.senck@univie.ac.at
Date of birth: 16th March 1980
Place of birth: Ludwigshafen am Rhein, Germany

EDUCATION HISTORY

2012 PhD in Biological Anthropology under the scientific direction of GW Weber. University of Vienna (Austria)

2007 Diploma: Anthropology, Paleoanthropology and Zoology with a major in Anthropology. Johannes Gutenberg – Universität Mainz (Germany)

FELLOWSHIP AND GRANT

03/2007 – 12/2009 Early Stage Researcher in the *European Virtual Anthropology Network – EVAN – Marie Curie Actions* MRTN-CT-2005-019564

01/2010 – 01/2012 NSF Hominid Grant 2007, NSF 01-120, "The Mechanics of Primate and Early Hominid Feeding within the Context of Hypotheses about Australopithecine Diets"

SCIENTIFIC COMMUNICATIONS – PODIUMS & POSTER(S)

International meetings with peer review submission.

2011 **Senck S**, Bookstein FL, Weber GW. (2011) *Morphological integration between palatal orientation, cranial base and orbits in Pan and Pongo*, Leipzig, Germany, 23rd – 24th September 2011. Oral presentation.

2011 **Senck S**, Bookstein FL, Weber GW. (2011). *Cross-species virtual reconstruction of fossil and extant hominoid crania.* American Association of Physical Anthropologists, Minneapolis, USA, 12th - 16th April 2011. Oral presentation.

2010 **Senck S**, Coquerelle M, Weber GW. (2010). *Covariation between facial and mandibular shape in Hylobates and Pongo with respect to facial orientation.* American Association of Physical Anthropologists, Alburquerque, USA, 14th - 17th April 2010. Poster.

2009 **Senck S**, Katina S, Henke W, Weber GW. (2009). *Craniofacial Shape Changes in Pongo pygmaeus pygmaeus – sexual dimorphism and bimaturism*. American Association of Physical Anthropologists, Chicago, USA, 31st March - 4th April 2009. Poster.

2008 **Senck S**, Bookstein FL, Weber GW. (2008). *Virtual reconstruction of hominoid crania: reconstructing one part from the rest*. European Anthropological Association Congress. Odense, Denmark, 27th - 31st August 2008. Oral presentation.

2008 Singh N, **Senck S** (2008). *Ontogeny of airorhynchy in male- female orangutans: analysis of palate and frontal bone*. American Association of Physical Anthropologists, Columbus, USA, 9th - 12th April 2008. Poster.

PUBLICATION(S)

International journals with peer review submission.

2011 Benazzi S, **Senck S** (2011). *Comparing 3-dimensional virtual methods for reconstruction in craniomaxillofacial surgery*. J Oral Maxillofac Surg. 69(4):1184-94.

2011 Kranioti EF, Holloway R, **Senck S**, Ciprut T, Grigorescu D, Harvati K (2011). *Virtual Assessment of the Endocranial Morphology of the Early Modern European Fossil Calvaria From Cioclovina, Romania.* The Anatomical Record: Advances in Integrative Anatomy and Evolutionary Biology 294:1083-1092.

TEACHING ACTIVITIES

2012 *Three-dimensional medical imaging. An introductionary workshop.* Edinburgh, Great Britain, 15th – 16th February. Co-organizor, lecturer, and supervision of participants.

2011 *Micro-Computer Tomographie und die Handhabung von Volumendaten*. Vienna, Austria, 19th - 20th May. Tutor.

2010 *Micro-Computer Tomographie und die Handhabung von Volumendaten*. Vienna, Austria, 6th - 7th December. Tutor.

2010 *Micro-Computer Tomographie und die Handhabung von Volumendaten*. Vienna, Austria, 13th - 14th May. Tutor.

2009 *Micro-Computer Tomographie und die Handhabung von Volumendaten*. Vienna, Austria, 7th - 8th December. Tutor.

2009 *Micro-Computer Tomographie und die Handhabung von Volumendaten*. Vienna, Austria, 18th - 19th May. Tutor.

2008 *Micro-Computer Tomographie und die Handhabung von Volumendaten*. Vienna, Austria, 14th - 15th December. Tutor.

2008 *Multivariate techniques for growth and evolution of form*, UNVI, Vienna, Austria, 6th- 10th July.

2008 *Klinorhynchy and airorhynchy: facial orientation in primates.* Workshop on bone histology and growh & growth and development of the craniofacial complex. Madrid, Spain, 28th - 30th May. Invited lecture.

ATTENDED WORKSHOPS

09/2010 Synergies in biomechanics and anthropology. University of Vienna, Vienna, Austria.

09/2009 Applying EVAN toolkit in VA, medicine, Industry. YORK, England.

07/2008 Multivariate techniques for growth and evolution of form, University of Vienna, Vienna, Austria.

05/2008 Bone histology and growth (CSIC) + growth and development of the craniofacial complex (DHAL) CSIC, Madrid, Spain.

03/2008 Brain evolution, development and morphometrics, ATOM, Paris, France.

11/2007 Functional morphology and evolution of mammalian dentition, RISE, Frankfurt/Main, Germany.

11/2007 Programming in R and the handling of sliding semi-landmarks in Edgewarp, warping in AMIRA. University of Vienna, Vienna, Austria.

10/2007 Rapid prototyping technology. ZUMT, Dornbirn, Austria.

10/2007 Nespos Training, NEMU, Mettman, Germany.

07/2007 Communication with broad public and journalists Language: German. GEO, Hamburg, Germany.

04/2007 Techniques for the quantification of growth and evolution of form. University of Toulouse, Toulouse, France.

COMPUTER SKILLS AND FOREIGN LANGUAGES

German native speaker
English fluent in reading and writing
French basic in reading and speaking

Computer skills: Amira, Rapidform, Edgewarp (Linux), Viewbox, Polyworks, Morphologika, Morpheus, ImageJ, Landmark, R software (programming statistical analyses), Open Office, Illustrator, Photoshop.